RE-ENTRY ⊕ SYSTEMS

DEPARTMENT

Philadelphia, Pa.
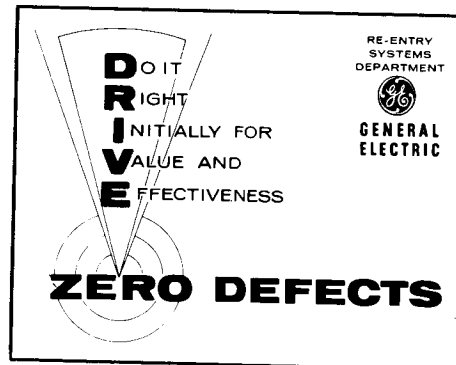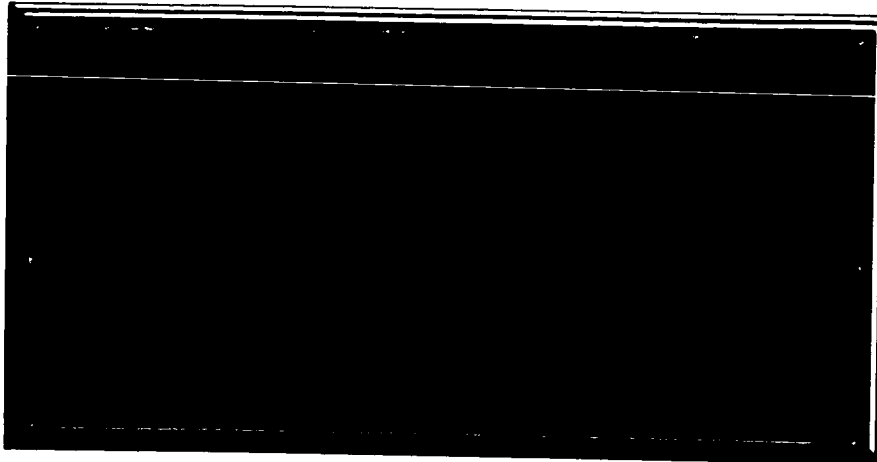
DRIVE
DO IT
RIGHT
INITIALLY FOR
VALUE AND
EFFECTIVENESS

ZERO DEFECTS

RE-ENTRY
SYSTEMS
DEPARTMENT

GE

GENERAL
ELECTRIC

GENERAL 🔵 ELECTRIC

FINAL ENGINEERING REPORT

AEROTHERMOELASTIC EFFECTS

ON UNMANNED ENTRY VEHICLES

FOR MARS

BY E.G.MENKES

PREPARED FOR

JET PROPULSION LABORATORY
CALIFORNIA INSTITUTE OF TECHNOLOGY
PASADENA, CALIFORNIA

25 OCTOBER 1966

GENERAL ⊛ ELECTRIC

i

FOREWORD

The purpose of this document is to present the final results of a study to determine the effects of aerothermoelastic effects on unmanned entry vehicles for Mars. The study was performed by the Re-Entry Systems Department, Missile and Space Division of the General Electric Company. The work was administered under the direction of the Jet Propulsion Laboratory, California Institute of Technology, Pasadena, California. Mr. J. Spiegal was project engineer for JPL.

The study was divided into seven phases, as follows:

> Phase   I - Vehicle Configuration Selection
> Phase   II - Pressure Distribution Definition
> Phase III - Thermal Distribution and Heat Shield Requirements
> Phase IV - Vehicle Design Specification
> Phase   V - Mode Shape and Frequency Determination
> Phase VI - Aerothermoelastic Evaluation
> Phase VII - Conclusions and Recommendations

Overall technical direction of this study was handled by T. E. Hess, Supervising Engineer, Optimization and Synthesis, Structural Mechanics, RSD. Cognizant Engineer was E. G. Menkes. Dr. J. C. Houbolt served as consultant to RSD during the course of the study. The final report includes the special efforts of several people at RSD. Special recognition is given to:

> G. Merlo: Vehicle Selection and Design
> A. Kirsch: Aerodynamic Flow Field
> W. Pyron: Modes and Frequencies
> E. Vogel: Heat Flux and Shield Design
> R. Marhefka: Flight Mechanics
> C. Kyriss: Aerodyamic Flow Field
> G. Kachadourian: Acoustic Noise Excitation

TABLE OF CONTENTS

LIST OF ILLUSTRATIONS

LIST OF ILLUSTRATIONS (Cont)

LIST OF TABLES

x

LIST OF TABLES (Cont)

SUMMARY

Entry vehicles designed for operation in the relatively low density level of the Mars atmosphere are examined for aerothermoelastic problems. These lightly loaded (low mass/cross-sectional area) vehicles tend to be relatively flexible. This characteristic, coupled with the deceleration loads, separated hot gas flow, oscillatory body motion, and thermal gradients in the shield raises the spector of aerothermoelastic problems. The specific phenomena investigated include flutter, buffeting forced vibration, acoustics, and static aeroelasticity. The results indicate no severe aerothermoelastic problems exist for the families of Mars entry vehicles investigated. This finding can be traced back to the fact that very low dynamic pressures exist for Mars entry so that there is negligible energy available in the airstream to excite the various aeroelastic phenomena.

SECTION 1

INTRODUCTION

Entry vehicles designed for operation in the low density atmosphere of Mars tend to be large, bluff, lightweight structures. Such structures are necessarily quite flexible, when compared to Earth entry vehicles, leading to significant structural deflections. The possible coupling of these deflections with aerodynamic forces, aggravated by entry heating, raises the specter of aerothermoelastic problems.

The objective of the present study is to identify potential aerothermoelastic problems; analyze the factors involved and recommend methods of solving or circumventing the problems identified. To accomplish this end, a set of typical vehicle configurations are selected, and examined for a variety of possible problem areas. These areas include flutter, buffeting, forced vibration, acoustics, and static aeroelasticity. The consequences of entry heating, including elevated material properties and thermal gradients, are considered in evaluating the severity of each problem area.

Before considering the actual study, it is informative and instructive to note some of the differences in the fundamental flight parameters for entry at Earth and at Mars. From the following table, it is seen that the entry velocities are approximately the same, but that the

Parameter	Mars	Earth
V_e Velocity (FPS)	23,000	24,000
ρ_o Density (Slug/ft^3)	.000025	.0024
q_∞ Dynamic Pressure (PSF)	450	300,000

Martian atmospheric density is extremely small compared to the density on Earth. Thus q (dynamic pressure) for Mars entry is very small compared to Earth entry. For example a maximum q for Mars entry appears to be about 450 PSF, while representative values for Earth entry may be on the order of 300,000 PSF. Thus because the q involved for Mars entry is so small, it might be anticipated that the possibility of encountering aeroelastic problems is a minimum. The idea is that with the low q's, there is little energy contained in the airstream to cause difficulty.

1

Three different shape families of entry vehicles are investigated as shown in Figure 1. These are the sphere-cap (Apollo type), the sphere-cone ("coolie hat"), and the smooth-flare (tension shell). With these forebody shapes, several different aft bodies shapes are considered. These are the open back (i. e. no aft body), convex cone frustum, and spherical cap.

A matrix of representative structural design concepts are established for each of the entry vehicle families. Dimensions and sizes are determined from the critical loading conditions associated with predicted six degree of freedom entry trajectories (Table 1). Three types of construction, unstiffened monocoque, ring-stiffened monocoque, and honeycomb sandwich are evaluated for the shell structures. Materials considered in choosing the optimum material/construction concept are fiberglass, beryllium, magnesium, and aluminum.

The approach used in this study was to design a matrix of Mars entry vehicles, investigate their aerothermoelastic characteristics, and reach conclusions. Recommendations are then made for a broad range of Mars vehicle designs based on these specific evaluations.

SECTION 2

DEFINITION OF PROBLEMS INVESTIGATED

Two distinct categories of aerothermoelastic phenomena are examined in this study, stability problems and response problems. The specific problem areas evaluated are:

A. Static and Dynamic Instabilities

   (1) Static Divergence

   (2) Longitudinal (or Accordion) Mode Instability

   (3) Flexible "Shuttlecock" Instability

   (4) Spin-Short Period Resonance

   (5) Panel Flutter

B. Forced Response

   (1) Acoustic Noise Excitation

   (2) Shock Instability

   (3) Buffeting and Wake Noise

Each of these items are now discussed further and sketches are given to depict the nature of the potential problem better.

A. (1) Static Divergence:

Static divergence is defined, for purposes of this study, simply as static instability, or buckling due to the quasi-steady aerodynamic loading. It can be investigated either with or without considering the change in pressure distribution which occurs as deformation takes place, and some consideration to this change was given in this study.

Two basic types of static divergence problems are envisioned, "umbrella collapse" for the sphere-cone, and "nose divergence" for the tension shell.

Sphere-Cone/Open Back ("Umbrella Collapse"):
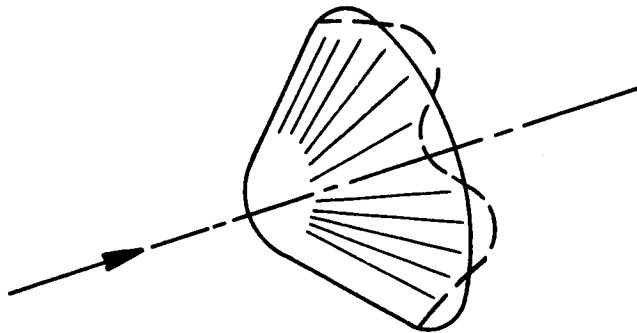
The first possible failure mode is described by the phrase used above, umbrella collapse. It is associated with the induced circumferential compressive stresses due to the pressure behind the bow shock. If the shell were designed without an aft ring, that is, having a high drag skirt with all internal mass concentrated in the nose, then the compressive stresses developed in the shell could cause buckling. In this study, on the other hand, an aft ring is provided to allow for vehicle mounting, handling, etc.

In this case the question to be answered is "what size ring is necessary to prevent this type of instability?" In the course of the vehicle design specification this ring was sized based on a criteria derived from traditional considerations and past experience. Subsequently, this criteria is re-examined to insure that it is adequate for the applications of interest here, namely, large blunt shells.

The net result of studying the umbrella collapse mode is the verification of current criteria for aft ring design.

4

Tension Shell Nose Divergence:
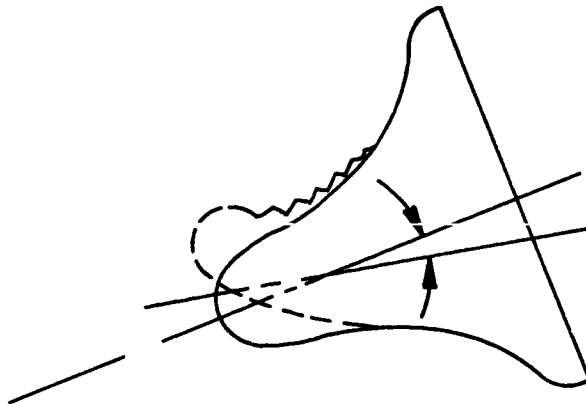
During the vehicle design phase of this study, structural gages were specified for a tension shell design of the external shape supplied by JPL. Included in this design specification is an evaluation of the shell capability to withstand angle of attack loading. Obviously, if the body bending loads are high enough, the state of tension will not be obtainable on one side of the vehicle. If this is so, it is necessary to determine whether the aeroelastic effects aggravate the situation.

A. (2) Longitudinal or Accordion Mode Instability of Tension Shell:

With the payload mounted in the nose of the vehicle and a large heavy aft ring inherent in the tension shell design, the possibility exists that aerodynamic coupling with the main longitudinal mode of the vehicle could occur.
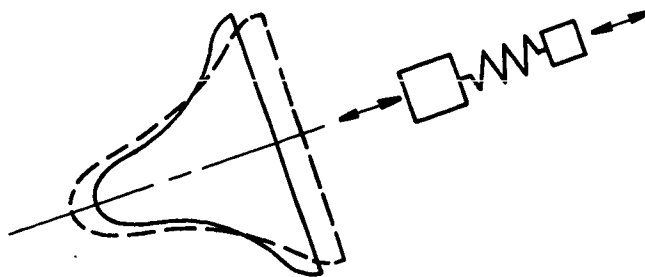
This phenomenon occurs due to the fact that as the shell vibrates in this mode, it induces local motion in the air resulting in unsteady aerodynamic flow. This unsteady flow may couple with the structural modes and lead to a self-induced vibration condition analogous to that of wing flutter.

A. (3) Flexible "Shuttlecock" Instability:
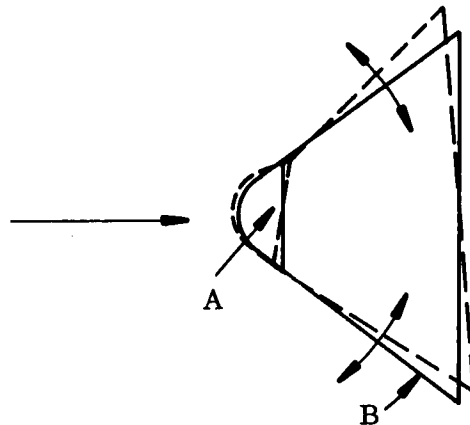
This is a "free-free" type or first order mode where mass A (the payload package mounted in the nose) rotates in opposition to cone B. With this mode two problems must be investigated:

    a. Coupling of this mode with the induced oscillating air loads leading to another type flutter condition.

    b. Coupling of this mode with either or both the short period and spin frequencies.

The first problem of self-induced oscillation is examined in the same way as the accordion mode, since it is really the same phenomenon. The only difference is that the mode being excited is different.

For the second problem, a comparison is made of the proximity of the structural frequencies to the spin and short period frequencies. If they are sufficiently close, the extent of resonance and motion amplification must be considered and consideration given to avoidance of the problem by changing structural stiffness and/or the motion frequencies.

6

A. (4) Spin – Short Period Resonance:
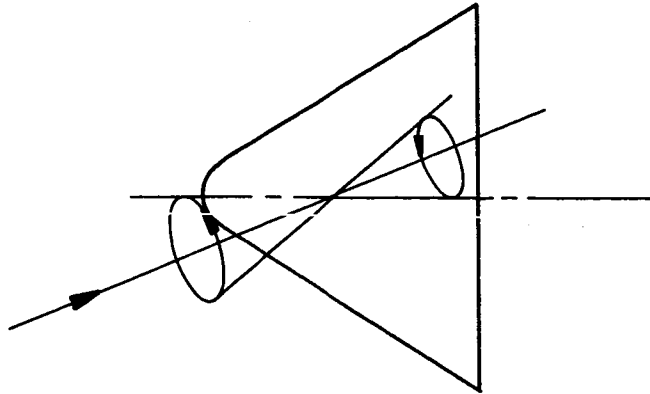
In this case, the trajectory motions were examined to insure that the spin and short – period frequencies were not close enough to each other to induce a roll or "coning" type resonance. If this becomes a problem, its effects on the previously discussed instabilities must be assessed.

A. (5) Panel Flutter:
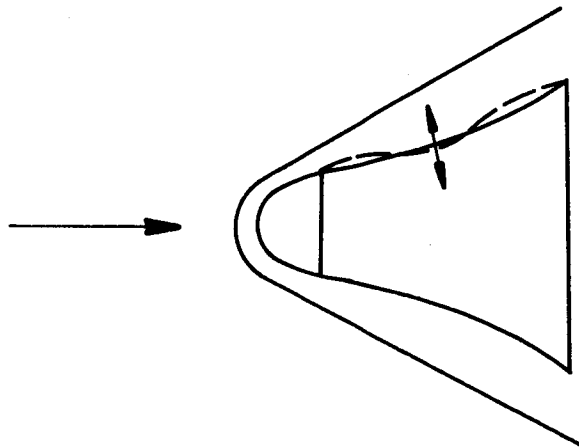
The possibility of panel flutter must be investigated on the tension shell and the sphere cone since both these configurations will experience supersonic flow over some areas of the shell surface. On the tension shell, the fact that tension exists is beneficial and this is accounted for.

For the tension shell, the complete shell modes are of concern; whereas for the ring siffened shells, panel vibration between rings is more appropriate.

B. (1) Acoustic Noise Excitation:

Turbulent boundary layer

Panel motion
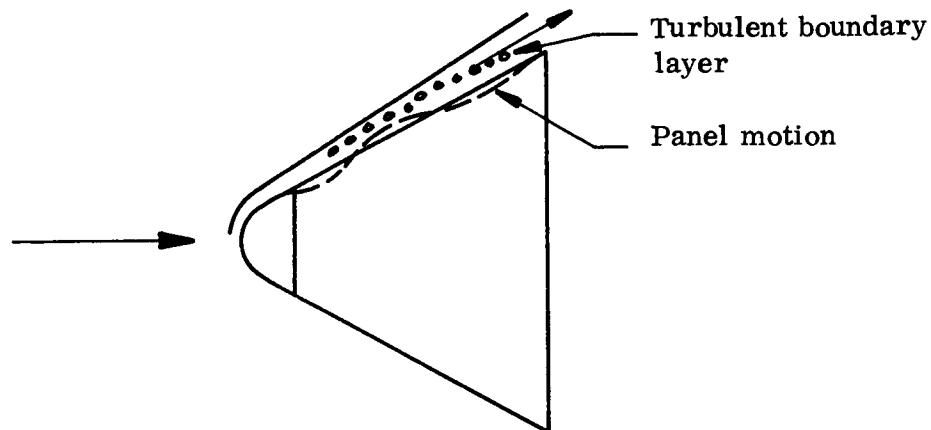
Excitation of the skin by random turbulent noise pressures are possible. These pressures plus the added influence of convection along the skin may cause excitation of the natural modes of vibration of the structure. This problem is investigated using a technique recently developed at General Electric - Re-entry Systems Department, references 1 and 2.

B. (2) Shock Instability:
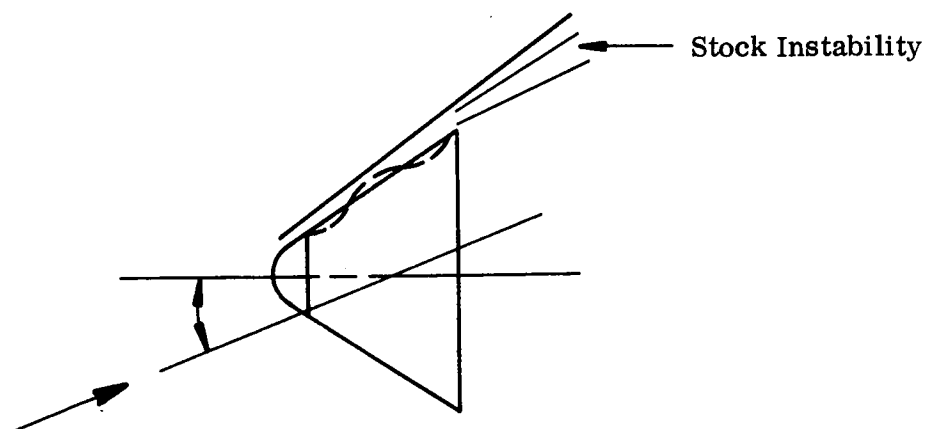
Stock Instability

The shock instabilities, which exist during entry into the Martian atmosphere, could occur in such a way as to excite panel and shell motion on the vehicle. The possibility of this resulting in a response which could effect the structural integrity of the vehicle is investigated. This problem will be more serious with the tension shell shape rather than with the other two shapes. It should also be pointed out that this must be a somewhat limited investigation due to the sparsity of data which exists. However, whatever information is available is used to make an assessment.

B. (3) Buffeting and Wake Noise:

Wake noise and recirculation of flow may excite panel motion in the aft structure of those configurations with aft structures, or on the skirt of the open back vehicles. Again in this case, due to the limited data available, the problem can be considered only in the general sense. The evaluation which is done, however, employs basically the same technique as being used in B. (1), namely that by Dr. Houbolt.

Wake Shear Layer

Recirculation Region
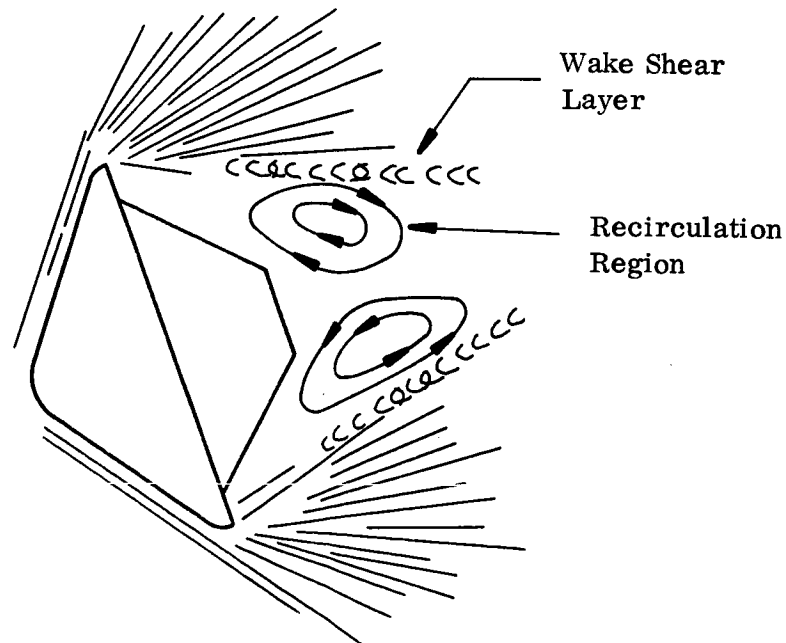
General Considerations:

All of these previously discussed phenomenon must be considered in light of other effects which exist, namely,

a. Thermal effects will result in reduction of material properties and development of a thermal stress field. These thermal effects can possibly aggravate the situations being studied.

b. Centrifugal forces produced by spin will influence the modes and frequencies of the structures. Consideration is given to this.

Another consideration, which is important here, is the basic flight worthiness of the various shapes. That is, do they all possess the required static and dynamic stability exclusive of aerothermoelastic considerations? Since conclusive data to the contrary is not available, it must be recognized that consideration of problems is being given on vehicles which may be unflyable. Therefore, it must be assumed that they are stable and can fly the trajectories specified by JPL.

SECTION 3

ANALYSIS AND DISCUSSION

3.1 VEHICLE DESIGN SELECTION

CONFIGURATION SELECTION

This phase of the study involves the selection of the actual forebody/aft body combinations to be investigated. The philosophy followed is to analyze those combinations most representative of probable vehicle designs, as they are now known, and to cover all the configurations of interest to JPL. Until the assessment of potential problem areas is completed, which is the prime objective of this study, it is neither advisable nor economical to plunge into an evaluation of all forebody/aft body combinations.

Since the sphere-cone forebody configuration is the one of major interest and most representative of early Mars landing missions, it is given prime consideration. Therefore, the sphere-cone forebody with an open back and $M/C_D A$ of 0.2 is considered the nominal vehicle. Figure 2 shows the complete matrix of vehicles that was studied. The scaled sketches of these shapes are shown in Figures 3 to 10.

VEHICLE DESIGN SPECIFICATIONS

Selection of Critical Trajectories:

From a structural design point of view, the critical conditions are those which yield the maximum g levels. Table 2 lists the maximum g levels encountered for each of the trajectories that were furnished by the Jet Propulsion Laboratory. The trajectory input data furnished by JPL is listed in Table 1. As can be seen from Table 2, the maximum g levels occur for the VM 8 atmosphere. To reduce the number of trajectories, run numbers A-1, 46, and 19 were chosen as the critical trajectories for each of the respective $M/C_D A$ groupings. In addition to these trajectories, number 41 was investigated to determine the effect of the zero spin case.

Design of Vehicle Forebody and Aftbody:

Structures were designed for each of the configurations shown in Figure 1 using the material/ type of construction combinations listed in Table 3a. Structural sizes and dimensions have been determined for each of the concepts being considered. A major tool that has been used to quickly and accurately determine dimensions and sizes for the structures is the GE-RSD Structural Loads and Optimization Program, (Ref. 3) Utilizing this unique and extensive two part computer program, internal structural loads and structural weights have been calculated along with the associated skin thicknesses, ring sizing, ring spacing, etc. In some particular instances, where the program could not handle certain configurations (sphere cap and tension shell), the calculations were done by hand and the criteria used is included in this document.

The first step in the design of all the vehicle configurations is to approximate the shape and location of the payload in order that the mass characteristics furnished by JPL be matched with a reasonable degree of accuracy. To simplify this, it was assummed that the payload was cylindrical in shape and the length and diameter were determined such that the vehicle c.g., weight, inertia, etc. were approximately equal to the mass characteristics furnished by JPL. Having established the mass characteristics of each of the vehicles, use was made of the General Electric SILC - SILO (ref. 3). Computer analysis or hand calculations were performed where this program was not applicable. In some cases minimum gage limitations governed the selection of structural thickness. The minimum structural gages considered by the SILC SILO program are shown in Table 3b. Design of each of the vehicles are described in detail as follows:

    a.   Vehicle No. 1-Sphere Cap - Due to the shape and location of the payload, this configuration was not applicable to the computer programs. Therefore, a criteria was devised to rapidly assess the structural thicknesses that are required. It is assummed that the vehicle is loaded with a uniform pressure as follows:
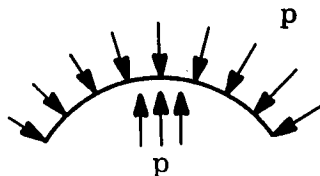
where P is the axial load due to the inertia load of the payload and p is imaginary uniform pressure required to maintain static equilibrium. This is equivalent to the aerodynamic loading minus the shell inertia. To calculate the discontinuity stresses in the area of the payload, the following loading conditions are added together to result in the actual loading condition:

Case 1   plus   Case 2
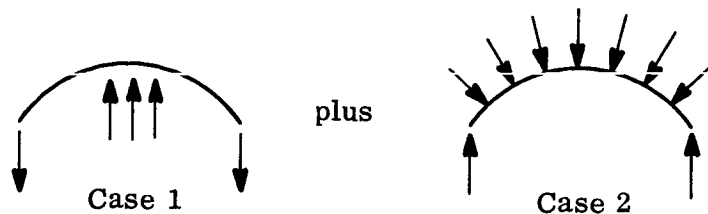
Cases 1 and 2 can be found in reference 4. Based on the critical stress in the area of the payload, and using a safety factor of 1.0 based on yield, the thicknesses required for both the monocoque and honeycomb shells were determined. The design of the aft body is based on external collapsing of the conical frustrum subjected to a base pressure of 1.53 psf at a Mach No. of 18.2. It was found that minimum gage requirements were sufficient for the design of the aft body. The results of the sphere cap forebody and conical frustrum aft body are listed in Tables 4 to 7.

b. Vehicles No. 2, 3 and 4 Sphere Cone - The design of this type of configuration can be handled by the SILC SILO optimization program. The resulting designs are based on one of the following criteria; (1) buckling, (2) membrane strength, (3) or minimum gage. The results of the design of Vehicles No. 2, 3, and 4 can be found in Tables 8 to 19. Included in this data is trajectory No. 41 which is intended to study the effects of zero spin.

c. Vehicle No. 5 Sphere Cone - The only difference between this configuration and the other sphere cones is that No. 5 includes a spherical cap aft cover. The forebody was designed in the same manner as was the other sphere cone configurations. Since the program can't handle the sphere cap aftbody, this was designed by hand based on an external base pressure of 1.54 psf at a Mach No. of 18.2. The results for this design are listed in Tables 20 to 23.

d. Vehicle No. 6 Tension Shell - Due to the shape and loading of this type of configuration, it is not applicable to the SILC SILO computer program. The design of a vehicle of this type can be subdivided into three categories, i.e.: (1) nose cap, (2) tension shell, and (3) aft ring. Design of the nose cap is simply a matter of designing a shell subjected to an external collapsing pressure. The tension shell portion of the vehicle is based on the maximum membrane tensile stress. It is assummed that the tension shell shape furnished by JPL was developed such that no compressive stresses exist in the shell. Based on this

13

assumption, the aft ring must be structurally capable of resisting the meridional loading and the external pressure surrounting it only; no compressive hoop stresses exist in the aft portion of the tension shell.

Design of Aft Ring for Tension Shell:

Since the aft portion of the tension shell consists of a local radius of 6.5 inches, (See Figure 9), geometry dictates that part of the ring cross section consists of a circular arc. To insure that a smooth transition occurs between the tension shell and the ring, it is assummed the shell attaches to the ring at $Y/R_b = .90$ (See Figure 9). To minimize the resultant ring weight, a hollow cross section of the following proportions was assummed:
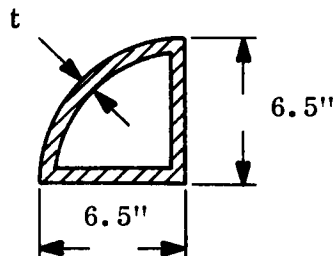
This leaves the determination of one design parameter, namely the thickness t. Two criteria have to be satisfied; the working stress level must be less than the allowable, and secondly, local buckling of the ring webs must not occur.
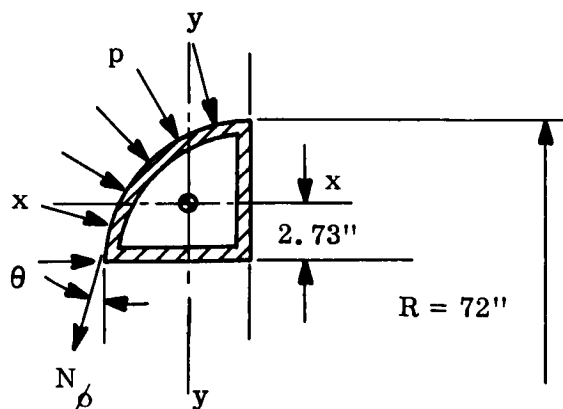
where

$p = 2.9$ psi

$N_\phi = 2.20$ lbs/inch

$\theta = 15^o$

Total radial force per unit length, $Q = 6.5\,p + N_\phi \cos 15^o$

$Q = 21.2$ lbs/inch

14

Total ring rolling moment per unit length: $M = 3.77 \, N_\phi \, \text{Cos} \, \theta - 2.73 \, N_\phi \, \text{Sin} \, \theta$

$$M = 6.45 \text{ inch-lbs/inch}$$

For a geometry of this shape

$$I_x = I_y = 137.5 \, t$$

$$A = 23.2 \, t$$

The maximum ring stress that will be encountered is as follows:

$$\sigma = \frac{QR}{A} + \frac{MR}{I/c}$$

$$\sigma = \frac{21.2(72)}{23.2 \, t} + \frac{6.45 \, (72)}{137.5t/3.77} = \frac{78.6}{t}$$

Assuming simply supported edge conditions, the critical buckling stress of the web is as follows:

$$\sigma_{cr} = 3.60 \, E \, \frac{t^2}{6.5} = .085 \, E \, t^2$$

In order that local crippling of the web does not occur set $\sigma = \sigma_{cr}$ and solve for the thickness required.

$$t_{buckling} = \left[\frac{925}{E} \right]^{1/3}$$

Based on strength the thickness required is as follows:

$$t_{strength} = \left[\frac{78.6}{\sigma_{all}} \right]$$

where σ_{all} equals the allowable stress level. The maximum of these two criteria was chosen as the governing thickness. It must be pointed out that due to the small magnitude of the loads the buckling of the web governed in all instances and the resultant stress level in the ring cross section was very low. The results for the tension shell structural design can be found in Tables 24 to 26.

Design of Aft Ring for Sphere Cone and Sphere Cap:

The aft rings for the sphere cone and sphere cap configurations must be structurally capable of resisting the following load conditions:

    (1)   Boost loads of 10 g's vertical and 2 g's lateral

    (2)   Buckling due to external pressures during re-entry

The assummed ring cross section it as follows:

$$A = .10d^2$$

$$I_{xx} = td^3/3$$

$$S_{xx} = \frac{.10d^3}{3}$$
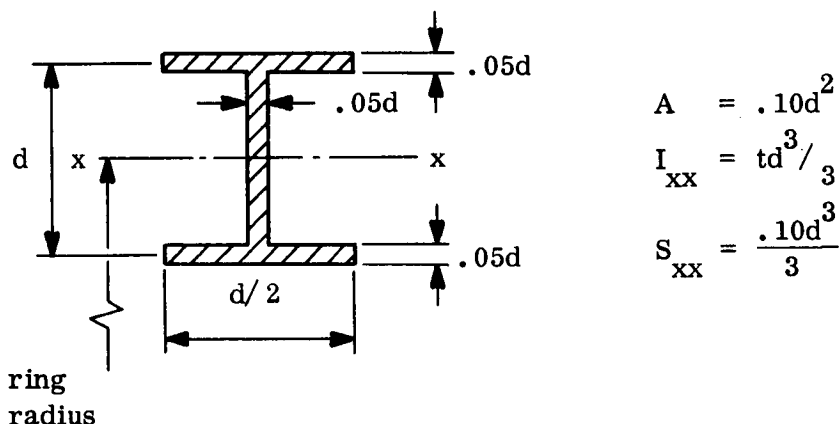
To determine the ring stress level due to the vertical boost loading at 10 g's assuming vehicle is supported at the aft end, consider the following diagram:
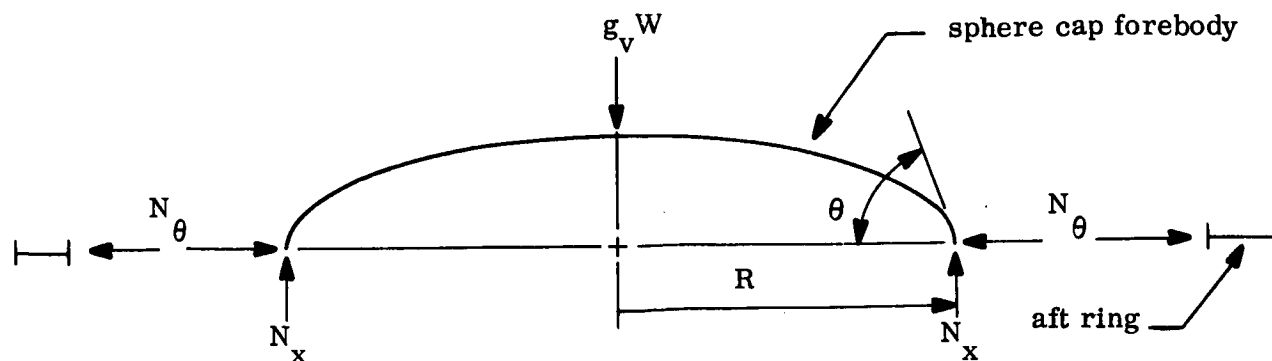
where

g_v vertical boost load g's

W vehicle weight, pounds

N_x vertical meridional loading, lbs/inch

N_θ horizontal loading, lbs/inch

R vehicle radius at aft end, inches

$$N_x = \frac{g_v W}{2\pi R}$$

$$N_\theta = \frac{g_v W}{2\pi R \tan\phi}$$

Let the entire value of the kick load, the loading which tends to expand the ring, be resisted by the ring, then the hoop stress level in the ring due to the vertical boost load is as follows:

$$\sigma_1 = \frac{N_\theta R}{A_{ring}} = \frac{5 g_v W}{\pi d^2 \tan\phi}$$

Assume the applied load on the ring due to lateral g loading is distributed sinusoidally over half of the ring:
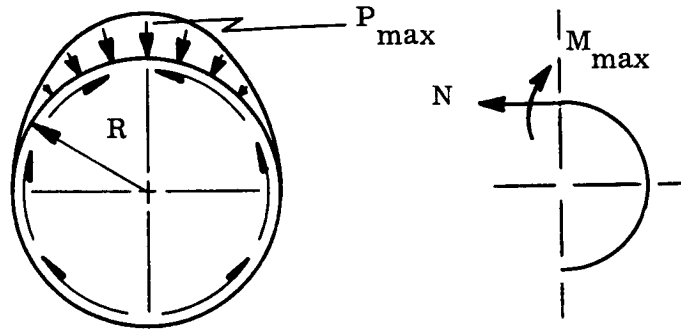
then P_{max} may be shown to be:

$$P_{max} = \frac{2\,g_1\,W}{\pi R}$$

where g_1 is the lateral g's acting on the weight W. The maximum moment and corresponding axial load is found to be:

$$M_{max} = .06832\,P_{max}\,R^2$$

$$N = .75\,P_{max}\,R$$

The ring stress level due to lateral loading is as follows:

$$\sigma_2 = \frac{15\,g_1\,W}{d^2} + \frac{4.08\,g_1\,W\,R}{d^3}$$

Combining σ_1 and σ_2 the total stress level is as follows:

$$\sigma = \frac{W}{\pi d^2}\left[\frac{5\,g_v}{\tan \phi} + 15 g_1\right] + \frac{4.08 g_1\,WR}{\pi d^3}$$

18

Given the allowable stress level, the above equation can be used to calculate the depth of ring required to satisfy the boost loading conditions.

Now the kick load in the aft ring of the vehicle due to external aerodynamic pressures during entry is determined. This criteria will be applied only for the 60° sphere cone configuration, since the sphere cap thicknesses have been designed for discontinuity stresses, and are sufficient to resist any compressive stresses at the aft end.
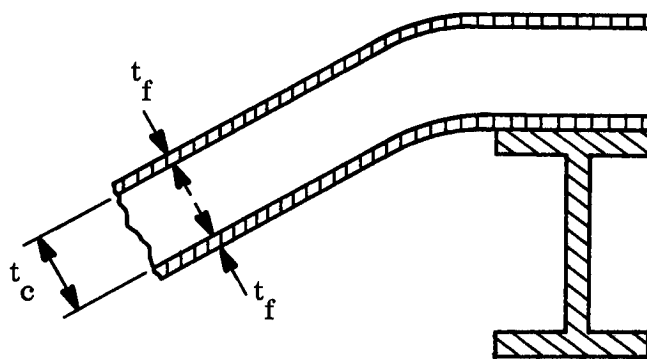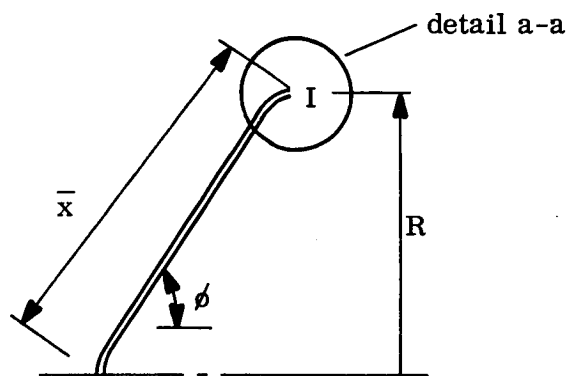
Detail a-a

The kick loading Q in the ring is calculated on the basis of no radial deflection of the ring, and a pinned joint condition. This is conservative, since ring relaxation is neglected, thus resulting with a slightly large kick load. The loading Q can be calculated using the following: (from Ref. 5).
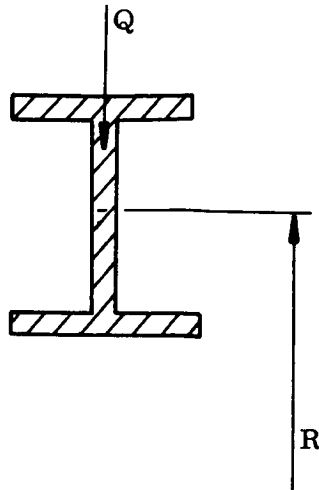
$$Q = \frac{W}{C_{WQ}}$$

Where

$$W = (1 - \mu/2) \frac{p \ R_2^2 \ \mathrm{Sin} \ \phi}{E_{eff} \ t_{eff}}$$

$$C_{WQ} = \frac{U}{E_{eff}} \ W_3 \sqrt{\frac{2 \ R_3^3 \ \mathrm{Cos} \ \phi}{t_{eff}}}$$

p = aerodynamic pressure

R_2 = $R/\mathrm{Cos} \ \phi$

μ = Poisson's ratio

U^4 = $12 \ (1 - \mu^2)$

W_3 = $f \ (\zeta) \approx 1$

ζ = $2 \lambda \ \sqrt{\overline{x}}$

λ^4 = $\dfrac{12 \ (1 - \mu^2)}{t_{eff}^2 \ \tan^2 \phi}$

To calculate an equivalent monocoque shell of the same stiffness, the following equations are used:

$$t_{eff} = \sqrt{3} \ (t_c + t_f)$$

$$E_{eff} = \frac{2 \ E_f \ t_f}{t_{eff}}$$

Having determined the load Q from the previous equations, it now remains to investigate the ring for buckling due to a radial loading. The critical load Q_{cr} is given as follows:

$$Q_{cr} = \frac{3 \ E_R \ I_R}{R^3}$$

Where E_R = modulus of elasticity of the ring material

I_R = moment of inertia of the ring

In checking the ring for buckling, any inertia relief of the shell has been neglected. The only loading that is considered is the aerodynamic pressure acting on the shell. Results for the aft ring designs for the sphere cap and 60° sphere cone are listed in Tables 27 and 28. Rings that are designed based on buckling due to external pressure have been so designated. All other rings are based on boost loading conditions.

Selection of Optimum Structural Materials for Forebody Configurations

In order to reduce the number of materials to be investigated from four to two, the materials that result in the minimum weight design will be retained for further study. Figures 11 thru 24 depict the weights of the forebody and heat shield for each of the vehicles under study. It must be noted that for vehicles No. 2, 3, 4, and 5 the beryllium honeycomb has been designed for only one back face temperature. These designs were generated thru the use of the SILC-SILO computer program which assumes that the inner face of the honeycomb is at a constant 100°F while the outer face attains the structural backface temperature. This

induces severe thermal stresses and consequently due to the high modulus of elasticity) it is not allowed to operate at more than $100^{\circ}F$. However, for vehicle No.'s 1 and 6 the SILC-SILO program was not used and the design calculations were generated by hand. In order to establish the trend that would exist if honeycomb thermal stresses were ignored, the beryllium was designed up to $1200^{\circ}F$. The other materials are also effected by thermal stresses, but the effect is not as great as the beryllium. Whether thermal stresses in the honeycomb were considered or not, does not affect the selection of the two optimum materials, but of course will make a slight difference in the selection of the optimum working backface temperature. The materials that result in minimum weight design are shown in Table 29 for each of the vehicles. The materials listed for Vehicle No. 2 include both the spin and no spin cases.

Some of the fiberglass honeycomb shells, and one monocoque, are based on 0.03 inch minimum gauge which results in a heavier structure. However it has been ascertained that 0.02 inch is feasible, thus resulting in lighter structures. The designs that are affected are indicated on the figures. In determining the two minimum weights, the 0.02 inch fiberglass was considered instead of the 0.03 inch. Even though the fiberglass has been eliminated in some instances from a structural weight standpoint, it will still be considered for all designs because of its desirable transparent radio frequency properties.

Figures 25 thru 26 depict the unit weights for the nominal vehicle No. 2. Since the sections of the vehicle forward and aft of the payload attachment consists of different design parameters (skin thickness, ring spacing, etc) the unit weights are divided into two sections. For definition of sections 1 and 2, see Figures 5 and 7.

Shell Bending Effects for the 60-Degree Sphere Cone Voyager Aeroshell
The design practice of selecting structural gages for the Voyager aeroshell is based on shell membrane theory. That is, the effect of shell bending is neglected in the first approximation for sizing the main structural loadcarrying member, the 60-degree conical frustrum.

60° Conical Skirt

Spherical Nose Cap

In the present study the consequences of this design approximation are examined. Two basic structural configurations are considered, identified as (a) "long shell", and (b) "short shell".
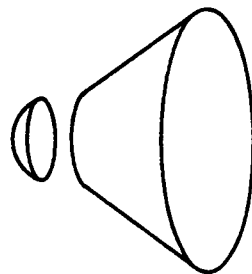
a) Long shell   b) Short shell
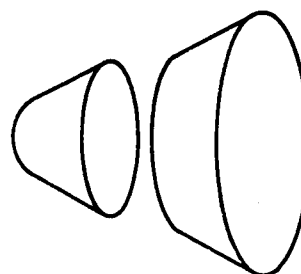
In both cases, the cone is constructed of phenolic glass honeycomb sandwich, supported by rings at the f'w'd and aft edges. For case (a) the f'w'd ring (i.e. the payload support ring) is located at the tangent point between the sphere and the cone. The payload support ring is located farther aft for case (b), so that the conical section between rings is much shorter.

A complete shell theory (one which includes both bending and membrane effects) is used to predict the shell stress resultants for both cases. In this manner, the extent of the bending stress region is determined. Also, the differences between simple membrane and the more complete shell theory are examined for the inplane stress resultants N_x and N_θ.

Assumptions:

1. Thin shell theory is applied to determine the behavior of a honeycomb sandwich shell.

2. Symmetric loading due to aerodynamic loading only is considered.

3. Only the conical portion of the Voyager 60-degree sphere - cone aero-shell is investigated.

4. Load-carrying capacity and stiffness contribution of the ESM heat shield is neglected.

5. Thermal stresses are not considered.

Results:

The regions of influence for shell bending effects are shown in Figures 27 and 28. For the long cone, case (a), these regions are confined to either end of the cone, and an appreciable section exists in the middle which is free of bending effects. For the shorter cone, case (b), the end effects overlap and interact with each other. Thus, it appears that shell bending stresses can be important, depending on the length of the shell. These results apply to a shell of sandwich construction. For monocoque construction, the extent of bending effects is limited to a very narrow region near the edges.

A comparison of the stress resultants as predicted by membrane theory and complete shell theory is shown in Figure 28 for case (a). It appears that the membrane theroy gives very good estimates of the N_x shell stress resultants. For the hoop stress resultants N_θ, membrane theory gives good predictions, except for a localized region near either end of the cone.

These results apply to the symmetric loading case. The same conclusions regarding the extent of shell bending effects should be generally true for the nonsymmetric case of flight at some finite angle of attack.

24

Case (a), the longer cone, is the more realistic structural configuration from various design considerations. For this cone, the design approximation using membrane theory is quite satisfactory. The majority of the shell does operate as a membrane, and the bending effects are confined to local regions adjacent to the edges. The increase in shell stresses near the edges may be adequately handled by a local doubler or taper in thickness.

Regarding the importance of bending effects, it should be noted that the present study is for sandwich rather than monocoque construction. Sandwich construction results in a much stiffer shell, and consequently the bending effects are greatly emphasized. Thus, the honeycomb sandwich provides a "worst case" comparison, and the bending effects are much smaller for monocoque or ring-stiffened construction.

Methodology:

To investigate the importance of shell bending effects, an idealized model of the 60-degree sphere-cone Voyager aeroshell is considered. This idealized model is a conical frustrum supported by rings at either end, and loaded by normal pressure. The stress resultants are determined by numerical integration of the governing thin shell equations. A digital computer program (ref. 6) is used to perform the integrations.

The use of thin shell theory to analyze the honeycomb sandwich shell is a reasonable approach, as the effect of shearing deformations is small for the cases considered. The honeycomb sandwich is treated as an equivalent signle thickness shell, by the use of an effective thickness and modulus. Treating only the conical portion of the aeroshell is sufficient for this study, since only the gross effects of shell bending are desired, rather than a detailed stress analysis. Neglecting the structural contribution of the ESM heat shield appears reasonable, since the modulus of the shield is smaller than the modulus of the shell by three orders of magnitude.

1. Geometry and Material Properties - Two conical frustrums, representing two different design appraoches for the Voyager aeroshell, are considered.
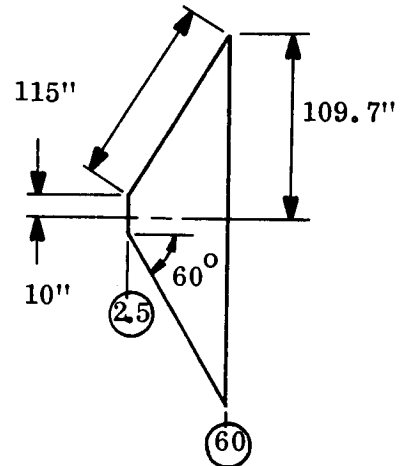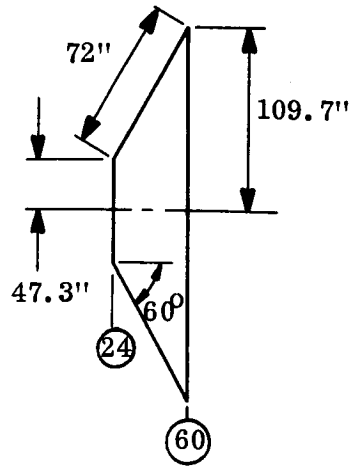
The shell wall is constructed of phenolic glass honeycomb, operating at a nominal temperature of 100°F.

$$t_c = .607"$$

$$t_f = .030"$$

$$E = 29.5 \ (10)^5 \ \text{psi}$$
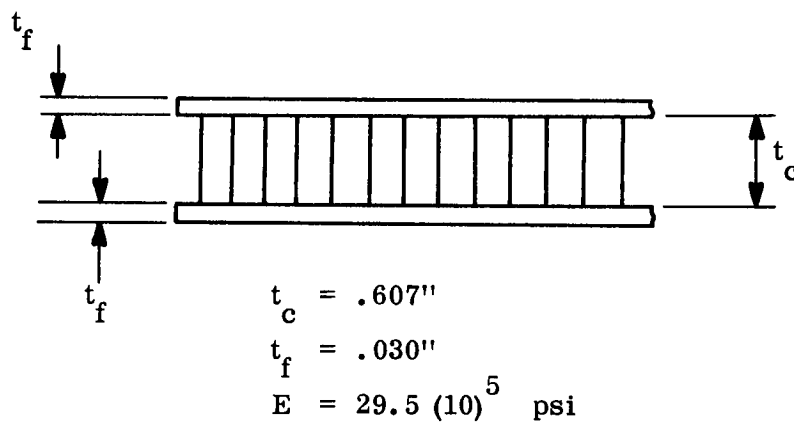
The shell effective properties are determined by considering an equivalent thickness and modulus which provides the same extensional and flexural rigidity as the honeycomb sandwich (ref. 7).

$$h_{cone} = \sqrt{3} \ (t_c + t_f) = 1.1032 \ \text{in}$$

$$E_{cone} = 2 \frac{E_f t_f}{h} = 1.604 \ (10)^5 \ \text{psi}$$

$$\nu = .3$$

26

Either end of the conical frustrum is elastically supported by a phenolic glass ring with the following properties:
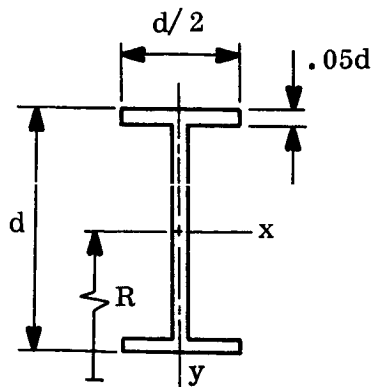
$d = 3.25"$

$E = 29.5 (10)^5 \text{ psi}$

$A = .10d^2 = 1.056 \text{ in.}^2$

$I_{yy} = d^4/960 = .1162 \text{ in.}^4$

2. Applied Loads - For the purposes of this investigation, the conical frustrum is considered to be loaded by normal pressure only. The magnitude of this pressure is derived from the following critical load condition:

Trajectory	A - 1
Atmosphere	VM-8
$m/C_D A$	.25
dia.	18'
C_p max	1.951
axial g	57.5 (earth g's)
q_∞	447 psf

For symmetric loading ($\alpha = 0$), the pressure distribution along any conical meridian is constant.

$$C_p / C_{p\ max} = .785$$

Thus, the local pressure is found to be.

$$p = (C_{p\ max}) \left(\frac{C_p}{C_{p\ max}} \right) \quad q_\infty + p_\infty = 4.75 \text{ psi}$$

Where $p_\infty \cong 0$ for Mars.

3. Shell Analysis - The conical shell frustrum, loaded by normal pressure, and restrained by f'w'd and aft elastic rings, is analyzed by means of the "Multi-shell" program (ref. 6). For numerical accuracy, the cone is divided into several members by a series of circumferential cuts. These individual members are identified by numbering system shown in Figure 29.

Boundary conditions applied at either end of the truncated cone are:

f'w'd edge: zero edge moment

zero edge shear

zero axial deflection

aft edge: zero edge moment

zero edge shear

zero axial load

The stress resultants computed by Multishell, and plotted in Figures 30 to 35 are:

M_x =   local shell moment (in. lb/in)

N_x =   inplane axial load (lb./in)

N_θ =   hoop load (lb./in)

For an indication of the relative magnitude of shell bending and membrane stresses, the point of maximum moment near the f'w'd edge is considered.

$$M_x = t_c \, \sigma_f \, t_f$$

$$(\sigma_f)_{bending} = \frac{M_x}{t_c t_f}$$

$$(M_x)_{max} \cong 224 \, \frac{IN \, LB}{IN} \quad STA \ .27$$

28

$$\sigma_{fb\ max} = \frac{224}{(.6)\ (.3)} = \pm\ 12400\ psi$$

$$N_x = 2t_f\ \sigma_f$$

$$\sigma_f = \frac{N_x}{2t_f}$$

$$(N_x) = 820\ \frac{LB}{IN}\ @\ Sta\ 27$$

$$\sigma_f = \frac{820}{.06} = 13,700\ psi$$

Thus, we conclude the bending stresses are on the same order magnitude as the membrane stresses in the region of maximum moment.

4. Estimate of Attenuation Length - As an approximate check on the computer program results, an estimate for the extent of local shell bending effects is made. The estimate is based on an attenuation length ($\beta X = 3$) for thin cylindrical shells, extending to a point where edge effects have died down to about 5% of the maximum:

$$x = 3\sqrt{ah}\ \Big/ \sqrt[4]{3\ (1-\nu^2)}$$

The radius of curvature (a) is taken to the conical surface, and h is the effective thickness, equal to 1.10 inches.

Sta 2.5
   a = 2 (10.0) = 20 in.
   x = 11.0 inches

Sta 24
   a = 2 (47.3) = 94.6 in
   x = 24.2 inches

Sta 60
   a = 2 (109.7)=219.4 in
   x = 36.6 inches

These attenutation lengths compare favorably with those shown in Figures 30 and 33 but do tend to over estimate the extent of bending effects.

The previous results are for honeycomb sandwich construction. Since sandwich construction provides a stiffer shell than monocoque construction, the bending effects tend to be exaggerated. To determine the extend of bending effects for a monocoque shell, consider a thickness of 0.020.

Sta. 2.5
a/h = 1000
x/a = .075
x = 1.5 inches

Sta. 24
a/h = 4.730
x/a = .034
x = 3.22 inches

Sta. 60
a/h = 10.950
x/a = .0223
x = 4.88 inches

These attenutation lengths are extremely short compared to those for honeycomb construction. Thus neglecting bending effects for the design of a monocoque aeroshell appears to be a satisfactory approach.

5. Inertia Relief - The stresses computed previously are those due to aerodynamic pressure loading only. The deceleration forces tend to reduce these stresses somewhat. This inertia relief effect is examined here for the conical frustrum with rings at stations 24 and 60.
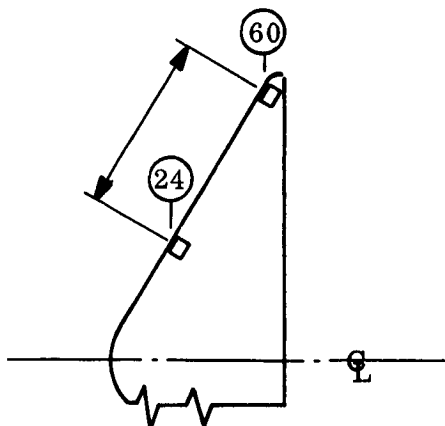
Critical Axial G's

G_x = 57.5 earth g's Case A-1

Fiberglass Sp. Wt.

ρ = 0.067 #/in^3

Aft Ring	$R = 108''$
	$A = 1.056 \text{ in}^2$
	$\text{Vol} = 2\pi RA = 2\pi (108)\, 1.056 = 716 \text{ in}^3$
	$\text{WT} = \text{Vol } \rho = 716\,(.067) = 48 \text{ LB} = 48/2\pi R$
	$\qquad\qquad\qquad\qquad\qquad = 0.071\, \dfrac{\text{LB}}{\text{IN}}$

Cone

$L = 72''$

$t_f = 2\,(0.030) = 0.060''$

$\text{WT} = t_f\, \rho = 0.060\,(.067) = 4.0\,(10)^{-3}\, \dfrac{\text{LB}}{\text{IN}^2}$ Faces

$t_c = 0.067''$

$\rho_{core} = 0.05 \#/\text{ft}^3$

$\text{WT} = \dfrac{0.607\,(.05)}{(12)^3} = 0.0175\,(10)^{-3}\, \dfrac{\text{LB}}{\text{IN}^2}$ Core

$t_{Shield} = 0.68$

$\rho_{SH} = 36 \#/\text{ft}^3$

$\text{WT} = \dfrac{0.68\,(36)}{(12)^3} = 14.2(10)^{-3}\, \dfrac{\text{LB}}{\text{IN}^2}$

Inertia
Relief $\cong$ $\text{Gx(WT)} = 57.5\,(18.2)\,(10)^{13} = 1.05$ Psi Axial

Compared to the 4.76 psi normal aerodynamic pressure applied to the shell, the inertial relief amounts to about 20%.

EFFECT OF THERMAL STRESSES

An estimate of the effect of thermal stresses on the shell structure of the sphere-cone entry vehicle was performed using a complete shell theory, including membrane and bending effects. The structural model and analytical approach are similar to those described in the section on "Shell Bending Effects".

Results are shown in Figure 36 to 39 for the honeycomb shell where the stresses resultants N_x and N_θ are plotted versus axial distance from the nose. It is seen that the effect of thermal stresses in confined to a narrow region adjacent to the structural rings at either end of the conical frustrum. Thus, no significant in-plane stresses due to thermal gradients are developed in the primary shell structure. This is to be expected as the temperature

gradients through the honeycomb thickness, and along a shell meridion are negligible, as shown in Section 3.2.3. For the monocoque shell, the conclusion that no significant stresses are developed due to thermal gradients is even more evident, as essentially no gradients exist in the structural wall (Section 3.2.3).

EFFECT OF CENTRIFUGAL FORCES

An estimate of the effect of centrifugal forces on the shell structure of the sphere cone entry vehicle was performed using shell membrane theory. The results should be generally applicable to the primary structural shell, except for small regions adjacent to the structural rings. The extent of these regions are investigated in the section on "Shell Bending Stresses".

The shell forces are developed following the approach of ref. 8.
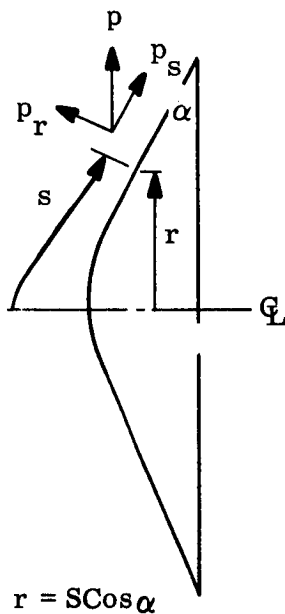
Inertia loading:

$$p = m(s) \omega^2 r \tag{1}$$

Pressure Components:

$$p_s = p \cos \alpha = m\omega^2 s \cos^2 \alpha$$
$$p_r = p \sin \alpha = m \omega^2 s \cos \alpha \sin \alpha \tag{2}$$

Hoop Stresses:

$$N_\phi = p_r s \cot \alpha \tag{3}$$

Axial Stresses:

$$N_s = -\frac{1}{s} \int (p_s - p_r \cot \alpha) \, s \, ds \tag{4}$$

$r = S\cos\alpha$

Subst. (2) into (3)

$$N\phi = m\omega^2 s^2 \cos \alpha \sin \alpha \cot \alpha$$

$$N\phi = m \omega^2 s^2 \cos^2 \alpha = m\omega^2 r^2 \tag{5}$$

32

Subst.   (2)   into   (4)

$$N_s = -\frac{1}{s} \int m\omega^2 (\overbrace{\cos^2\alpha - \cos\alpha \sin\alpha \cot\alpha}^{\cos^2\alpha}) \, s^2 \, ds$$

thus

$$N_s = \text{const}$$

but $N_s = 0 @ s = 1$ $\therefore$ $N_s = 0$

The results are shown in Figure 40 where the shell stress resultant N_ϕ is plotted as a function of axial distance from the nose. Estimates of the maximum stress resultant N_x are made for five different structural configurations. These configurations encompass the range of structural gages and shield thickness determined previously. For the specified spin rate of 1 rad/sec., these maximum stress resultants are about 30 percent of the maximum stress resultants due to airload pressure. However, the hoop loads (N_ϕ) due to spin are tensile, while those due to aerodynamic pressure are compressive, so that the two tend to relieve each other. Based on these results, it is felt that centrifugal stesses will not significantly influence the range of designs considered.

3.2 AEROTHERMAL ENVIRONMENT

3.2.1 PRESSURE DISTRIBUTION

Aerodynamic pressure characteristics determined for the fore-body families of re-entry vehicles (Figures 41 to 52) include body surface pressure distributions at angle of attack and base pressures.

These aerodynamic characteristics were evaluated at maximum g level flight environments from given Mars entry trajectories for the purpose of selecting the optimum structural materials for these fore-body configurations and for the determination of the aerothermoelastic effects on unmanned entry for Mars.

The flight environments at maximum g level are presented in Table 30 for several trajectory runs. The maximum value of the pressure coefficients (C_p max) has been evaluated from normal shock calculations for each of these flight conditions. The value of C_p max for the trajectory runs in the VM-7 atmosphere (20 percent CO_2 - 80 percent N_2) are approximate as they were evaluated from normal shock data in 9 percent CO_2 - 91 percent N_2 and 48.8 percent CO_2 - 51.2 percent N_2 atmospheres. The corresponding stagnation environment for the trajectory runs of Table 30 are given in Table 31.

As observed in Table 30, the maximum g levels occur in the hypersonic region for a range of Mach numbers between M = 14 and M = 28. The hypersonic distribution on the 60-degree sphere-cone for the windward, 90-degree, and leeward conditions are presented in Figures 41 through 47 for angles of attack of 0 degrees, 5 degrees, 10 degrees, and 15 degrees and for two base diameters D = 12 ft. and D = 18.5 ft. These pressure distributions were obtained from References 9 and 10 and are based on modified as well as adjusted Newtonian pressures to satisfy within the tolerances the total coefficients also given in Reference 10. The pressure from the point of tangency of the cone and the radius r to the base were evaluated by a Prandtl-Meyer expansion assuming that the sonic point for all cases is located at an angle of 46.5-degrees with respect to the free stream velocity vector.

34

The hypersonic pressure distributions for the smooth flare configuration are presented in Figures 48 and 49 for angles of attack of 0 degrees and 12 degrees, respectively. These pressure distributions were obtained from References 11 and 12 and were evaluated in this reference from the best available data for this configuration. A Prandtl-Meyer expansion was used to evaluate the pressures over the shoulder to the base of the vehicle.

The hypersonic pressure distributions for the sphere-cap configuration are given in Figures 50 and 51 for angles of attack of 0-degree and 15-degree, respectively. These pressure distributions were obtained from References 13 and 14 and were evaluated from the best available data for this configuration. The Prandtl-Meyer expansion was used for this case also. The C_p max required for the pressure distributions for all three configurations is available in Table 30 for the flight conditions of interest.

Base Pressures:

The base pressure ratio as a function of Mach number for the sphere-cone, sphere-cap, and smooth-flare are depicted in Figure 52. These are semi-empirical curves that were determined from Reference 15. This reference proposes a method of predicting base pressures for axi-symmetric vehicles based on a large amount of re-entry vehicle flight test data.

3.2.2 HEAT SHIELD REQUIREMENTS

Considering the current hypothetical Martian atmosphere models, maximum values of time-integrated heating and entry time will occur for the VM-3 atmosphere. Thus, to limit the structural temperatures to a maximum design value, heat shield requirements are based upon the VM-3 model. The properties utilized in this analysis for the VM-3 atmosphere are shown in Table 35. These properties were obtained from Reference 16.

Point mass trajectories for zero angle of attack were provided by Reference 17 for the VM-3 with $M/C_D A$ ranging from 0.1 to 0.5. In determining shield thickness requirements, the most severe trajectory conditions were employed, i. e. a VM-3 atmosphere with the following Initial Re-entry Conditions:

Altitude	722000 feet
Velocity	19500 feet/second
Path Angle	20 degrees
Ballistic Parameter	0.1 to 0.5 slugs/feet^2

Due to the number of different configurations being studied, the stagnation point heating rates (in the form of $\dot{q}_{stag} \sqrt{Rn}$), which are generated by the Flight Mechanics Point Mass Trajectory Program, Reference 18, were used in determining convective heating rates for all vehicles. The stagnation point heat transfer equation used in this program is an approximate technique developed by S. Scala, Reference 19, for aerodynamic heat transfer at hypersonic speeds into foreign atmospheres and is given by

$$\dot{q} \sqrt{Rn} = (9.18 + 0.663 \, \overline{M_\infty}) \, 10^{-10} \, \rho_\infty^{0.5} \, V_\infty^3$$

Where

$\dot{q}_s$ — Stagnation convective heating – BTU/FT^2 sec

Rn — Nose radius – feet

$\overline{M_\infty}$ — Free stream molecular weight – Mole/lb mole

V_∞ — Free stream velocity ft/sec.

ρ_∞ — Free stream density lbs/ft^3

Stagnation point heating rates were obtained for each configuration considering base diameters of 12 feet and 18.5, respectively. From these stagnation heating rates local heating rates were obtained using the following rationale:

As a result of the very low density atmosphere, only laminar heating will be experienced. This is based on a transition Reynolds number of 500,000 derived from local flow conditions and wetted length (References 20 and 21). Employing Lee's hemispherical distribution over the spherical portion of the nose, Reference 22, and using the stagnation pressure and local pressure relationships of Reference 23, convective heat transfer ratios of ($\dot{q}$ local/$\dot{q}$ stag) as a function of x/Rn were established for each configuration. The pressure distributions employed are shown in Section 3.2.1 (References 9 to 14). The convective heating profiles ($\dot{q}$ local/$\dot{q}$ stag) versus x/Rn are shown in Figures 53, 54 and 55.

In evaluating the ESM shield thickness requirements for various backface temperatures, the parametric heat shield study made by P. Cline, Reference 24 was used. The trajectory and configurations used in Reference 24 compare reasonably well with the inputs used in this study. The difference in the Martian atmospheric models -- the 10 mb in Reference 12 and the VM-3 in this study -- proved negligible when heating rate comparisons were made. Therefore, the parametric curves of Reference 12, i.e., ESM shield thickness as a function of peak convective heat rate for backface temperatures of $200^{\circ}F$, $450^{\circ}F$ and $700^{\circ}F$ and $M/C_{D}A$ 0.1 to 0.5, were used for generating the ESM shield requirements as a function of x/Rn for the Sphere Cone, Smooth Flare and Sphere Cap vehicles. These plots are shown in Figures 56, 57, 58, 59, 60, 61, 62, and 63, respectively. Shield thicknesses are shown for both 12 feet and 18.5 feet vehicle base diameters. It should be noted that hot gas radiation heat transfer rates were not included since at low entry velocities the stagnation hot gas radiation is negligible.

3.2.3 AERODYNAMIC HEATING

The VM-8 atmosphere will have lower total heating loads but higher temperature gradients as a result of the higher heating rates. Consequently the thermal analysis will be conducted on the nominal vehicle considering the VM-8 atmosphere. The vehicle configuration investigated consisted of ESM/Aluminum sandwich and ESM/Fiberglass sandwich. The pertinent parameters were:

Sphere Cone (60°) = Rn/R_{B} = 0.2
Base Diameter   = 18.5 feet
Ballistic Parameter   = 0.25 slug/feet^2

Temperature histories and gradients were determined for both the ESM Aluminum Honeycomb and the ESM Fiberglass Honeycomb shield structure. Since the ESM shield thicknesses are based upon the analysis in Section 3.2.2, the temperature gradients shown have been calculated for the JPL A-1 trajectory with the following initial re-entry conditions:

Altitude:	805000 feet
Velocity:	2500 feet/second
Path Angle:	20 Degrees
Ballistic coefficient:	0.25 slugs/feet^2

VM-8 Martian Atmospheric Model

This trajectory is shown in Figure 64. Heating rates were determined as defined in Section 3.2.2. Heat flux histories for the stagnation point, tangency point, and the end of skirt for the nominal 60° Sphere Cone Vehicle are shown in Figure 65.

The heat transfer rates at the tangency point and the end of skirt were inputed to the digital one-dimensional Reaction Kinetics Ablation Program (REKAP), Reference 25, to predict the temperature response of the following shield structure composites.

Fiberglass Honeycomb

$\dot{q} \rightarrow$ .345"
ESM
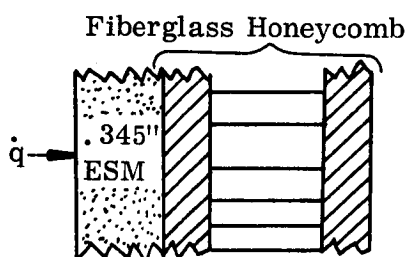
Note: Ring and thin skin effects are considered with and without the honeycomb structures.

Aluminum Honeycomb

$\dot{q} \rightarrow$ .506"
ESM
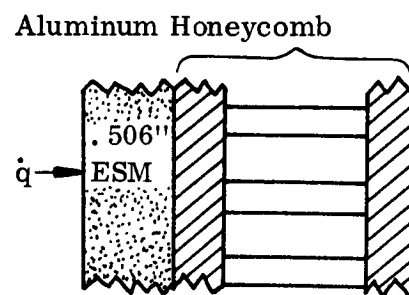
The ESM shield thicknesses chosen for this study were determined from Section 3.2.2 to approximate the desired backface temperature for a given structure.

The development of a REKAP model for ESM was reported in Reference 26. Table 36 presents the input parameters required for the current ESM REKAP Model. Table 37 lists thermal property data for all the structures considered.

ESM shield material over the following Fiberglass structures were evaluated:

    a.   Fiberglass Honeycomb

    b.   Fiberglass thin skin

    c.   Fiberglass thin skin plus structural rings

Temperature histories and profiles for the above composites are presented in Figures 66 through 71 for both the tangency point and the end of skirt.

ESM shield material over the following aluminum structures were evaluated.

    a.   Aluminum Honeycomb

    b.   Aluminum thin skin

    c.   Aluminum thin skin plus structural rings.

Temperature histories and profiles are reported in Figures 72 and 73 (tangency point and end of skirt respectively) for only the ESM/Aluminum honeycomb shield structure composite since a negligible temperature rise is experienced at the ESM backface.

Description of Charring Ablator Mathematical Model

To describe the thermal behavior of a material in a re-entry environment, Reference 25, it is necessary to solve the transient heat conduction equation for each element of material through the char (if a char exists), the reaction zone, and the virgin material continuously

and simultaneously throughout the re-entry heating period. In order to solve these second-order differential equations simultaneously, it is necessary to prescribe several boundary conditions. These boundary conditions are: (1) at the surface the net heat transfer rate to a nonpermeable surface is reduced by both surface re-radiation, and the mass transfer effect of the injection of the decomposition gases into the boundary (blocking action), (2) at the backface of the virgin plastic or supporting substructure the heat conducted out is zero.

In general, the heat conducted into a material element is equal to the sum of the heat stored in the element, the heat absorbed in the decomposition of the material element, the heat absorbed by the decomposition gases passing through the material element and the heat absorbed by cracking of recombination of the decomposition gases. The general heat conduction equation, valid in both the porous char and virgin material is written in cylindrical co-ordinates as:

$$K \frac{\partial^2 T}{\partial r^2} + \frac{\partial K}{\partial T}\left(\frac{\partial T}{\partial r}\right)^2 + \left[\frac{\partial K}{\partial P}\frac{\partial \rho}{\partial r} + \frac{K}{r}\right]\frac{\partial T}{\partial r} =$$

$$= \rho\, C_p\, \frac{\partial T}{\partial t} + \left[\rho v\left(\frac{\rho-\rho_c}{\rho v}\right)^n \sum_{i=1}^{m} A_i\, e^{-\Delta E_i/RT}\right]H_{GF} + \left[C_{pG} + \frac{\partial H_r}{\partial T}\right]\dot{m}g\frac{\partial T}{\partial r}$$

where

$$\dot{m}g = \int_{x_{BF}}^{x} \rho v\left[\frac{\rho-\rho_c}{\rho v}\right]^n \sum_{i=1}^{m} A_i\, e^{-\Delta E_i/RT}\, dx$$

At the material surface - boundary layer interface boundary condition (1) is the thermal energy balance written as:

$$\dot{q}_{net} = \dot{q}_c + \dot{q}_{HGR} - \dot{q}_{RR} - \dot{q}_{BLOCK}$$

where

$\dot{q}_c$ = hot wall convective heat flux = $H (h_r - C_p BL\ T_w)$

$\dot{q}_{HGR}$ = hot gas radiation = $\sigma\,\alpha\,w\epsilon\,_G T_e^{\,4}$

$\dot{q}_{Rad}$ = radiated heat flux = $\sigma\,\epsilon_w T_w^{\,4}$

$\dot{q}_{BLOCK}$ = transpiration cooling

For laminar flow

$$\dot{q}_{BLOCK} = \dot{q}_c \left[\frac{\overline{M}_{BL}}{M_{GAS}} \right]^{1/3} (.69)\ \frac{\Phi_o}{P_r^{\,1/3}} \quad\quad \text{Reference 21}$$

For turbulent flow

$$\dot{q}_{BLOCK} = \dot{q}_c \left[1 - e^{-.38} \left(\frac{C_{p_{GAS}}}{C_{p\,BL}} \right) \Phi_o \right] \quad\quad \text{Reference 22}$$

$$\Phi_o = \int_{Frontface}^{Backface} \dot{m}_G dx \left(\frac{h_r - h_w}{\dot{q}_c} \right)$$

At the backface of the virgin plastic or supporting substructure, the second boundary condition is:

$$K_v \left(\frac{\partial T}{\partial r} \right)_{BF} = 0$$

By solving the above equations simultaneously and continuously through the heating period, the surface and subsurface temperatures and material degradation time histories are obtained.

3.3 AEROTHERMOELASTIC EVALUATION

3.3.1 SHOCK LAYER ENVIRONMENT

Several real gas normal shock and isentropic flow calculations have been carried out in the VM-8 atmosphere (pure CO_2) to determine shock layer environments along the stagnation streamline. The conditions for potential panel flutter (spersonic flow) on a 60-degree sphere-cone have been determined. Local flow conditions for several specific vehicles and trajectories are shown.

METHODOLOGY

The body surface flow properties as a function of $C_P/C_{P\,max}$ are given in Table 32 and 34. tabulation is generally valid for all the VM-8 trajectories, the error being less than one percent. It is assumed that there are no secondary shocks in the flow.

The skirt pressure for the 60 percent sphere cone configurations is given in Table 33. From Tables 32 and 33, it is seen that the flow along the skirt is subsonic for all φ at $\alpha \leq 10$ degrees, as $C_P/C_{P\,max}$ is greater than 0.58, and is supersonic on the leeward side ($\varphi = 180$ degrees) for $\alpha = 15$ percent. From Table 30 it is seen that the maximum absolute value of the effective angle of attack, α', is 13.5 degrees. Over the angle of attack range of 10-15 degrees it is found that the skirt pressure coefficient of Table 33 is given by

$$\frac{C_P}{C_{P\,max}} = \left(\frac{C_P}{C_{P\,max}}\right)_\eta + K \left[1 - \left(\frac{C_P}{C_{P\,max}}\right)_\eta\right]$$

where $\left(\dfrac{C_P}{C_{P\,max}}\right)_\eta = \left\{ \sin\theta\,\cos\alpha + \cos\theta\,\sin\alpha\,\sin\varphi \right\}^2$

$\theta = 60^o$

$K = 0.066$

to within one percent.

The solutions of this equation for $C_P/C_{P\,max} = 0.58$ are the conditions for which $M = 1$. Using this approach, it is found that for $\alpha' < 12$ degrees the flow along the skirt is subsonic for all φ, therefore only Run numbers 46 and 16 are critical. Taking $\alpha' = 13.5$ degrees, it is found that the range of φ over which the panel flow is supersonic is $\varphi = 180$ degrees $\pm \Delta\varphi$, $\Delta\varphi < 31$ degrees.

To account for the real gas effects for the shape families under investigation, local flow conditions are determined for several specific vehicles and trajectories (Figures 77 through 91). These local flow conditions are subsequently used in evaluation of various static and dynamic instabilities, and in forced response of the structural panels.

3.3.2 MODE SHAPES AND FREQUENCIES

The shell/vehicle frequencies and mode shapes classified as the "Accordian" and "Shuttle-cock" type modes are presented for vehicles one through six in Figures 92 through 104. A finite element technique based on the matrix displacement method (Reference 27 and 28) was used to develop dynamic model stiffness and consistent - mass matrices. These matrices were computed directly by the SABOR III Computer Program (Reference 29 and 30). Natural frequencies and mode shapes were then calculated by the GE-RSD Computer Program FREE (Reference 31) which accepts the SABOR stiffness and mass matrices as input.

To establish the accuracy of the theoretical method used, the mode shapes and frequencies of a fixed end, 60 degree truncated cone (Reference 32)and a "free-free" tension shell (Reference 33) were compared with SABOR predictions. The results of these comparisons show good correlation.

ASSUMPTIONS

The basic assumptions of this analysis are:

1. Thin shell theory applies.

2. Axisymmetric, isotropic shells.

3. Multilayered shells can be represented by a single "equivalent layer."

4. Rigid payload, attached with "pinned" type connection at payload/shell surface juncture.

5. Portion of shell forward of payload attachment point is assumed to be rigid.

6. Afterbodies (on applicable vehicles) are assumed to be rigid.

RESULTS

Figures 92 through 104 show the "Accordian" and "Shuttlecock" modes for vehicles one through six. These modes and corresponding frequencies were obtained using aluminum at 100°F as a basic material. Frequencies for vehicles at other temperatures and other materials were calculated using scaling techniques. These scaled frequenceis are listed in Tables 38 through 40. The scaling shows that the controlling factor was the reduction of shield mass at the higher design temperatures. This reduction in mass offset the reduced stiffness due to temperature and, in general, led to increased frequencies.

The accordian mode natural frequencies range from 28 cps to 248 cps, while the shuttle cock mode natural frequencies range from 13 to 115 cps (with one exception) for the class of vehicles studied. The one exception occurs for the "shuttlecock" frequencies of the sphere cone with sphere cap afterbody (vehicle no. 5). These frequencies are seen to be rather low (Table 40), relative to those obtained for the other vehicles. This anomaly is caused by the extreme forward location of the payload attachment (near the cone apex),

44

which reduces the radius of the payload attachment ring. This small radius ring degrades the ability of the shell to resist bending moments due to payload inertia. It is recommended that the payload attatchment ring be relocated further aft, so that the shuttlecock frequencies for vehicle no. 5 are comparable to those of the other vehicles.

Figures 105 and 106 show SABOR predicted frequencies and modes shapes of a fixed-end 60° truncated cone and a "free-free" tension shell with payload, and compares them with the predictions of References 32 and 33. Correlation of SABOR with Reference 32 theoretical results for the 60° cone shows SABOR to be in excellent agreement. Comparisons of SABOR and Reference 33 results for the tension shell should be interpreted qualitatively since the shell was orthotropic. Also, the method of payload attachment was not clearly defined. SABOR predictions were obtained assuming average properties for the shell modulus ($E = \left[E_s + E_\theta \right] /2$) and a "pinned" payload. However, the comparison is seen to be reasonably close, certainly within the limiting assumptions imposed.

METHODOLOGY

SABOR Program: The SABOR III program uses a finite element idealization for axis-symmetric shells and utilizes the matrix displacement method to calculate stiffness and consistent mass matrices. This finite element idealization consists of a series of conical frusta joined at "nodal circles". These nodal circles are the stations at which the shell generalized coordinates are explicitly defined. Shell displacements are assumed to vary circumferentially as a finite Fourier series. The coefficients of this series are the generalized coordinates defined at each nodal circle. In addition, a power series expansion is assumed in the meridional direction between nodal circles. The coefficients of this series are defined implicitly in terms of the generalized displacements (boundary values) at nodal circles. From the standpoint of shell theory, the SABOR III program is based on the strain-displacement relation derived in Reference 27 from the text of Novozhilov.

FREE PROGRAM: Normal modes and natural frequencies were obtained using the GE-RSD program FREE. This program is based on a Jacobi diagonalization technique which reduces a real symmetric matrix to a diaganal form by performing a series of plane rotations, systematically eliminating all off diagonal elements. The Jacobi technique is a proven approach for accurately obtaining the eigenvectors and eigenvalues of a lumped parameter elastic system.

ANALYTICAL MODELS: Analytical models were constructed using nine nodal circles for the open back configurations and 11 nodal circles for the vehicles with afterbodies. Heat shield stiffness and mass effects were included in all calculations. Shell effective properties were determined for the heat shield/honeycomb (or monocoque) type combination by deriving an equivalent thickness and modulus. This equivalent structure provides the same extensional and flexural rigidity as the multilayered construction (Reference 34). A similar approach was used to account for the aft ring flexibility. Payload mass terms used in this analysis are derived as follows:

Payload Mass Terms - The motion assumed by SABOR, at a particular nodal circle, is of the form: (Figure 107a)

46

$$U(\theta) = \sum_{n=0}^{m} q_1^n \cos(n\theta)$$

$$V(\theta) = \sum_{n=0}^{m} q_2^n \sin(n\theta)$$

$$W(\theta) = \sum_{n=0}^{m} q_3^n \cos(n\theta)$$

$$\beta(\theta) = \sum_{n=0}^{m} q_4^n \cos(n\theta)$$

These assumed displacements form an orthogonal set of functions such that the equations of motion become uncoupled in harmonics. This uncoupling greatly reduces the size and complexity of the problem to be analyized by allowing one to solve the equations of motion just for those harmonics containing the particular modes of interest.

The payload mass terms needed for the accordian and shuttlecock modes in the SABOR program are derived using a kinetic energy approach.

ACCORDIAN MODE: This is the fundamental axial type mode of the zeroth harmonic. The motion induced on the rigid payload due to the zeroth harmonic displacements at the payload attachment nodal ring is pictured in Figure 107b.

Note that for the zeroth harmonic, the assumptions of a rigid, "pinned" payload require that the velocity contributions of $\dot{q}_3^0$ and $\dot{q}_4^0$ be zero. The velocity components of the differential mass element are:

$$\begin{Bmatrix} V_x \\ V_y \\ V_z \end{Bmatrix} = \begin{aligned} &= \\ &= \\ &= \end{aligned} \begin{bmatrix} 0 & Y_i/R & 0 & 0 \\ 0 & X_i/R & 0 & 0 \\ 1 & 0 & 0 & 0 \end{bmatrix} \begin{Bmatrix} \dot{q}_1^0 \\ \dot{q}_2^0 \\ \dot{q}_3^0 \\ \dot{q}_4^0 \end{Bmatrix}$$

The basic form of the kinetic energy is:

$$T = \frac{1}{2} \int_{vol} \overline{V} \cdot \overline{V} \, dm = \frac{1}{2} \int_{vol} \left[V_i \right] \left\{ V_i \right\} dm$$

$$\therefore T = \frac{1}{2} \int_{vol} \left\{ \dot{q}_i^o \right\}^T \begin{bmatrix} 1 & 0 & 0 & 0 \\ 0 & \dfrac{X_i^2 + Y_i^2}{R^2} & 0 & 0 \\ 0 & 0 & 0 & 0 \\ 0 & 0 & 0 & 0 \end{bmatrix} \left\{ \dot{q}_i^o \right\} dm$$

Integrating over the total payload mass, one obtains the desired mass matrix of the payload in the form:

$$\frac{1}{2} \left\{ \dot{q}_i \right\}^T \left[M_{i_j} \right]_{payload} \left\{ \dot{q}_i \right\}$$

where

$$\left[M_{ij} \right]_{payload} = \begin{bmatrix} M & 0 & 0 & 0 \\ 0 & I_{zz}/R^2 & 0 & 0 \\ 0 & 0 & 0 & 0 \\ 0 & 0 & 0 & 0 \end{bmatrix}$$

The inertia term I_{zz}/R^2 contributes only to the torsional type modes of the first harmonic, but is included for the sake of completeness.

SHUTTLECOCK MODE: This is the fundamental "beam" type mode of the first harmonic. The motion induced on the payload due to the first harmonic displacements at the payload attachment nodal circle is pictured in Figure 108.

48

Notice that again, the contribution of β (Figure 107a), to the payload motion is zero, and, the rigid payload assumption requires that $q_2 = -q_3$ (circular cross sections remain circular). Proceding, the velocity of a differential payload mass element is:

$$\left\{ \begin{array}{l} V_x \\ V_y \\ V_z \end{array} \right\} = \begin{array}{l} = \\ = \\ = \end{array} \begin{bmatrix} 0 & 0 & 0 & 0 \\ -Z_i/R & -1/2 & 1/2 & 0 \\ Y_i/R & 0 & 0 & 0 \end{bmatrix} \left\{ \begin{array}{l} \dot{q}_1' \\ \dot{q}_2' \\ \dot{q}_3' \\ \dot{q}_4' \end{array} \right\}$$

Substituting into the kinetic energy expression and integrating over the payload mass, one obtains:

$$\left[M_{ij} \right] \text{ cargo} = \begin{bmatrix} I_{xx}/R^2 & M\bar{z}/2R & -M\bar{z}/2R & 0 \\ M\bar{z}/2R & M/4 & -M/4 & 0 \\ -M\bar{z}/2R & -M/4 & M/4 & 0 \\ 0 & 0 & 0 & 0 \end{bmatrix}$$

where $\bar{z}$ is the axial distance from the nodal ring to the payload c.g.

FREQUENCY SCALING: To avoid a needless waste of computer time, scaling equations were derived which use the basic material (aluminum @ 100°F) vehicle frequencies to calculate frequencies for the other materials. To check the accuracy of these scaling equations, selected computer runs were made using fiber glass at 100°F as a shell material (Figures 109 through 112). A comparison of these frequencies with those predicted by scaling relations in Tables 38 through 40 shows acceptable agreement, certainly within the scope of this study.

The approach used on the scaling techniques was to develop simplified systems capable of reproducing the frequencies obtained on the more complex vehicle. The simplifing assumption that the strain energy is of an extensional nature was made on the basis of

results obtained from preliminary computer runs. These runs showed that large changes in the flexural stiffness had a negligible effect on the accordian and shuttlecock modes.

ACCORDIAN MODE: This mode is equivalent to that obtained from the following simplified system:

Here: $f = \dfrac{1}{2\pi} \sqrt{\dfrac{K_a (M_c + M_v)}{M_c M_v}}$

where

M_c = Mass of Payload + Nose

M_v = Mass of Vehicle Aft of Payload

K_a = Accordian Stiffness coefficient

For the accordian mode, the strain energy is assumed to be of an extensional nature; therefore, K is proportional to E t. Assuming the frequency has been computed for the aluminum material vehicles, the frequency of a particular vehicle using another material can be calculated from:

$$f = f_{AL} \sqrt{\frac{(Et)}{(Et)_{AL}} \frac{(M_c + M_v)}{(M_c + M_v)_{AL}} \frac{(M_v)_{AL}}{(M_v)}}$$

a cancelation was afforded by noticing $(M_c)_{AL} \approx (M_c)$

SHUTTLECOCK MODE: This mode can be obtained from the following simplified system:

$f = \dfrac{1}{2\pi} \sqrt{\dfrac{K_s (I_c + I_v)}{I_c I_v}}$

50

where I_c = Mass moment of inertia of payload and nose about an axis at the center of payload attach nodal ring

I_v = Mass moment of inertia of aft vehicle portion about same axis as I_c

K_s = Shuttlecock stiffness coefficient.

As in the accordian mode, the strain energy is assumed to be of an extensional nature, so K_s is proportional to Et. The shuttlecock frequency of a particular vehicle constructed of a material other than aluminum can be calculated from:

$$ f = f_{AL} \sqrt{ \frac{(Et)}{(Et)_{AL}} \frac{(I_c + I_v)}{(I_c + I_v)_{AL}} \frac{(I_v)_{AL}}{(I_v)} } $$

Notice that $(I_c)_{AL} \approx (I_c)$.

EFFECTS OF ASSUMPTIONS

1. and 2.   Voyager construction is well suited to the shell theory used (thin skin, ESM is isotropic, etc.).

3.   The comparison of SABOR with the theory of Reference 33 (Tension Shell), shows the equivalent section approach to be valid since this vehicle was multilayered.

3.   Payload was "pinned" for convenience since the actual fixity was not known. This assumption should not have an appreciable influence on the type modes being studied since the effect is of a "local" type.

4.   Assumptions of a rigid nose and afterbody were made since these portions of the vehicle are relatively light and contribute very little strain energy to the modes being studied due to the isolation tendencies of the heavy, rigid payload and the stiff aft ring. Also, the afterbody attachment details were not known.

In general, it is felt that the successful correlation of SABOR predicted modes and frequencies (of the shells in References 32 and 33) with predictions from other theories should serve to validate the basic assumptions used in this analysis.

The existence of conventional shell modes for these vehicles is recognized; however they are not explicitly needed in the evaluation of static and dynamic aeroelastic instabilities or in the forced response calculations which follow. A number of investigations have been made and some unpublished work by NASA exists for these shell modes. These investigations, as well as some preliminary calculations made here, place these shell frequencies in the 100 to 500 cps range.

The effect of static airload stresses on the shell natural frequencies may be approximated by the following equation:

$$\omega^2 = (\omega_o)^2 \ (1 + \eta)$$

where $1 + \eta$ gives the reduction due to preload. Here (ω_o) is the shell natural frequency when no mid-plane stresses exist (i.e. $\eta = 0$).

$$\eta = \frac{a^2 \left[N_\theta + \dfrac{a^2}{b^2} N_\chi \right]}{D\pi^2 \left[\left(1 + \dfrac{a^2}{b^2} \right)^2 - \dfrac{2a^3}{\pi R^2} + \dfrac{a^4}{\pi^4 R^4} \right]}$$

where

N_θ = hoop stress resultant

N_χ = meridional stress resultant

a = characteristic wave length in circumferential direction

b = characteristic wave length in meridional direction

D = flexural stiffness

Some estimates of the reduction in natural frequency were made using the approximation, giving $(1 + \eta) = .95$. Therefore membrane stresses may be neglected in our consideration of shell natural frequencies. Since the reduction effect is small, the present approximation does appear reasonable. Note also that the membrane stresses due to rotation are small, so that the effect of vehicle spin on natural frequencies is negligible.

Of course the natural modes of free vibration are essential ingredients to any aeroelastic evaluation as done here. We wish to point out that knowledge of these modes is also necessary for evaluating structural response during launch and max. q ascent flight.

Modes required for such an evaluation are determined here, but the examination of the launch and boost environment is beyond the scope of this study.

3.3.3 STATIC & DYNAMIC INSTABILITIES

3.3.3.1 Static Divergence

(a) Sphere - Cone/Open Back ("Umbrella Collapse")

This failure mode of the aft ring is associated with the induced circumferential compressive stresses due to pressures behind the bow shock. All vehicles studied here have an aft ring, designed to withstand loads encountered during handling, boost, and re-enetry conditions. In considering re-entry conditions, (which is the condition at which umbrella collapse may occur) a discontinuity analysis was conducted (See Section 3.1, Design of Aft Ring) to determine the size of the ring that is required to simulate an essentially simple support edge condition for the aft end of the shell. The simple support edge condition is selected as the buckling criteria for design of the shell subjected to external pressure. This procedure is expected to result in a reasonable, yet conservative ring size. The ring is then checked to insure that it does not buckle under the statically applied loading condition.

To investigate the coupling between aerodynamic forces and structural deformations in the umbrella mode, consider the following deformation pattern:

———— Original shape

— — —Deformed shape
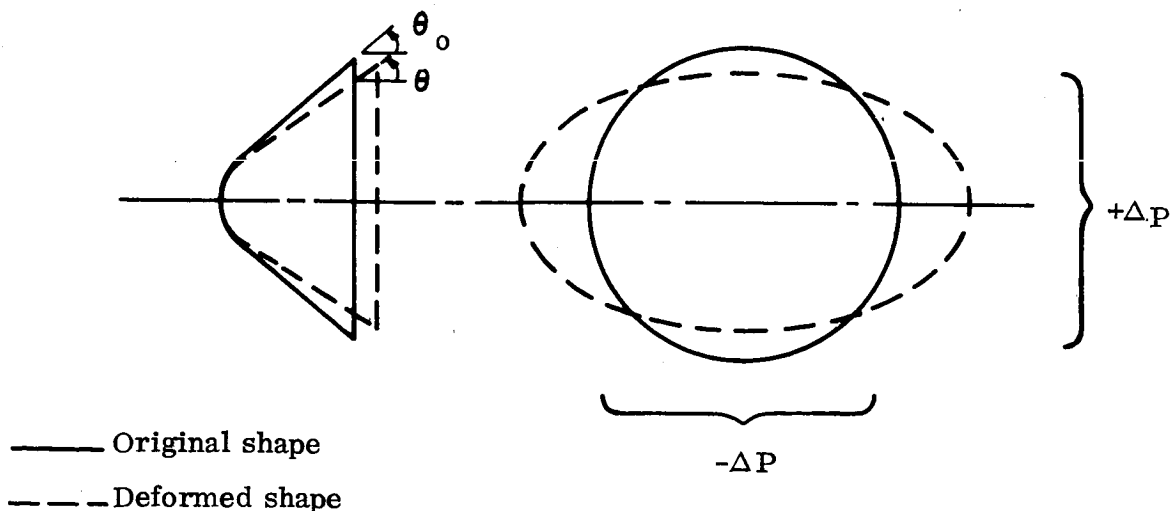
This deformation pattern is associated with collapse of the aft ring in the lowest energy static buckling mode. Newtonian theory may be used to predict the increment in pressure (Δp) due to the deformation:

$$\frac{\Delta \left(c_p / \bar{c}_p \right)}{\Delta \theta} = \sin 2\theta_o$$

where

c_p = pressure coefficient

$\bar{c}_p$ = maximum pressure coefficient

$\Delta \theta$ = change in slope due to structural deformation $= \theta_o - \theta$

θ_o = original slope

This equation predicts a local increase in pressure where the slope is increased due to deformation, and a local decrease in pressure where the slope is decreased. Examining the change in slope due to umbrella mode deformation, it is seen than the increment in aerodynamic pressure tends to restore the deformed shape back to the original shape. Thus the coupling effect between aerodynamic forces and structural deformations is beneficial for the umbrella collapse mode. Therefore it can be concluded that the criteria used to design the aft ring (see section 3.1, Design of Aft Ring) is adequate.

b. Tension Shell Nose Divergence:

In order to investigate the problem of static divergence of the tension shell nose, the time point in the trajectory which results in the maximum bending moment must be located. This time point will occur at the instant of maximum $q\eta$ (the product of the dynamic pressure (q) and total angle of attack (η). Trajectory number 46 (the one used to design the tension shell as it provides the maximum g levels) was investigated to determine the time at which maximum $q\eta$ occurs. The results are shown on figure 114. It can be concluded that the maximum $q\eta$ occurs at approximately the same time as maximum q which designs the vehicle. Based on the pressure distributions of section 3.2.1, integrated vehicle loads were generated

thru the use of the SILC computer program ref. 3. Plots of the axial load and bending moment vs. axial station are shown on figures 115 and 116. Using these loads the total meridional stresses on the windward side of the vehicle were determined and are shown on figure 117. The results indicate that the resultant stress level is tension at all time with the exception of an area near the aft end where the net resultant is approximately equal to zero. The region affected is very small, and it is felt that consideration of the shell flexural stiffness will preclude any problem. The unsymmetrical aerodynamic pressure distribution will cause a change in the geometric configuration which will in turn alter the pressure distribution. This coupling between pressures and deformations is considered in the following section.

c. Coupling between Aerodynamic Forces and Structural Deformations

To investigate the coupling effect between forces and deformations for nose divergence, the dynamic pressure which would be required to cause divergence in the first lateral elastic mode (the "shuttlecock" mode) is determined. Regarding the phenomenon of divergence, it is controlled entirely by the elastic behavior of the vehicle, providing some mechanism exists which preserves static equilibrium or "trimmed flight". However the vehicles considered in this study do not fly at a trim angle of attack, but rather oscillate about zero angle of attack. The divergence analysis is thus conducted in a "quasi-static" sense, so that the tendency towards divergence at an angle of attack, which corresponds to the amplitude of the oscillatory angle of attack, is determined.
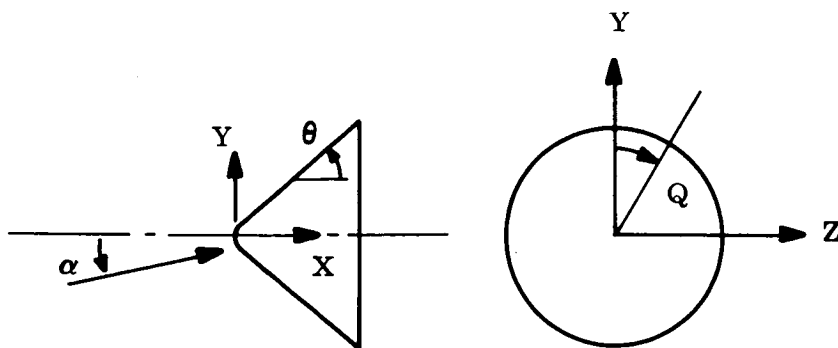
From reference (43) the equilibrium deformation in the first lateral elastic mode is:

$$\left(\frac{\delta}{L}\right) = \frac{C_{N\alpha}^{\delta}\left[\alpha_T + \Delta\alpha_T\right]}{\dfrac{K_\delta L}{q_\infty S} - C_{N\delta}}$$

where

$\left(\dfrac{\delta}{L}\right)$ = normal coordinate evaluated from the uncoupled first lateral eq. of motion

$C_{N\alpha}^{\delta}$ = aeroelastic normal force coefficient slope

$C_{N\delta}$ = modal force coefficient slope

α_T = rigid body angle of attack

$\Delta\alpha_T$ = flexible body increment in angle of attack

S = reference area

L = reference length

K_δ = generalized stiffness = $M_\delta\,\omega_n^2$

M_δ = modal mass of the first lateral mode

ω_n = frequency of the first lateral mode

q_∞ = free stream dynamic pressure

The divergence dynamic pressure is determined from the "blowing-up" of the solution to this equation. Letting the denominator vanish, obtain:

$$(q_\infty)_{div} = \frac{K_\delta L}{S\,C_{N\delta}}$$

An estimate of the modal force coefficient slope ($C_{N\delta}$) may be determined by considering the local aerodynamic force normal to the surface due to structural deformation in the first lateral elastic mode:

$$dF_N = \Delta C_p \, q_\infty \, dA$$

where:

ΔC_p = increment in pressure coefficient due to deformation

dA = $R(x) \, d\varphi \, dx / \cos\theta$

Estimating ΔC_p by Newtonian theory:
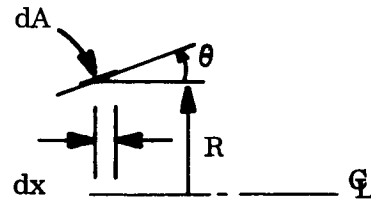
$$\frac{\Delta(C_p/\overline{C}_p)}{\Delta\theta} = \sin 2\theta \, (\cos^2\alpha - \sin^2\alpha \cos^2\varphi) + \sin 2\alpha \cos\varphi \cos 2\theta$$

where:

$\Delta\theta$ = increment in θ due to deformation

$\overline{C}_p$ = maximum value of C_p

α = angle of attack

φ = circumferential location

Combining these equations, the local elemental lateral force dF may be written:

$$dF = dF_N \cos\varphi = \overline{C}_p \left[\frac{\Delta(C_p/\overline{C}_p)}{\Delta\theta} \right] q_\infty \, R(x) \, \frac{\partial\Phi}{\partial S} \, \delta \, \frac{\cos\varphi \, dx \, d\varphi}{\cos\theta}$$

where:

$$\Delta\theta = \frac{\partial\Phi}{\partial S}\delta$$

$\dfrac{\partial\Phi}{\partial S}$ = slope of the mode shape

δ = magnitude of displacement in first mode

Now the modal force in the first lateral elastic mode is:

$$d F_{\delta} = d F \, \Phi(x, \varphi)$$

where

$$\Phi(x, \varphi) = \text{mode shape}$$

The modal force coefficient $(C_{N\delta})$ is then defined by:

$$\iint d F_{\delta} = q_{\infty} \, S \, C_{N\delta} \left(\frac{\delta}{L}\right)$$

Combining these equations:

$$C_{N\delta} \left(\frac{S}{L}\right) = \overline{C}_p \int_o^L \int_o^{2\pi} f(x, \varphi) \cos\varphi \, d\varphi \, dx$$

where

$$f(x, \varphi) = \left[\frac{\Delta(C_p / \overline{C}_p)}{\Delta\theta}\right] \frac{R(x)}{\cos\theta} \, \Phi(x, \varphi) \, \frac{\partial\Phi}{\partial S}(x, \varphi)$$

As a first approximation, $f(x, \varphi)$ may be represented in the circumferential direction with a cosine distribution:

$$f(x, \varphi) \cong \bar{f}(x) + \bar{\bar{f}}(x) \cos\varphi$$

where the components are:

$$\bar{f}(x) = \left[f(x, o) + f(x, \pi)\right] / 2$$

$$\bar{\bar{f}}(x) = \left[f(x, o) - f(x, \pi)\right] / 2$$

Note that $\bar{f}(x)$ does not conbribute to the integral $\int_0^{2\pi} f(x,\varphi) \cos\varphi \, d\varphi$. Thus the expression for $(C_{N\delta})$ becomes:

$$C_{N\delta} \left(\frac{S}{L}\right) = \bar{C}_p \frac{\pi}{2} \int_0^L \left\{ f(x, 0) - f(x, \pi) \right\} \, dx$$

This integral has been evaluated numerically to provide $C_{N\delta}$ for the following conditions:

Angle of attack $= \alpha = 15^{\circ}$

Material $=$ Aluminum at 100°F

Stiffness: $K_{\delta} = .406 (10)^5$ lb/in (sphere-zone)

$\quad\quad\quad\quad K_{\delta} = .975 (10)^5$ lb/in (tension shell)

The dynamic pressure required to cause divergence $(q_{\infty})_{\text{div.}}$ is found to be:

$$(q_{\infty})_{\text{div}} = \begin{cases} 49(10)^3 \text{ psf} & \text{sphere-cone} \\ 55(10)^4 \text{ psf} & \text{tension-shell} \end{cases}$$

Since the divergence dynamic pressure is several orders of magnitude greater than the flight dynamic pressure for Mars entry, we conclude that nose divergence is not a problem.

3.3.3.2 Longitudinal (Accordian) Mode Instability

Coupling of structural deformations in the first longitudinal or accordian mode with the unsteady aerodynamic forces behine the bow shock can lead to an instability, not unlike wing flutter. A composite picture of these structural deformations and the local Mach number is shown in Figure 127 and 128, for the forebody shapes investigated. For the spherical cap and sphere cone forebodies, the local flow is subsonic over the entire forebody. For the smooth flare shape, the local flow is in the low supersonic regime for the forward part of the vehicle, the shocks down to subsonic over the aft flare.

It appears that the unsteady aerodynamic tools required to analytically investiagte this problem are not readily available. A separate study is recommended here to further investigate this phenomena. However, it is rather doubtful that an instability does exist here. Probably the best approach would be wind tunnel studies with a suitable model.

A proposed model to simulate the free flight longitudinal dynamics is shown in Figures 118 and 119. This model is mounted in the tunnel along a circumferential line of simple supports, which coincides with the node line for the accordian mode. This node line is depicted in Figure 92 through 104 for the structural configurations investigated here. For the sphere cone forebody shapes, the node line is located sixty to seventy percent of the forebody length aft of the nose. For the sphere cap the nodal location is twenty to thirty percent (of the forebody length) aft of the nose. For the smooth flare, the nodal line is located at about the ninety percent location, or where the aft ring occurs.

A shaker is placed to excite the vehicle at the payload location, and the impedance is continually monitored. The change in impedance as a function of flow velocity or dynamic pressure is the important parameter to be measured. This change in impedance is used as a criteria for impending instability. If the impedance reduces as the flow velocity is increased, the onset of an aeroelastic instability is indicated.

3.3.3.3 Flexible "Shuttlecock" Instability and Aft Ring Parametric Resonace

The coupling of structural motions and unsteady aerodynamic forces, resulting in a possible "shuttlecock" instability, must be treated in the same manner as the accordian mode. Figures 129 and 130 show the structural deformations in this mode and the Mach number of the local flow. Due to the subsonic and transonic nature of the local flow in the shock layer, an unsteady aerodynamic analysis is required. Such an analysis is beyond the scope of this study, and forms the basis of recommendations for future effort.

The possibility of an aeroelastic instability problem for this mode is more pronounced than for the accordian mode. A wind tunnel test must be devised to investigate the possible existance of a mechanism for coupling between the "shuttlecock" structural deformations and aerodynamic forces. Non-steady shocks and expansions mught excite this structural mode like the low speed phenomena associated with the von Karman vortex street excitation of structural modes (galloping transmission lines, etc.)

A proposed wind tunnel model for investigating this phenomena is shown in Figures 120 and 121. The model is mounted at the nodal point for this mode which is located on the vehicle axis, some twenty to thirty percent behind the nose. A shaker is placed to excite motion in this mode and the impedance is monitored. By continual measurement of the impedance, it is possible to detect the onset of an aeroelastic instability, or any possible non-linearities which may be present.

A possibility exists for coupling between short period oscillation airloads and the structural response of the aft ring. The oscillatory airloads due to short period oscillation causes an oscillatory compressive hoop load in the aft ring. If the short period frequency is close to the ring bending natural frequency, a coupling condition known as "parametric resonance" may result. To investigate this coupling, the methods of reference 35 are applied. For certain relationships between the frequency of the load and the natural frequency of the bending vibrations of the ring, the initial form of the ring becomes dynamically unstable and develops intense bending vibrations. The regions of instability become apparent when the frequency ratio (θ/Ω) is plotted versus the excitation parameter (μ), as in Table 41.

θ = short period oscillation frequency

Ω = reduced natural frequency = $\omega_k \sqrt{1 - q_o/q_k}$

$q(t)$ = ring pressure loading = $q_o + q_t \cos \theta t$

ω_k = ring natural frequency

$$= \frac{k(k^2-1)}{R^2} \sqrt{\frac{EJ}{m(k^2+1)}}$$

q_k = static instability pressure = $\dfrac{EJ}{R^3}(k^2-1)$

μ = excitation parameter = $q_t/2(q_k - q_o)$

J = ring moment of inertia

These equations were applied to determine if the vehicles considered in this study lie outside the regions of instability. Results are shown in Table 41. It is seen that in all cases the ring natural frequencies are higher than the excitation frequencies, causing the design points to fall below the instability regions. Thus the possibility of parametric resonance may be ruled out.

3.3.3.4 Spin-Short Period Resonance

For certain type entry vehicles, aerodynamic or mass asymmetries associated with a nominally symmetric vehicle can cause a coning type motion during entry of a spinning vehicle. This coning condition can couple with the short period motion and lead to a resonance condition, called roll resonance or coning resonance. Severe loading conditions may result, which may lead to a failure of the vehicle to perform its mission.

Persistent roll resonance is as mentioned, a condition characterized by the frequencies in pitch and roll remaining nearly equal for an extended period of time, which results in an amplification of the non-rolling trim angle of attack. A discussion of the phenomena, its cause and effects is given in Reference 36.

As discussed in Reference 36, persistent roll resonance is more apt to be a problem for the more slender entry vehicle. For the blunt, high drag configurations considered for Mars entry vehicles, roll resonance is not a problem unless extremely large asymmetries exist. For exospheric flight, the roll resonance condition is non-existant, as long as the moments of inertia about the pitch and roll axis are unequal. For atmospheric entry, and for the case where the roll inertia exceeds the pitch and yaw inertia (vehicles one, two, four, five, six) and the vehicle is statically stable, the resonance condition cannot occur.

Referring to Reference 37, resonance occurs when $\left| \omega_0 \right| = \left| \Delta \omega \right|$, where these frequencies are defined by:

$$\omega_0 = \left[\frac{-Cm\alpha}{B} \quad q\infty \, Sd \; + \; \left(\frac{pA}{2B} \right)^2 \right]^{1/2}$$

$$\Delta\omega = p \left[1 - \frac{A}{2B} \right]$$

where

A   =   roll moment of inertia

B   =   pitch moment of inertia

$C_{m\alpha}$ =   slope of Cm vs α curve

d   =   reference diameter

p   =   roll rate

$q\infty$ =   free stream dynamic pressure

S   =   reference area

ω_0 =   basic short period oscillation frequency

$\Delta\omega$ =   component of total pitch frequency resulting directly from roll.

If the roll moment of inertia exceeds the pitch and yaw moments of inertia, then the basic frequency ω_0 always exceeds $\Delta\omega$, as long as the vehicle is statically stable ($Cm\alpha < 0$). Thus vehicles one, two, four, five, and six, cannot get into the resonance condition during entry. Trajectory No. 46 has been analyzed in order to provide a verifying example for this conclusion.

Table 43 depicts the numberical results for a blunt 60 degree cone angle capsule as a function of time, altitude, and roll rate. It is seen that the condition $\omega_0 > \Delta\omega$ always exists, regardless of the magnitude of roll rate, thus veryifying that the resonance condition cannot occur. It should be noted that ω_0 varies directly and significantly with dynamic pressure (q). For a vehicle with the aerodynamic and mass properties utilized herein, the value of ω_0 approaches that of $\Delta\omega$ only at very high or very low altitudes, when in either case the dynamic pressure is virtually non-existant.

For the bluff, high drag configurations considered for Mars entry vehicles, the steady resonance condition is not a problem even if the roll moment of inertia is the miminum moment of inertia, as for vehicle three. This is because steady resonance does not occur until angle of attack has damped to near trim values. The damping characteristics of a high drag configuration are rather poor resulting in angle of attack oscillations down to altitudes approximating those at which retardation system deployment would occur. At these altitudes, the resonance frequency is quite low, so that even if resonance were attained, the roll rate and loading associated with resonance would be small. Very large asymmetries would be required to produce resonance even at the low altitudes.

Asymmetry Studies

A study was performed to determine the effects of vehicle mass an inertia asymmetries on the motion of the Mk - 2 (52 degree sphere cone) Voyager configuration during entry. The study was performed using the VM-3 atmosphere and entry conditions of:

Altitude	722K ft.
Velocity	14160 ft/ sec.
Path Angle	16 degrees

An entry angle of attack of 32 degrees and an initial roll rate of 25 RPM was used. The nominal weight and balance data used was:

Weight	1200 lb
Moments of inertia (Roll)	192 slug - ft^2
(Pitch)	125 slug - ft^2
(Yaw)	125 slug - ft^2
Diameter	12 ft.

Longitudinal c. g. 38 inches from stagnation point

In this study lateral c. g. locations up to three inches and products of inertia up to 2 slug-ft^2 were used in the investigation. Even the worst combination of asymmetries investigated (lateral c. g. of three inches along the body y axis and a product of inertia, I_{xz} = 2 slug-ft^2) did not appreciably alter the angle of attack envelope or peak lateral loads. The roll rate change for the worst case investigated was 12 RPM. The angle of attack envelope and the roll rate histories for the symmetrical for the worst case asymmetries are shown in Figure 122. The trim angle of attack for the asymmetric case results mainly from the three inch c. g. offset. From this study it can be concluded that this class of entry vehicle is highly insensitive to asymmetries of the size expected, and the problem of persistent roll resonance is nonexistent.

3.3.3.5 Panel Flutter

Stability boundaries for flutter of flat panels are usually presented in terms of the flutter parameter (λ), from Reference 38.

$$\lambda = \frac{\rho a v L^3}{D}$$

where

ρ	=	local density
a	=	local sound speed
v	=	local velocity
D	=	stiffness
L	=	panel length

The panel length (L), may also be treated as the wave length of the flutter mode. For a semi-infinite flat plate, with no in-plane load, Figure 123, (Reference 38), shows the flutter boundaries. The horizontal dotted lines corresponding to $\lambda/\pi^4 = 3.52$ and 6.52, for simply supported and clamed edges, respectively, are the results that would be obtained if the aerodynamic damping is neglected. Values of the damping coefficient g_a (Figure 123) usually found in practice are less than 0.5, so that there is little difference between the actual flutter boundary and the horizontal dotted line.

The effect of in-plane load, due to applied quasi-static air pressure or thermal gradients, is shown in Figure 124. The cirtical value of λ is plotted against r, which denotes the ratio of the applied axial load to Euler buckling load for pin ends. It is seen that an applied tension field raises the flutter boundary, while compression pre-stress lowers the flutter boundary.

Estimates of a curved panel flutter boundary may be used to provide an indicator of the possibility of panel flutter. This approach is expedient to realistically evaluate panel flutter, since the theoretical flutter mechanism for thin shells in not well understood. It has been stated (Reference 39), that all published theories of flutter of cylindrical shells yield pessimistic results regarding shell instability, since many vehicles have flown successfully with skin thicknesses thinner than theoretically recommended gages for safety against panel flutter.

Curved panel flutter boundaries have been presented in terms of the flutter parameter ϕ (Reference 39).

$$\Phi = \left(\frac{q}{\beta E}\right)^{1/3} \frac{R}{t}$$

where

$q \quad = \quad$ local dynamic pressure

$E \quad = \quad$ modulus of elasticity

$\beta^2 \quad = \quad M^2 - 1$

M = Mach number

r = radius of curvature

t = panel thickness.

Experimentally defined flutter boundaries for a cylindrical shell (Reference 39), and a finite aspect ratio curved panel (Reference 40), are respectively:

$$\phi_{crit} = 7.0 \text{ (cylinder)}$$

$$\phi_{crit} = 12.5 \text{ (panel)}.$$

From the results of Section 3.3.1, (Shock Layer Environment), it appears that local supersonic flow is not attained on the surface of the sphere-cap and sphere-cone shapes, (vehicles one to five) except for an extremely limited region. This local supersonic region occurs on the leeward side when the 60 degree shpere-cone shape is at high angles of attack (α greater than 12 degrees). Such angles of attack are attained only at the peaks of the pitch oscillation cycle. At maximum dynamic pressure, the maximum amplitude of pitch oscillation is 16.3 degrees, occuring for trajectory run No. 46 (see Table 42). Comparing these two angles, (12 degrees and 16.3 degrees), show that local supersonic flow only occurs for an instant during each cycle, thus the possibility of panel flutter is remote for the family of shapes encompassing vehicles one to five.

For vehicle six, the smooth flare, local supersonic flow is attained over a significant region (see the curves of Section 3.3.1). To evaluate the possibility of panel flutter, the flutter parameters ϕ and λ are determined at several vehicle locations (Table 44). The most critical combination of materials, construction, and vehicle location occurs for fiber glass at a design temperature of 700°F, near the midsection of the smooth flare forebody. For this critical combination of conditions, the flutter parameters ϕ and λ are shown in Figure 125 and 126 with radius (R) and wavelength (L) as free parameters. Conservative flutter boundaries are shown on these figures by dotted lines. As the computed values of ϕ and λ are not near the boundaries within the range of R and L considered, it is not even

67

necessary to determine the exact values of R or L. Comparing the flutter boundaries for ϕ and λ with the values attained in this study, it is seen that the possibility of panel flutter is remote for the smooth flare shape.

3.3.4 FORCED RESPONSE

3.3.4.1 Acoustic Noise Excitation

Laminar and turbulent boundary layer calculations were performed for both the sphere-cap, sphere-cone and smooth-flare configurations using the viscous interaction, zero angle of attack drag program of Reference 42. It was found that the boundary layers for these configurations are laminar.

The transition criteria used is based on blunt body transition data which show boundary layer transition occuring at local Reynolds numbers on the spherical nose cap of approximately 500,000 for ablating bodies (References 20 and 21). In all cases it was found that the peak Reynolds number on the spherical nose cap was generally less than the critical values by an order of magnitude.

The laminar boundary layer displacement thicknesses were evaluated for both the sphere-cone and the smooth-flare configurations, Figures 131 and 132, respectively, as a function of the axial distance along the body. For the smooth-flare configuration, the calculations were not conducted downstream of the location of the secondary shock.

Since the boundary layer is expected to be laminar there is no acoustic excitation problem for the structural modes. To account for the remote possibility of a turbulent boundary layer, the following evaluation of acoustic noise excitation was performed.

Estimates of the pressure fluctuations within turbulent boundary layers have been alarmingly high for the last generation of higher performance earth re-entry vehicles and have been the source of some concern. Possible structural excitation due to turbulent boundary layer noise is treated in Reference 1. It is shown there that possible structural excitation is suppressed because the acoustic energy is spread over a wide frequency range, and because of the negating effects of spatial correlation of the boundary layer turbulence.

68

Investigations were conducted on the study vehicles up to the point needed to verify that boundary layer acoustic excitation does not present a problem. Three configurations were considered, and the results of the investigation are shown in Tables 46, 47, and 48. The underlying reasons for the absence of an acoustic noise problem are (1) the strong non-correlation effects due to a thin boundary layer, (2) the low σ (DB) values obtained, and (3) the relative magnitude of the mass of the wall. The conclusion that acoustic noise excitation is not a problem even with a turbulent boundary layer is not surprising in view of the low dynamic pressures encountered, (450 PSF for Mars compared to 300,000 PSF for ballistic Earth entry), and therefore, the low energy levels available.

Some of the characteristic frequencies and pressure levels are now examined. The overall acoustic pressure, σ_c, was obtained using the relationship:

$$\sigma_c = 0.007 \, q_c$$

subscript c refers to conditions just outside and local to the turbulent boundary layer. This relationship was used on the basis that M_c is less than unity.

The frequency spectrum level of boundary layer acoustics was determined using the relationship.

$$\emptyset \, (f) \; = \; \frac{4 \dfrac{\delta^*}{.7 \, V_c} \, \sigma^2}{1 + \dfrac{\omega \, \delta^*}{.7 \, V_c}}$$

where δ^* = turbulent boundary layer displacement thickness

For the region $\omega \approx 0$, obtain:

$$\emptyset \, (f) \; = \; \frac{4 \delta^*}{0.7 \, V_c} \, \sigma^2$$

The frequency associated with the boundary layer acoustics listed in Tables 46, 47, and 48, were obtained on the basis of the relationship:

$$\frac{\omega \delta^*}{0.7 \, V_c} = 1$$

which is shown in Reference 1 to be the frequency region of maximum contribution to the rms power. These frequences are seen to be very high, ranging from 80000 to 250000 cps. The significance of this is that there is relatively little acoustic energy in the low frequencies (below 2000 cps), where the resonant frequencies of the structure fall.

Estimates of the vibration of the shell structure were made on the basis of the relationship developed in Reference 1:

$$\frac{\phi_{\ddot{z}}^{(f)}}{g^2} = \frac{16}{\pi^2} \; \frac{\eta_1 \eta_2 \; \dfrac{\dot{\delta}^*}{.7 V_c} \; \sigma^2}{\eta^2 w^2 \; \dfrac{\beta^2}{\beta cr^2}} \quad , \quad (g^2 / cps)$$

where $\phi_{\ddot{z}}$ = spectral density of shell modal response

η_1 = 0.07 = longitudinal spatial correlation factor, Reference 1

η_2 = 0.03 = transverse spatial correlation

ηW = effective surface weight density

$\dfrac{\beta}{\beta cr}$ = damping coefficient, assumed to be 0.01.

These results predict the shell vibration due to a turbulent boundary will be at levels less than $1 \times 10^{-5} \, g^2 / cps$. This correlates with the conclusion drawn earlier in this section that acoustic noise excitation is not a problem.

3.3.4.2 Shock Instability

Experiments must be relied upon to determine the effect of shock instabilities on the structural response of the vehicle. Possible locations for shock instabilities are at the corner of the 60 degree sphere-cone forebody, and on the smooth flare forebody where the secondary shock occurs. The various forebodies may have shock instabilities occuring as the vehicle experiences short period oscillations. These shock instabilities cannot be

predicted analytically. However, since the Mars entry dynamic pressures are low there would appear to be little energy available in the shock to excite structural modes, so that in all probability, no problem exists here; just as the observation made earlier for boundary layer acoustic noise excitation. Some tunnel experiments would verify whether shock or expansion instabilities do occur, and if so what the non steady pressure levels might be.

A tunnel test is suggested to study the behavior of the secondary shock on the smooth flare configuration. A mechanical linkage can be used to oscillate the tunnel model at the short period frequencies predicted to occur in free flight (i.e. 0 to 2 cps).

3.3.4.3 Buffeting and Wake Noise

The inviscid wake edge characteristics for the sphere-cone configuration are given in Table 45 for three representative flight conditions. The corresponding base pressures were taken from Figure 52. An isentropic expansion from the local conditions upstream of the base shoulder to the representative base pressure was assumed for evaluating the inviscid wake edge characteristics.

The three cases investigated for boundary layer turbulence (Section 3.3.4.1) were also investigated for wake turbulence. The analysis consisted in the prediction of pressure levels and frequency content of the wake turbulence acoustics using the methods of Reference 2. The relationship used from this references are as follows:

a. overall acoustic pressure level in the wake

$$\sigma_b = \frac{.01\, M_b^2}{1 + .18\, M_b^2}\, p_b$$

where

σ_b = wake acoustic rms pressure, psf.

p_b = base pressure, psf

M_b = wake region Mach number

b. frequency spectrum of wake acoustic pressure

$$\phi(f) = \frac{4\sigma_b^2 S}{V_b} \left[\frac{1}{1 + \left(\frac{2\pi f S}{V_b}\right)^2} \right]$$

This relationship is shown in Figure 133 with $\frac{V_b}{4\sigma_b^2 S} \phi(f)$ plotted against the reduced frequency $\frac{fS}{V_b}$. This shows that the maximum spectrum level of wake acoustics is in the low frequency range. The critical frequency range was further defined by plotting $\frac{f\phi(f)}{4\sigma_b^2}$ as a function of the reduced frequency $\frac{fS}{V_b}$ (Figure 134). This function is proportional to the rms power of the wake acoustics and is seen to peak at $\frac{fS}{V_b} = \frac{1}{2\pi}$. The frequency of this max. power point was determined for the three cases investigated and was seen to lie in the the 120 - 140 cps range.

The overall acoustic pressures, σ_b, were also determined and were found to lie in the 0.06 to 0.10 psf range which is the 100-110 Db (relative to 0.0002 dyne/cm^2) range and roughly equivalent to the noise inside a DC - 6 airliner.

Although the wake acoustic energy is sure to be concentrated in the low frequency range i. e. below 140 cps, the pressure levels are low and no adverse effects will be experienced by the structures and contents.

An estimate of the vehicle shell vibration was made assuming the vehicle base is open so that the wake acoustic pressures will act directly as the shell surfaces. The following expression from Reference 1 was used

$$\frac{\phi_{\ddot{z}}(f)}{g^2} = \frac{4}{\pi^2} \frac{\eta_1 \eta_2 \phi(f)}{\eta^2 w^2 \frac{\beta^2}{\beta_{cr}^2}}$$

where $\phi(f) = \dfrac{4\sigma_b^2 S}{V_b}$

η_1 and η_2 = spatial correlation functions which are less than unity, but assumed = 1

ηW = equivalent weight density of the shell surface.

$\dfrac{\beta}{\beta_{cr}}$ = damping ratio, assumed = .01

S = distance from edge of vehicle base to apex of wake turbulence cone.

The three cases investigated resulted in predictions of vibration levels in the shell of less than 1×10^{-9} g^2/cps.

Thus it is concluded that structural excitation due to wake noise is not a problem, even for the open-back family of entry vehicles.

3.3.5 DESIGN CRITERIA

Establishment of criteria for accommodating potential aerothermoelastic problems in the structural design of Mars entry vehicles is one of the basic objectives of this study. This section will present a summary of the criteria used in evaluating the aerothermoelastic phenomena considered. These criteria may be used as guidelines for the evaluation of potential aerothermoelastic problems on future vehicle designs which fall within the family of large, bluff (high drag coefficient) vehicles for ballistic Mars entry, with a ballistic coefficient $(M/C_D A)$ on the order of 0.20 slug/ft^2.

Static Divergence: Two basic modes of failure are "umbrella collapse" and "nose divergence". The umbrella collapse mode is associated with induced circumferential compressive stresses in the structural shell, while nose divergence applies to the tension shell concept, and is associated with body bending loads due to angle of attack loading. An aft ring is designed such that buckling under quasi-static airloads is prevented, thus accommodating the static umbrella collapse mode. Tension shell nose divergence is accommodated by examining the state of stress in the shell under maximum body bending loads. If no significant areas of compressive stress develop under this loading, the nose divergence problem is not design limiting. The nose divergence mode should be examined for the influence of structural deflections on aero-dynamic pressures. The degree of coupling between the aerodynamic pressures and the structural deformations may be estimated by determining the dynamic pressure necessary to cause divergence in the first lateral elastic mode (the "shuttlecock" mode).

Dynamic Instabilities: Three possible dynamic instabilities should be investigated; (1) parametric resonance due to coupling between the short period oscillation airloads and the structural response of the aft ring, (2) accordian mode instability, and (3) shuttlecock mode instability. Coupling between short period oscillation airloads and ring structural response is examined for parametric resonance by comparing the ring natural frequencies with the rigid body short period frequencies. If the short period frequencies are much less than the ring natural frequencies, then parametric resonance is not design limiting.

The accordian mode instability refers to the coupling between unsteady aerodynamic forces and the motion of the vehicle in the main longitudinal mode. The criteria developed in this

report involves a combined analytical and experimental model to simulate longitudinal mode dynamics. The combined approach is used since at present the tools required to handle the unsteady aerodynamics do not exist. The suggested tests have the objective of learning whether this phenomena should be included as a design criteria. The procedure is as follows; first an analytical dynamic model is formulated and investigated to locate the nodal line. This nodal line is then used as the support point for a physical model with an accurately scaled stiffness distribution. The physical model is mounted in a wind tunnel along a circumferential line of simple supports, so that the free flight longitudinal dynamics are simulated. A shaker is used to excite the vehicle over a range of frequencies which include the natural frequency, and the impedance is continually monitored. The change in impedance is used as a criteria for impending instability. If the impedance reduces as the flow velocity is increased, the onset of an aeroelastic instability is indicated.

The shuttlecock instability refers to the coupling between unsteady aerodynamic forces and the motion of the vehicle in the main lateral mode. The type of criteria is the same as in the preceeding section for the accordian mode instability, except the model support point is modified to account for the shuttlecock mode nodal point.

If a problem arises with any of these dynamic instabilities, a design modification is indicated. The usual approach is to change stiffness or mass distribution, as these are the primary influences on system mode shapes and frequencies. In this connection, it is noted that the payload attachment point to the aeroshell may have a significant effect on natural frequencies.

Spin-Short Period Resonance

Roll resonance is a condition characterized by the frequencies in pitch and roll remaining nearly equal for an extended period of time, which results in an amplification of the non-rolling trim angle of attack. If the structural natural frequencies are well separated from the short period oscillation frequencies, roll resonance may be treated as rigid body phenomena. For the blunt, high drag configurations considered for Mars ballistic entry vehicles, roll resonance is not a problem unless extremely large assymmetries exist. Further in the case where the roll moment of inertia exceeds the pitch (and yaw) moment of inertia, and the vehicle is statically stable, the resonance condition cannot occur. In order to

evaluate the effect of assymmetries, a six-degree-of-freedom trajectory analysis must be performed. Such a study has shown that this class of entry vehicle is highly insensitive to reasonable size asymmetries.

Panel Flutter: As panel flutter is a supersonic phenomena, it is non-existent for those configurations where the local flow velocity is subsonic. For the blunt bodies under consideration, large areas of subsonic flow do indeed occur. The criteria applied here is to first establish those areas where supersonic local flow is possible, and next to calculate a flutter parameter for these areas. The proximity of the calculated flutter parameter to a reasonable flutter boundary will then reveal the probability of panel flutter. Suggested panel flutter parameters, and their associated critical values, are shown below:

$$\text{Flat Panel} \quad = \lambda = \rho a v \cdot L^3/D \leq 3.5$$
$$\text{Curved Panel} = \phi = (q/\beta E)^{1/3} R/t \leq 7.0$$

The critical value of the flutter parameter is influenced by a number of variables (see for example References 38 and 41). If the calculated flutter parameters are close to the critical values then experimental studies are called for. Actual panel geometry and loading conditions should be simulated with suitable wind tunnel models. The tunnel flow conditions are then varied parametrically to determine the actual flutter boundaries. Analytical studies of panel flutter for conical shells are in order to develop criteria for configurations such as in this study.

Acoustic Noise Excitation

The possibility of skin excitation by boundary layer noise exists if the boundary layer is turbulent. Suggested transition criteria to distinguish between a laminar or turbulent boundary layer is based on a local Reynolds number (referred to wetted length) of 500,000. In the case where the boundary layer is turbulent, the evaluation procedure is as follows (from ref. 2).

(1) Determine local flow conditions outside the boundary layer (M, p, v) and the boundary layer displacement thickness (δ^*).

(2) Estimate the overall acoustic level (σ) and the spectral density ϕ (f) from:

$$\sigma = \left[\frac{.0049\, M^2}{1 + .012\, M^2}\right] P$$

$$\phi(f) = \left[\frac{4\delta * \sigma^2/V}{1 + \left(\frac{2\pi f\delta *}{V}\right)^2}\right]$$

where

σ = Overall acoustic pressure due to the turbulent boundary layer, psf.

M = The Mach No local to but just outside the turbulent boundary layer.

p = The static pressure at the boundary layer, psf.

$\phi(f)$ = Acoustic power spectrum level at frequency f, $(psf)^2/cps$

$\delta *$ = Boundary layer displacement thickness, ft

V = Boundary layer convection velocity, fps.

f = Frequency of pressure fluctuation, cps.

(3) Criteria for estimating structural damage due to boundary layer acoustic noise is presented in the following chart:

Structural Damge Due to Acoustic Noise

Spectrum Level (Db/cps)	Overall Level (Db/0-5000 cps)	Relative Severity & Action Recommended
100 - 110	135 - 145	Usually no problem even under pro-longed exposure-further evaluation not necessary.
110 - 120	145 - 155	Usually no problem for short exposure (2-5 min) further evaluation recommended
120 - 130	155 - 165	May cause failure in short exposure. Further evaluation recommended
130 - 140	165 - 175	Failure in short exposure a strong possibility-further evaluation recommended including both analytical and experimental studies

(4) In cases where further evaluation is recommended, the dynamic response of the structure may be determined from (see ref. 1):

$$\phi_{\ddot{z}}(f) = \frac{4}{\pi^2} \frac{\eta_1 \eta_2 \phi(f)}{\eta^2 W^2 \left(\frac{\beta}{\beta_r}\right)^2}$$

where

$\phi_{\ddot{z}}(f)$ = Power spectral density response, g^2/cps

$\eta_1 \, \& \, \eta_2$ = Longitudinal and transverse spatial correlations factors.

$\phi(f)$ = Power spectral density of the acoustic pressure, $(psf)^2$/cps

$= \frac{4\,\delta^*}{V}\,\sigma^2$

ηW = Equivalent shell weight density, lb./sq. ft

$\dfrac{\beta}{\beta_{cr}}$ = Damping ratio

Because of the many simplifying assumptions which must be made in or to obtain a solution any analytic prediction of structural response to acoustic loading will be approximate. Where a marginal condition is indicated analytically further evaluation by experimental means are recommended. Testing in an acoustic reverberant chamber is most feasible, however spatial correlation effects must be corrected for.

Shock Instability: The suggested approach to determine the effect of shock instabilities on vehicle structural response is experimental. Various forebodies may have shock instabilities as the vehicle experiences short period oscillations. A suitable mechanical linkage may be used to oscillate the tunnel model at free flight short period frequencies. In all probability, no real problem exists for Mars entry, since the low level of dynamic pressure indicates little energy is available to excite structural modes.

Buffeting and Wake Noise

Criteria for determining response to noise generated in the wake flow field is based on the methods of Reference 2. The suggested approach is to first determine the wake flow field. Then the rms pressure level (σ_b) and spectral density ϕ (f) may be determined from:

$$\sigma_b = \frac{.01 M_b^{\,2}}{1 + .18 M_b^2} \, P_b$$

$$\phi(f) = \frac{4\sigma_b^{\,2} S}{V_b} \left[\frac{1}{1 + \left(\dfrac{2\pi f S}{V_b}\right)^2} \right]$$

where

P_b = Base pressure

M_b = Wake Mach. number

V_b = Wake velocity

S = Apparent wake cone surface length ($S = \eta \, r_b / \sin\theta$)

η = 1.0

r_b = Body base radius

θ = Wake cone angle

f = Frequency of pressure fluctuation, (cps)

Criteria for estimating structural damage due to buffeting and wake noise is similar to that presented in the previous chart for excitation due to boundary layer noise. In cases where further evaluation is recommended, the dynamic response of the structure may be determined from:

$$\phi_{\ddot{z}}(f) = \frac{4}{\pi^2} \frac{\eta_1 \eta_2 \, \phi(f)}{\eta^2 \, w \left(\beta/\beta_r\right)^2}$$

where

η_1 & η_2 = Longitudinal and transverse spatial correlation factors $\approx .4$ assuming perfect correlation which is a valid assumption,considering the relatively large scale of the wake characteristic dimensions.

If a marginal condition is indicated by the analytical evaluation, testing in an acoustic chamber is recommended.

General Considerations:

All of the phenomena previously discussed should be evaluated with the following effects in mind:

a.   Thermal stresses must be such that no local buckling or tensile failures occur.

b.   For a structural configuration with restraint such that significant mid-plane stresses are developed due to thermal gradients, the resultant degradation in stiffness must be considered.

c.   If the vehicle is spin stabilized, the rates of spin should be examined to preclude (1) severe structural loads due to centrifugal forces, and (2) any adverse effect on the modes and frequencies of the structure.

The natural modes and frequencies of a vehicle should always be established (with mid-plane stresses if large) as these form the basis of structural response studies as well as aerothermoelastic evaluations.

80

SECTION 4

SUMMARY OF RESULTS

Table 48 presents the problems studied and the results obtained for each of the aerothermoelastic phenomena studied. It was found that, in general, no aerothermoelastic problems should be incurred for the families of Mars entry vehicles investigated. Some recommendations are made for possible experimental studies on certain phenomena that cannot be treated by purely analytical means, as well as desirable full scale tests for natural frequency and mode shape determination.

The general finding that no aerothermoelastic problems exist can be traced to the fact that very low dynamic pressures exist for Mars entry. Since the dynamic pressures are so low, (compared to Earth entry), there is negligible energy available to excite the various aeroelastic phenomena.

Thermal effects in this study are primarily evident in the reduction of material properties, especially the elastic modulus. Thermal stress, or a reduction in stiffness due to thermal gradients, are not complications for the problems studied. The primary reason for this is the negligible thermal gradients through, and along, the structural shell wall.

Centrifugal forces developed by spin were found to be a negligible factor.

SECTION 5

RECOMMENDATIONS

Three specific tunnel tests are recommended to explore further certain aeroelastic problems identified in this study. These tests are described in the following sections:

    (a) Accordian mode instability - Section 3.3.3.2

    (b) Flexible "shuttlecock" instability - Section 3.3.3.3

    (c) Shock Instabilities - Section 3.3.4.2

An investigation is first necessary of course to ascertain whether tests of the type recommended are feasible in the tunnel facilities that are available.

In addition, the following general recommendations are made:

    (1) Full scale vibration tests of a prototype entry capsule are recommended to ascertain mode shapes and frequency ranges. In lieu of full scale tests, sub-scale model tests should be made.

    (2) The launch environment appears to be more severe than the Mars entry environment, therefore on the basis of the results of item one, troubles due to launch environment and max. q flight should be studied.

    (3) Until there is definite evidence that the vehicles are dynamically stable in flight, the stability characteristics should be investigated by means of model flight tests.

    (4) Earth flight test of a Mars entry vehicle would be desirable to demonstrate high risk design performance items which cannot be simulated in ground testing. These items include entry vehicle dynamic stability, aerodynamic deceleration, and retardation.

SECTION 6

NOMENCLATURE

A	area
A	roll moment of inertia (Sec. 3.3.3.4)
a	radius of curvature (also local sound speed)
B	pitch moment of inertia
C_D	drag coefficient
C_{pmax}	max value of pressure coefficient
$C_{M\alpha}$	slope of C_M versus α curve
D	stiffness $Et^3/12(1-\mu^2)$
d	diameter
E	modulus of elasticity
E_R	modulus of elasticity of ring material
E_{eff}	effective modulus of elasticity
E_f	modulus of elasticity of the faces
f	frequency
g	gravitational acceleration
g_v	vertical boost load g's
g_l	lateral g's
G_x	axial g's
g_a	damping coefficient
I	moment of inertia
I_c	mass moment of inertia of payload
I_v	mass moment of inertia of aft vehicle portion
I_R	moment of inertia of the ring
K	stiffness coefficient
K_s	stiffness coefficient for shuttlecock mode
h_{cone}	thickness of cone
h	effective thickness
L	panel length or wave length

M	Mach number (or mass)
M	moment (Sec. 3.1)
M_c	mass of payload and nose
M_v	mass of vehicle aft of payload
$\bar{M}_\infty$	free stream molecular wgt. mole/lb.
M_b	wake region Mach number
$M/C_D A$	ballistic coefficient
M_x	local shell moment (in./lb/in, Sec. 3.1)
M_{ij}	mass matrix
n	wave number (Sec. 3.3.3)
N	axial load (Sec. 3.1)
N_x	meridional loading (lbs/in, Sec. 3.1)
N_θ	hoop loading (lbs/in, Sec. 3.1)
N_S	axial stress (Sec. 3.1)
p	aerodynamic pressure
p	roll rate (Sec. 3.3.3.4)
P_b	base pressure
Q	total radial force per unit length
Q_{cr}	critical load
$\dot{q}_{BLOCK}$	transpiration cooling
$\dot{q}_{RAD}$	radiated heat flux
$\dot{q}_{HGR}$	hot gas radiation
$\dot{q}_c$	hot wall convective heat flux
$\dot{q}_s$	stagnation convective Btu/ft^2 sec.
q_i	generalized coordinate
q	dynamic pressure $\left(\dfrac{\rho V^2}{2}\right)$
R_N	nose radius ft.
R	radius

R_2	$R/\cos \phi$
r	radius of curvature (Sec. 3.3.3.5)
S	distance from edge of vehicle base to apex of wake turbulence (Sec. 3.3.4.3)
S	reference area
t_{eff}	effective thickness
t_c	thickness of core
t_f	thickness of face
V_∞	free stream velocity
v	local velocity
W	vehicle wgt. (lbs)
Z	axial distance from the modal ring to the cargo c.g.
α	angle of attack
β	rotation coordinate (Sec. 3.3.2)
β^2	$M^2 - 1$
β_x	attenuation length
γ	material density
ξ	$2 \lambda \bar{X}$
$\Delta \omega$	component of total pitch frequency resulting directly from roll
η	total angle of attack
λ	flutter parameter (Sec. 3.3.3.5)
μ, ν	Poisson's ratio
ρ	local density
ρ	fiberglass sp. wt. (Sec. 3.1)
σ	stress
σ_{all}	allowable stress level
σ_c	overall acoustic pressure
σ_{cr}	critical buckling stress
ϕ	flutter parameter (Sec. 3.3.3.5)
$\phi(f)$	frequency spectrum of wake acoustic pressure
ω_0	basic short period oscillating frequency
η_1	longitudinal spatial correlation function
η_2	transverse spatial correlation functions
ηW	equivalent weight density of the shell surface

SECTION 7

REFERENCES

1. Houbolt, J. C. "Structural Response of Re-entry Vehicles to Boundary Layer Noise", GE Report TIS 65 SD 223 A, March, 1965

2. Houbolt, J. C., "On the Estimation of Pressure Fluctuations in Boundary Layers and Wakes", GE Report TIS 66 SD 296, August, 1966

3. Hess, T. E., "Structural Internal Loads and Optimization Program - Revision A (SILC-SILO), GE Technical Memo 8156-76, April, 1964

4. Roark, R. J., "Formulas for Stress Strain", McGraw Hill New York, 1954

5. Taylor, C. E., and Wenk, E., "Analysis of Stresses in Conical Elements of Shell Structures", Proceedings of Second U.S. National Congress of Applied Mechanics, 1955

6. Beitch, L. "Multishell; A Digital Computer Program for the Analysis of Shells of Revolution Subject to Axisymmetric Loading" GE R61 - FPD 340, June, 1961

7. Hess, T. E., "Optimization of Spherical Shells", PIR SM 8156-547-1774, November, 1965

8. Flugge, W., "Stresses in Shells", Springer - Verlag, 1960

9. Hoyt, T. L., "Aerodynamics Characteristics of the Mk 2 Sphere Cone Baseline Configuration GE PIR AT 8152-918, November, 1965.

10. Hoyt, T. L,, "Preliminary Aerodynamic Characteristics of the Voyager 60 Sphere Cone Configuration" General Electric PIR AT 8152-977, March, 1966

11. McMullen, J. C. "Aerodynamic Characteristics of the Tension Shell Baseline Configuration" General Electric Co. PIR AT 8152-863, September, 1965

12. Alai, J. R. and Rand, R., "The Tension String Structure", TIS 65 SD 369, December, 1965.

13. McMullen, J. C. "Pressure Distribution for Voyager - Apollo Configuration, " General Electric Co., PIR AT 8152-762, June, 1965

14. Kyriss, C. L., "Flow Field Properties for an Apollo Configuration in the 10Mb NASA-MARS Atmosphere", General Electric Co. PIR 8152-901, November 1965

15. Cassanto, J. M. and Storer, E. M. "Method of Predicting Base Pressure for an Axi-Symmetric Ballastic Re-entry Vehicle at Zero Angle of Attack in Turbulent Flow", General Electric Company, RSD ATC FM 64-6, December, 1964

16. Vachon, D., "Vertical Distribution of the Recent JPL Voyager-Mars Engineering Model, " PIR 8126-124, General Electric Company, December, 1965

17. Marhefka, R. E. "Compendium of Entry from De-orbit (71/73) Trajectory Parameters", PIR 8153-1581, General Electric Company, May, 1966

18. Faust, J., "Flight Mechanics CREWS Program, Point Mass Trajectory, " Flight Mechanics, FM 58 September, 1963

19. Scala, S. Lecture Notes from Short Course on "Re-entry-and Planetary Entry" held at the University of Calif., March, 1966

20. Walker, G. K., "A Double Criterion for Establishing Most Probable Transition Reynolds Number", GE MSVD PIR HTT 8151-165, January, 1964.

21. Hecht, A. M. "Clarification of Transition Criteria", GE MSD PIR HTT - 8152-202, June, 1964

22. Lees, L., "Laminar Heat Transfer Over Blunt Nosed Bodies at Hypersonic Speeds", Jet Propulsion, Vol. 26, April, 1956

23. Walker, G., "Some Comments on Laminar and Turbulent Heat Transfer Equations", Aerophysics Technical Memo, No. 147, December, 1959

24. Cline, P. "Preliminary Release of Voyager Heat Shield Requirements" PIR HTT 8151-446, August, 1965

25. Gordon, P., "Analysis of a One Dimension Heat Conduction Digitial Computer Program, " GE TIS 64 SD 201, January, 1964

26. Florence, D., "Development of an ESM Rekap Model", TDM 8151-040, December, 1964

27. S. Klien, Percy, J. H., Pian, T. H. H., and Navaratna, D.R. "Application of the Matrix Displacement Method to the Linear Elastic Analysis of Shells of Revolution, " Massachusetts Institute of Tech., Aeroelastic and Structures Research Lab. ASRL TR 121-7, January, 1965

28. Klien, S., "Matrix Analysis of Shell Structures", S. M. Thesis, Department of Aeronautica and Astronautics, Mass. Institute of Tech., June, 1964

29. Percy, J. H. Navaratna, D. R. and Klien, S. "SABOR III A Fortran Program for the Linear Elastic Analysis of thin Shells of Revolution Under Asymmetric or Axisymmetric Loading by the Matrix Displacement Method", Mass. Institute of Tech. Aeroelastic and Structures Research Lab. TR 121-6, May, 1965

30. Kreiger, F. D., "SABOR III - MSD Users Manual," Structural Mechanics Technical Memo SM 8156-167, April, 1966

31. Kreiger, F. D. and Eagle, H. A. "FREE - Natural Frequencies and Mode Shapes of Linear Systems with No Damping," (GE Report to be published)

32. Goldberg, John E. and Bogdanoff, John L., "On the Calculation of the Axisymmetric Modes and Frequencies of Conical Shells," The Journal of the Acoustical Society, Vol. 32. No. 6, June 1960

33. Cohen, Gerald A., "Computer Analysis of Asymmetric Free Vibrations of Ring Stiffened Orthotropic Shells of Revolution," AIAA Journal, Vol. 3, No. 12, December, 1965

34. Menkes, E. G., "Thermo-Elastic Analysis of Beams, Plates and Shells Including the Effect of Variable Material Properites" Structural Mechanics Unit Technical Memo. No. 8156-11, August, 1962.

35. Boltin, V.V., "The Dynamic Stability of Elastic Systems", Holden-Day, Inc., San Francisco, Calif., 1964

36. Pettus, J. J., "Persistent Re-entry Vehicle Roll Resonanace" GE Document 65SD361, November, 1965

37. R. L. Nelson, "The Motions of Rolling Symmetrical Vehicles Referred to a Body Axis System", NACA TN-3737, November, 1956

38. Houbolt, J. C., "A Study of Several Aerothermoelastic Problems of Aircraft Structures in High-Speed Flight", Mr. S. Mitterlunger aus dem Institute for Flugzeugstatik and Leichtbau, Leenan (Zurich), 1958

39. Fung, Y. C. "Some Recent Contribution to Panel Flutter Research", AIAA Journal, Vol. 1, No. 4, April, 1963

40. Walker, R. W., Rosecrans, R., and Deveikis, W. D., "Flutter Investigation of Streamwise Oriented Arrays of Curved Panels Under Compressive Loading and Aerodynamic Heating", NASA TN D-2910, July, 1965.

41. Guy, L. D. and Dexon, S. C., "A Critical Review of Experiment and Theory for Flutter of Aerodynamically Heated Panels, " Dynamics of Manned Lifting Planetary Entry, J. Wiley & Sons, 1963.

42. Studerus, C. J., and Dienna, E. A., "Viscous Interaction Zero Angle of Attack Drag (VIZAAD) Program, " General Electric Co. TIS 64SD292, November, 1964.

43. Kirsch, A. A., "MBRV-Effects of Low Body Bending Frequency on Vehicle Performance; Part I, Aeroelastic Effects in Vehicle Trim", General Electric PIR AT 815-904, December 1965.

SECTION 8

BIBLIOGRAPHY

During the course of this study, a literature search on panel flutter of curved panels and cones was conducted. The following bibliography shows selected results from this search.

1. Saunders, H., "Determination of Supersonic Panel Flutter of Cylindrical Shells with In-plane Stresses", AIAA Journal, January, 1963

2. Librescu, L., "On the problem of Nonlinear flutter of Thin, Cylindrical, Inhomogeneous Structures", Revue de Mecanique Appliquee, Vol. 7, No. 5, 1962 (In French)

3. Kobayaski, S., "Supersonic Panel Flutter of Unstiffened Circular Cylindrical Shells Having Simply Supported End". Japan Society for Aeronautical and Space Sciences, Transactions, Vol. 6, No. 9, 1963.

4. Nowinski, J. L., "Large-Amplitude Oscillations of Oblique Panels with an Initial Curvature," AIAA Journal, June, 1964

5. Stearman, R., "Flutter of a Ring of Panels", AIAA Journal, August 1964.

6. Kildibekov, I. G., "Nonlinear Acoustic Oscillations of A Cylindrical Shell", Seriia Fiziko-Matematecheskikh Nauk, Vol. 17, No. 3, 1964 (In Russian)

7. Grigoliuk, E. I. and Lamper, R. E., "Some Theoretical and Experimental Investigations of the Self-Oscillations of Curvilinear Panels in a Gas Stream", Theory of Shells and Plates, Proceedings of the IVth All-union Conference, 1962 (In Russian)

8. Novichkov, I. U., "Nonsteady flutter of Cylindrical Panels", Theory of Shells and Plates, Proceedings of the IVth All-union Conference, 1962 (In Russian)

9. Dzygadlo, Z., "The Problem of Aeroelasticity of a Cylindrical Panel and a Plate Strip Taking into Consideration the Transversal Coupling", Polish Academy of Sciences, Inst. of Basic Technical Problems, Dept. of Vibrations, Vol. 5, No. 2, 1964

10. Dun, M. D., "An Exact Linearized Theory of Panel Flutter of a Finite Cylindrical Shell in a Supersonic Flow", Acta Mechamoca Sinica, Vol. 7, December 1964 (In Chinese)

11. Anderson, W. J., "Oscillatory Pressures in a Idealized Boundary Layer with an Application to the Panel Flutter of Cylindrical Shells", AIAA Symposium on Structural Dynamics, 1965

12. Dowell, E. H., "The Flutter of Infinitely Long Plates and Shells", AIAA Symposium on Structural Dynamics, 1965

13. Chang, Y. W., "Vibrations and Stability of Buckled Panels", ASCE Journal, Engineering Mechanics Division, Vol. 91, October 1965

14. Anderson, W. J., "Experiments on the Flutter of Flat and Slightly Curved Panels at Mach Number 2.81", California Inst. of Tech. Graduate Aeronautical Labs, June 1962

15. Hess, R. W. and Gibson, F. W., "Experimental Investigation of the Effects of Compressive Stress on the Flutter of a Curved Panel and at Supersonic Mach Numbers" NASA TND-1386, October, 1962

16. Leonard, R. W. and Hedgepeth V. M., "Status of Flutter of Flat and Curved Panels", NACA RM L57O24C, May 1957

17. Presnell J. G., and McKinney R. L., "Experimental Panel Flutter Results for Some Flat and Curved Titanium Skin Panels at Supersonic Speeds", NASA TND-1600, January 1963

18. Tuovila, W. J. and Hess, R. W., "Experimental Investigation of Flutter of Buckled Curved Panels Having Longitudinal Stringers at Transonic and Supersonic Speeds", NASA Memo 5-18-59L, 1959.

19. Brown, A. and Holt M., "Calculation of Aerodynamic Forces on Cylindrical Shells in Unsteady Supersonic Flow" California University, Berkeley, April 1963

20. Stearman, R. O., "Research on Panel Flutter of Cylindrical Shells", Midwest Research Institute, January 1964

21. McEdman, J. A., "Flutter of Curved and Flat Sandwich Panels Subjected to Supersonic Flow", NASA TND-2192, April 1964

22. Brown, R. A. and Holt, M., "Frequency Effects in Panel Flutter of Cylindrical Shells," California University, Berkeley, March 1964

23. Stepanov, R. D., "Flutter of Cylindrical Panels Moving in a Gas" AFSC FTD Engineering Collection of Selected Articles, 1963

24. Dugundji, J., "Research on Aerothermoelasticity", Final Summary Report, AFOSR 5148, June 1963

25. Krumhaar, H., "The Accuracy of Piston Theory when Applied to Cylindrical Shells", AIAA Journal, June 1963

26. Johns, D. J., "Some Panel Aeroelastic Instabilities" AGARD 474, September, 1963

27. Shirk, M. H. and Olsen, J. J., "Recent Panel Flutter Research and Applications" AGARD 475, September 1963

28. Perkins, T. M. and Brice, T. R., "An Investigation of the Aeroelastic Stability of Thin Cylindrical Shells at Transonic Mach Numbers" AEDC TR-66-93, May 1966
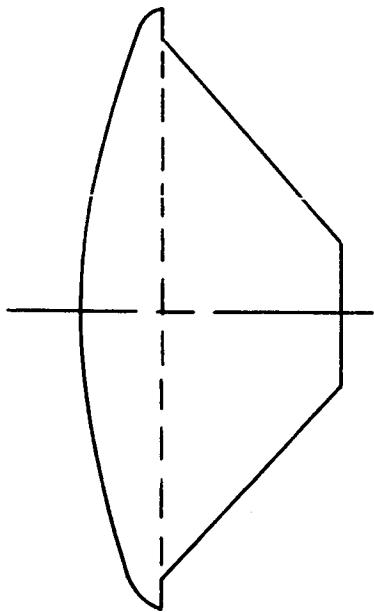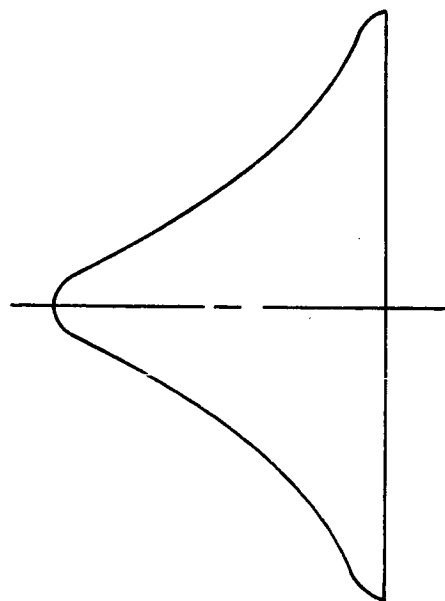
VEHICLE 1
SPHERE-CAP/ CONE FRUSTUM
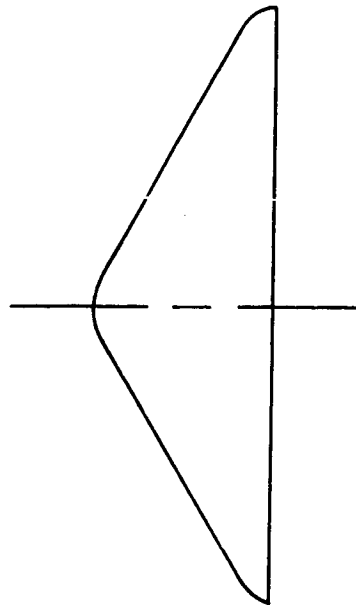
VEHICLES 2, 3, 4
SPHERE CONE/ OPEN
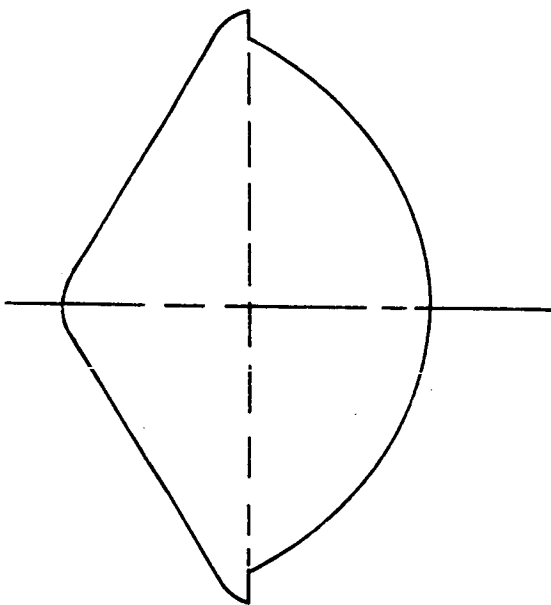
VEHICLE 5
SPHERE CONE/ SPHERE CAP

VEHICLE 6
SMOOTH FLARE/ OPEN

Figure 1. Entry Vehicle Shapes

VEHICLE NO.	1	2	3	4	5	6
GEOMETRY						
FOREBODY	Sphere Cap	Sphere-Cone	Sphere-Cone	Sphere-Cone	Sphere-Cone	Smooth Flare
AFTBODY	Cone Frustum	Open Back	Open Back	Open Back	Sphere Cap	Open Back
$M/C_D A$	0.20	0.20	0.25	0.30	0.20	0.20
W_E	1020.0	1020.0	3030.0	1530.0	1020.0	1020.0
DIA.	12.0	12.0	18.5	12.0	12.0	12.0
C.G./D	0.25	0.25	0.25	0.25	0.25	0.25
I_{PITCH}	270.0	270.0	2455.0	243.0	270.0	270.0
I_{ROLL}	300.0	300.0	2400.0	407.0	300.0	300.0

Figure 2. Vehicle Configuration Selection
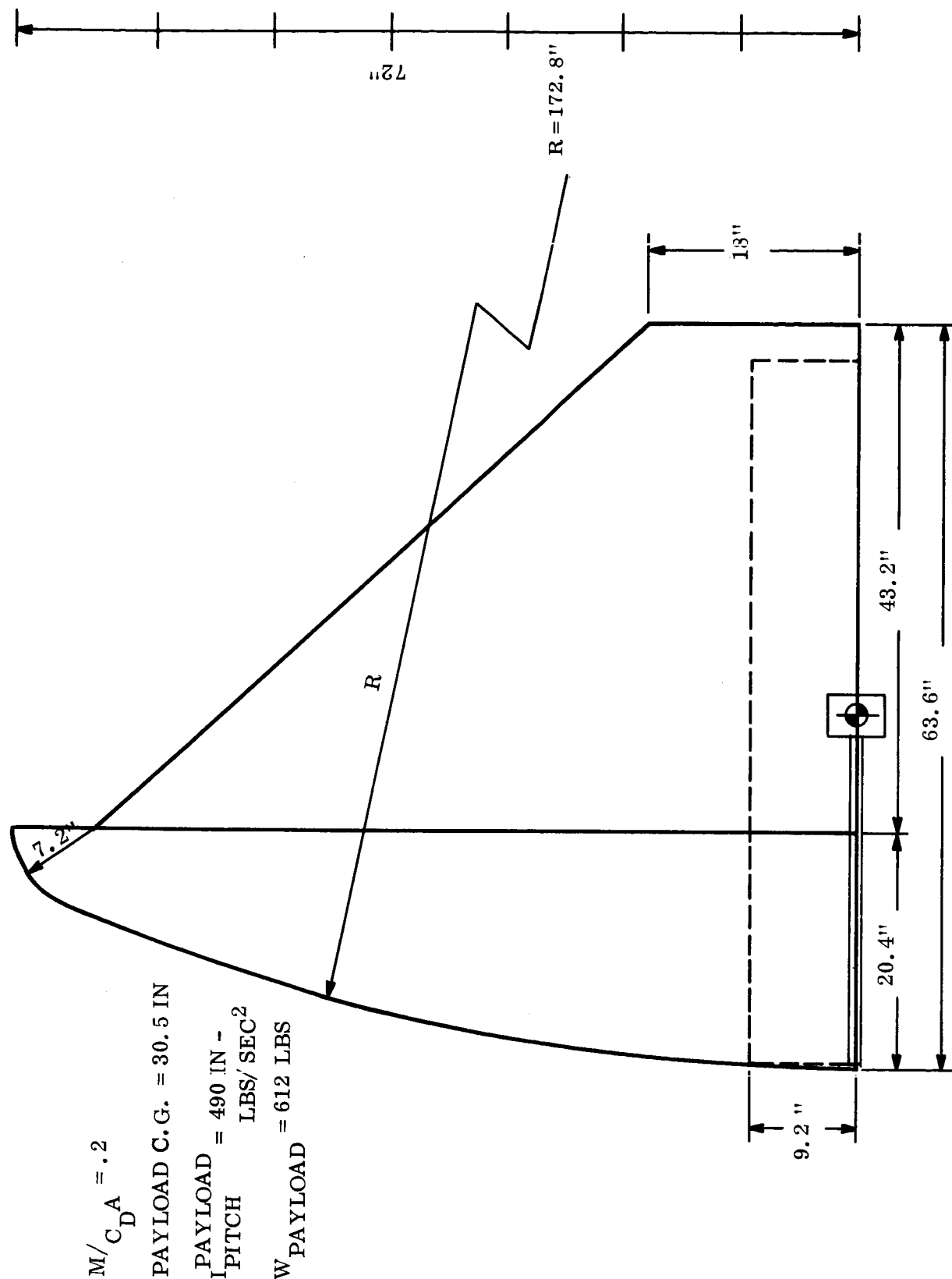
Figure 3. Sphere-Cap-Cone Frustrum Afterbody Run 46

R = 172.8"

72"

13"

43.2"

63.6"

20.4"

9.2"

7.2"

R

$M/C_D A = .2$

PAYLOAD C.G. = 30.5 IN

$I_{PITCH}^{PAYLOAD} = 490$ IN - LBS/SEC^2

$W_{PAYLOAD} = 612$ LBS

$M/C_DA = .2$

PAYLOAD C.G. = 39. IN.

$I^{PAYLOAD}_{PITCH} = 1473.12$ IN-LBS/SEC^2

$W_{PAYLOAD} = 510$ LBS

SECTION 1

SECTION 2

7.2"

60°

72."

14.4"

λ

12"

39"

43.5"
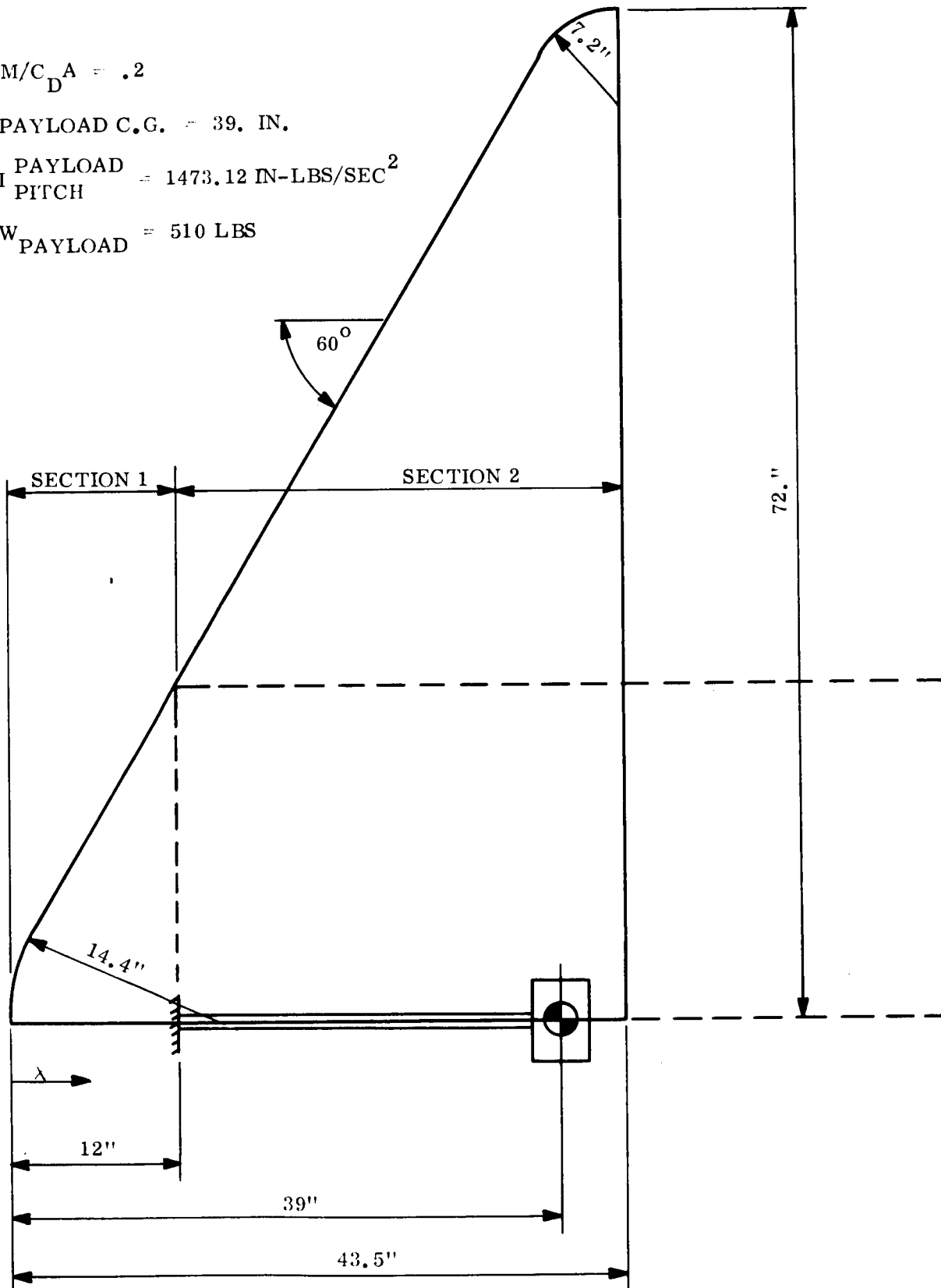
Figure 4. 60° Sphere Cone 12' Diameter Run 41 Vehicle 2

$M/C_DA = .2$

PAYLOAD C.G. = 39 IN.

$I_{PITCH}^{PAYLOAD} = 1473.12 \text{ IN-LBS/SEC}^2$

$W_{PAYLOAD} = 510 \text{ LBS}$

Figure 5. 60° Sphere Cone 12' Diameter Run 46 Vehicle 2
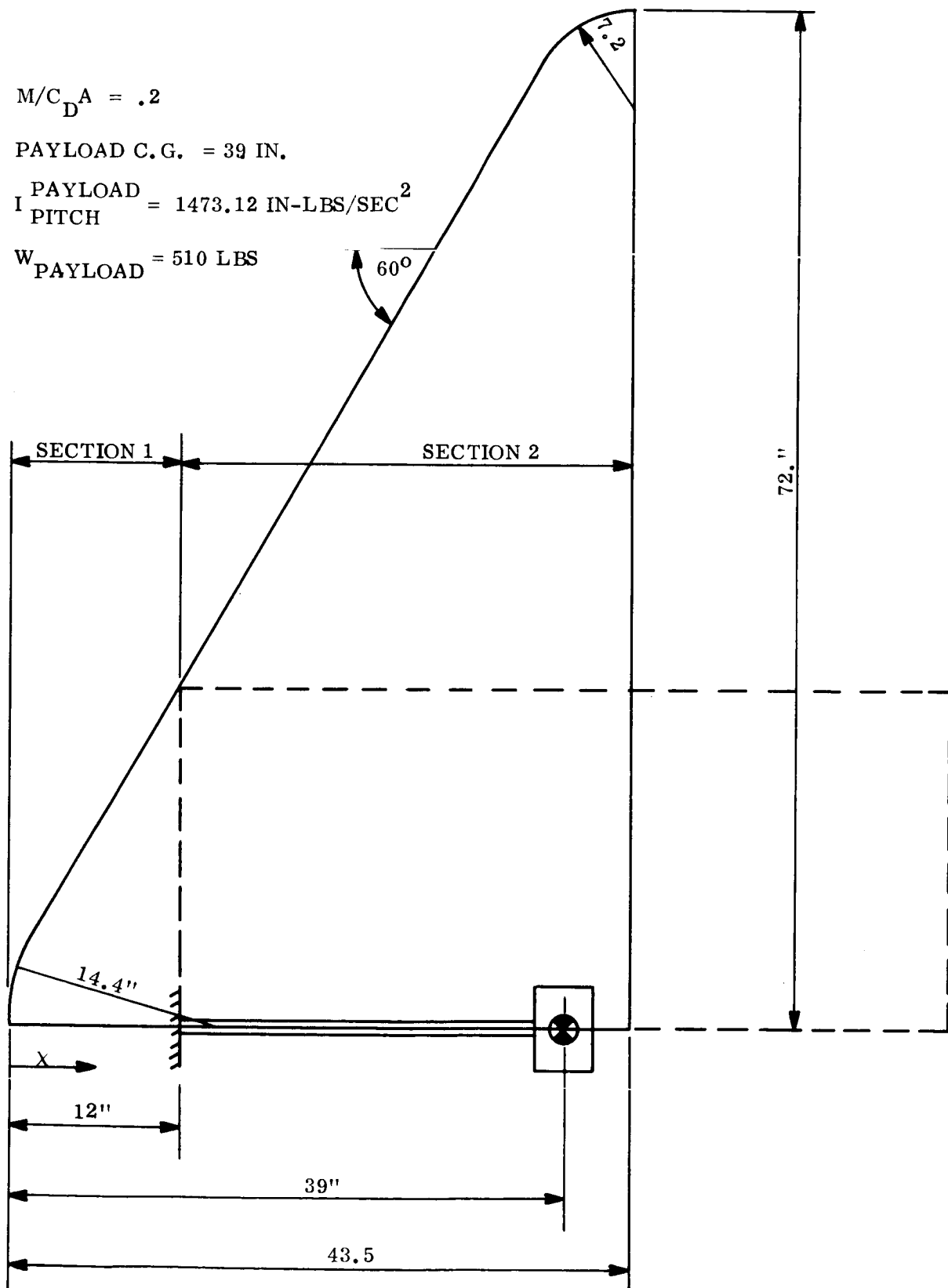
$M / C_D A = .25$

PAYLOAD C.G. $= 60$ IN.

$I \frac{PAYLOAD}{PITCH} = 9024.$ IN-LB/SEC^2.

$W_{PAYLOAD} = 1515$ LBS
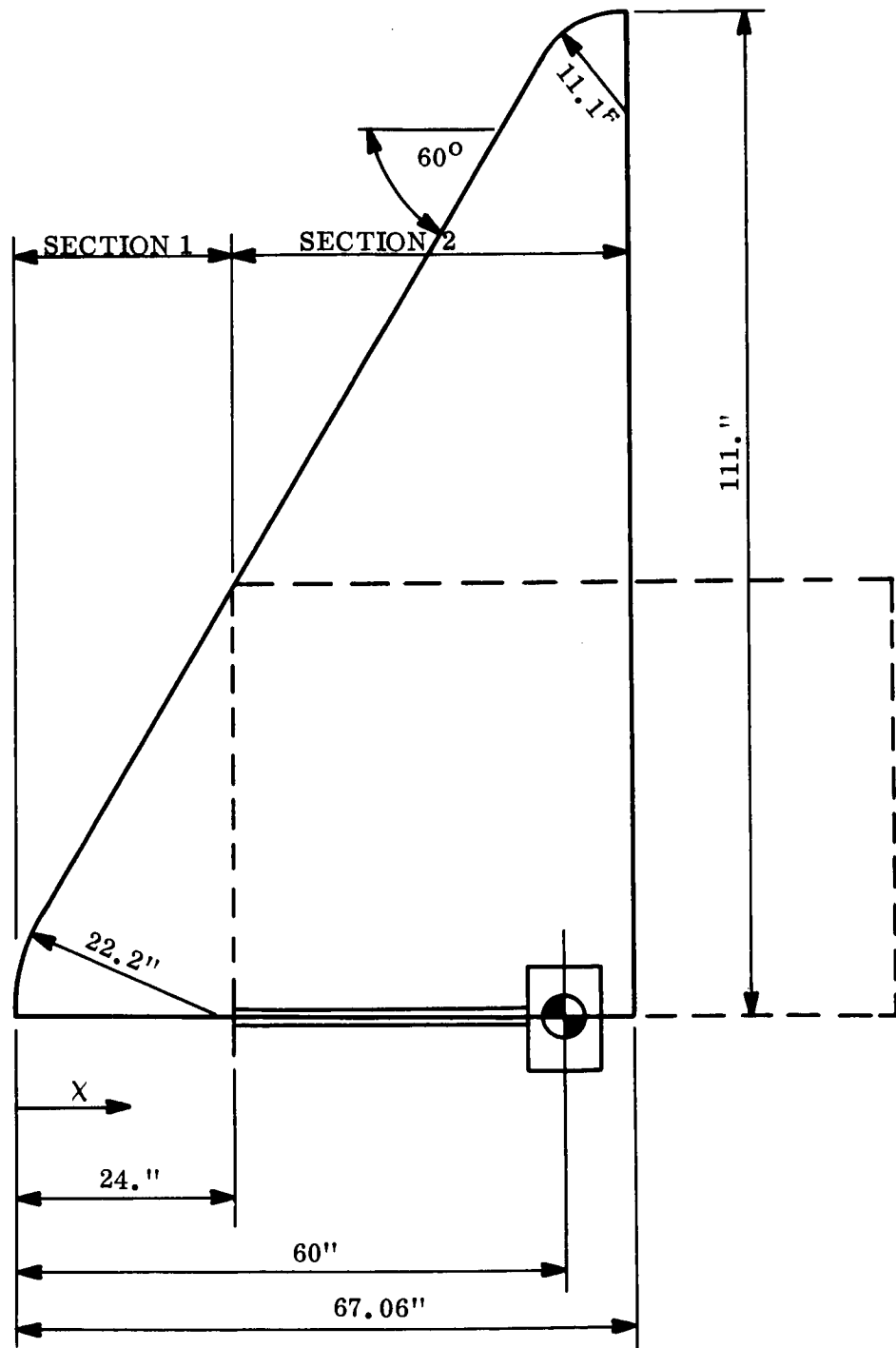
Figure 6. 60° Sphere Cone 18.5' Diameter Run A-1 Vehicle 3

$M/C_D A = .3$

PAYLOAD C.G. = 39.4 IN.

$I \begin{array}{l} \text{PAYLOAD} \\ \text{PITCH} \end{array} = 1805.51 \text{ IN-LB/SEC}^2.$

$W_{\text{PAYLOAD}} = 765 \text{ LBS}$
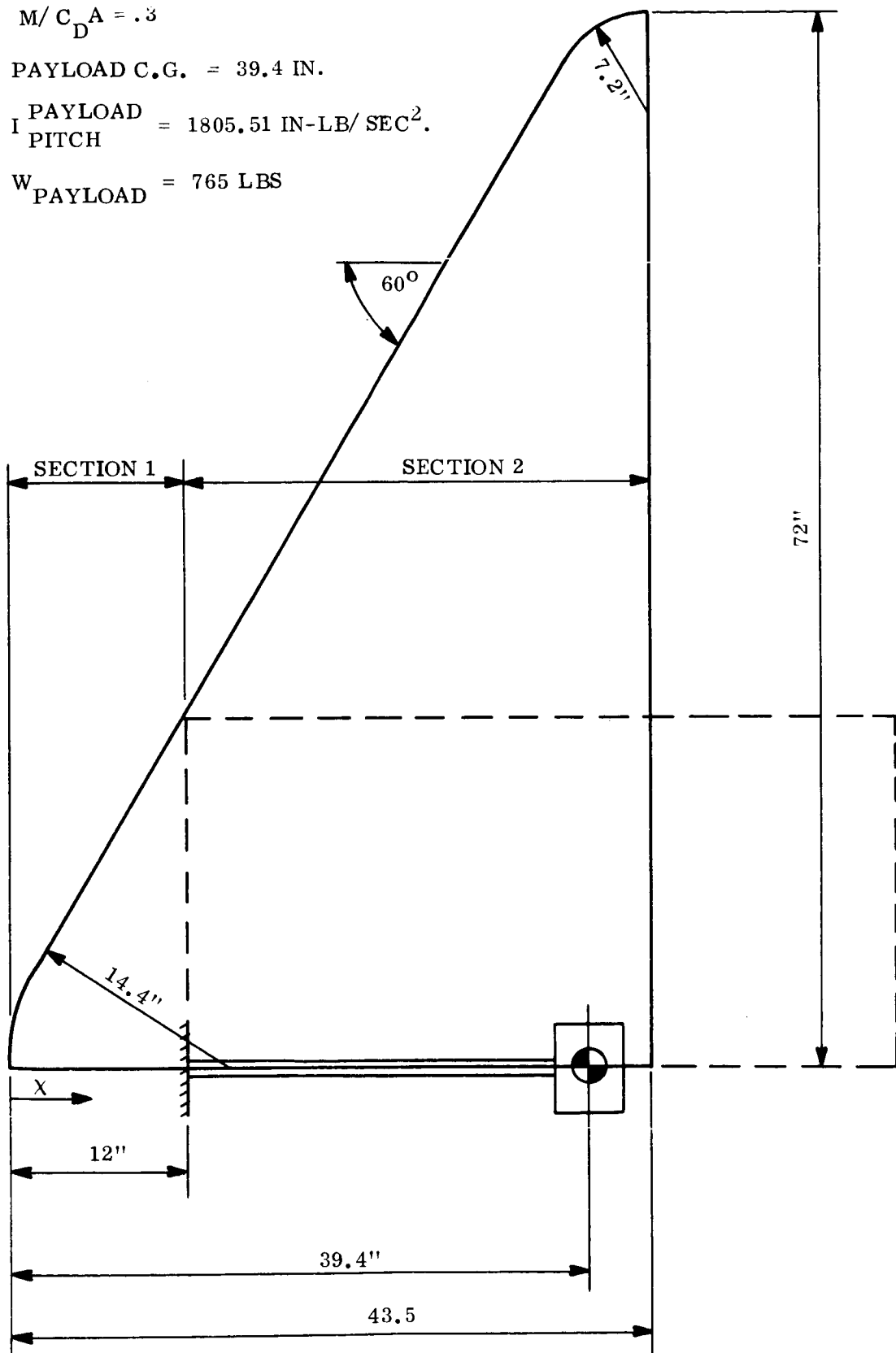
7.2"

60°

SECTION 1

SECTION 2

72"

14.4"

X

12"

39.4"

43.5

Figure 7.   60° Sphere Cone 12' Diameter Run 19 Vehicle 4
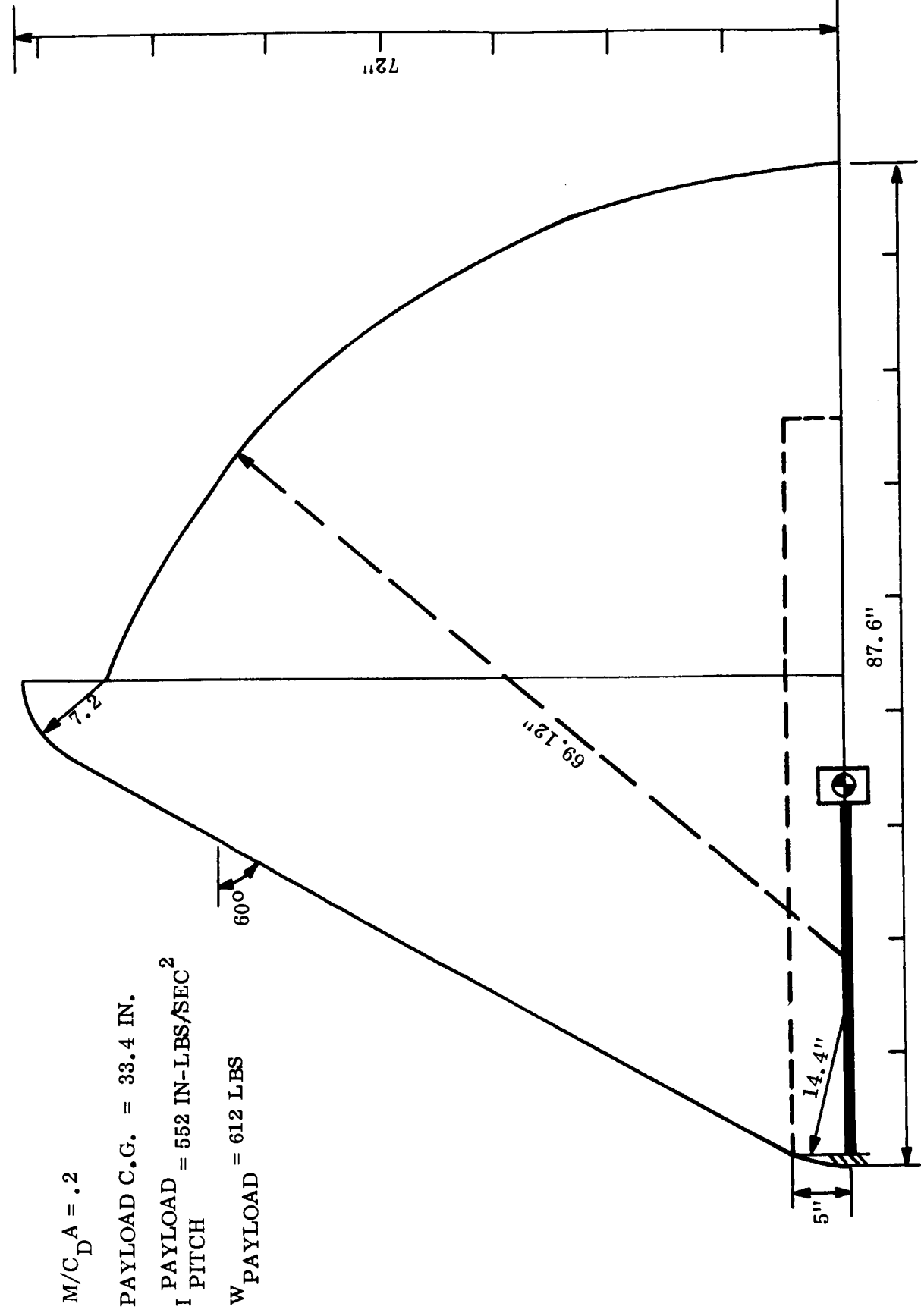
Figure 8. 60° Sphere Cone Forebody–Sphere Cap Afterbody Run 46 Vehicle 5

M/C$_D$A = .2

PAYLOAD C.G. = 33.4 IN.

I$^{PAYLOAD}_{PITCH}$ = 552 IN-LBS/SEC^2

W$_{PAYLOAD}$ = 612 LBS

72"

87.6"

69.12"

14.4"

5"

7.2

60°

Figure 9. Tension Shell Shape

M/C$_D$A = .2

PAYLOAD C.G. = 40 IN.

I $^{PAYLOAD}_{PITCH}$ = 273.6 IN-LBS-SEC^2

W$_{PAYLOAD}$ = 560 LBS

RING C.G. = 85 IN.

I $^{RING}_{PITCH}$ = 2052 IN-LBS/SEC^2

72"

85"

87"

40"
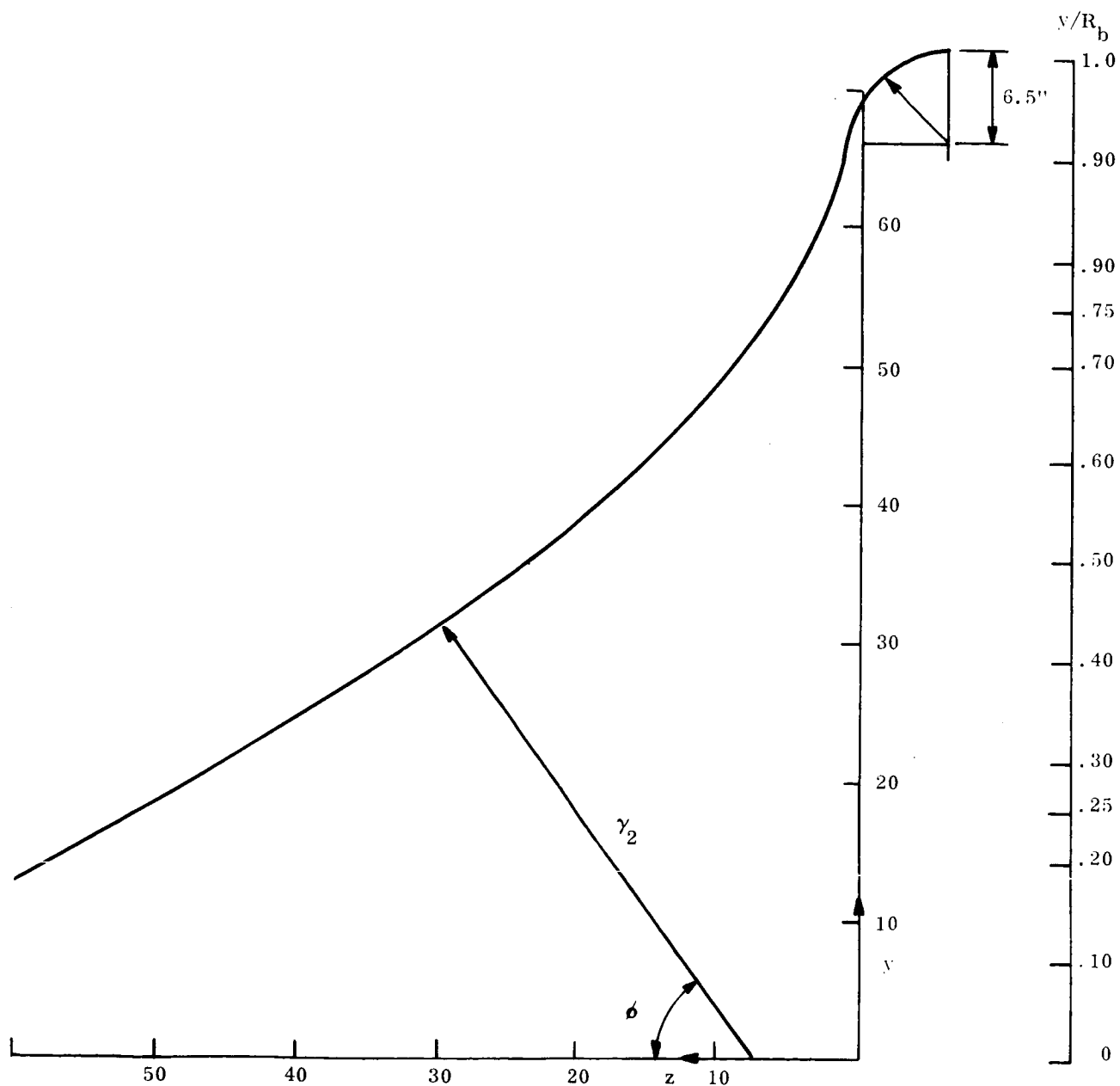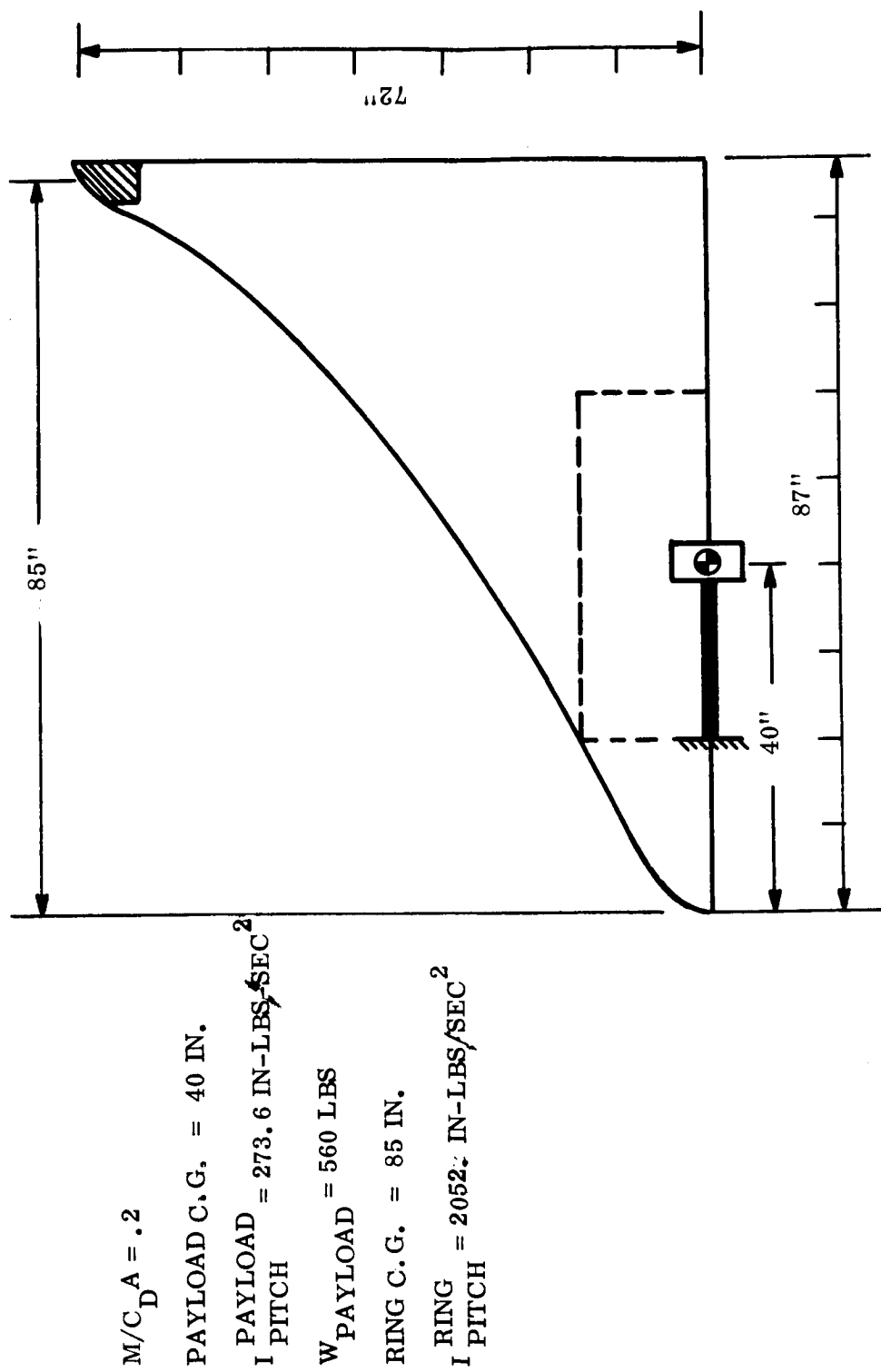
Figure 10. Tension Shell Shape

Figure 11. Sphere Cap-Cone Frustrum Afterbody, 12' Diameter, Run 46, Vehicle 1, Monocoque, $M/C_D A = .20$

105
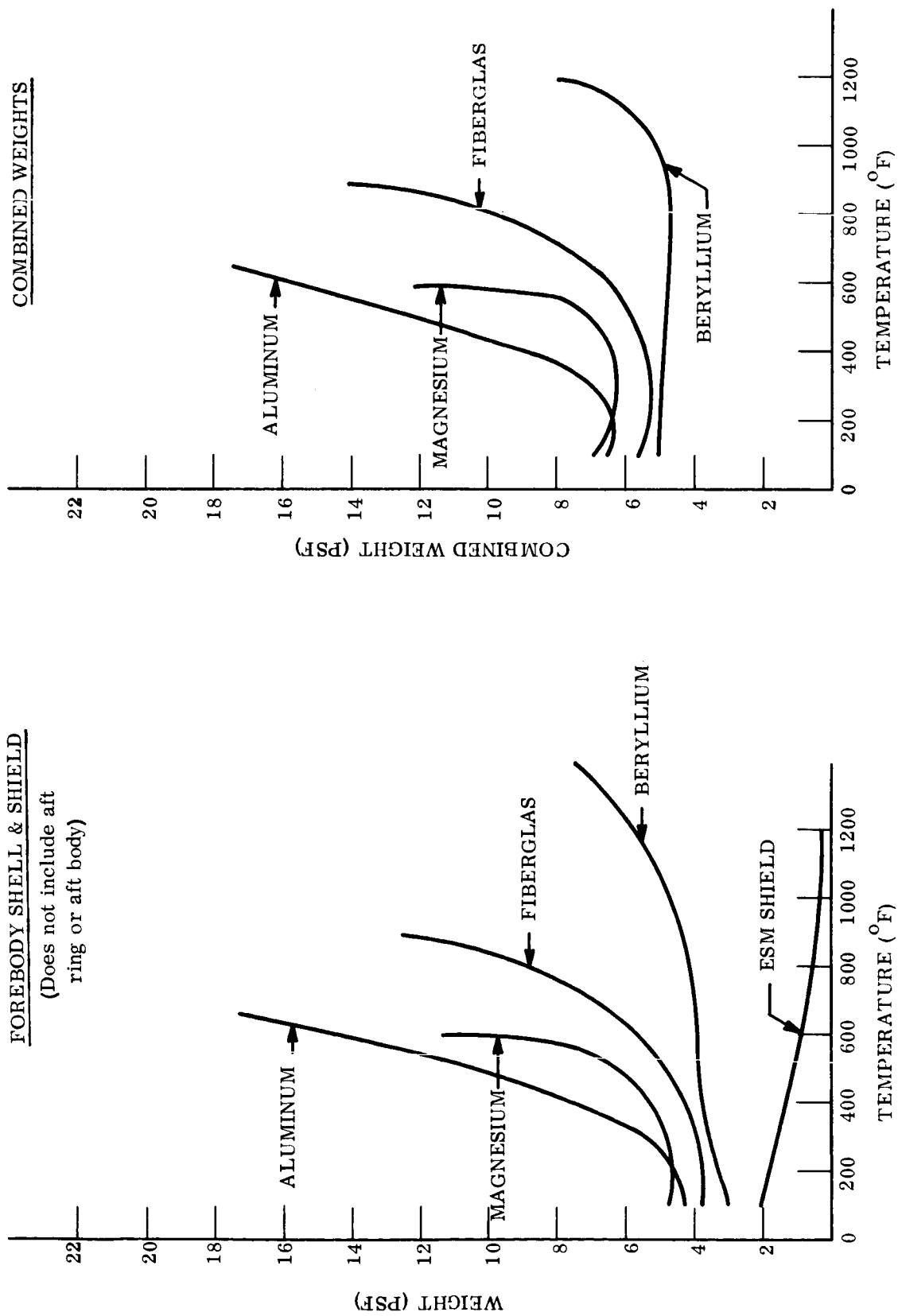
Figure 12. Sphere Cap – Cone Frustrum Afterbody, 12' Diameter, Run 46, Vehicle 1, Honeycomb, $M/C_D A = .20$

Figure 13. 60° Sphere Cone Forebody, 12' Diameter, Run 41, Vehicle 2, Zero Spin, Honeycomb, $M/C_D A = .20$

107

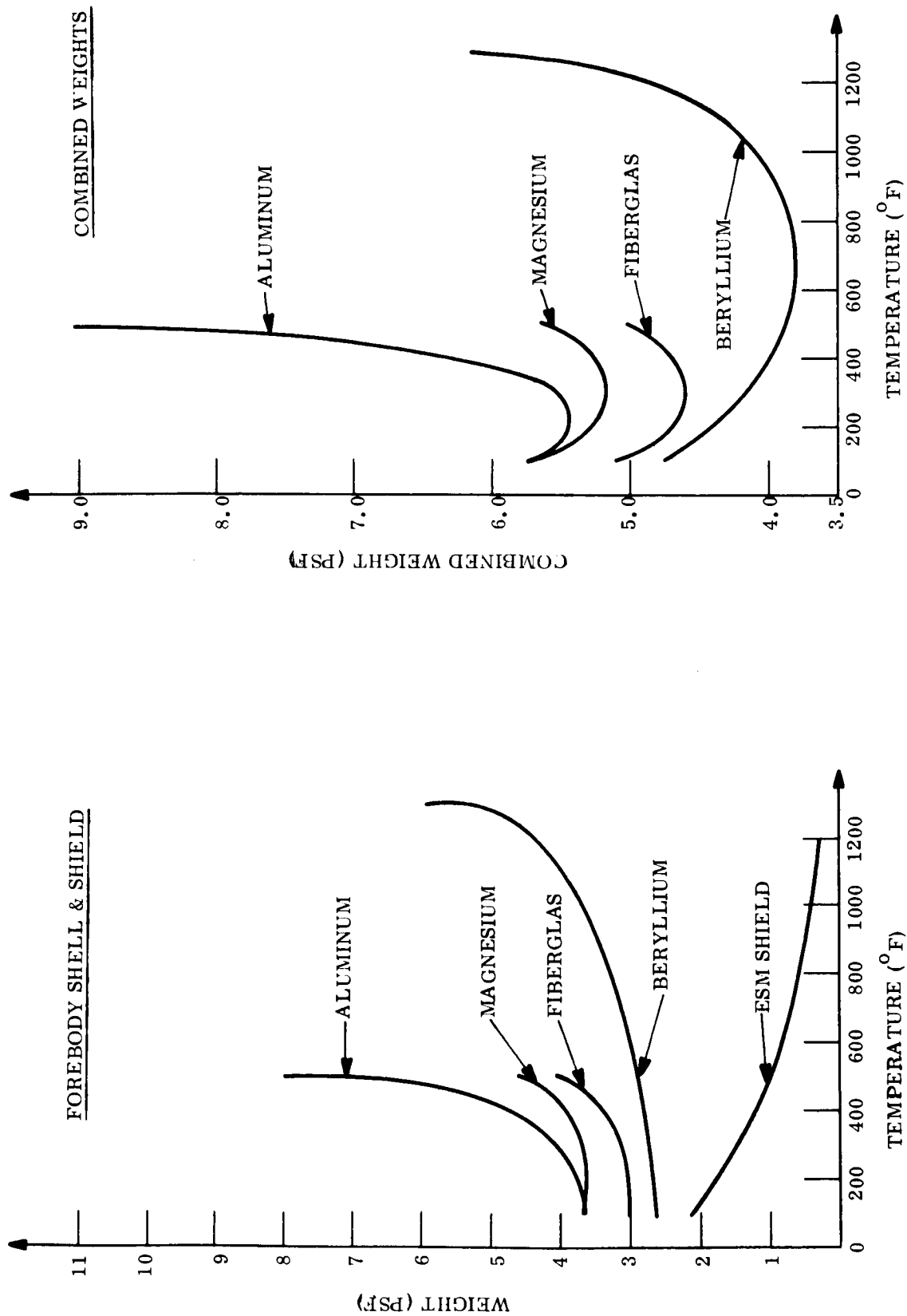Figure 14. 60° Sphere Cone Forebody, 12' Diameter, Run 41, Vehicle 2, Zero Spin, Ring Stiffened, $M/C_D A = .20$

Figure 15. 60° Sphere Cone Forebody, 12' Diameter, Run 46, Vehicle 2, Honeycomb, $M/C_D A = .20$

Figure 16. 60° Sphere Cone Forebody, 12' Diameter, Run 46, Vehicle 2, Ring Stiffened, $M/C_D A = .20$

110
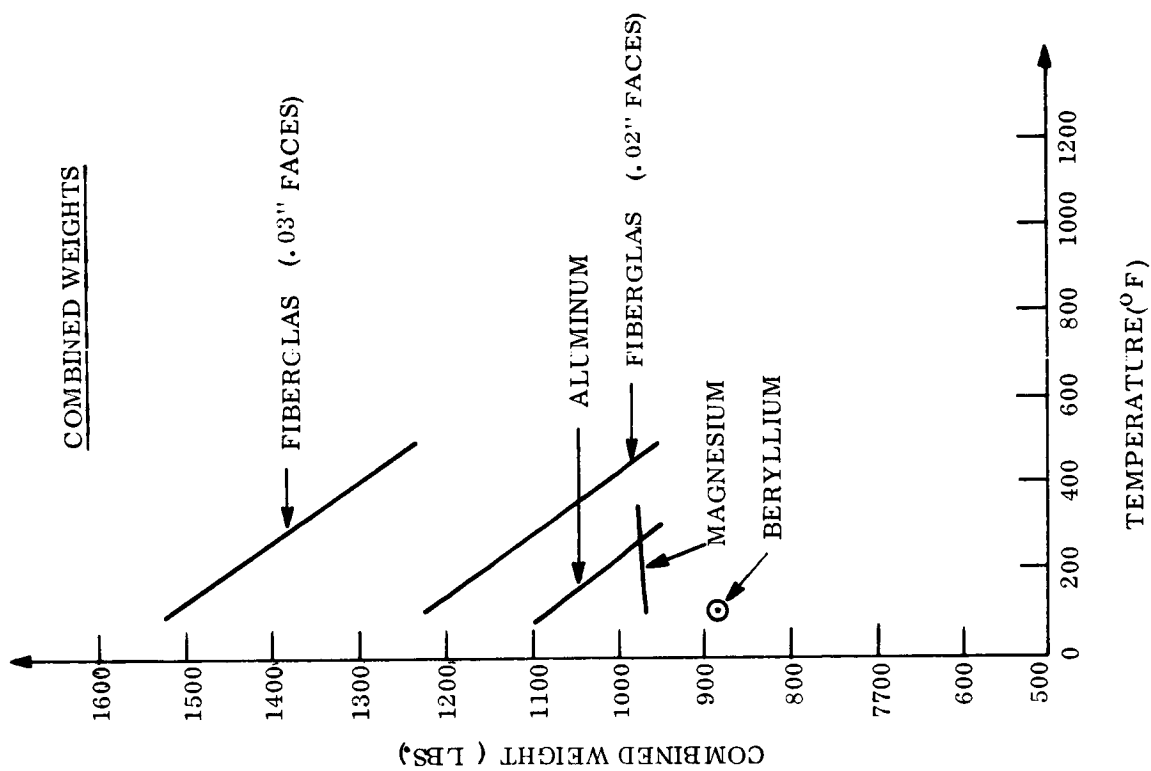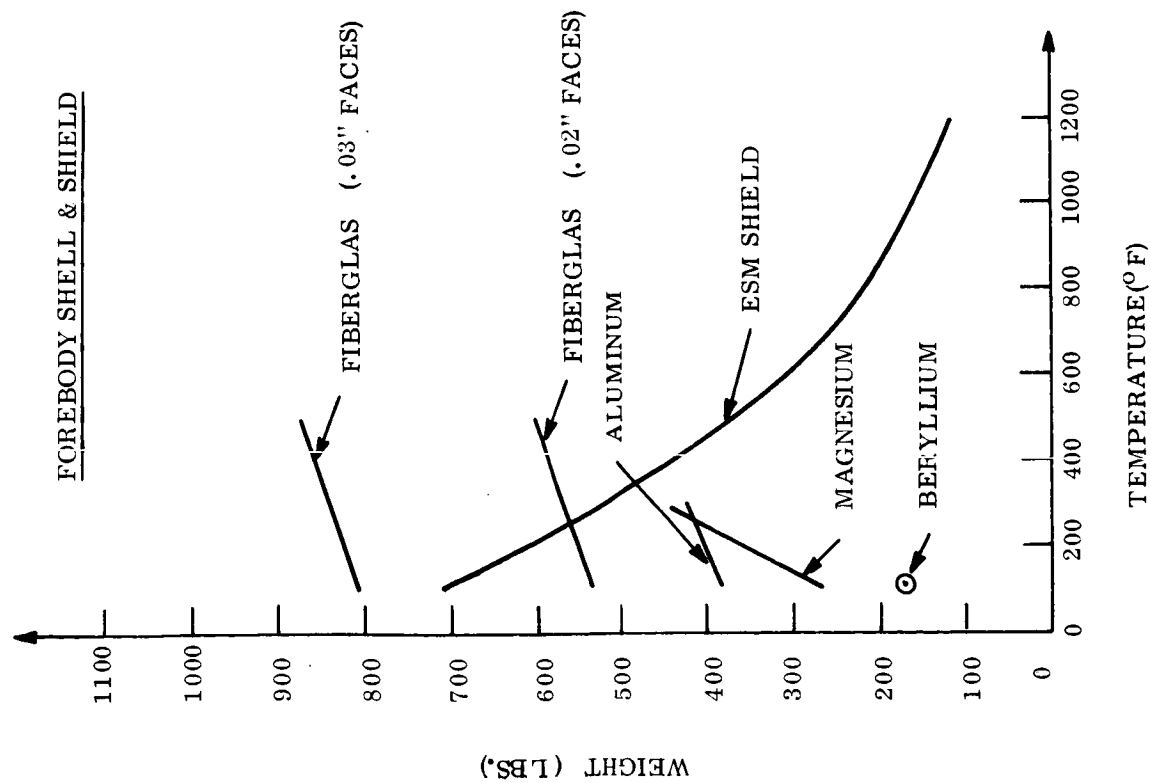
Figure 17. 60° Sphere Cone Forebody, 18.5' Diameter, Run A-1, Vehicle 3, Honeycomb, $M/C_D A = .25$
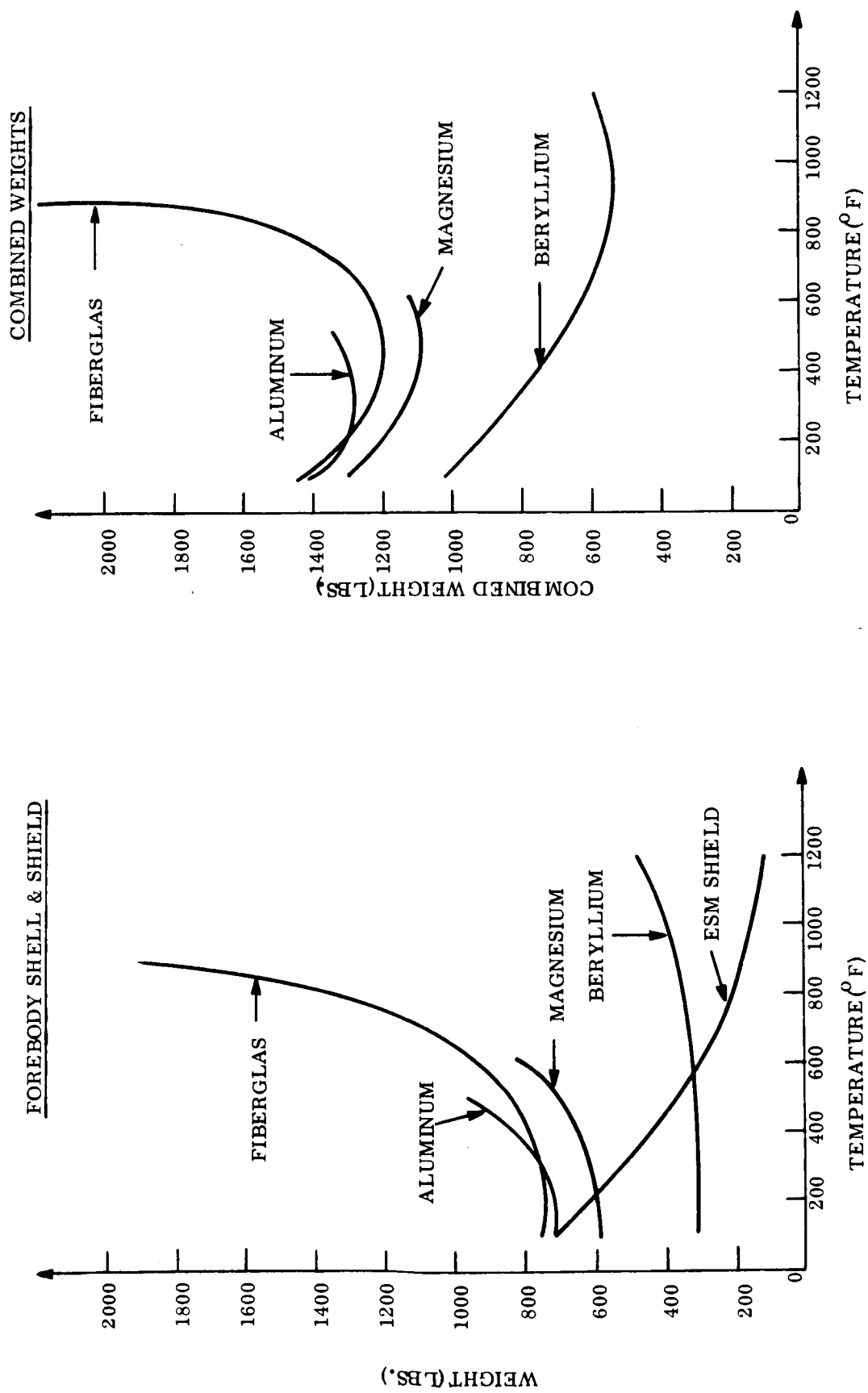
Figure 18. 60° Sphere Cone Forebody, 18.5' Diameter, Run A-1, Vehicle 3, Ring Stiffened, $M/C_D A = .25$
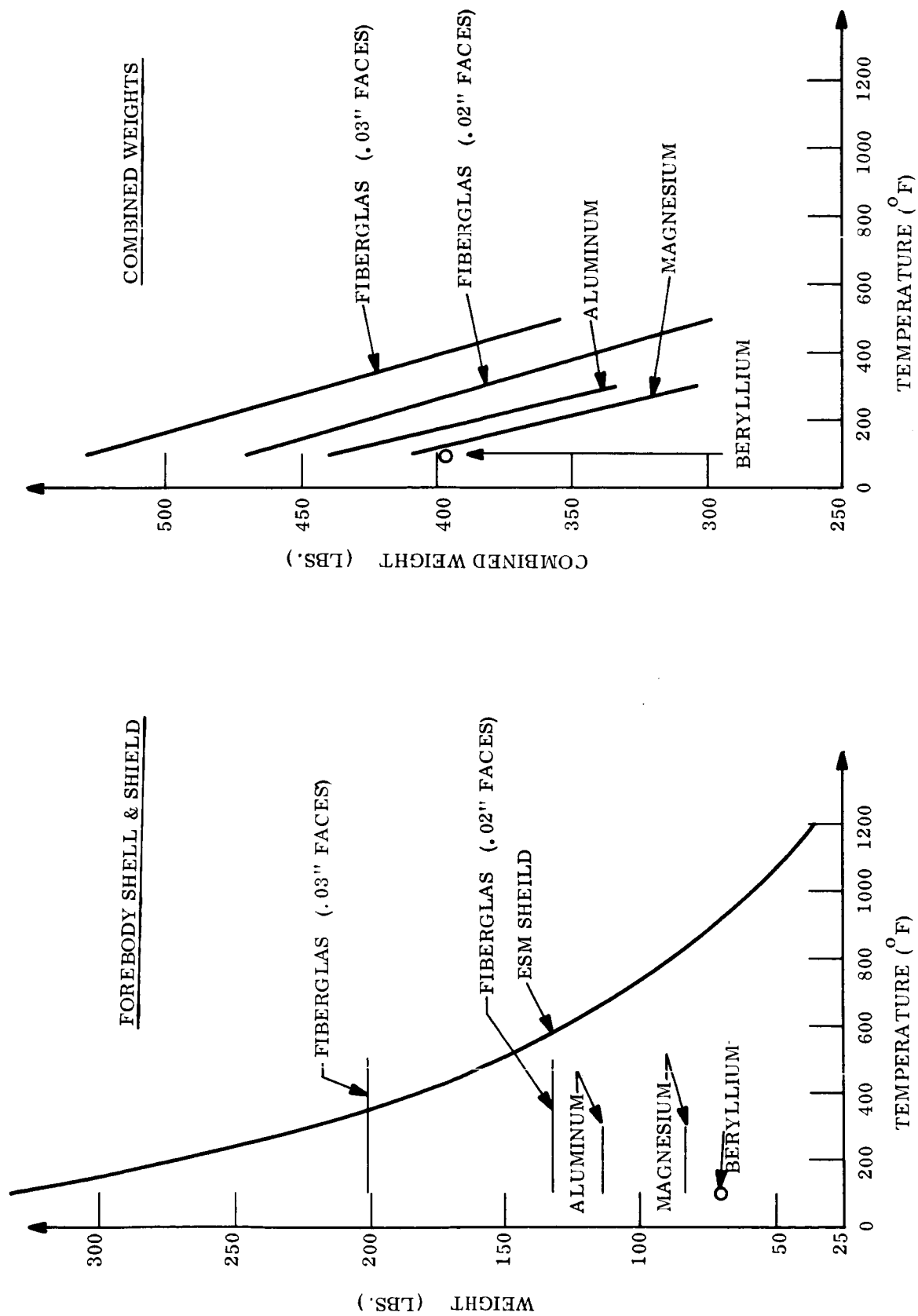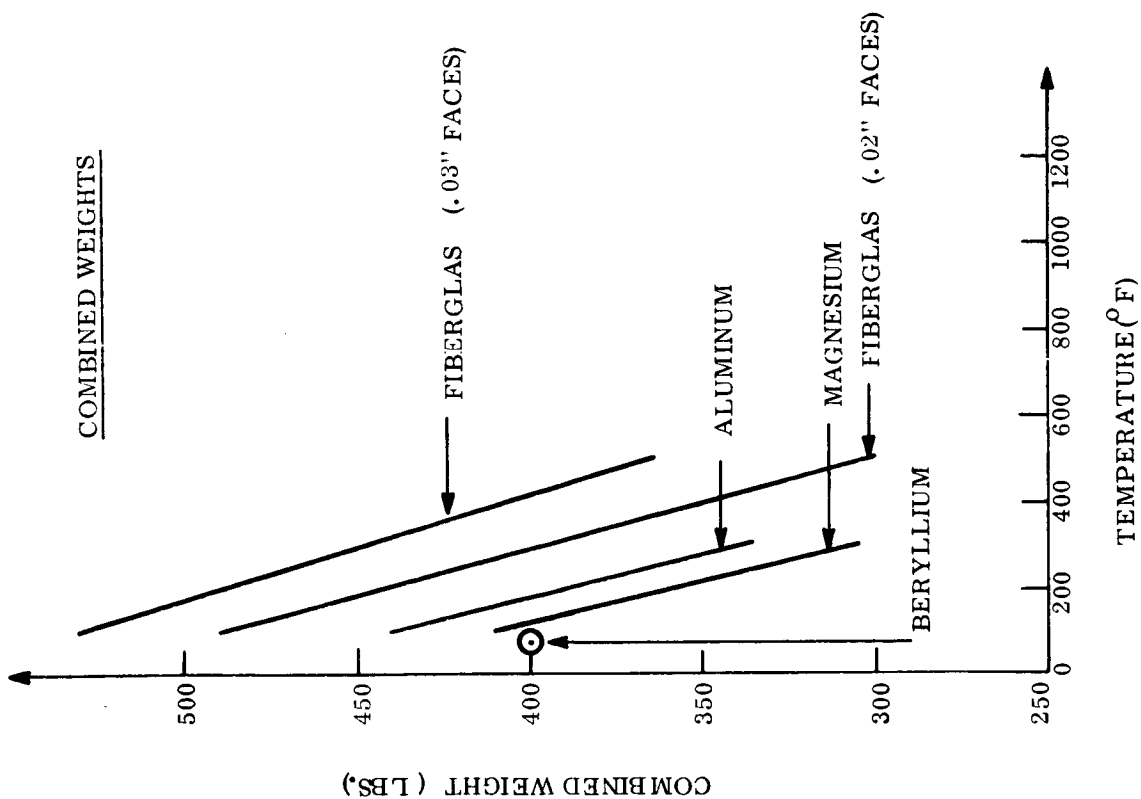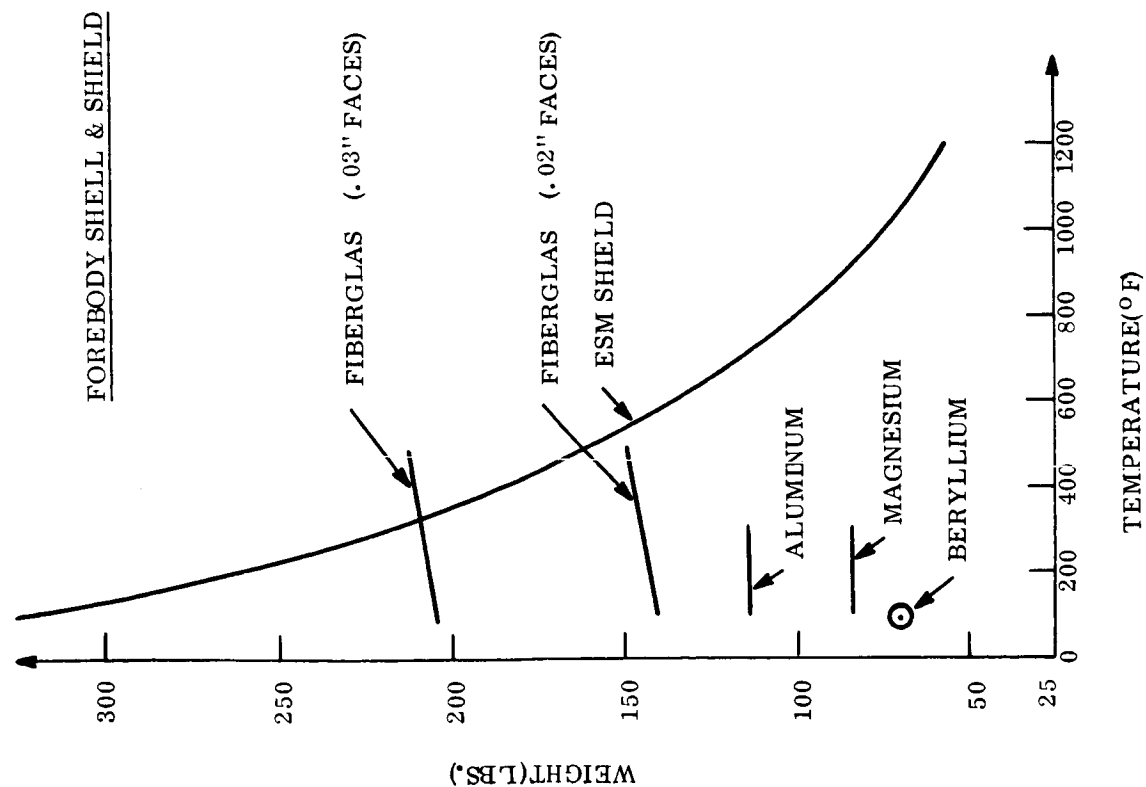
Figure 19. 60° Sphere Cone Forebody, 12' Diameter, Run 19, Vehicle 4, Honeycomb, M/C$_D$A = .30

113
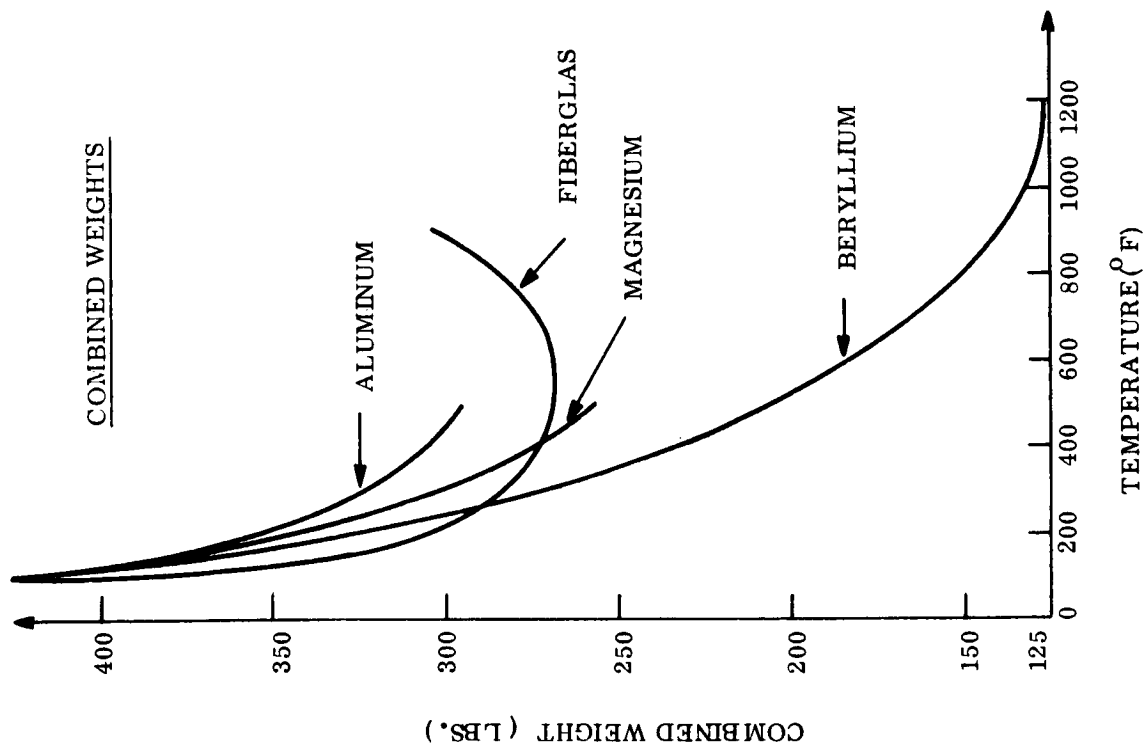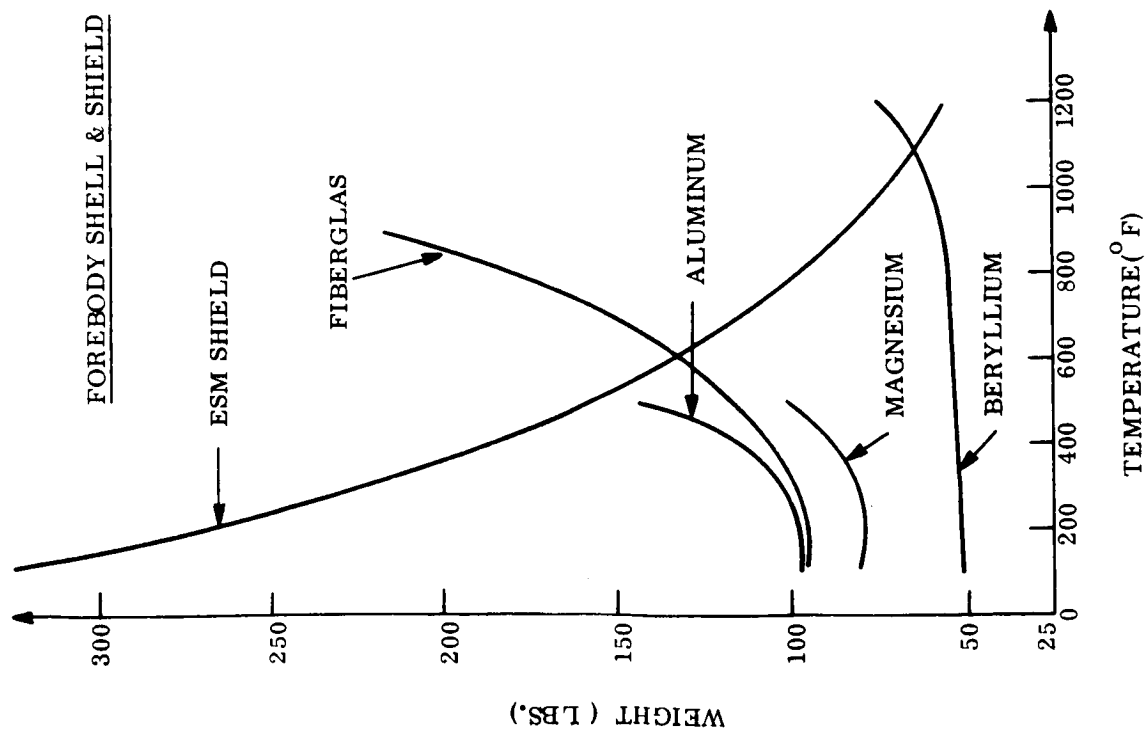
Figure 20. 60° Sphere Cone Forebody, 12' Diameter, Run 19, Vehicle 4, Ring Stiffened, $M/C_D A = .30$

114
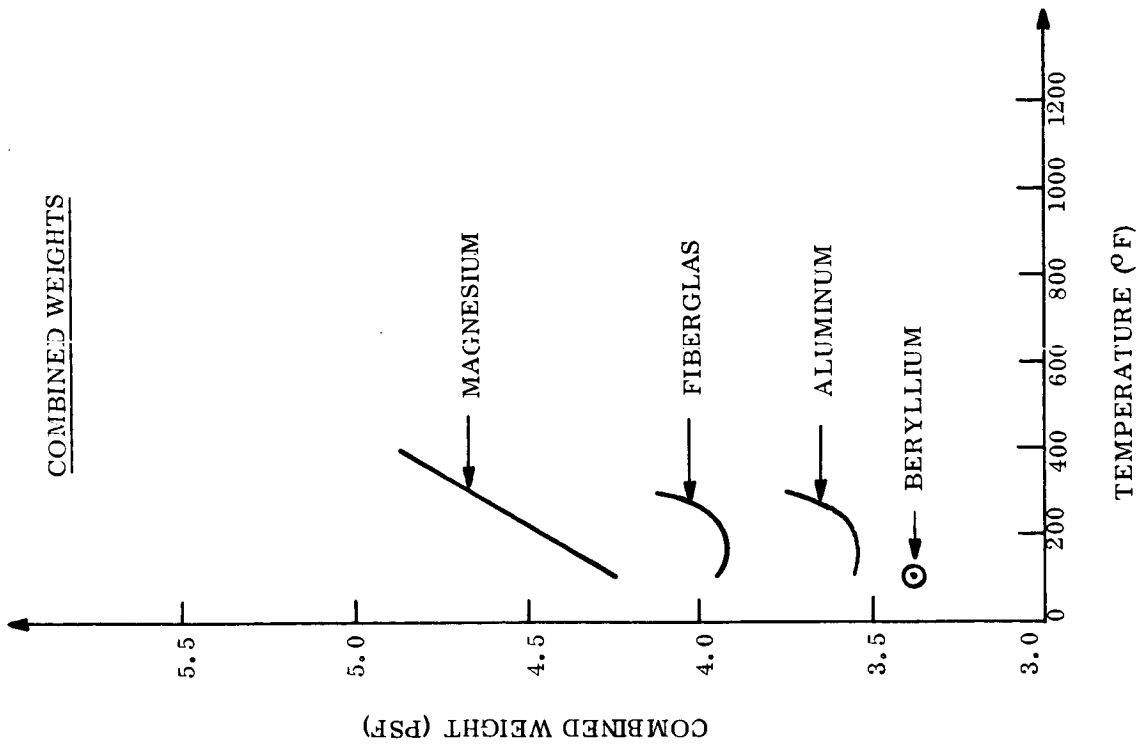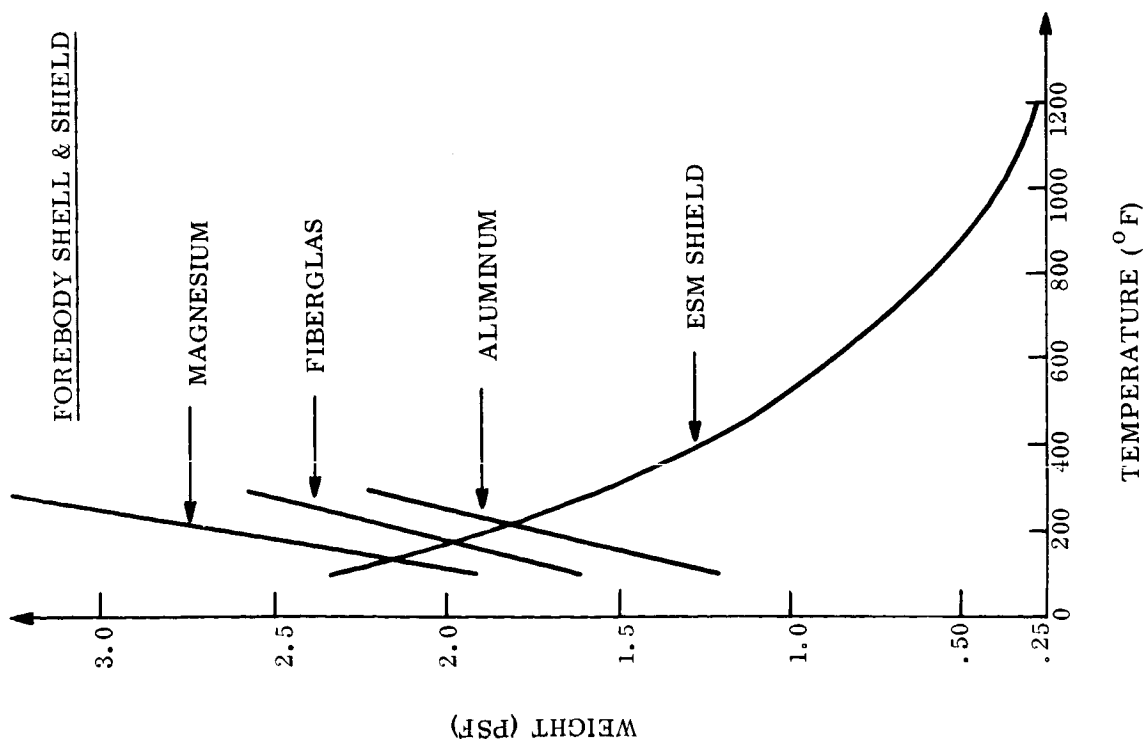
Figure 21. 60° Sphere Cone Forebody-Sphere Cap Afterbody,
12' Diameter, Run 46, Vehicle 5, Honeycomb, $M/C_D A = .20$

115
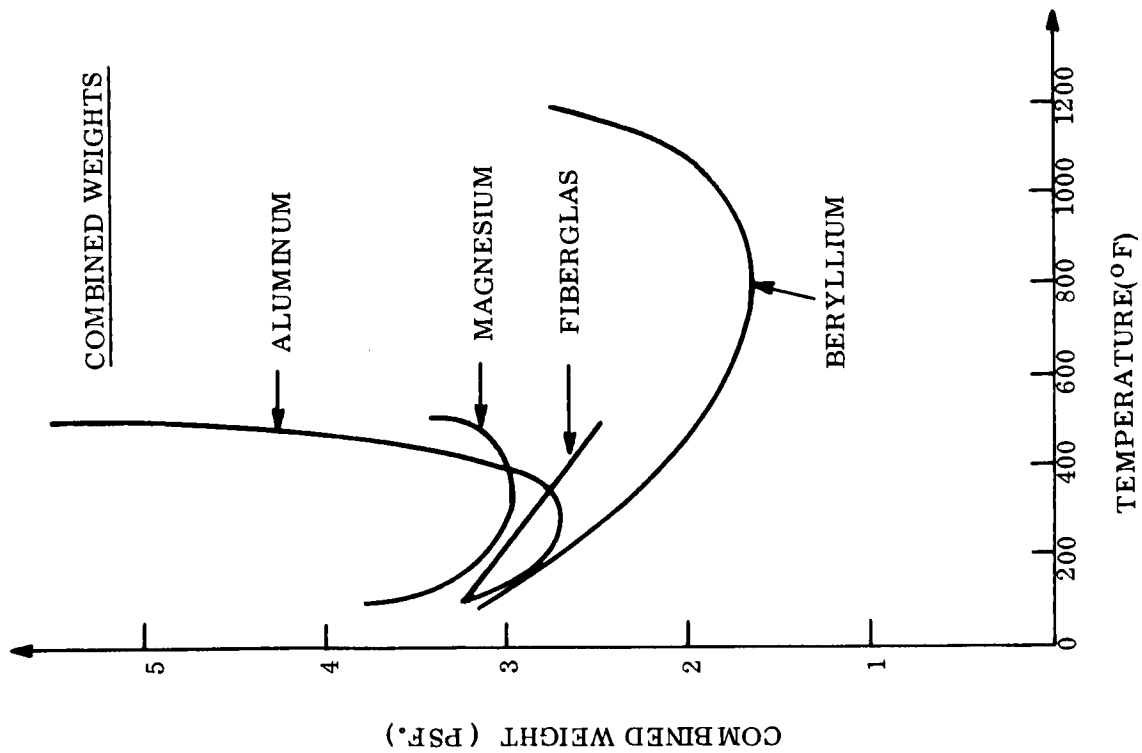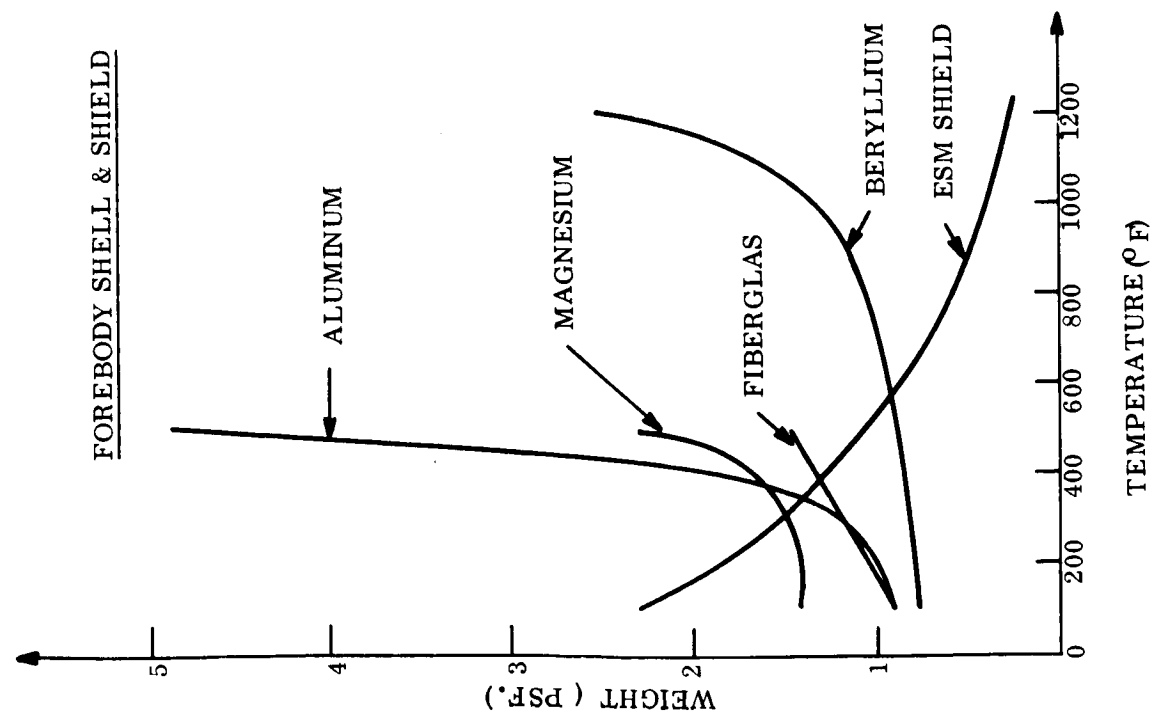
Figure 22. 60° Sphere Cone Forebody – Sphere Cap Afterbody,
12' Diameter, Run 46, Vehicle 5, Ring Stiffened, $M/C_D A = .20$
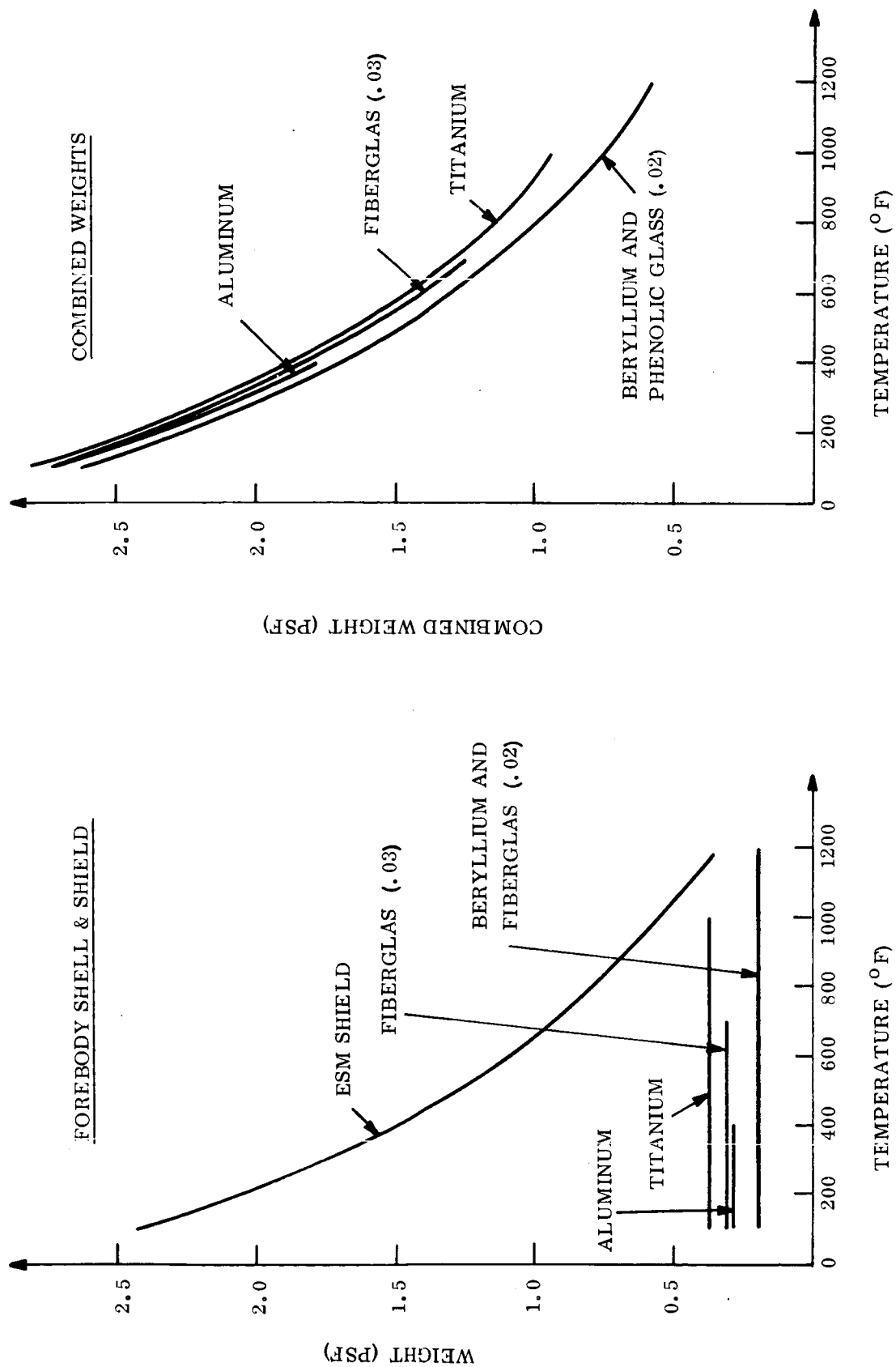
Figure 23. Smooth Flare Tension Shell, 12' Diameter, Run 46, Vehicle 6, Monocoque, $M/C_D A = .20$

117
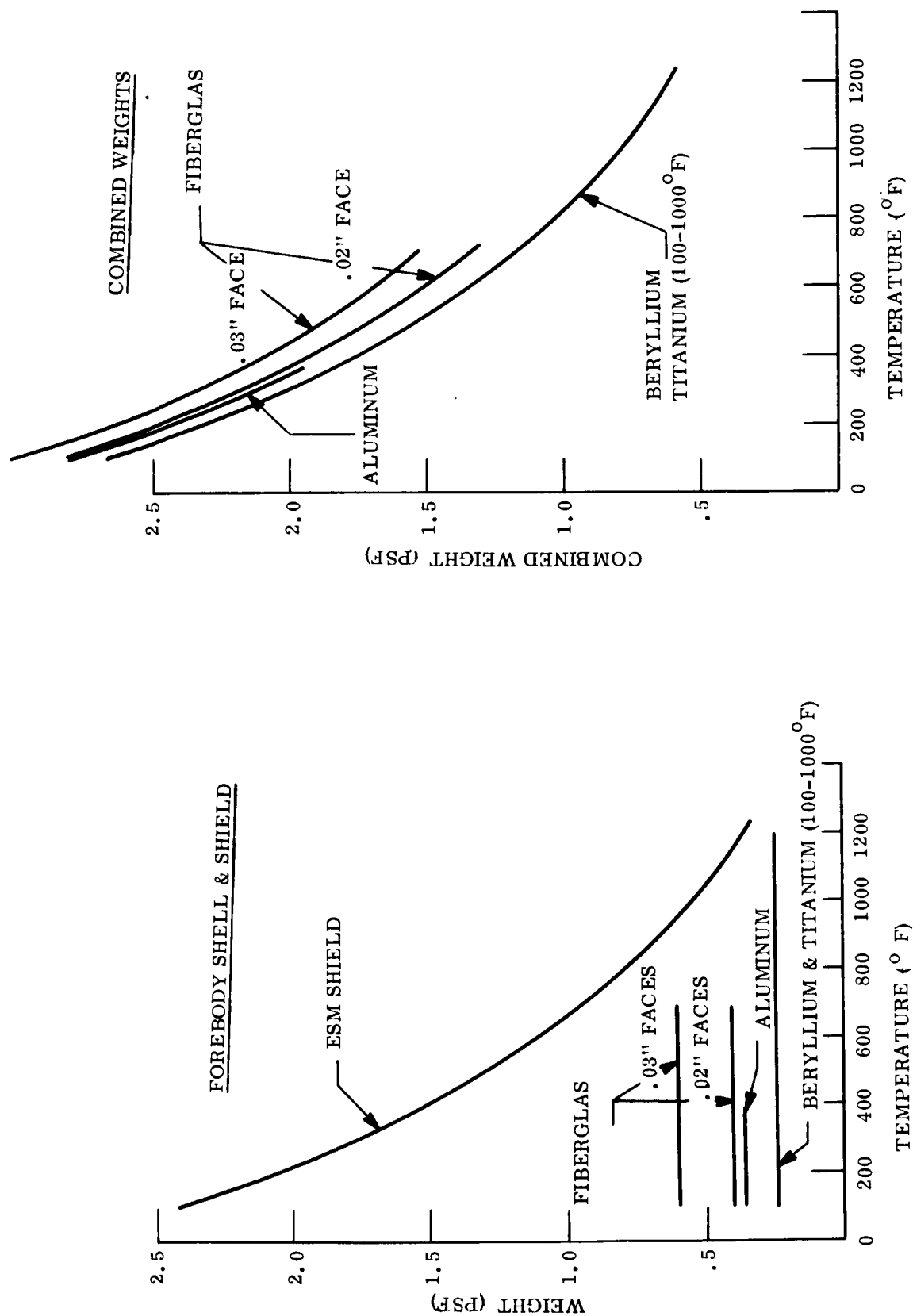
Figure 24. Smooth Flare Tension Shell, 12' Diameter, Run 46, Vehicle 6, Honeycomb, $M/C_D A = .20$

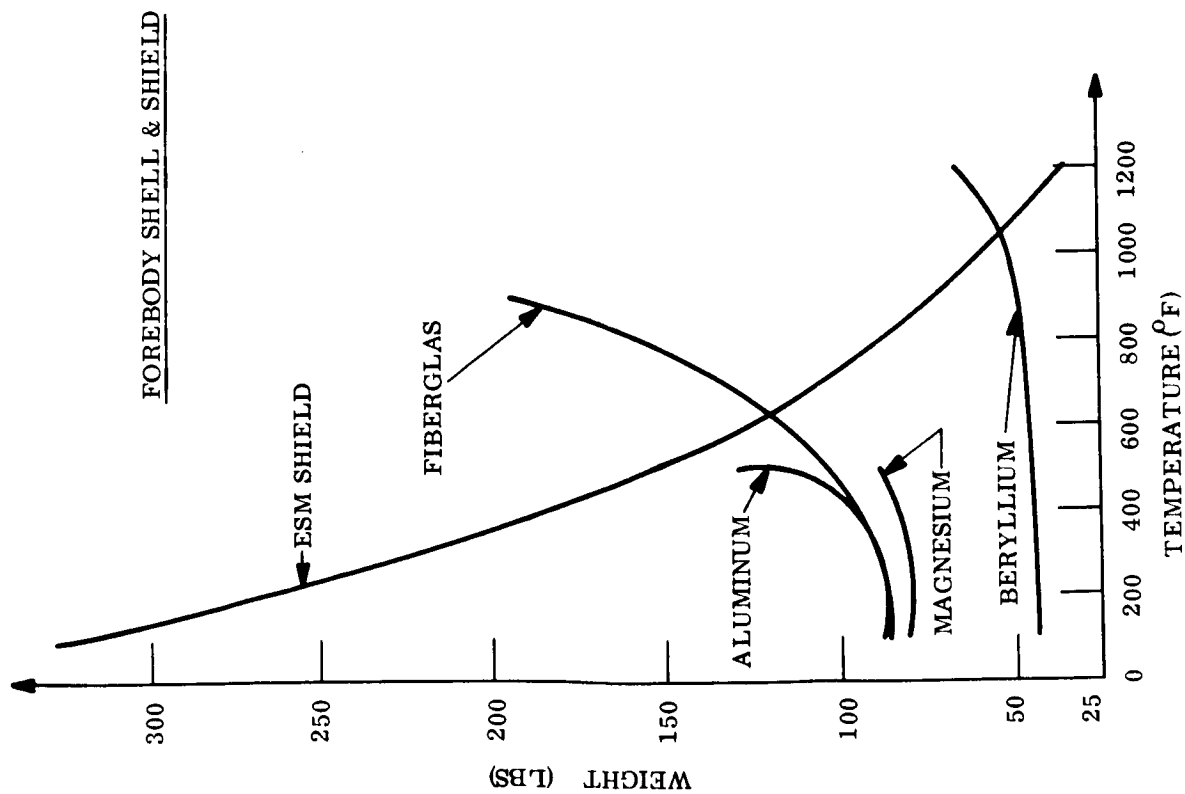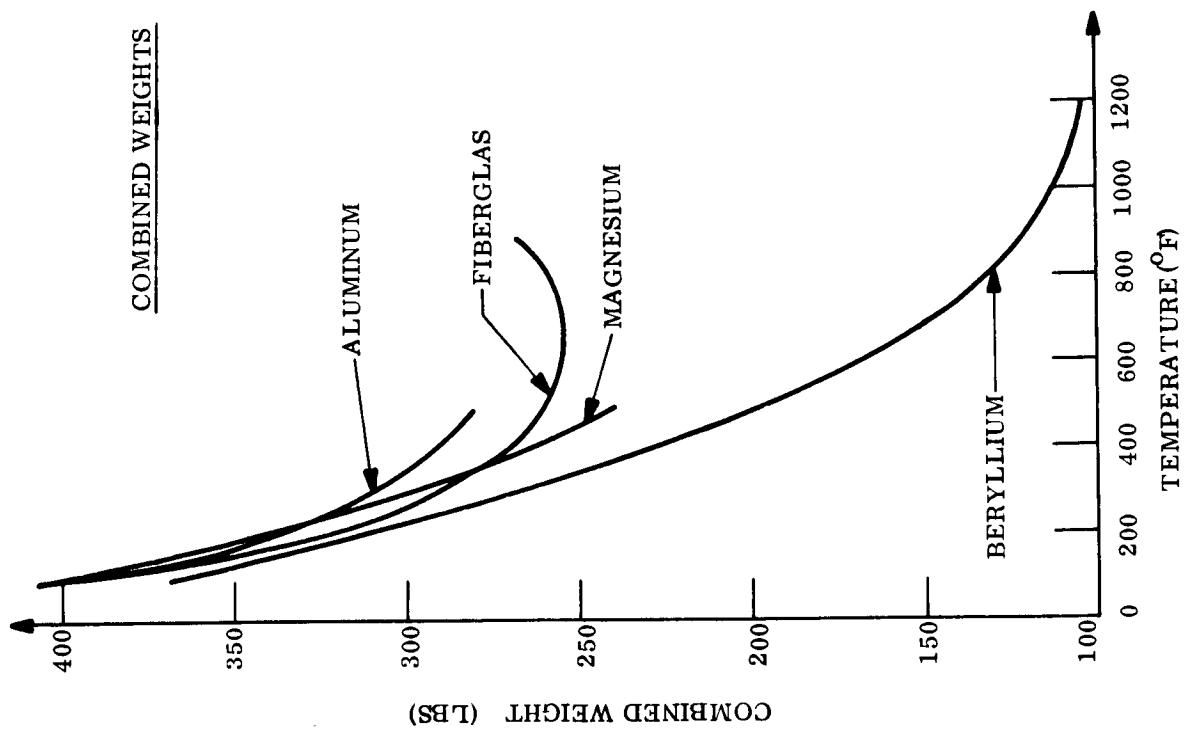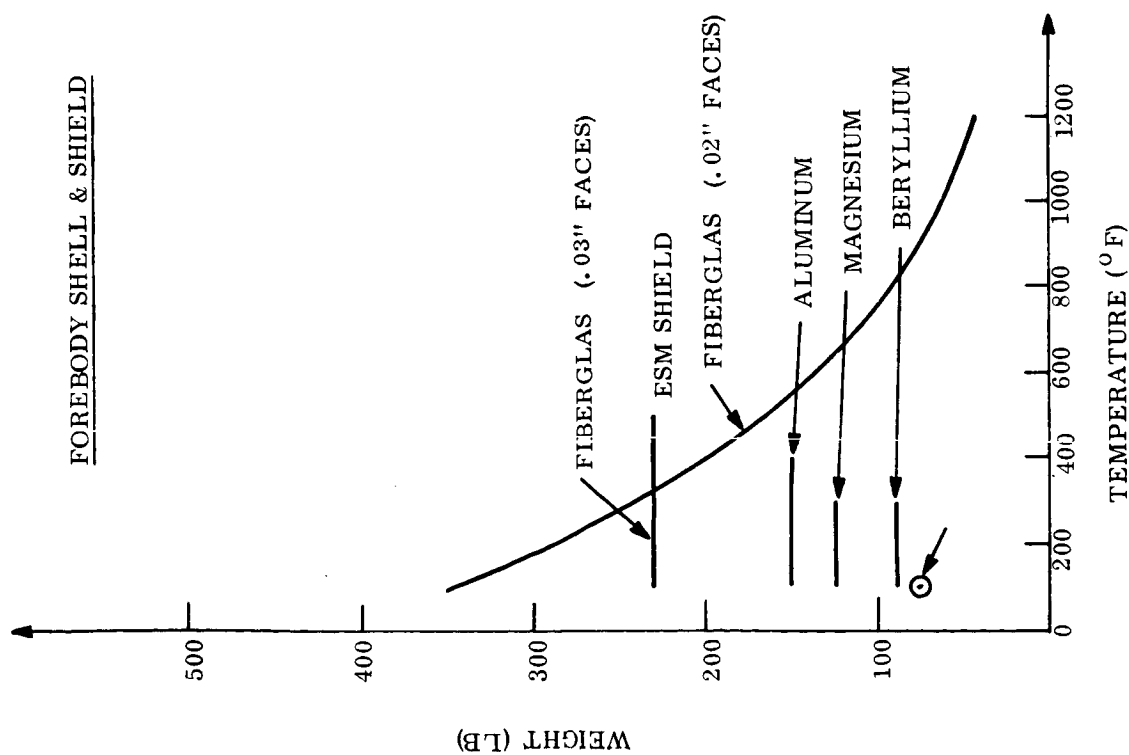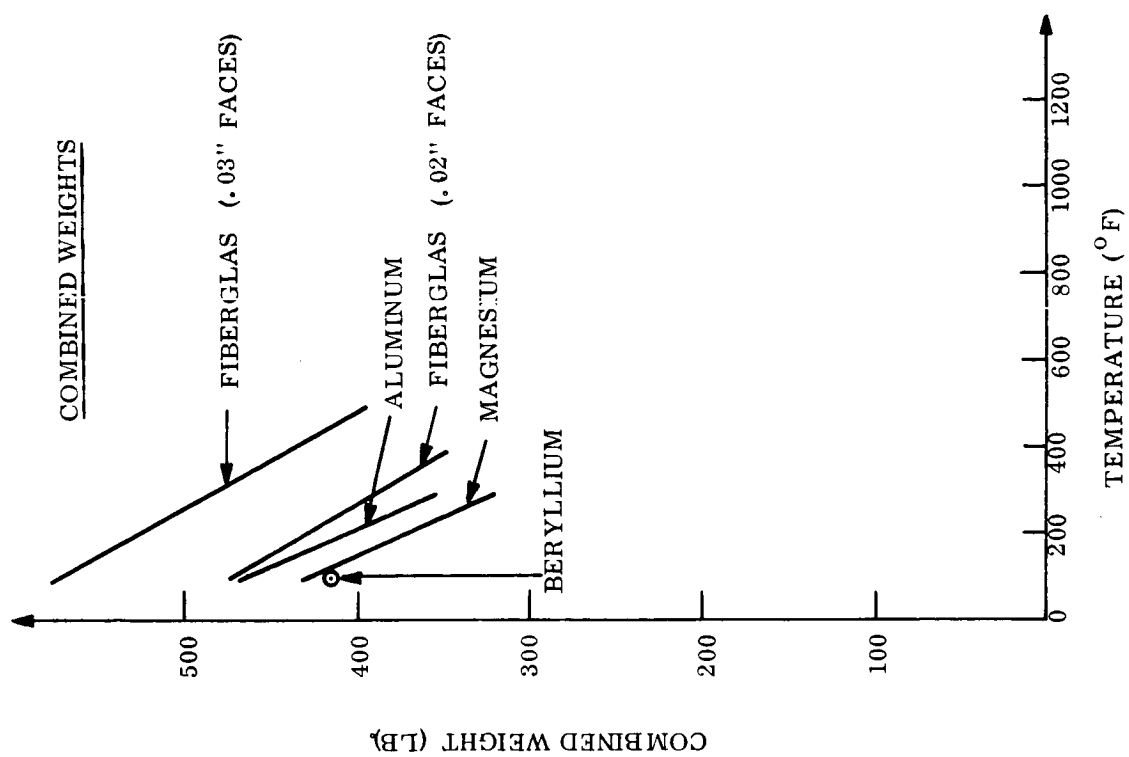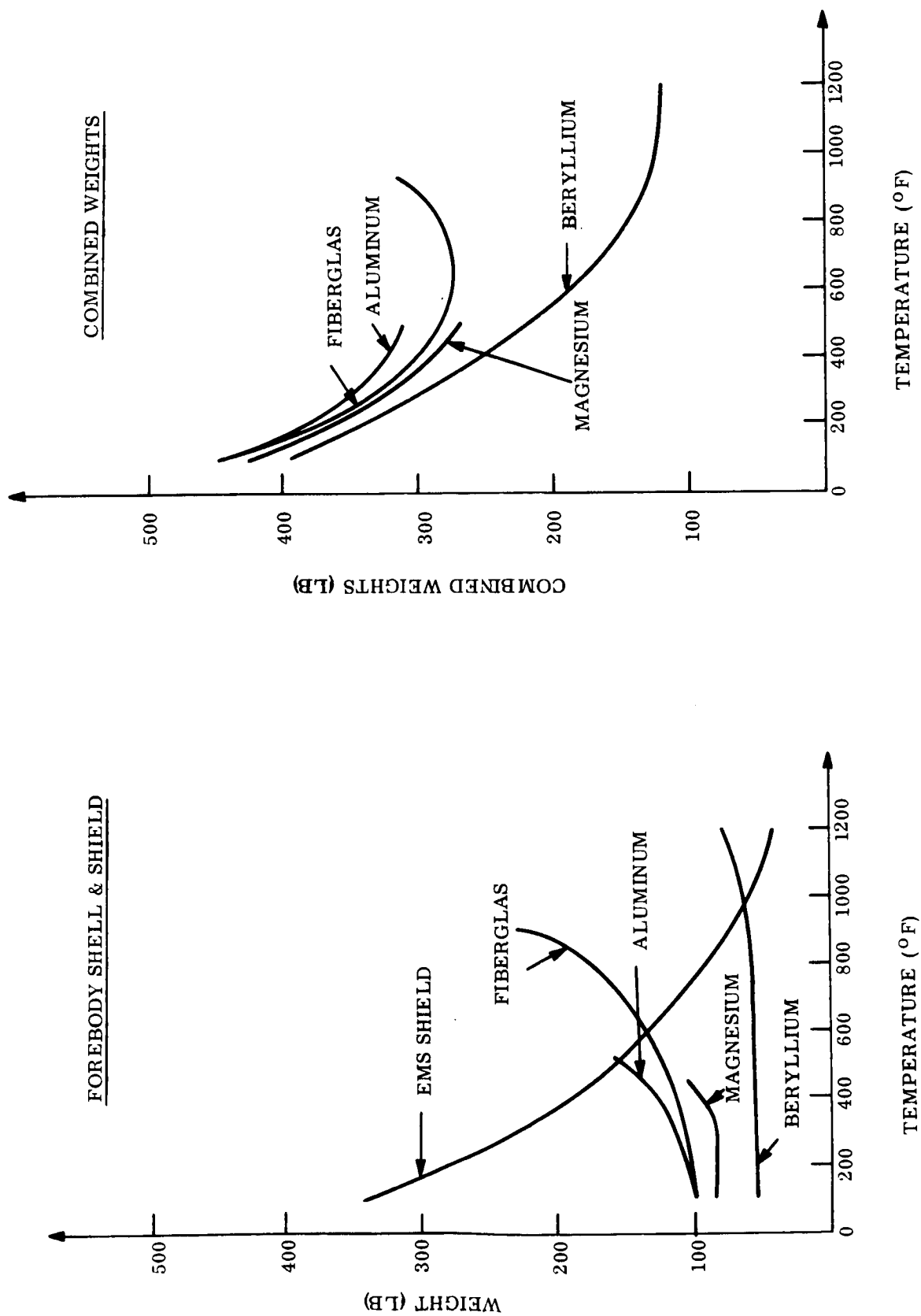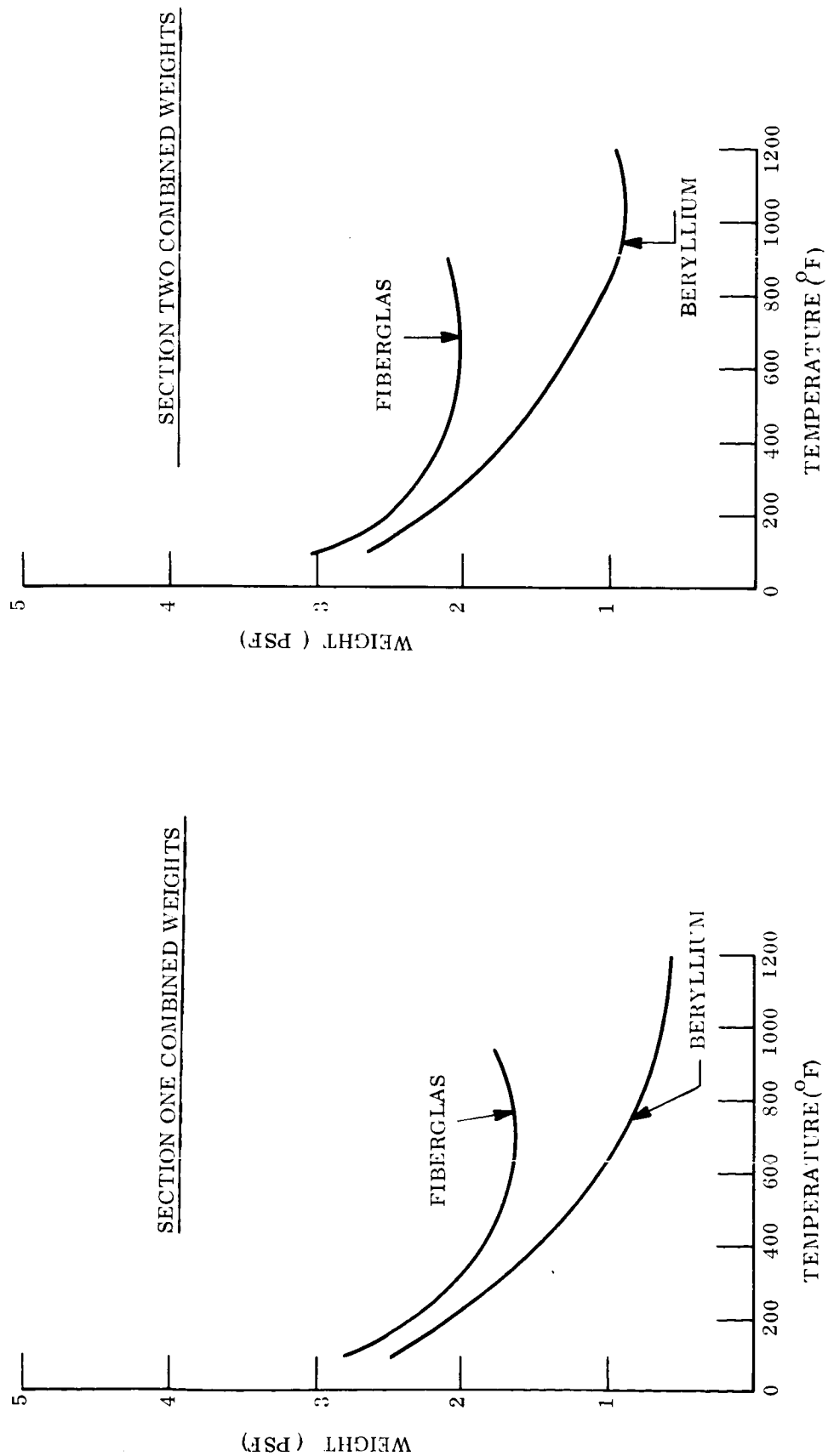Figure 25. 30° Sphere Cone Forebody, 12' Diameter, Run 46, Vehicle 2, Ring Stiffened, $M/C_D A = .20$
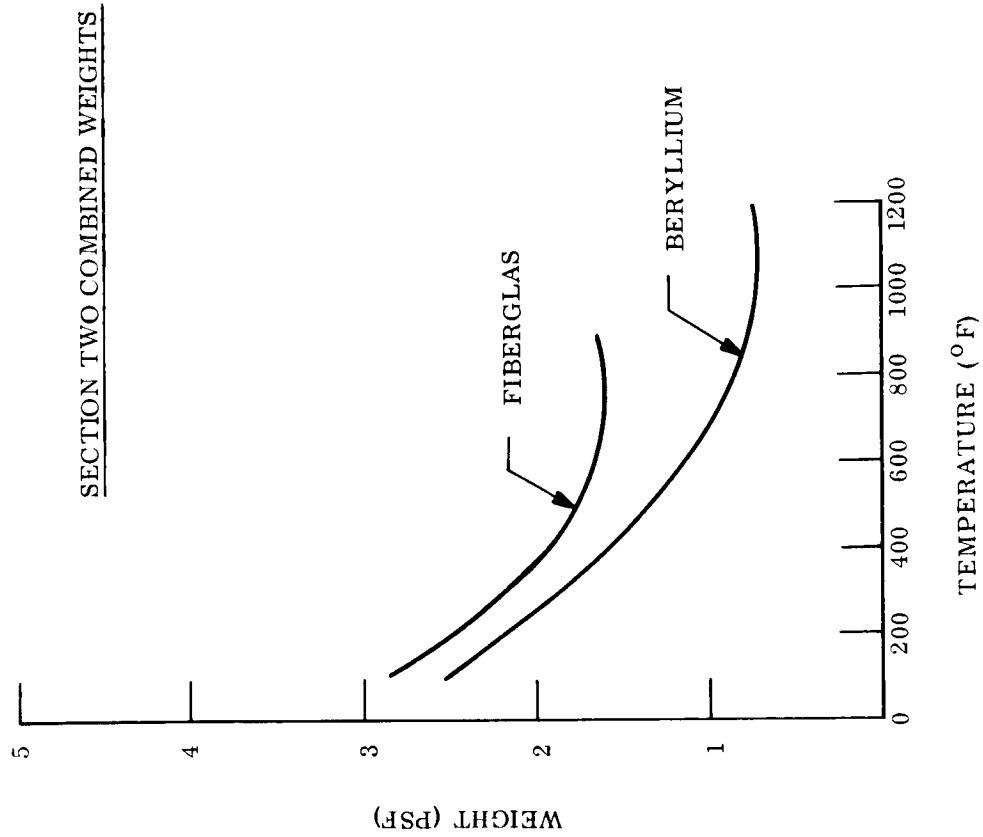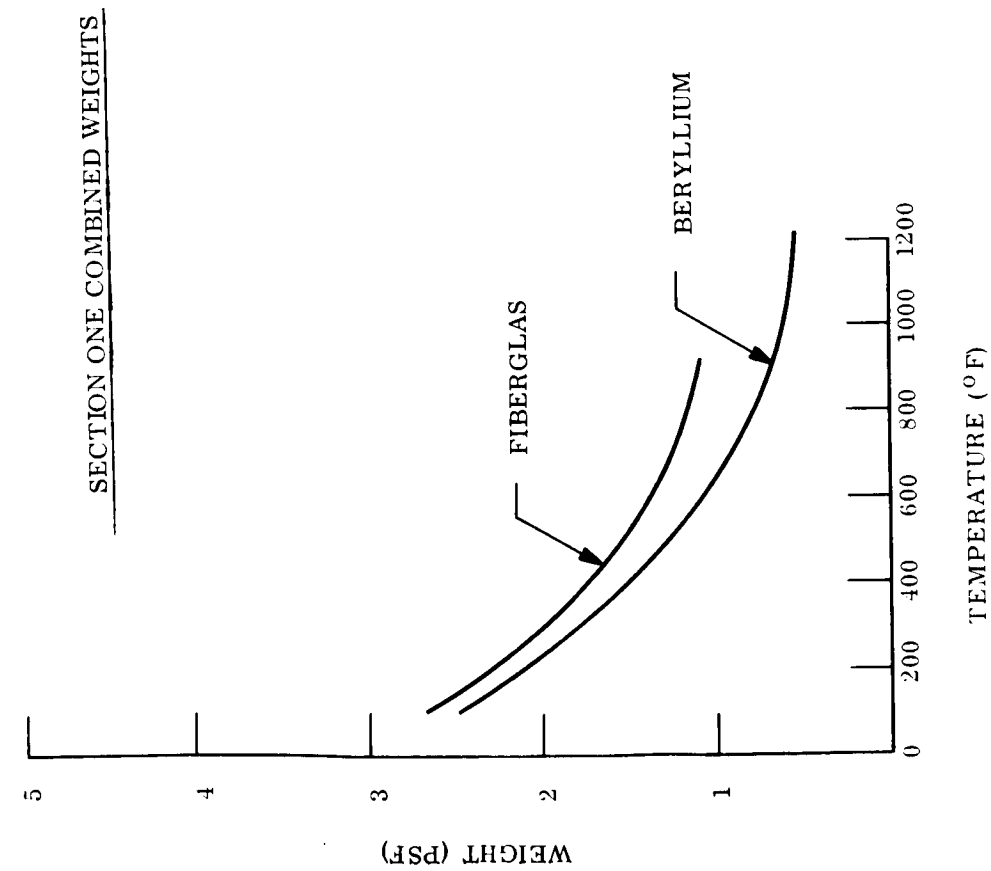
Figure 26. 60° Sphere Cone Forebody, 12' Diameter, Run 41, Vehicle 2, Ring Stiffened, $M/C_D A = .20$, Zero Spin

120

CASE (a) =
SHELL BENDING MOMENT FOR
STRUCTURAL RINGS LOCATED
AT STA. 2.5 AND 60.

CASE (b) =
SHELL BENDING MOMENT FOR
STRUCTURAL RINGS LOCATED
AT STA. 24 AND 60.
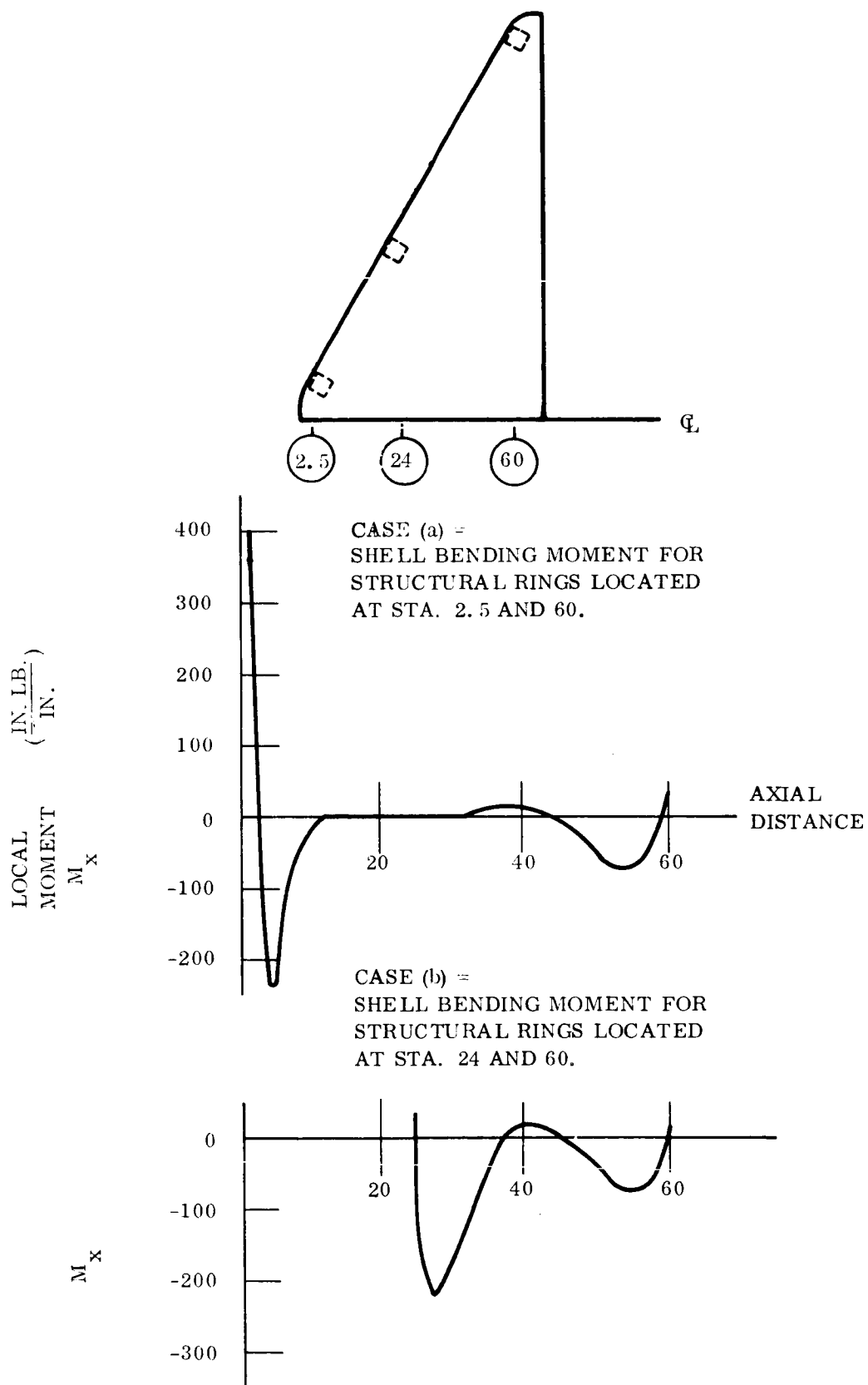
Figure 27. 60° Sphere Cone, 18.5' Diameter, Extent of Shell Bending Effects

121
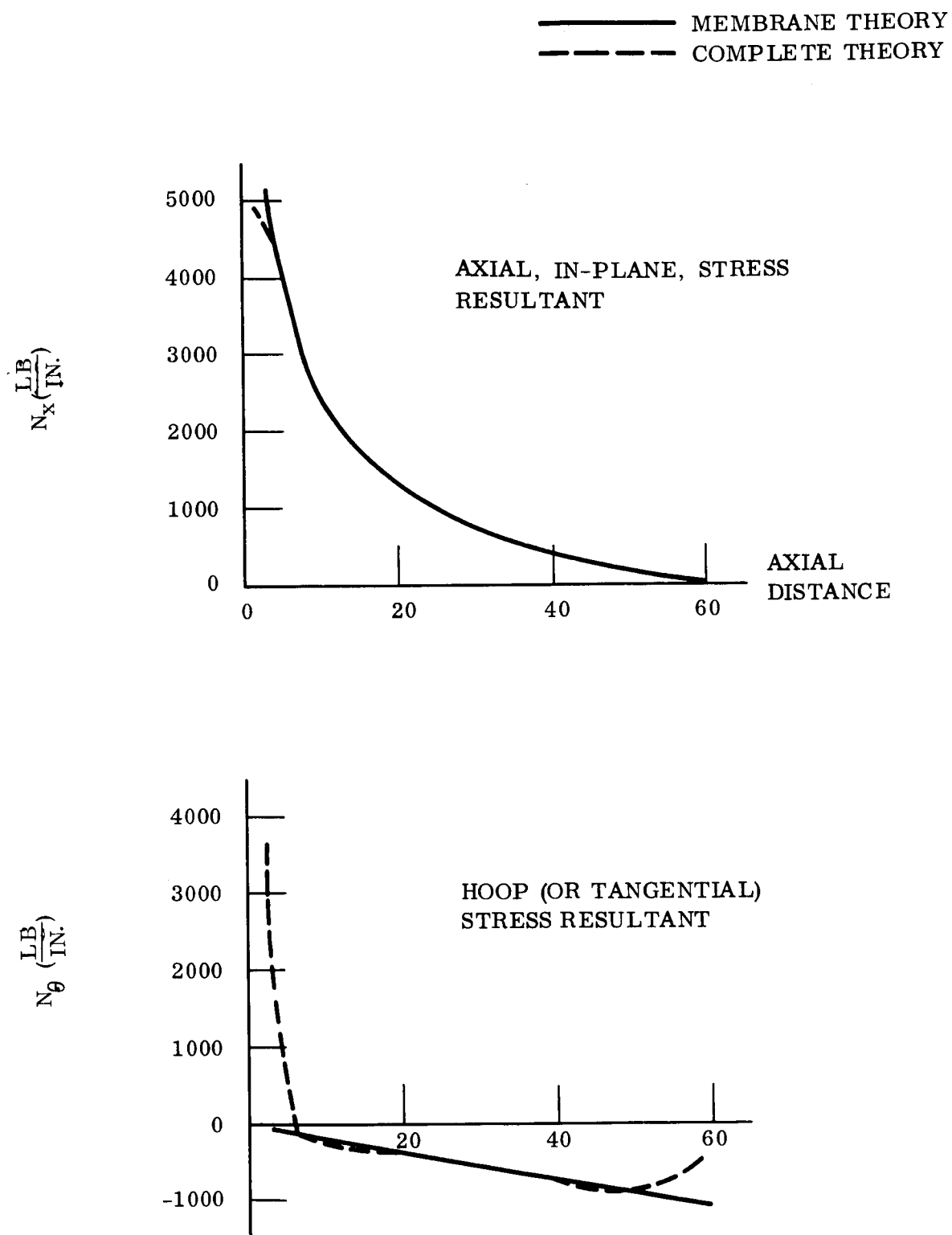
Figure 28. Comparison of Stress Resultants Predicted by
Membrane Theory and Complete Shell Theory
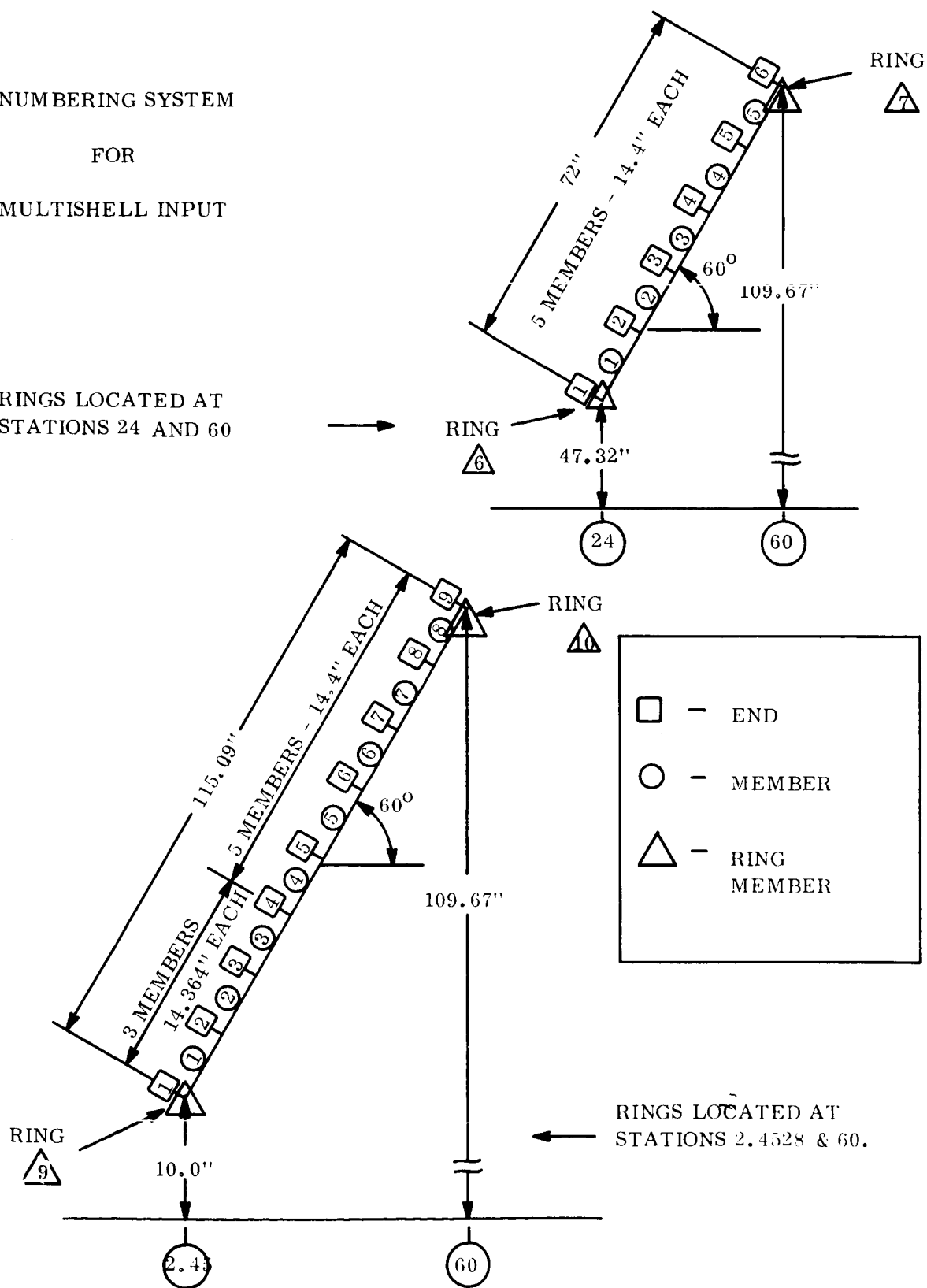
Figure 29. Idealized Structural Model of Conical Frustrum
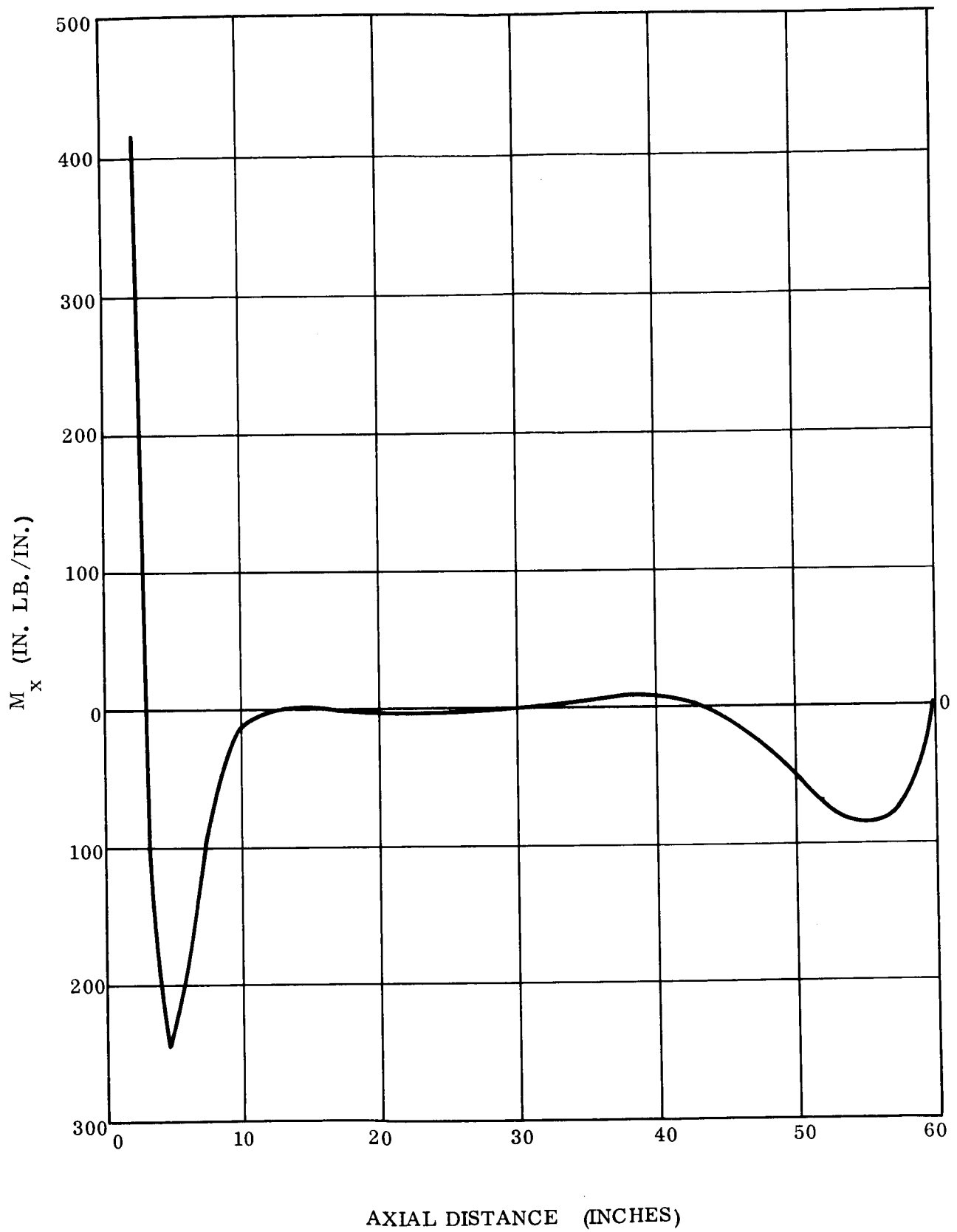
Figure 30.   Bending Moment, M_x vs Axial Distance for Case a
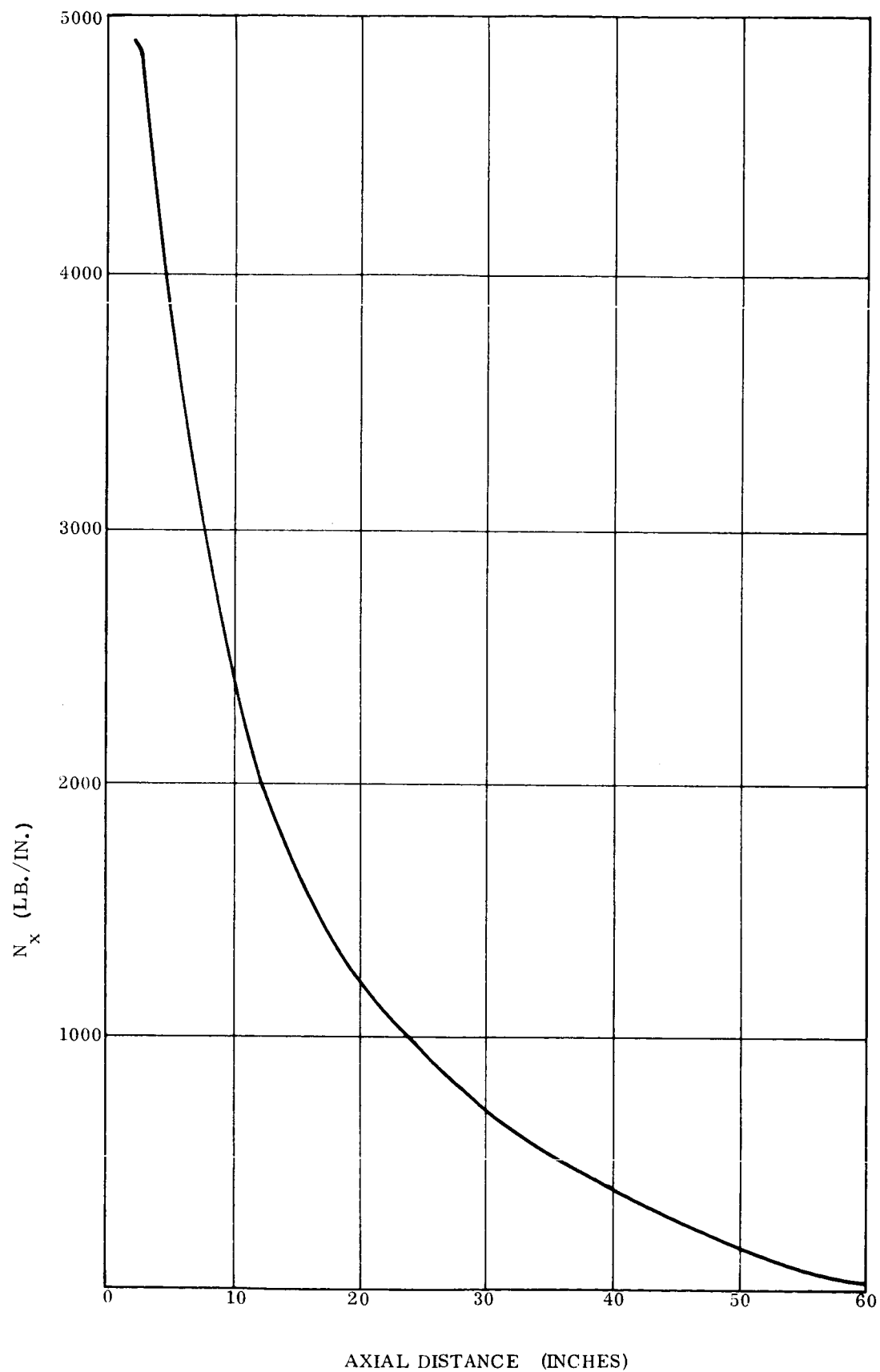
Figure 31.   Meridional Stress Resultant, N_x vs Axial Distance for Case a
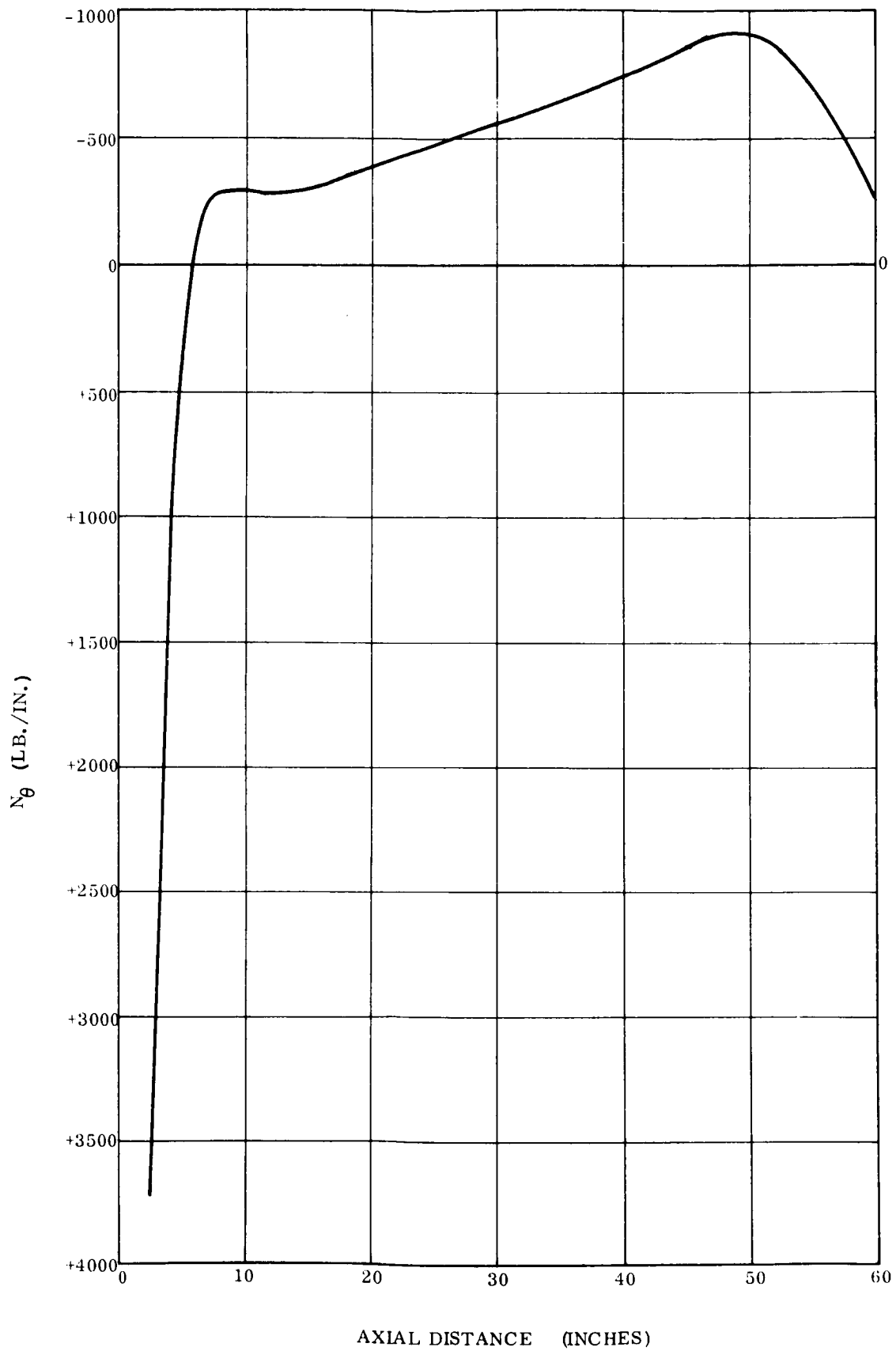
Figure 32. Tangential Stress Resultant, N_θ vs Axial Distance for Case a
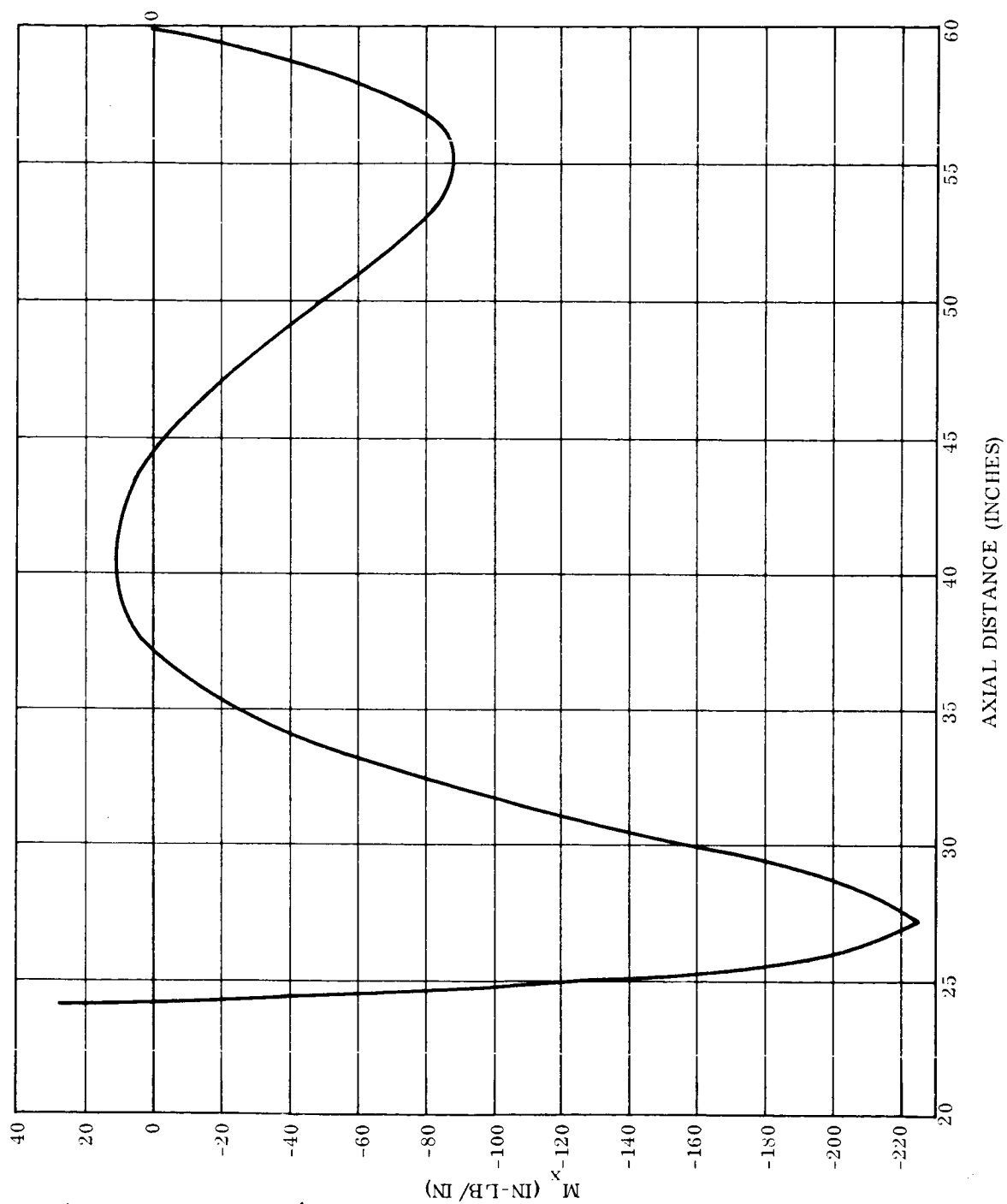
Figure 33. Bending Moment, M_x vs Axial Distance for Case B
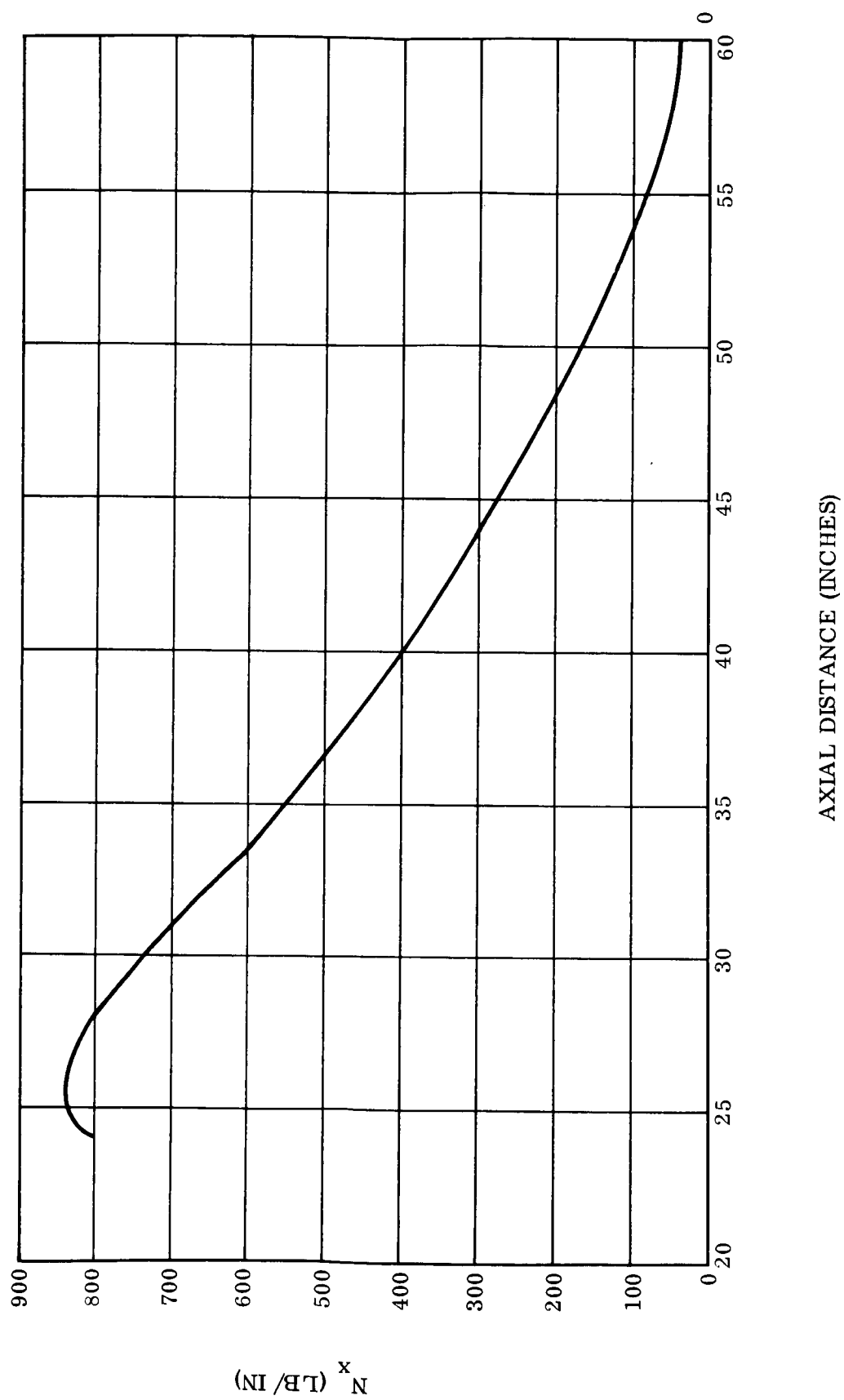
Figure 34. Meridional Stress Resultant, N_x vs Axial Distance for Case b

128
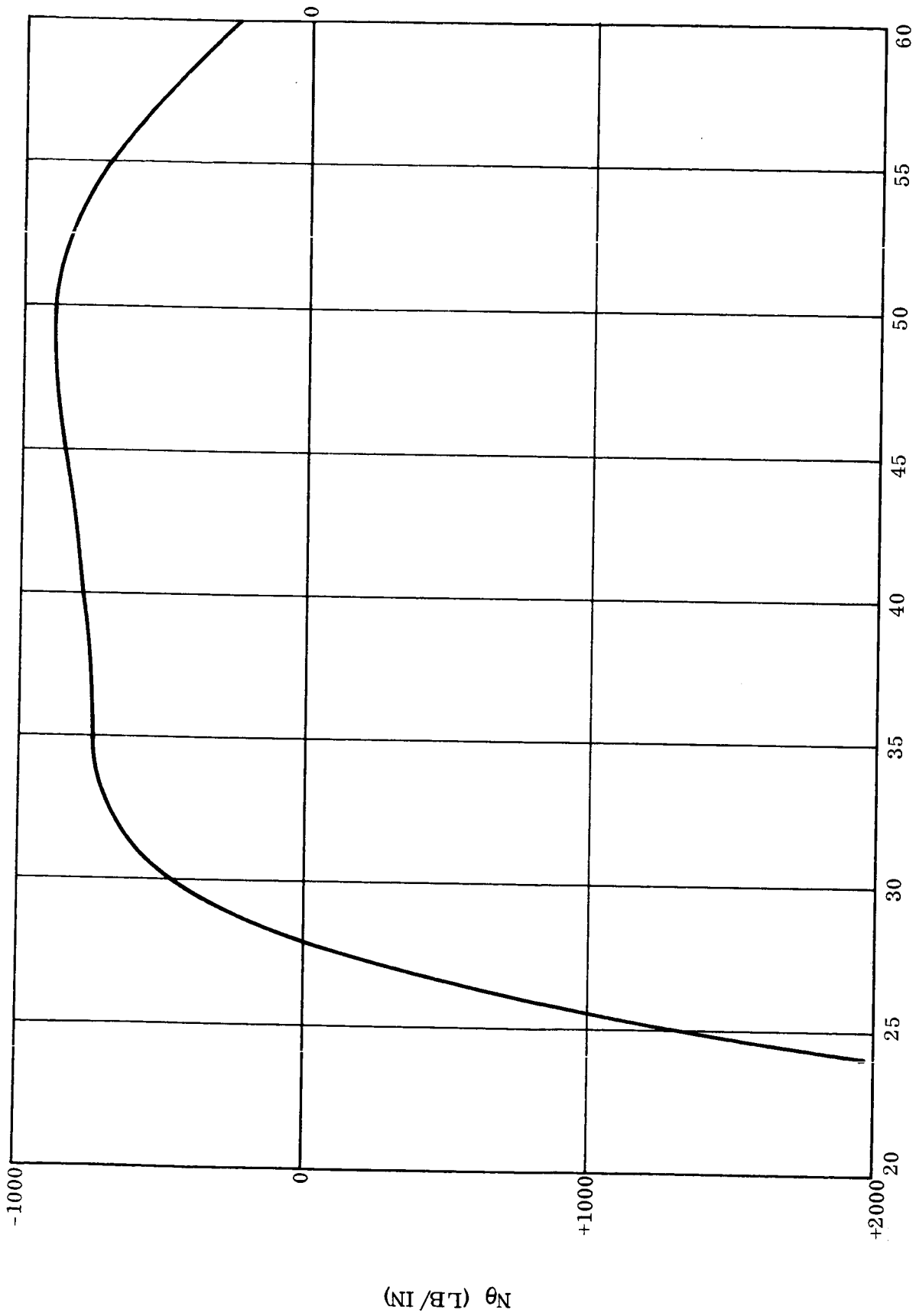
Figure 35. Tangential Stress Resultant, N_θ vs Axial Distance for Case b

129

$N_\theta/N_{\theta MAX}$ VS. AXIAL DISTANCE

AXIAL DISTANCE - INCHES
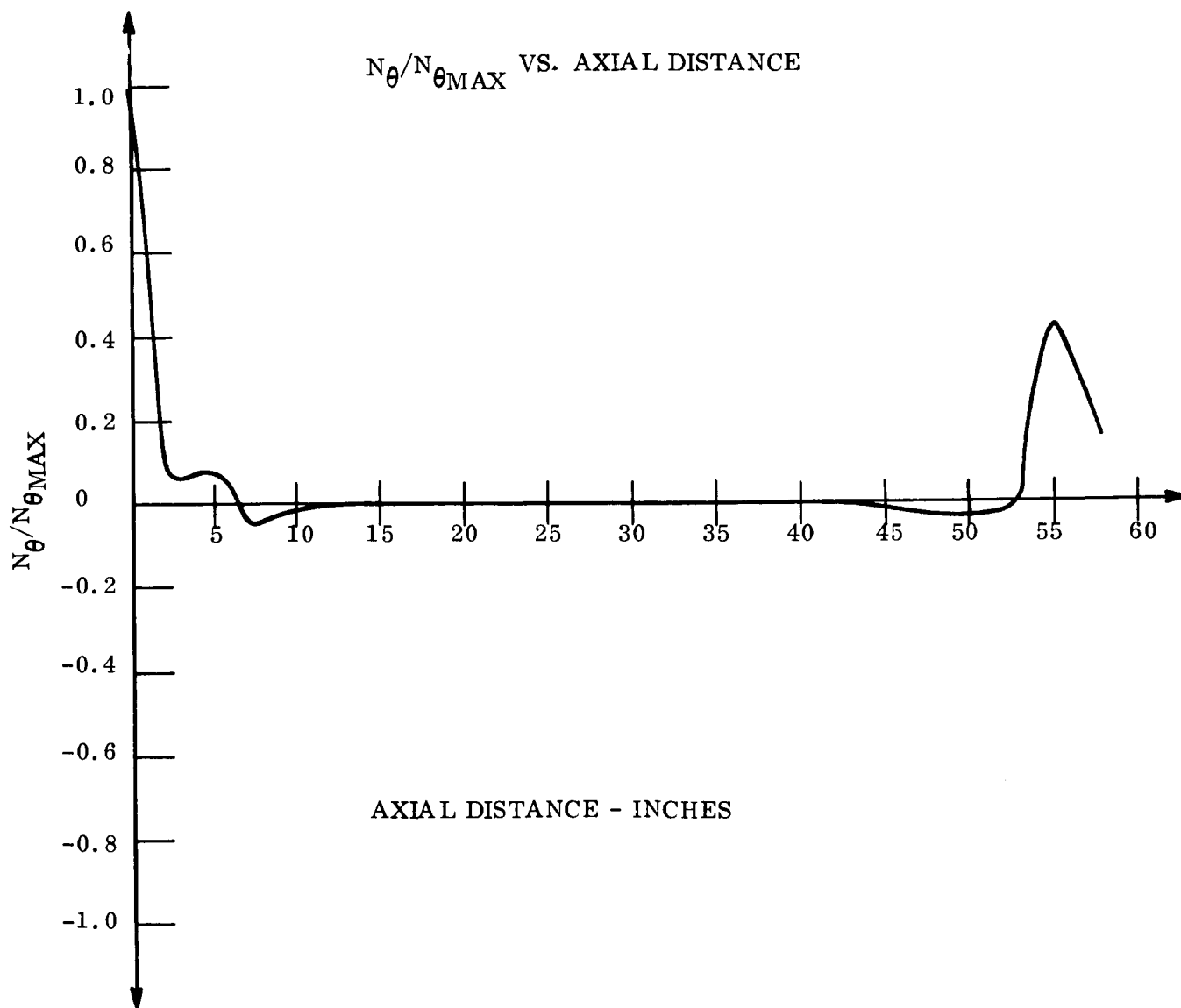
Figure 36. Tangential Thermal Stress Distribution, .030' Fiberglass Honeycomb

N_X/N_{XMAX} VS. AXIAL DISTANCE

AXIAL DISTANCE - INCHES
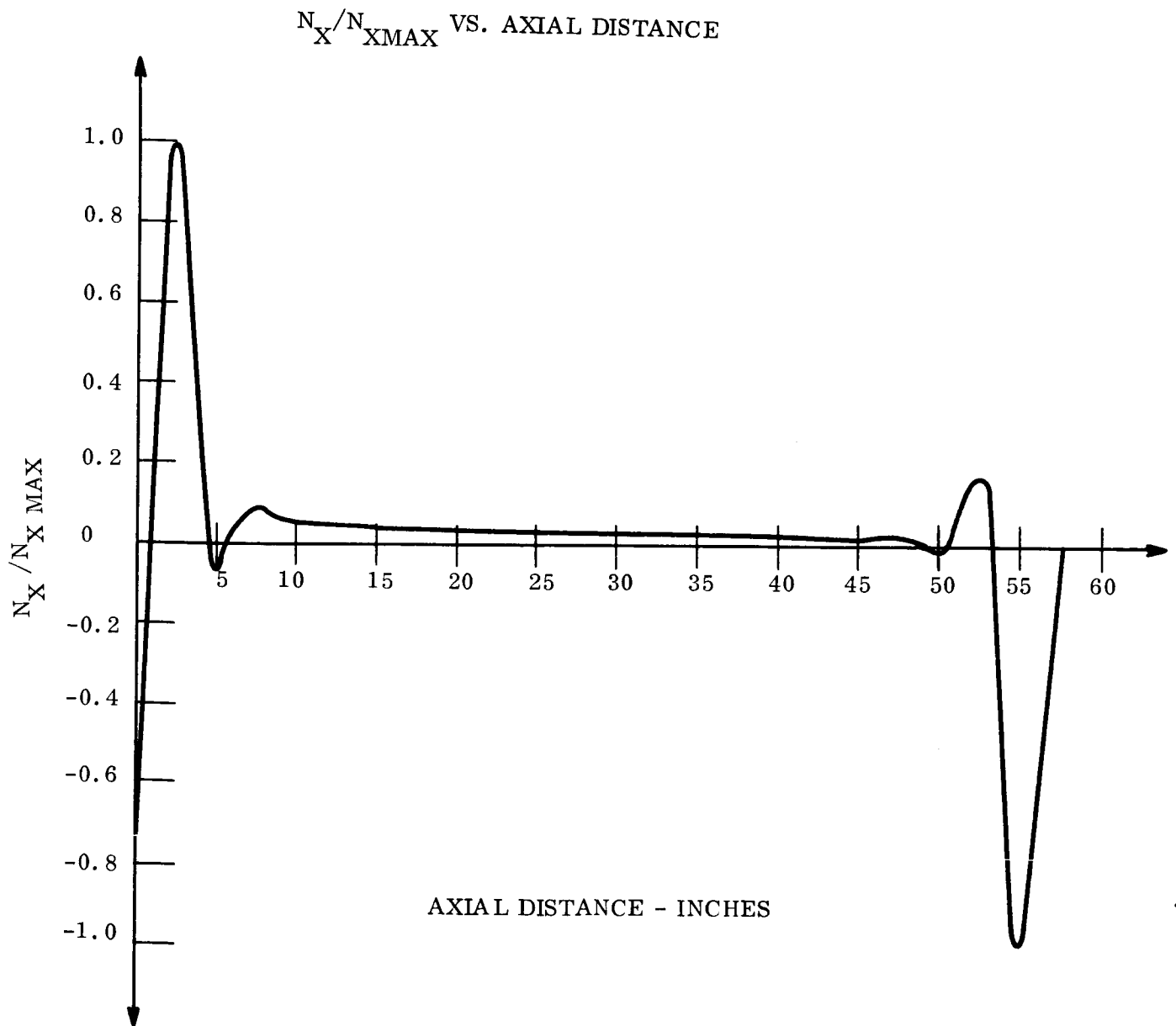
Figure 37. Meridional Thermal Stress Distribution, .030" Fiberglass Honeycomb

131
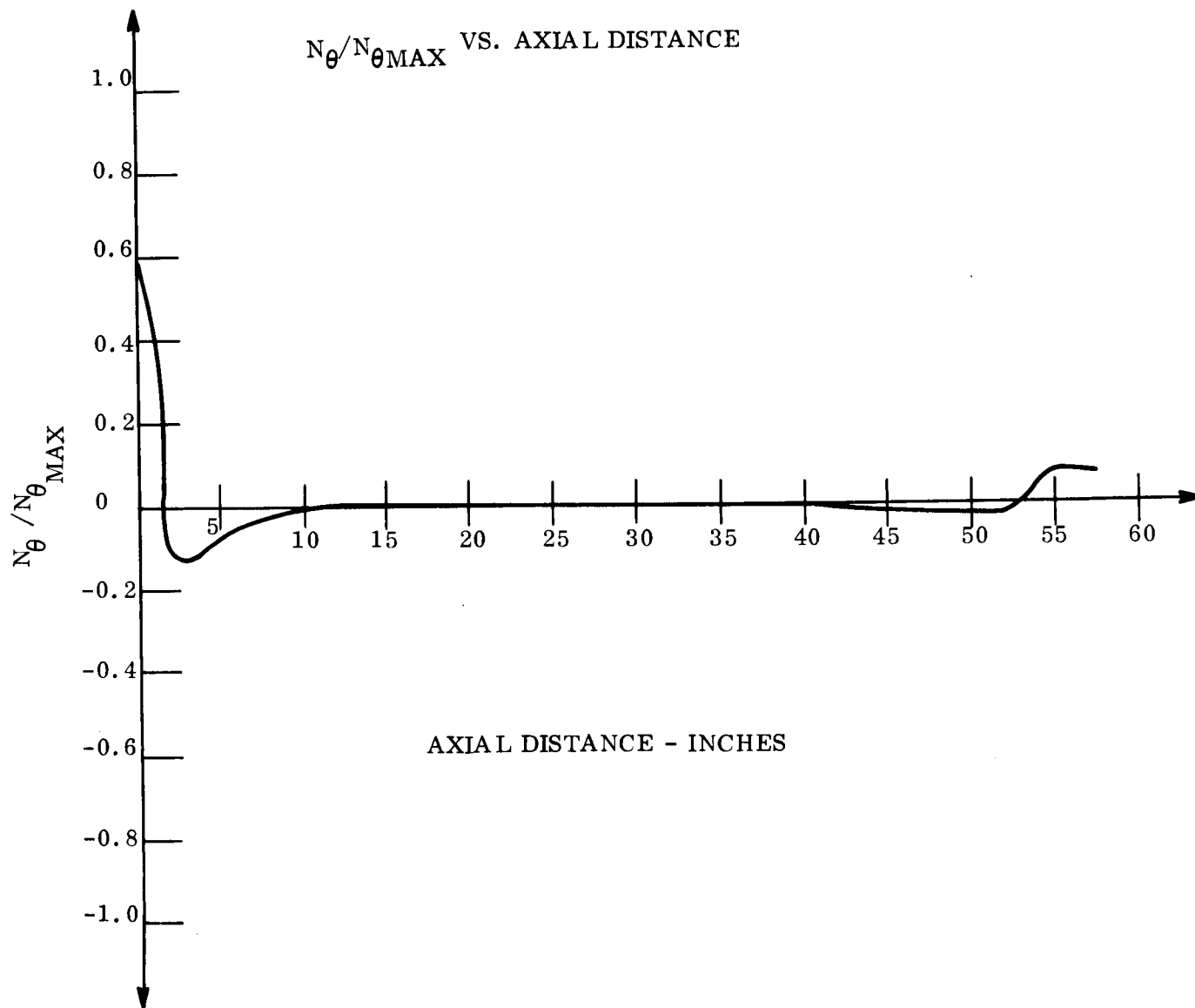
Figure 38. Tangential Thermal Stress Distribution, .020" Fiberglass Honeycomb
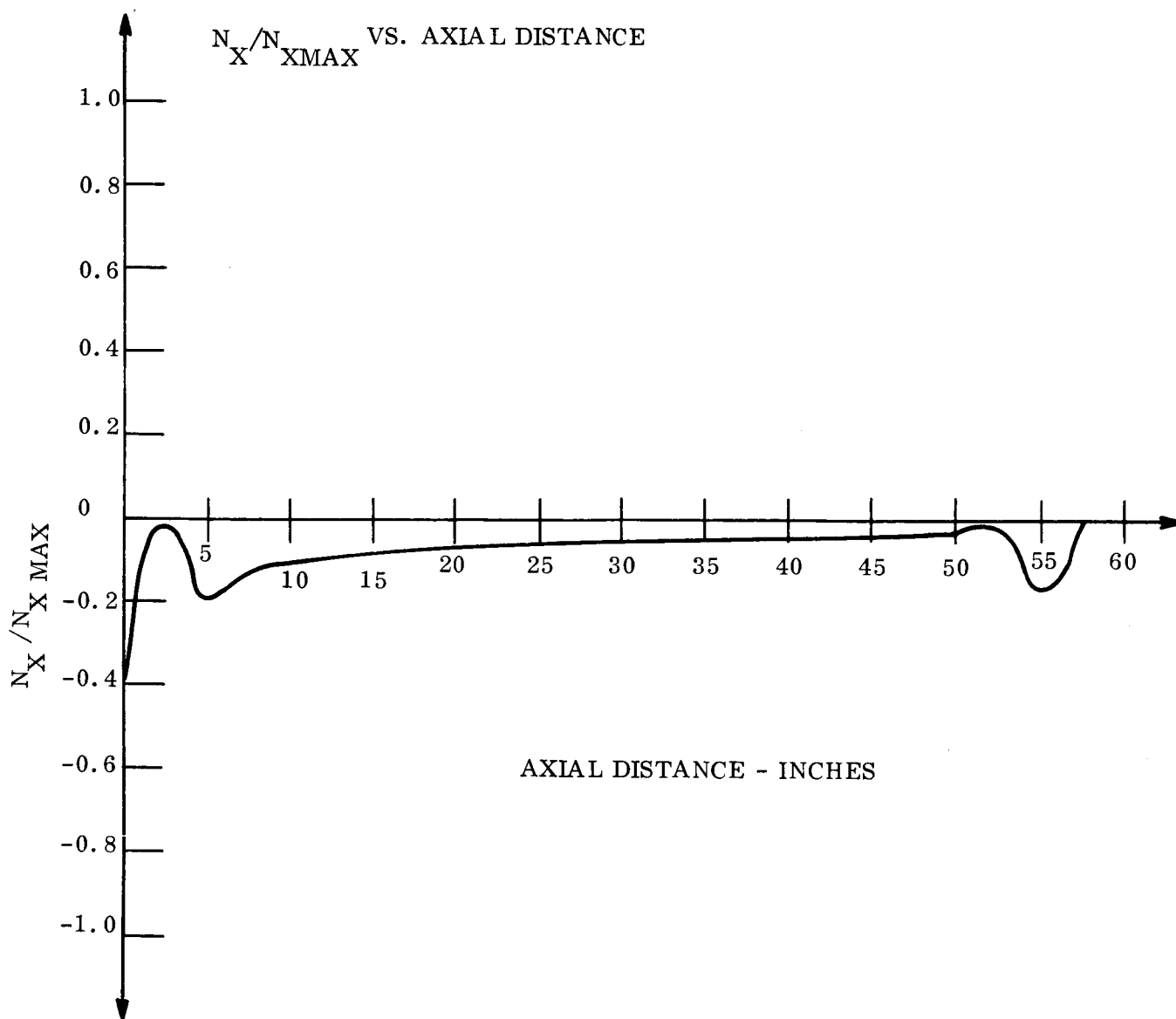
Figure 39. Meridional Thermal Stress Distribution, .020" Fiberglass Honeycomb

Figure 40. Distribution of Centrifugal Stresses in Conical Frustrum
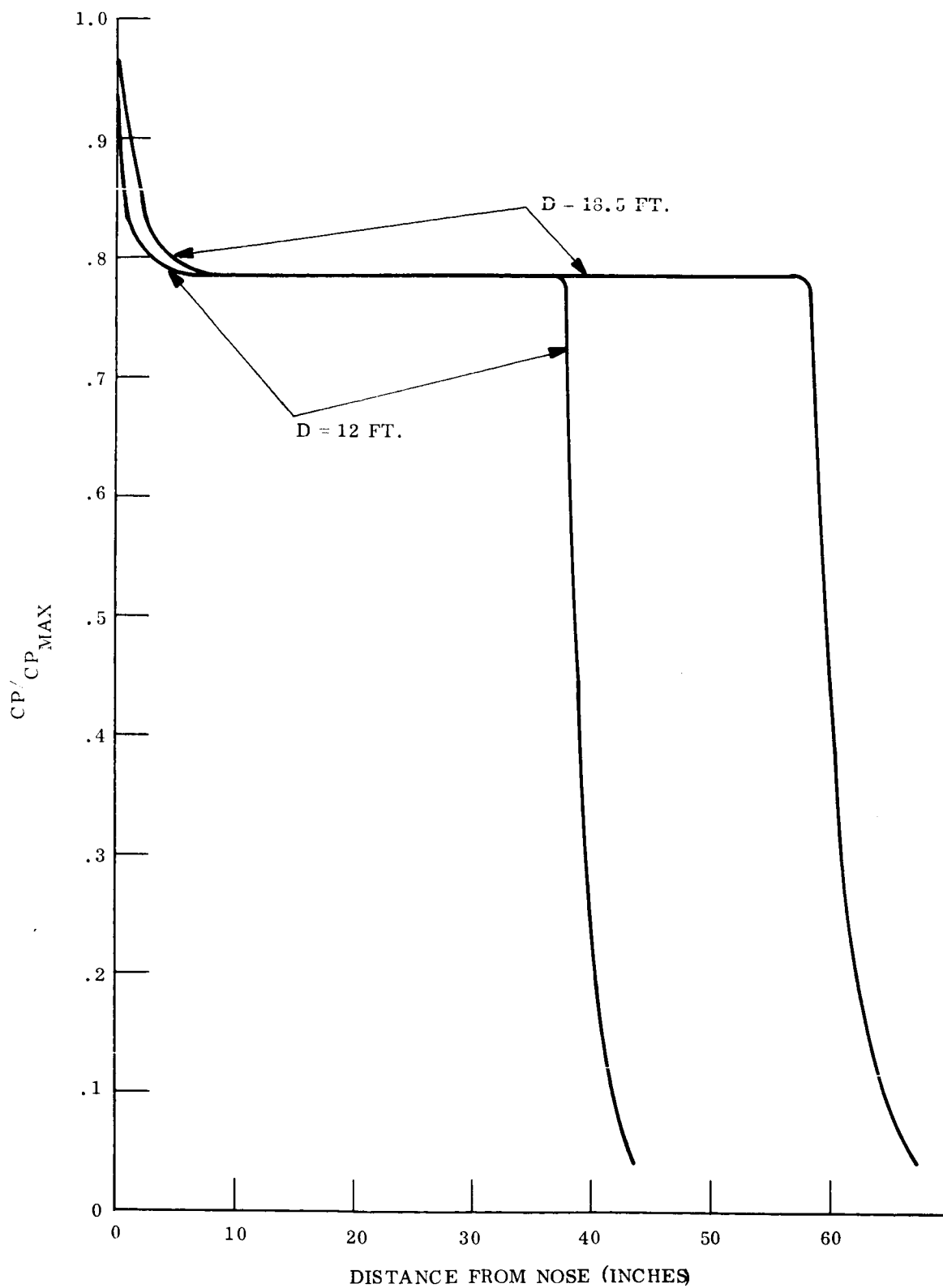
Figure 41. 60° Sphere Cone Pressure Distribution, $\alpha = 0°$
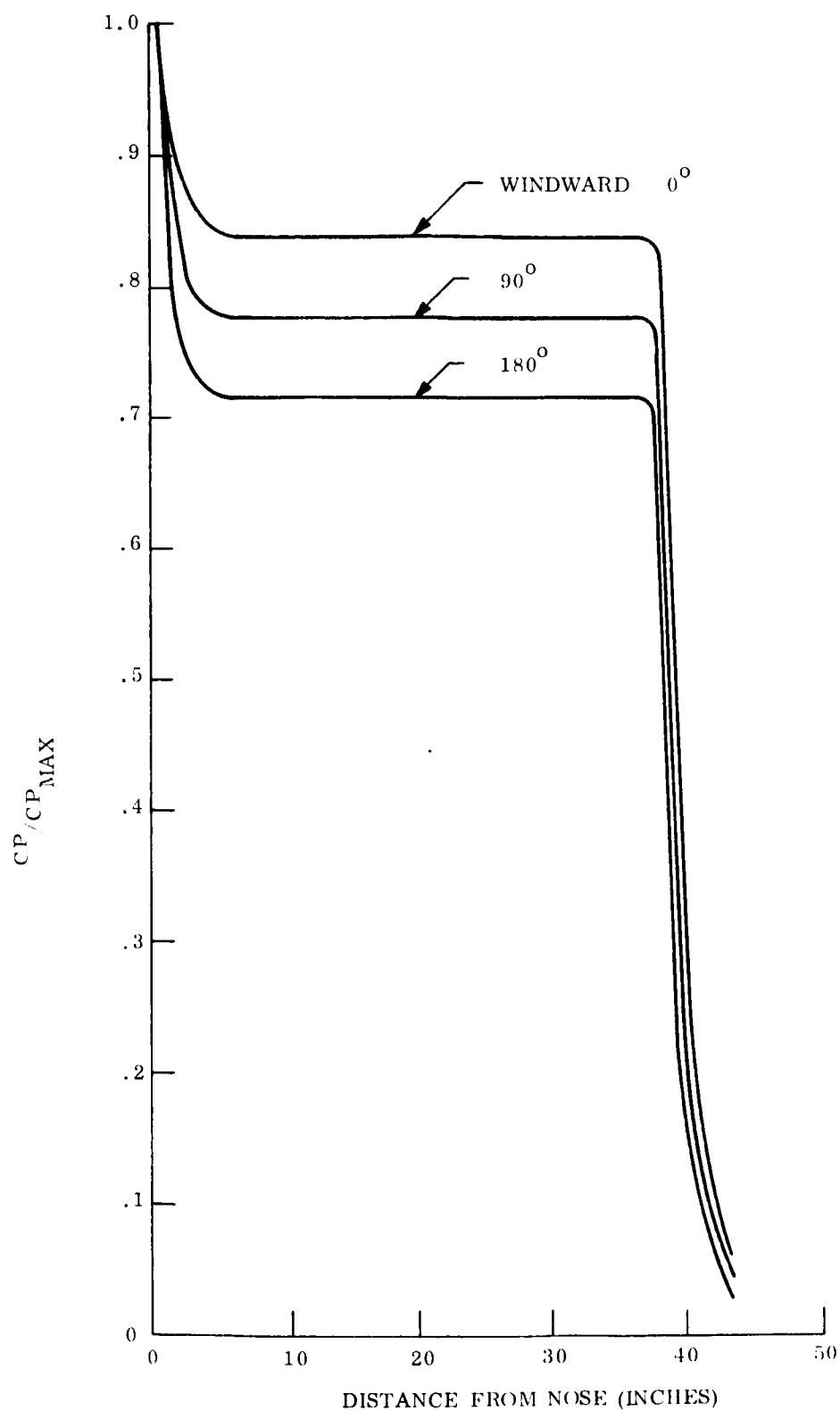
Figure 42. 60° Sphere Cone Pressure Distribution, $\alpha = 5°$, $D = 12'$
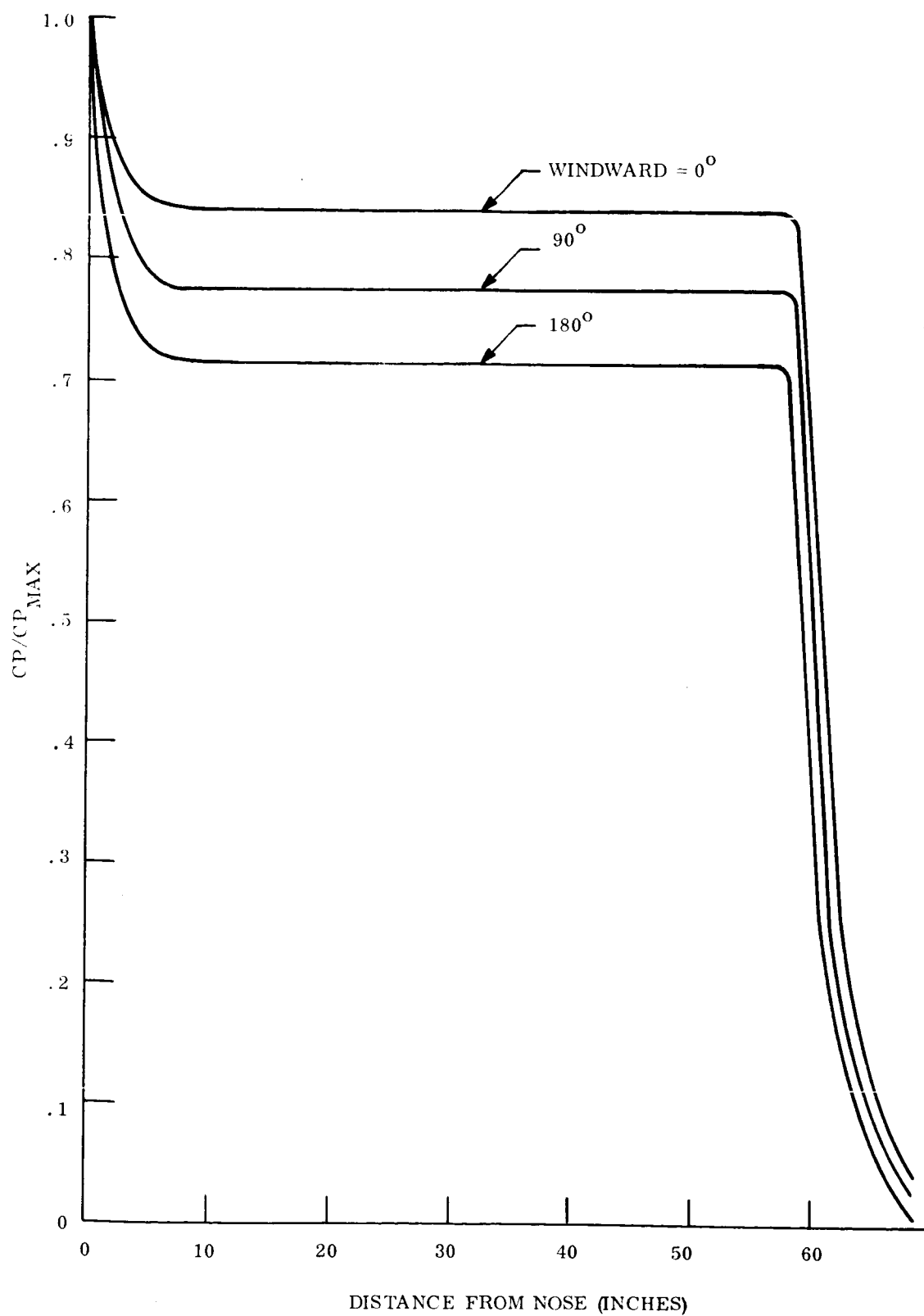
Figure 43. $60°$ Sphere Cone Pressure Distribution, $\alpha = 5°$, $D = 18.5'$
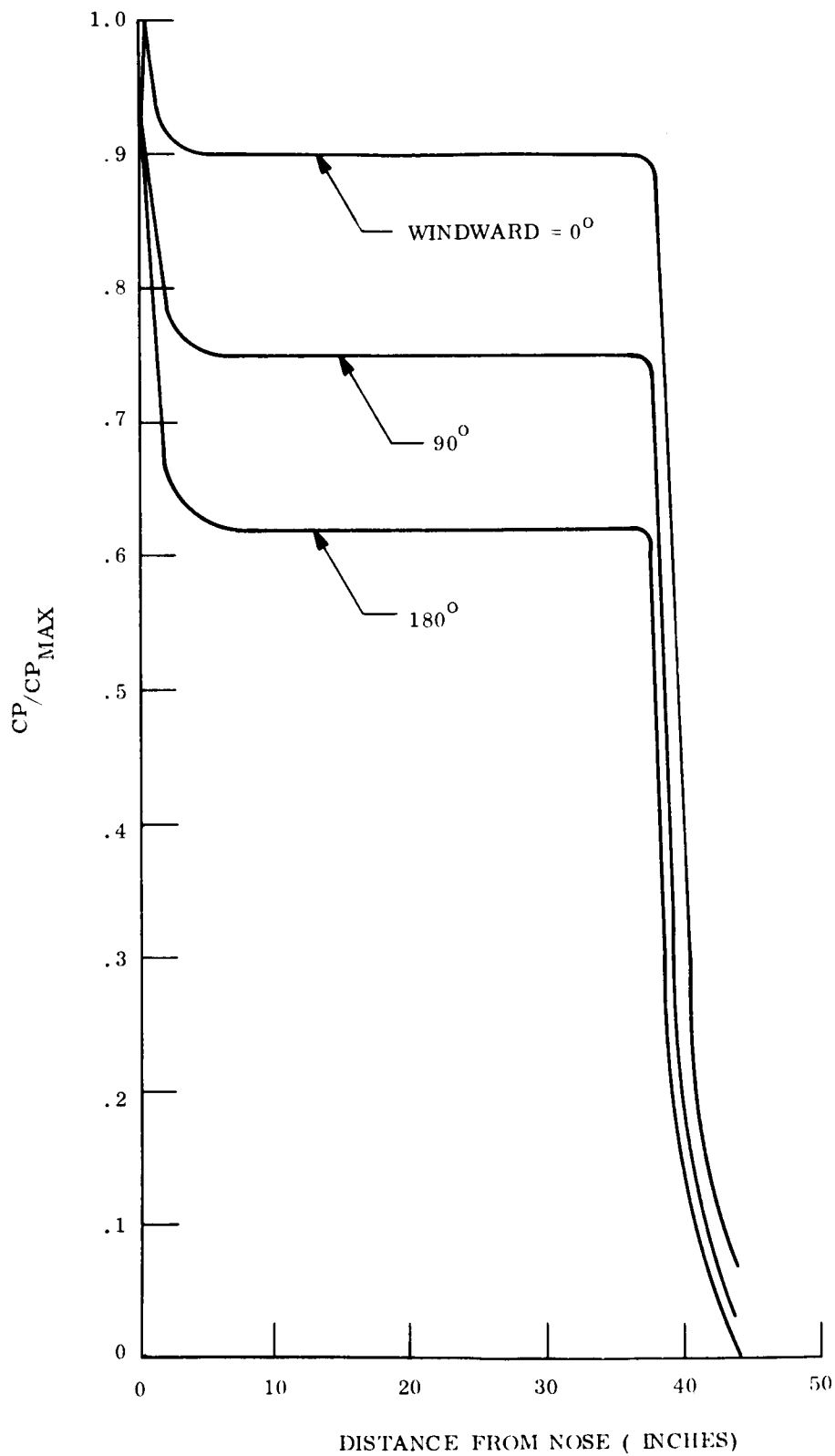
Figure 44. 60° Sphere Cone Pressure Distribution, $\alpha = 10°$, D = 12'
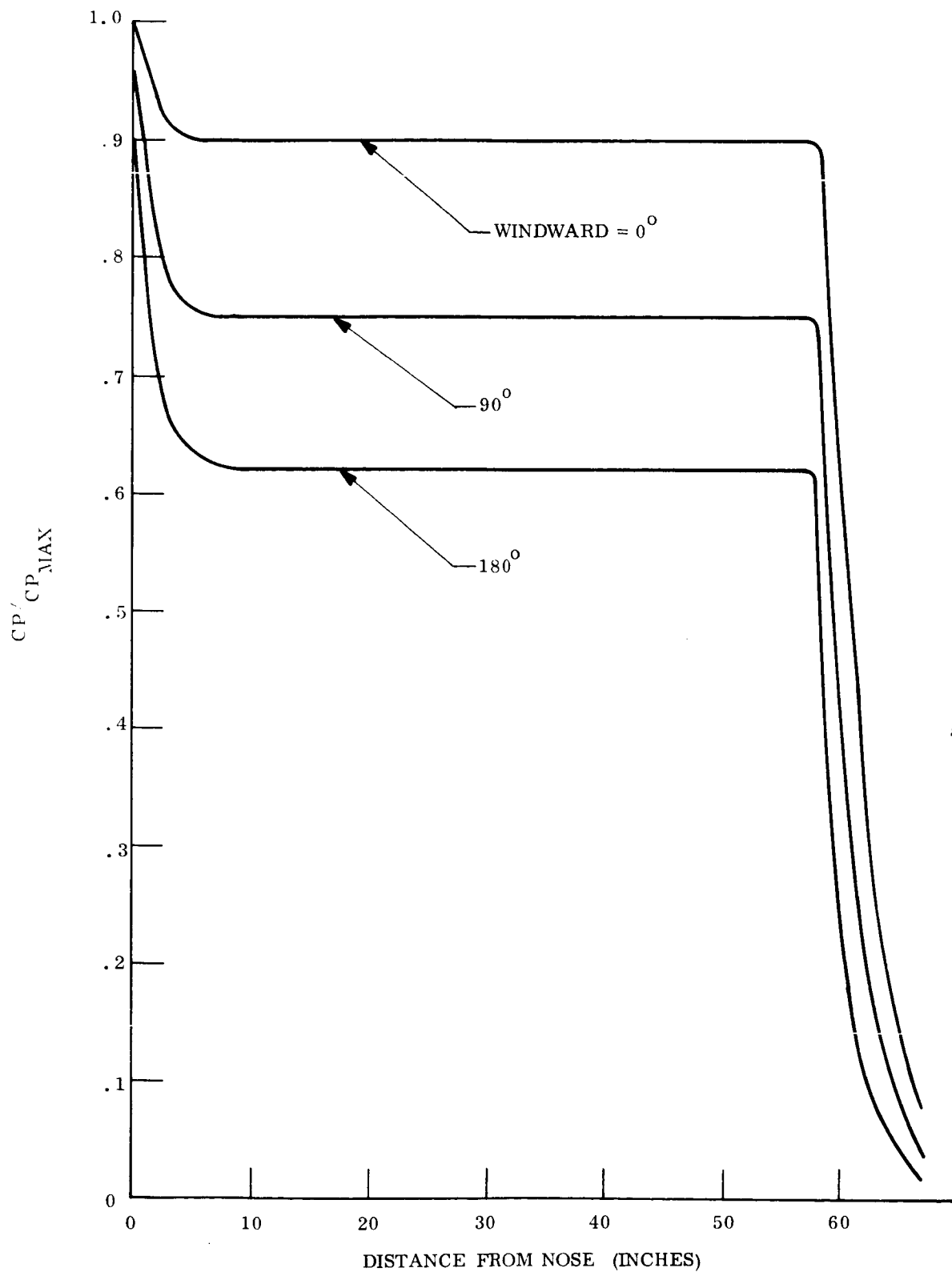
Figure 45. 60° Sphere Cone Pressure Distribution, $\alpha = 10^{O}$, D $= 18.5'$
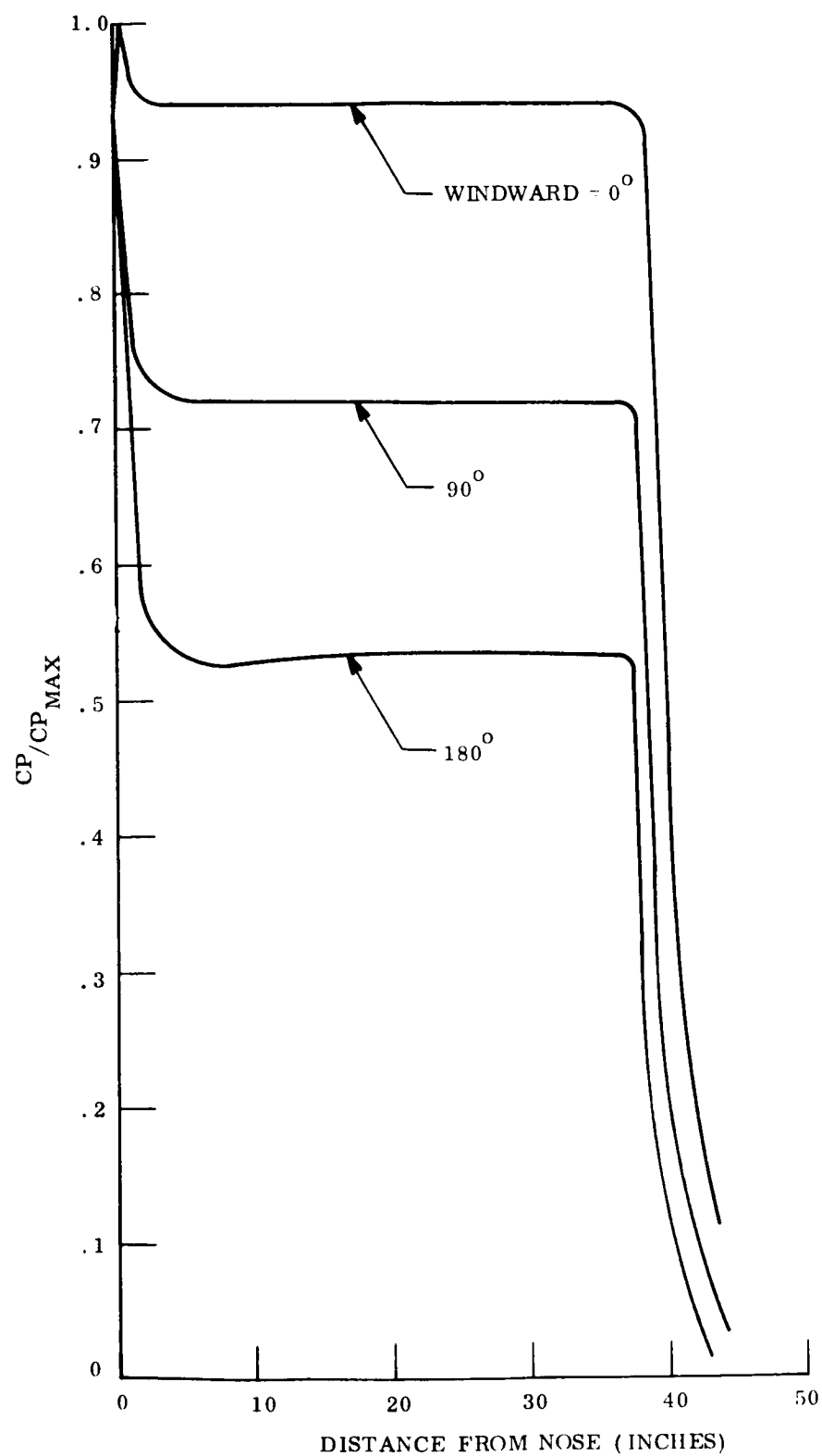
Figure 46. 60° Sphere Cone Pressure Distribution, $\alpha = 15°$, D = 12'
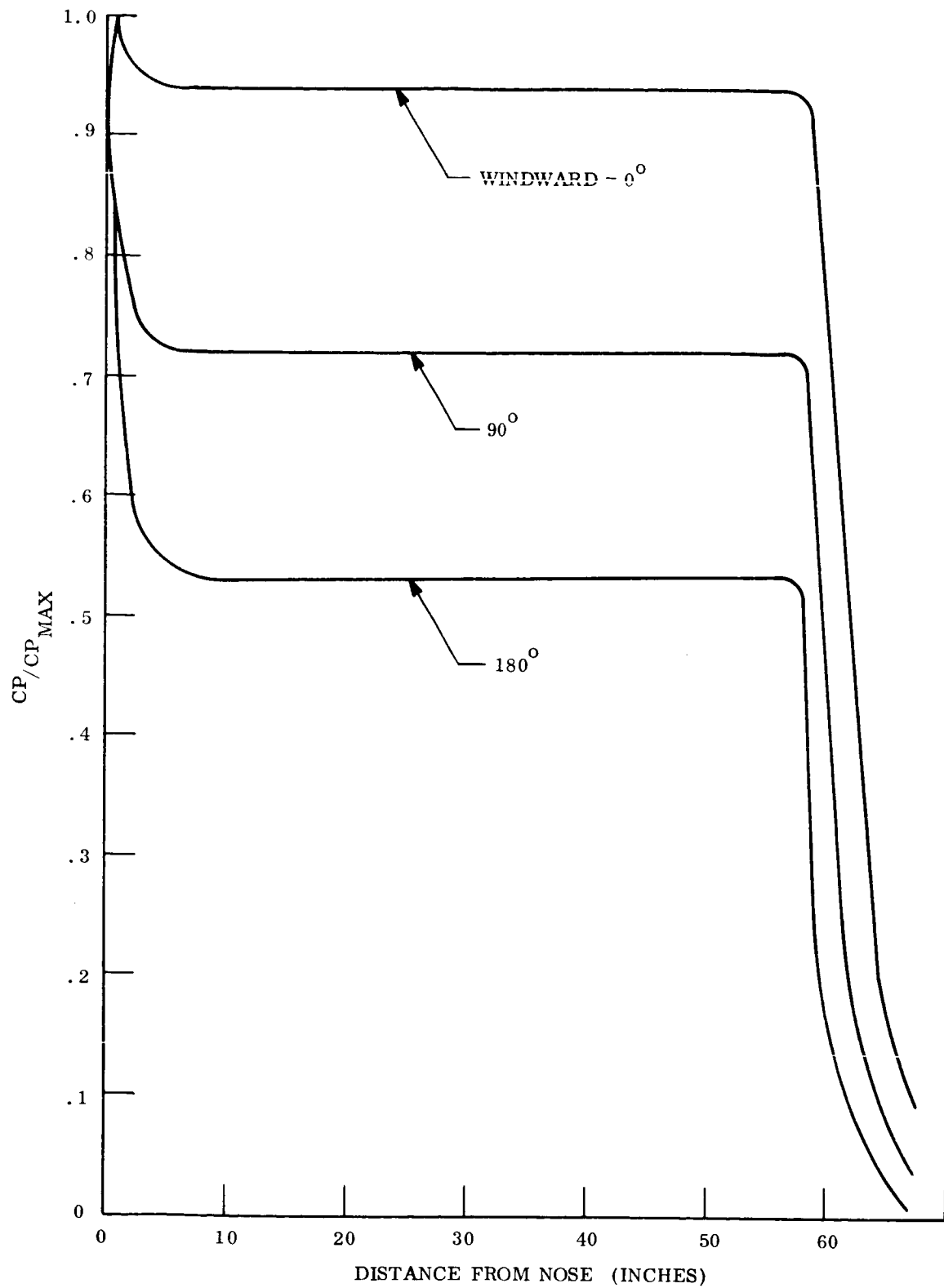
Figure 47. 60° Sphere Cone Pressure Distribution, $\alpha = 15^\circ$, $D = 18.5'$
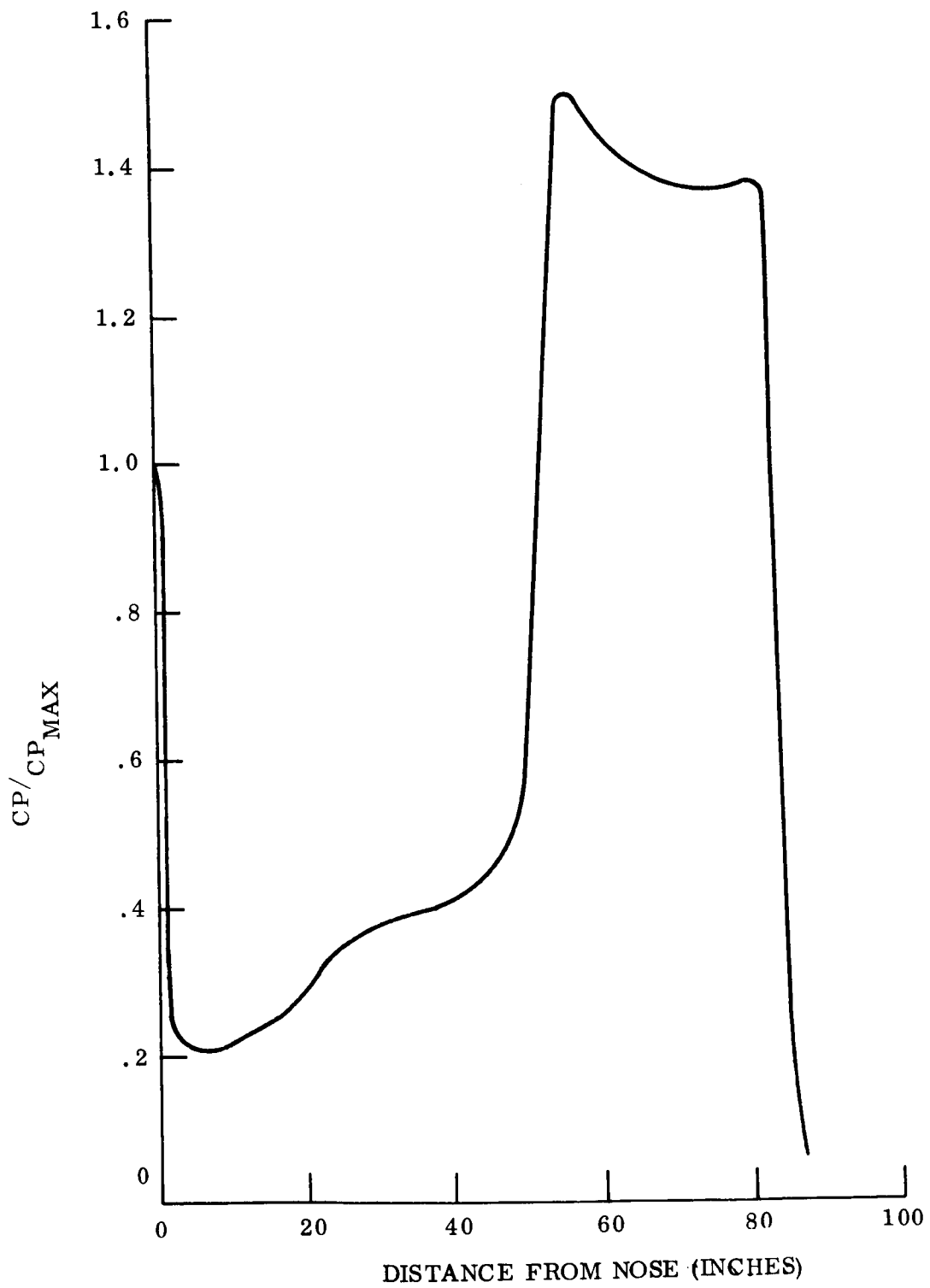
Figure 48. Smooth Flare Pressure Distribution, $\alpha = 0^{\circ}$, D = 12'
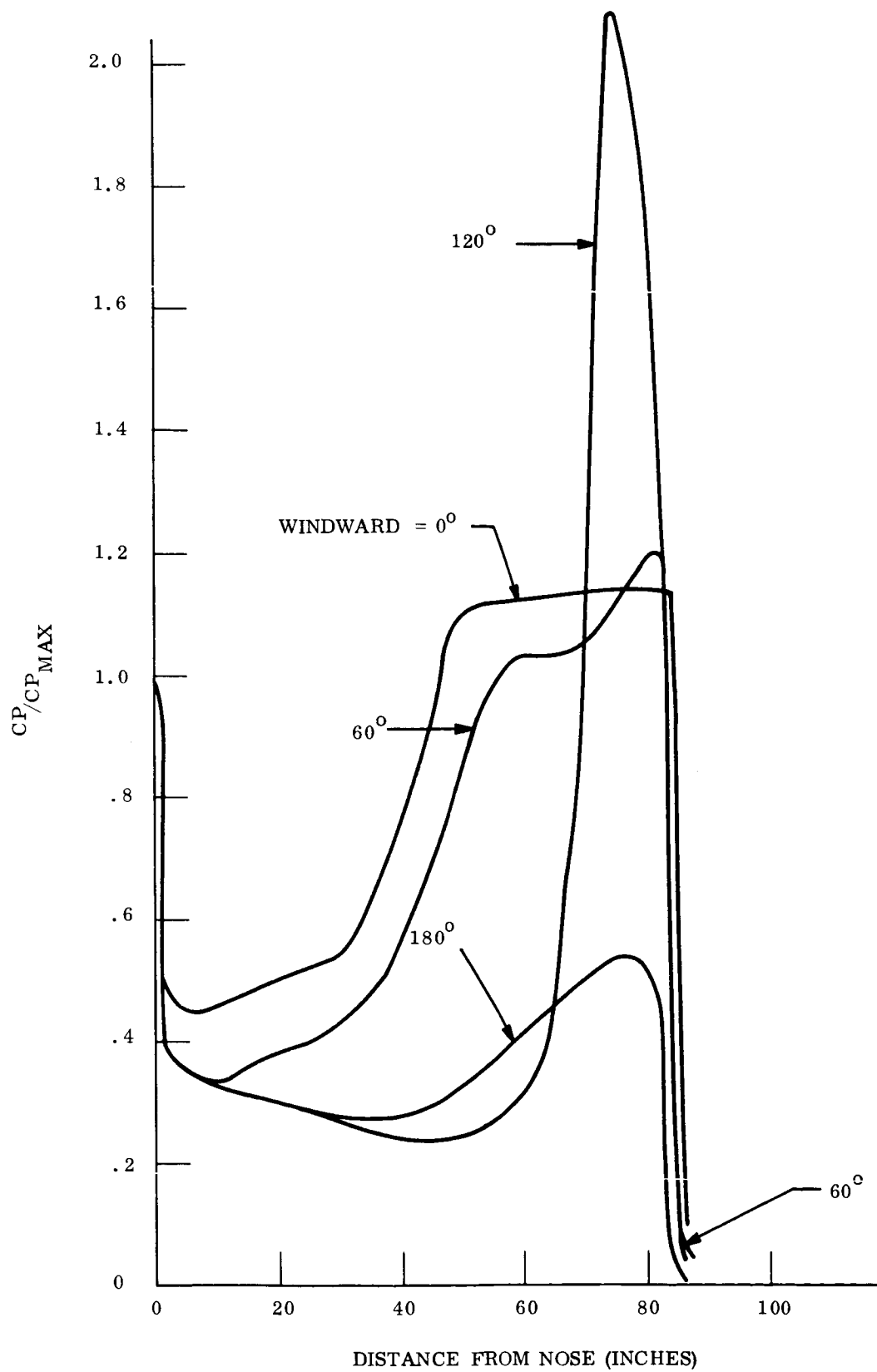
Figure 49. Smooth Flare Pressure Distribution, $\alpha = 12^{\circ}$, $D = 12'$
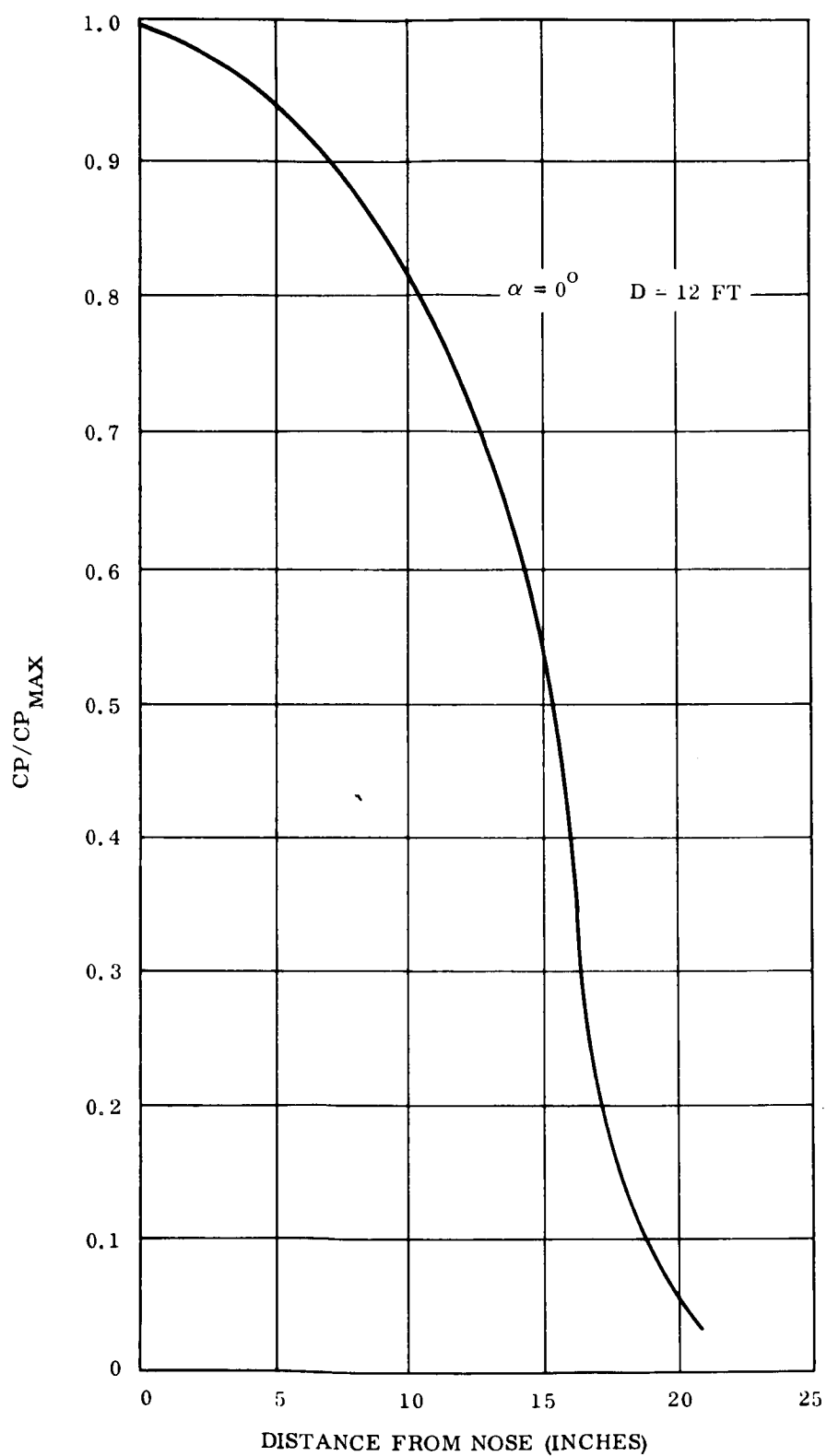
Figure 50. Sphere Cap Pressure Distribution, $\alpha = 0^{\circ}$, D = 12'
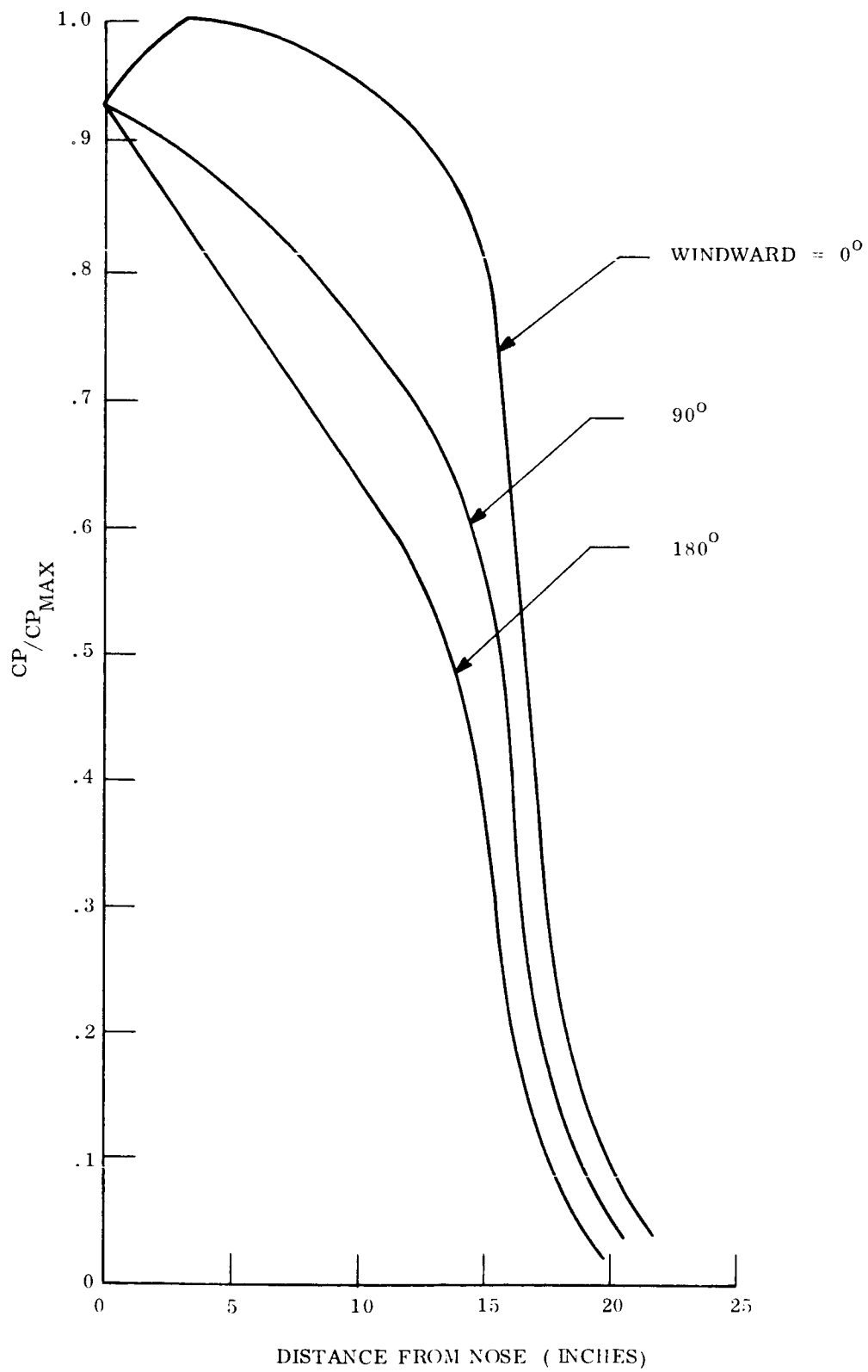
Figure 51. Sphere Cap Pressure Distribution, $\alpha = 15^{\circ}$, D = 12'
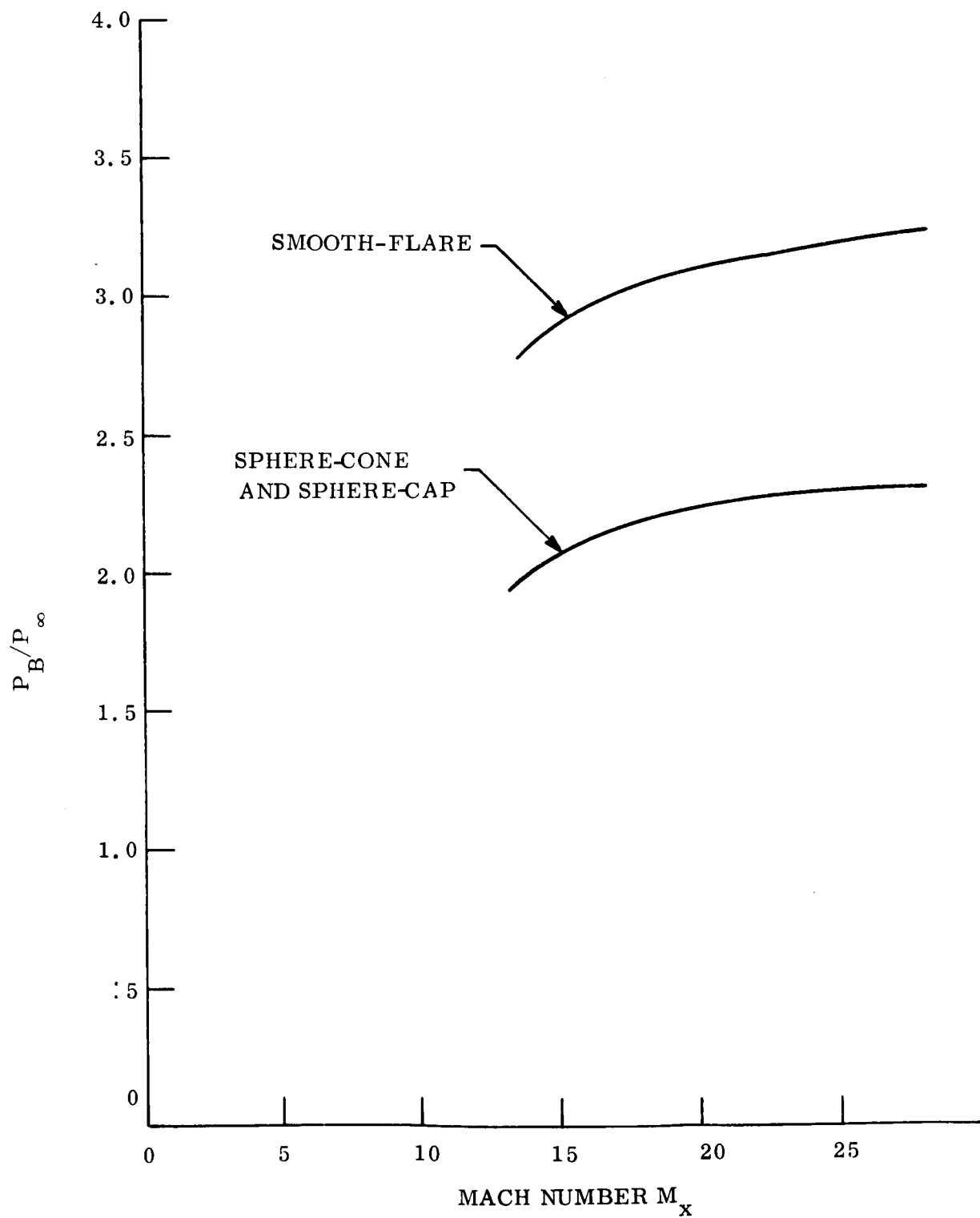
Figure 52.   Base Pressure Ratio as a Function of Mach No. $\alpha = 0^{o}$

NOTE:
1. R_n = NOSE RADIUS
2. R_B = BASE RADIUS
3. ZERO ANGLE OF ATTACK
4. COLD WALL HEAT FLUX

51.5° SPHERE CONE
$R_n/R_B = 0.47$

60° SPHERE CONE
$R_n/R_B = 0.2$
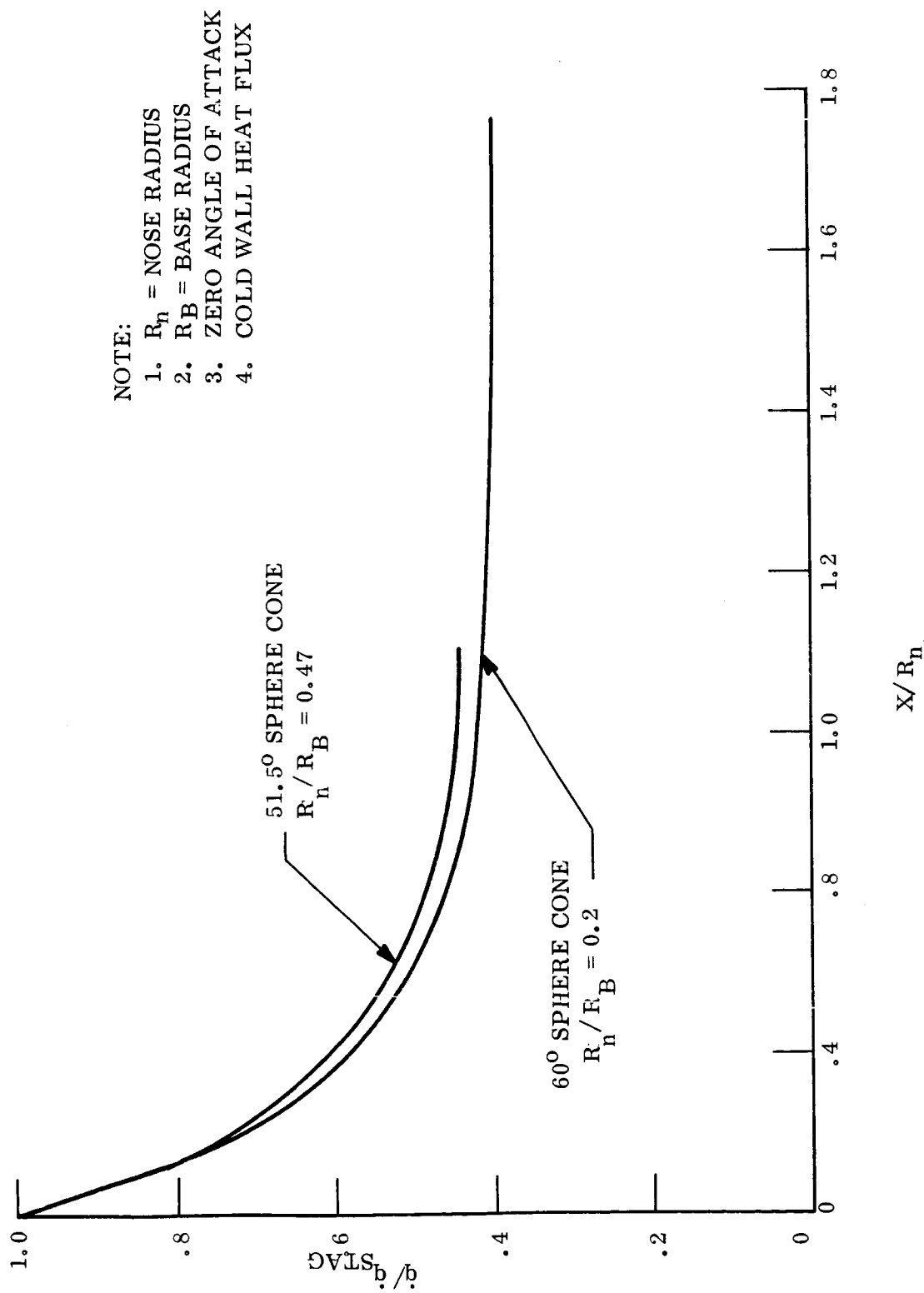
Figure 53. Sphere-Cone Aerodynamic Heating Profiles
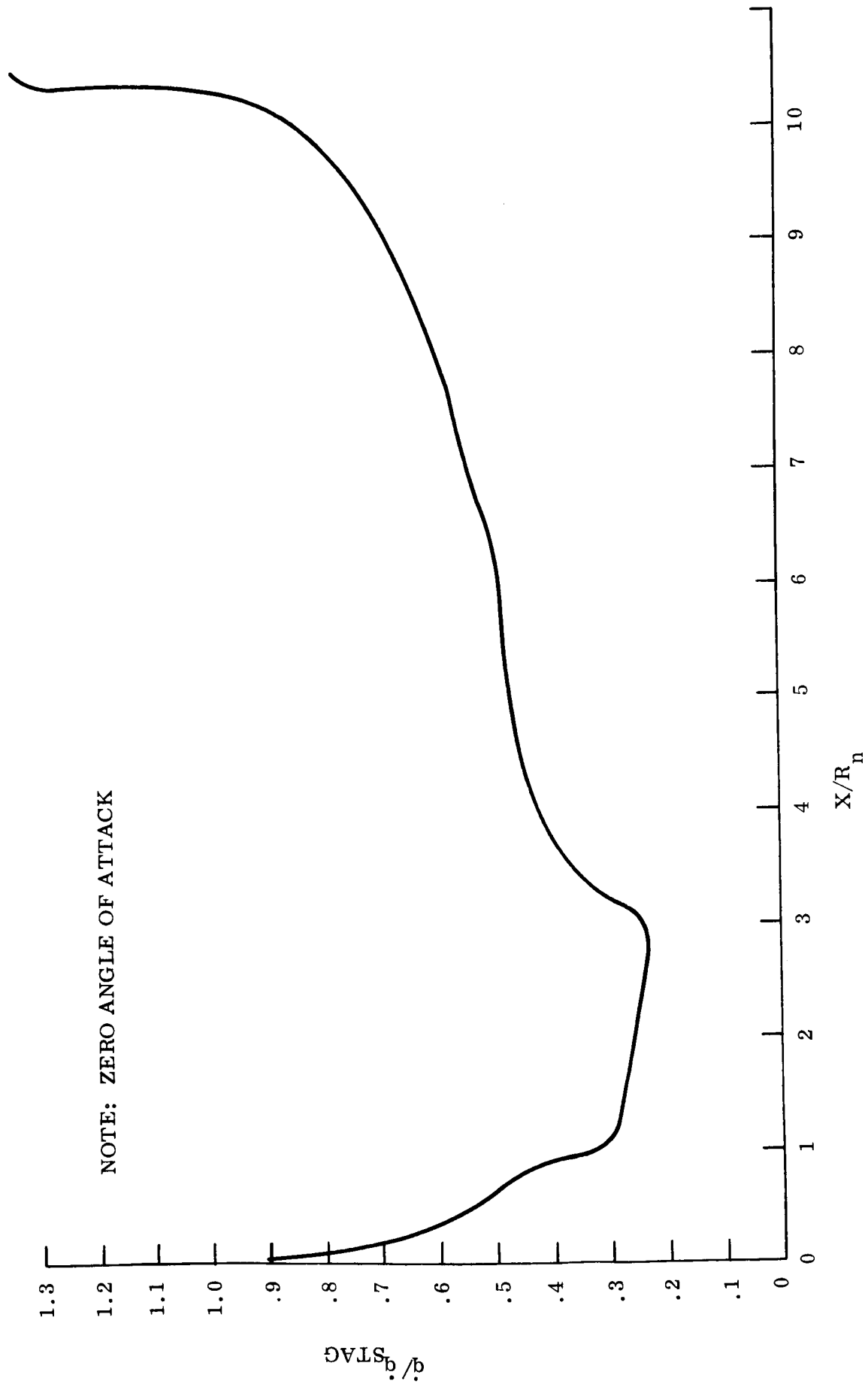
Figure 54. Smooth Flare Aerodynamic Heating Profiles

NOTE: ZERO ANGLE OF ATTACK

NOTE: ZERO ANGLE OF ATTACK
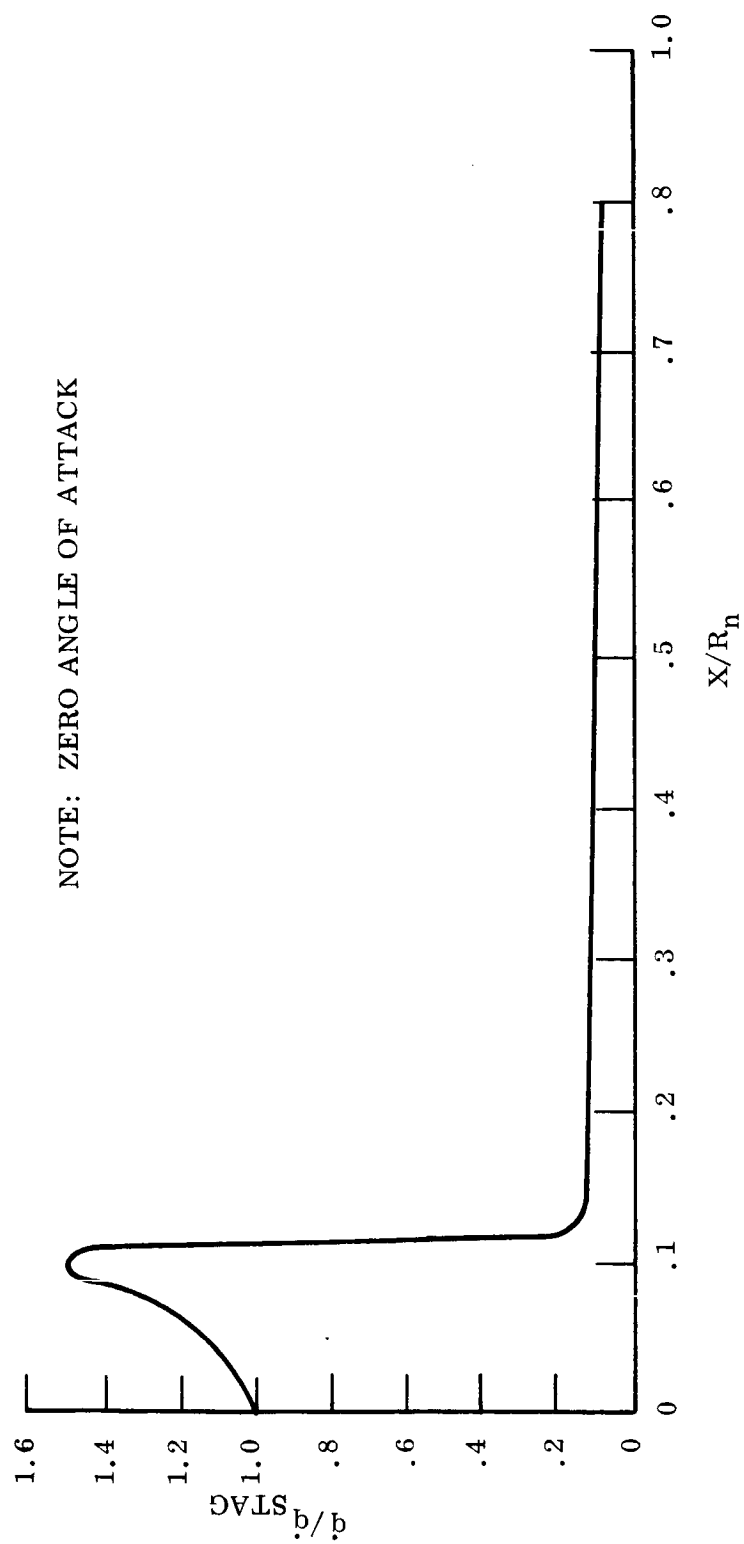
Figure 55. Sphere Cap Aerodynamic Heating Profiles

149

NOTE:

1. CONFIGURATION
   APOLLO SHAPE - R_n = 14.4 FT
   BASE DIAMETER = 12 FT

2. HEAT TRANSFER RATES
   VM 3 ATMOS, γ_e = 20°
   V_e = 19500 FT/SEC
   COLD WALL HEAT FLUX

3. R_n/R_B = 2.4

——— 200°F BACKFACE TEMP.

—————— 450°F BACKFACE TEMP.

—·—·— 700°F BACKFACE TEMP.

$.1 \, M/C_D A$
.4

$.1 \, M/C_D A$
.4
.4
.1

X/R_n

ESM (1004) SHIELD THICKNESS (INCHES)
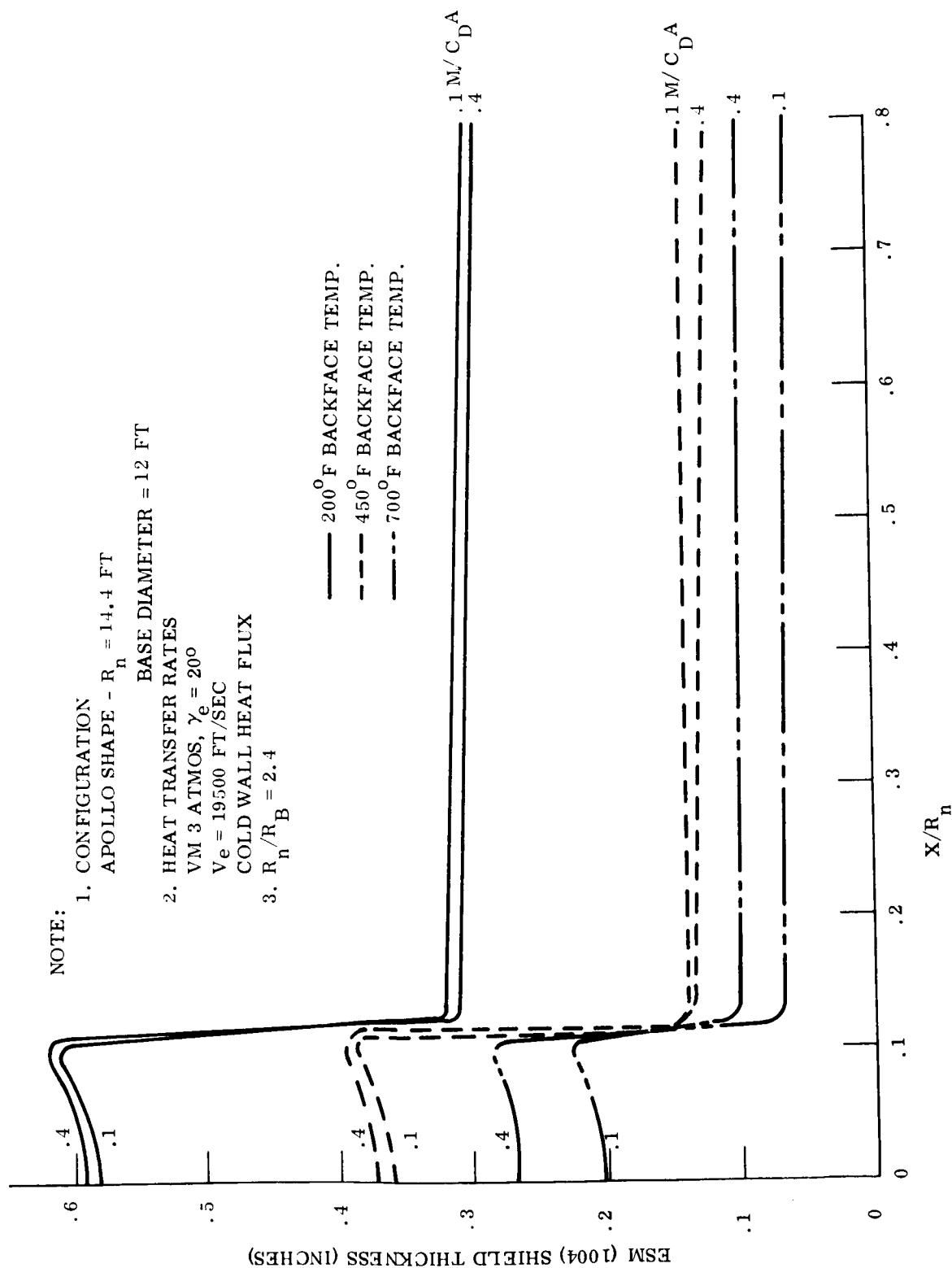
Figure 56.   Voyager Heat Shield Requirements – Sphere Cap 12' Base Diameter

150

Figure 57. Voyager Heat Shield Requirements – Sphere Cap 18.5' Base Diameter

NOTE:

1. CONFIGURATION
   APOLLO SHAPE R_n = 22.2 IN.
   BASE DIAMETER = 18.5 FT.

2. HEAT TRANSFER RATES
   VM 3 ATMOS, γ_c = 20°
   V_e = 19500 FT/SEC
   COLD WALL HEAT FLUX

3. R_n/R_B = 2.4

——— 200°F BACKFACE TEMP.
– – – 450°F BACKFACE TEMP.
–·–· 700°F BACKFACE TEMP.

ESM(1004) SHIELD THICKNESS (INCHES)

X/R_n

151
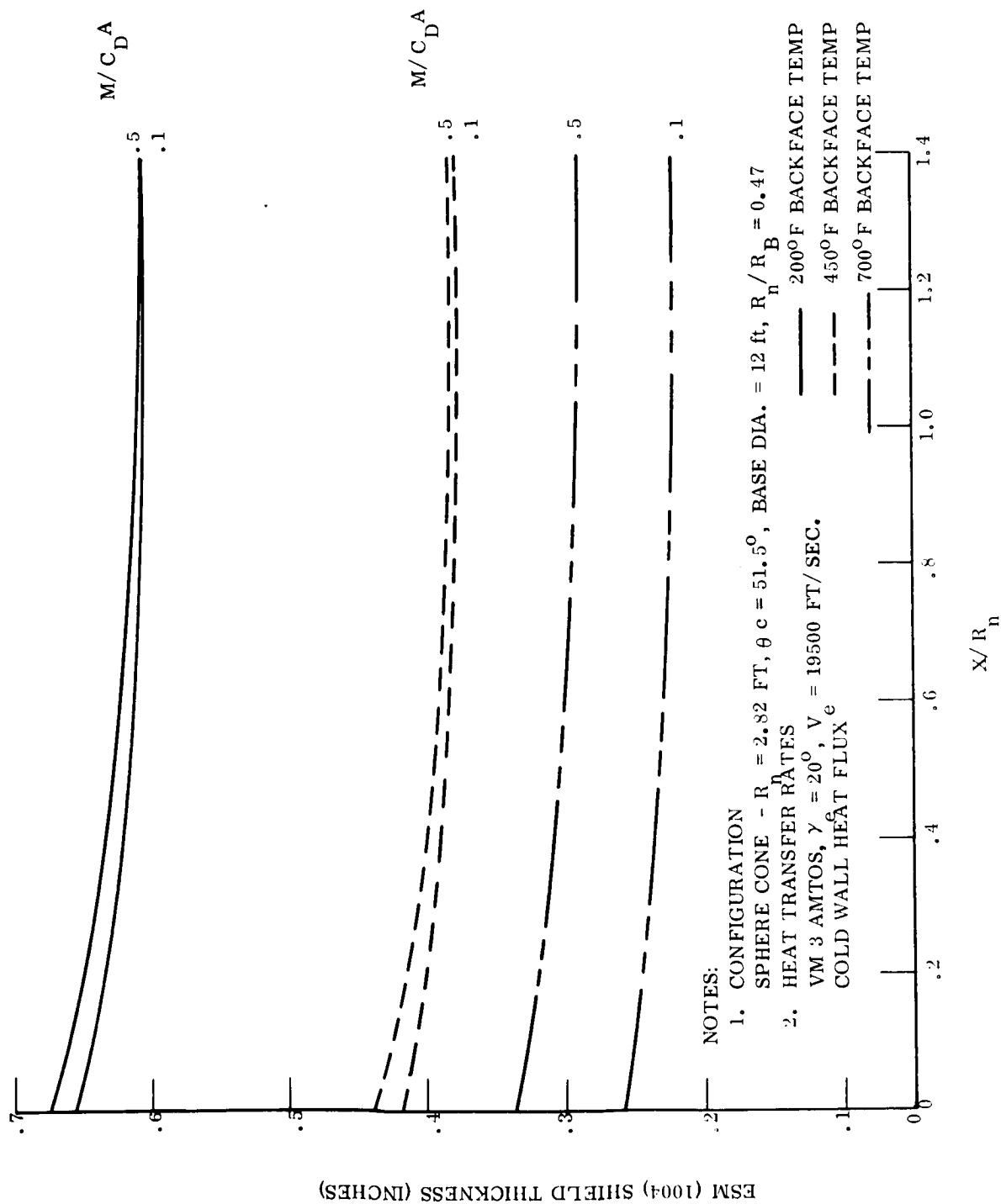
Figure 58. Voyager Heat Shield Requirements 51.5° Sphere Cone 12' Base Diameter
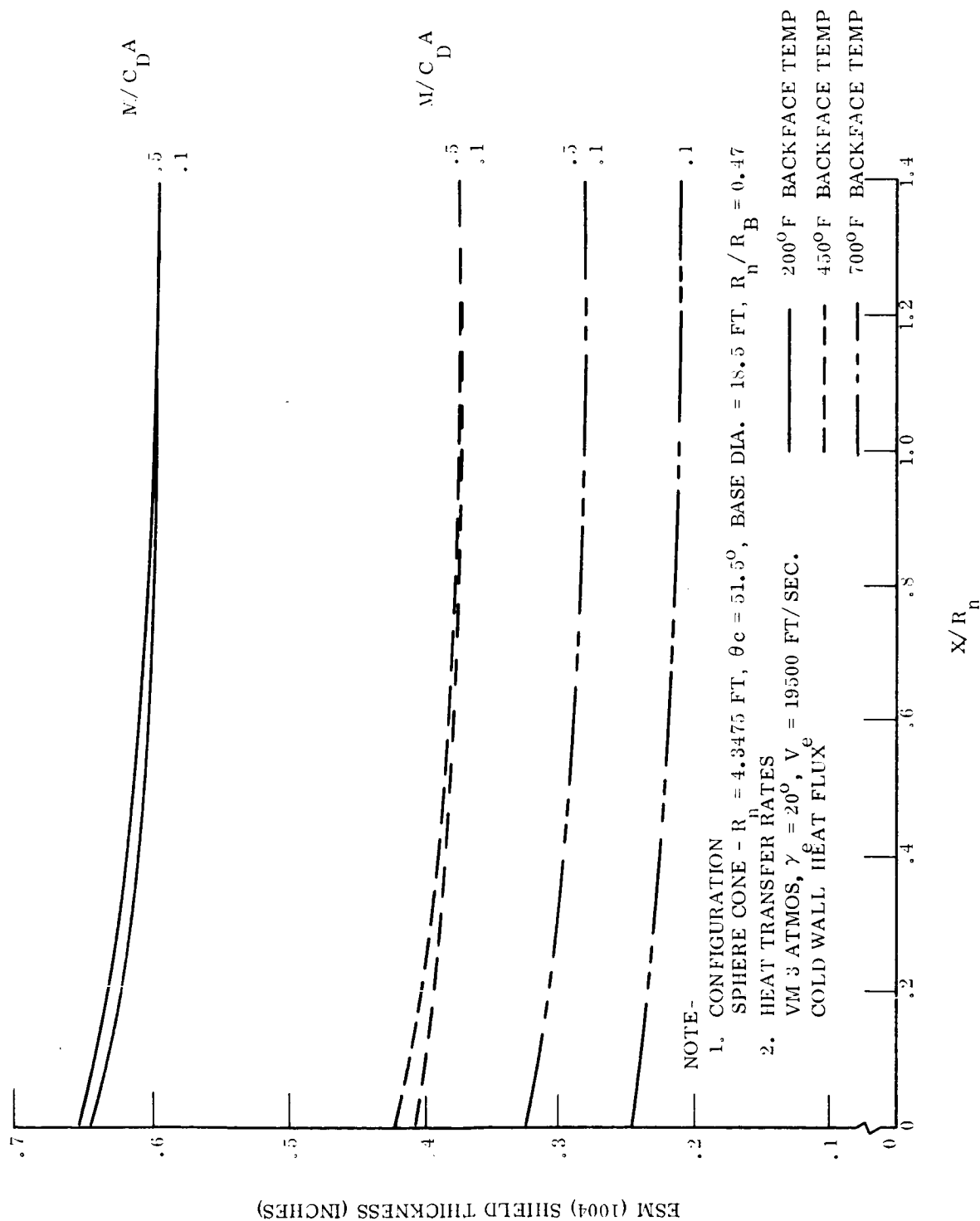
Figure 59. Voyager Heat Shield Requirements 51.5° Sphere Cone 18.5' Base Diameter

153
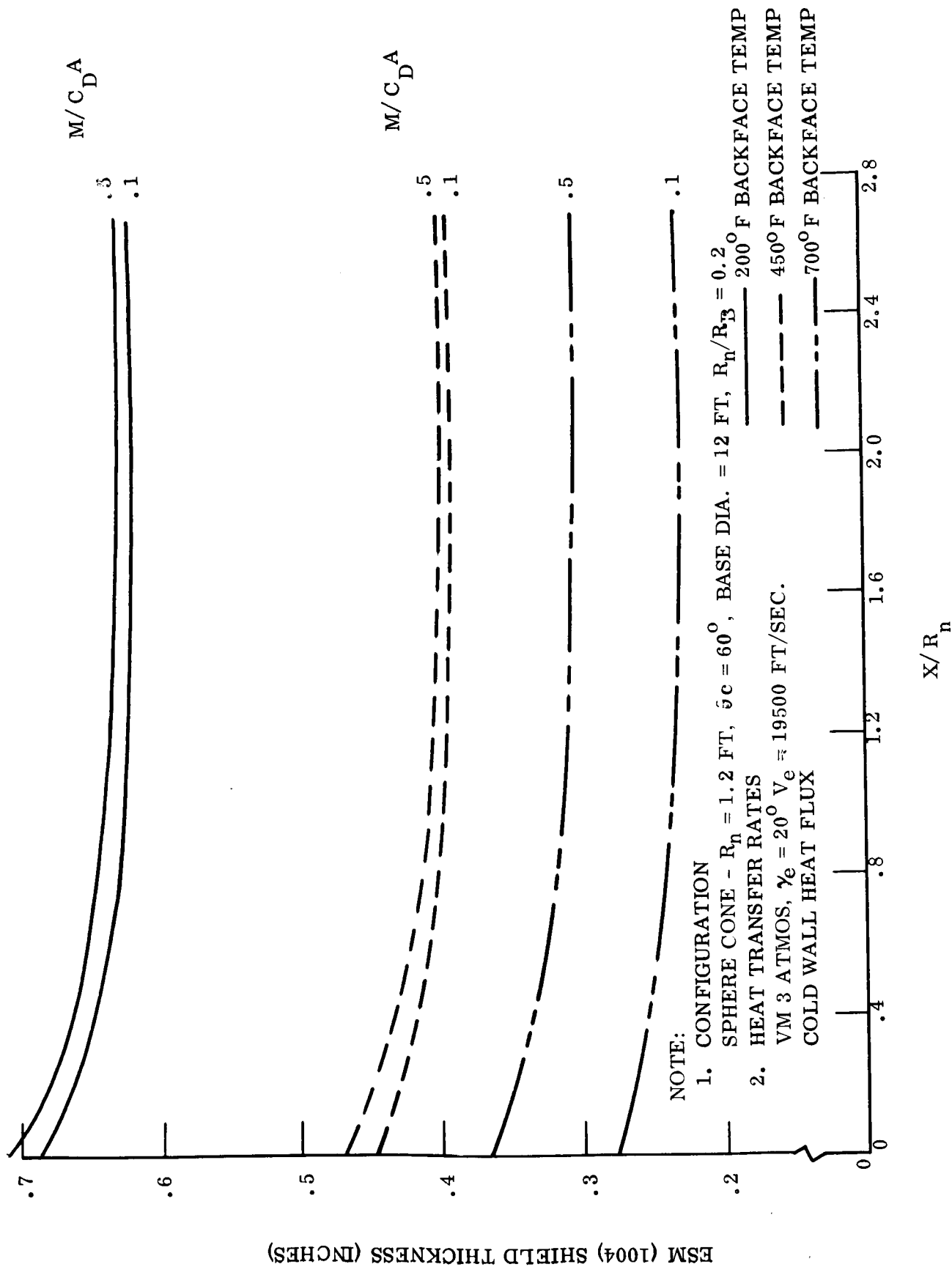
Figure 60. Voyager Heat Shield Requirements 60° Sphere Cone 12' Base Diameter

154
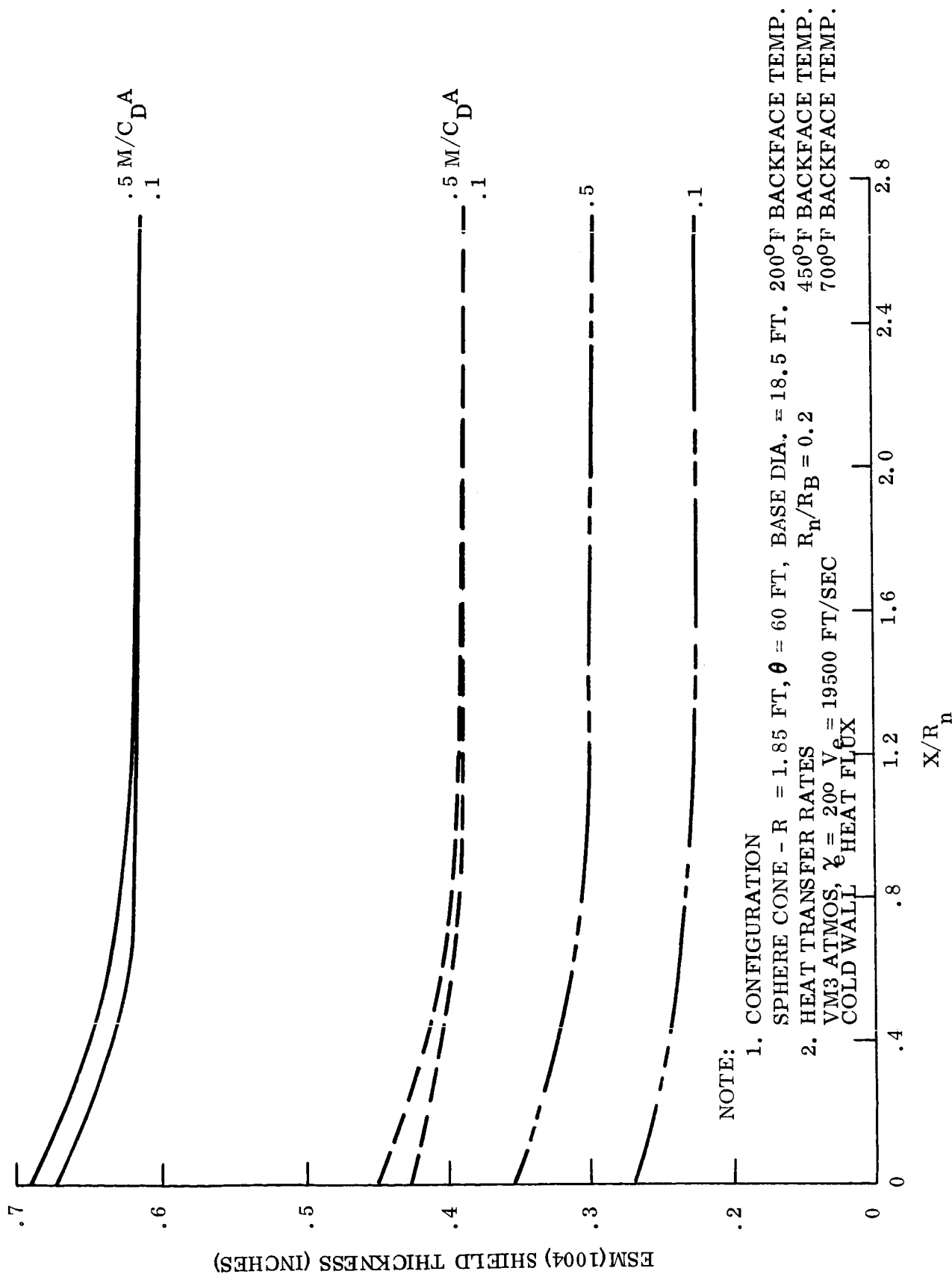
Figure 61. Voyager Heat Shield Requirements 60° Sphere Cone 18.5' Base Diameter

155
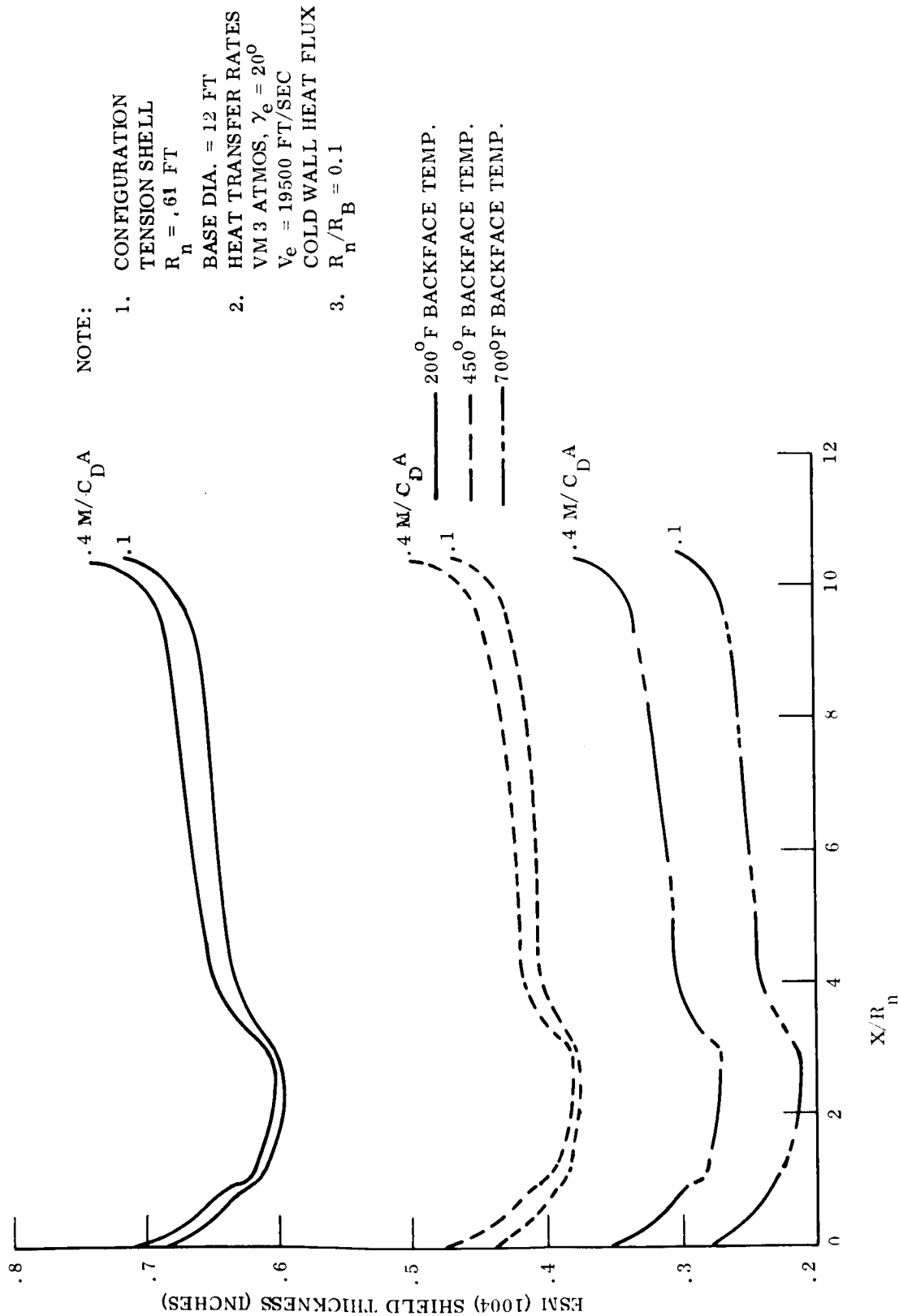
Figure 62. Voyager Heat Shield Requirements – Smooth Flare 12' Base Diameter

156
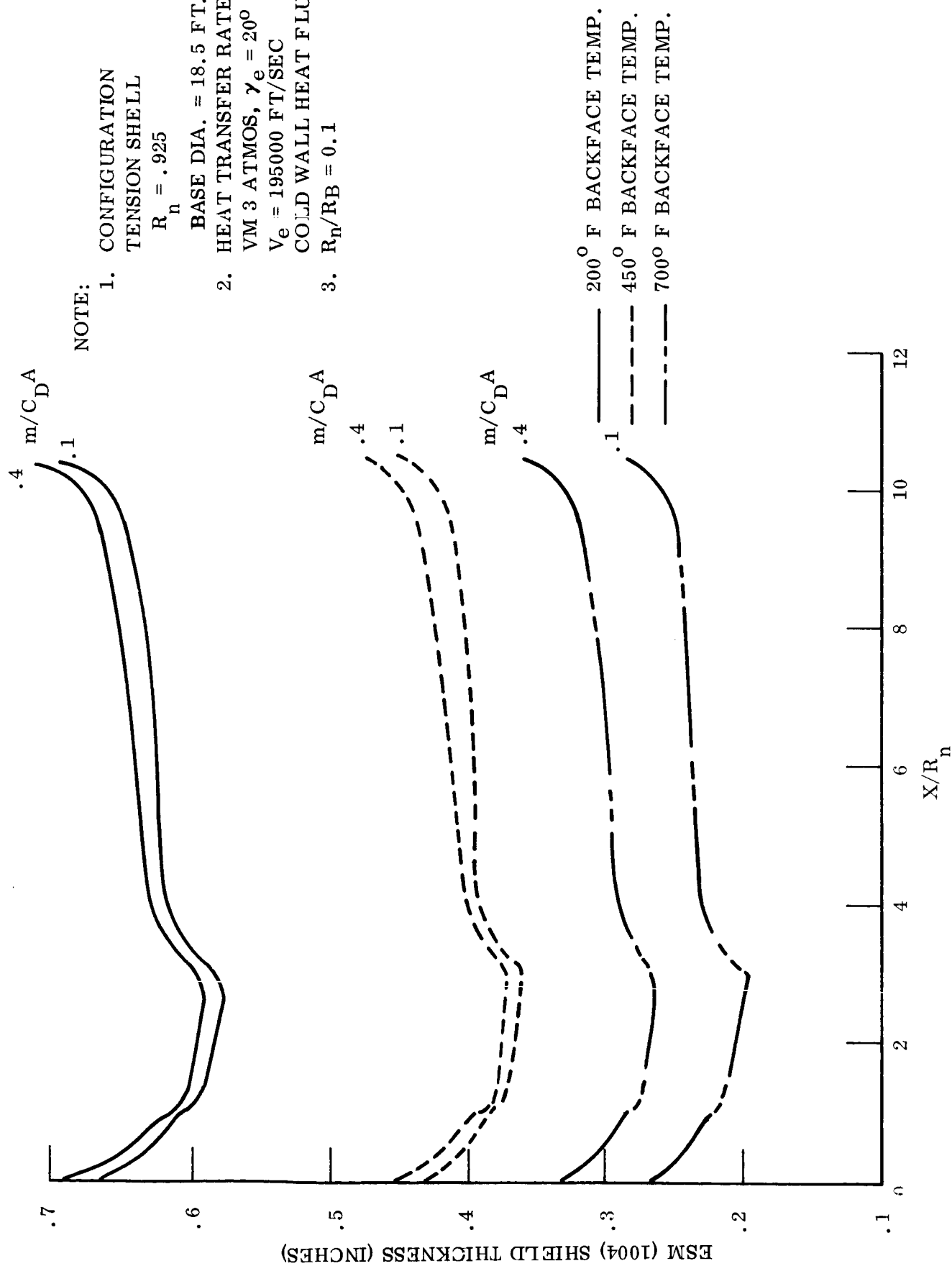
Figure 63. Voyager Heat Shield Requirements – Smooth Flare 18.5' Base Diameter

157
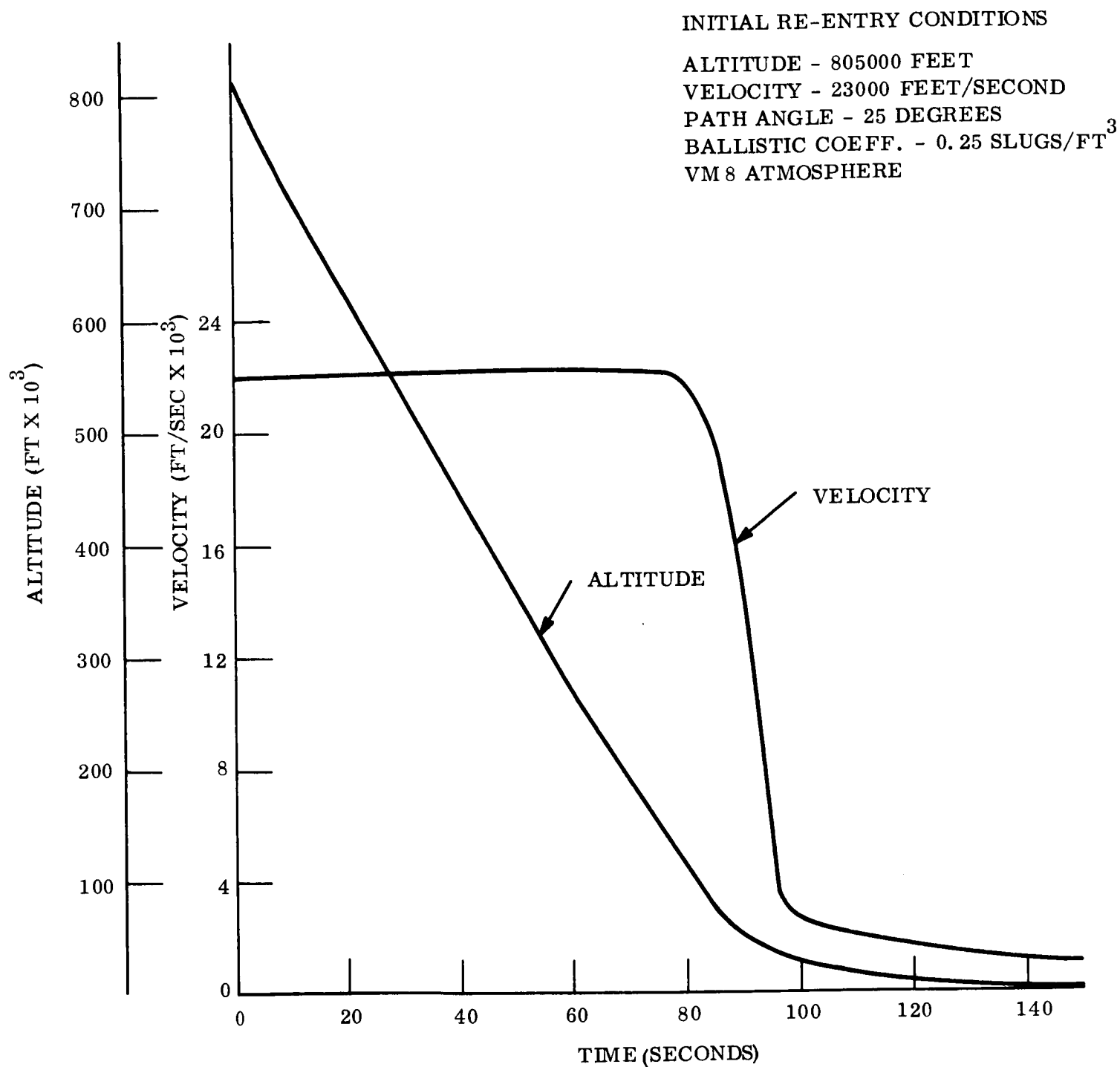
Figure 64. Voyager JPL No. A-1 Trajectory, 60° Sphere Cone, $M/C_D A = .25$, VM - 8
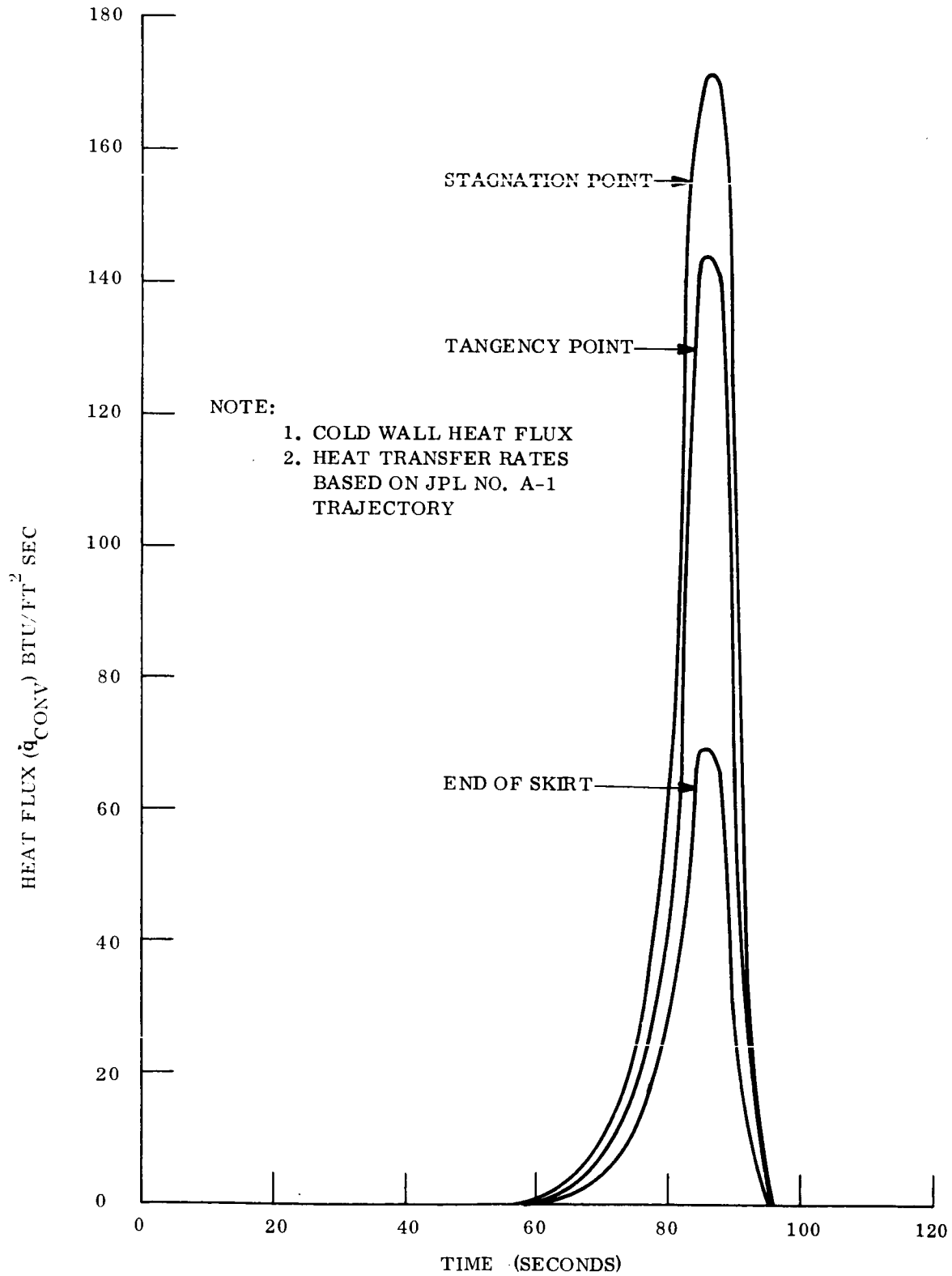
Figure 65. Voyager Convective Heat Flux Histories 60° Sphere Cone – Base Diameter 18.5'
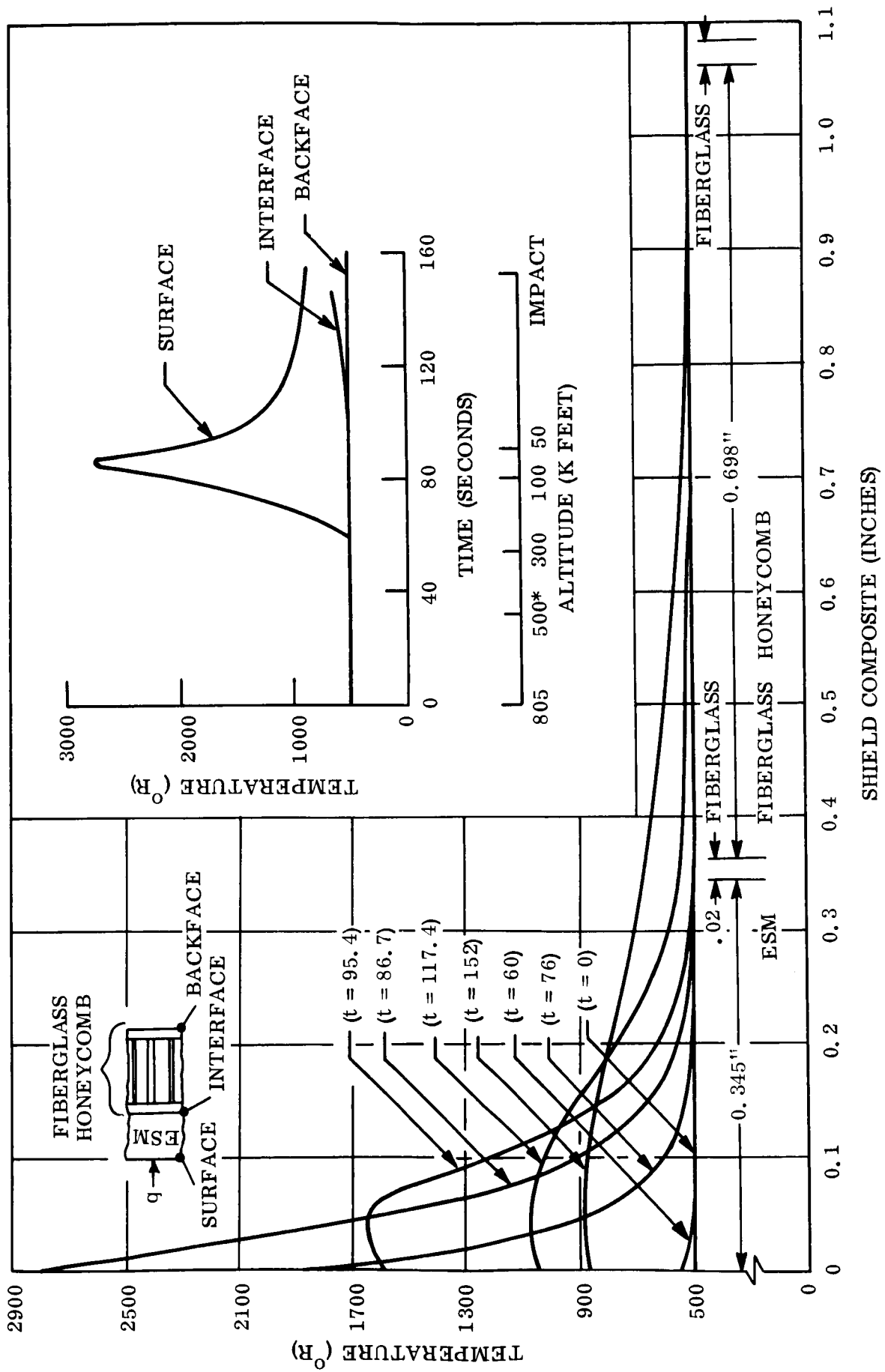
Figure 66.   Voyager Temperature Profiles & Histories 60° Sphere Cone R_n = 1.85' Trangency Pt.
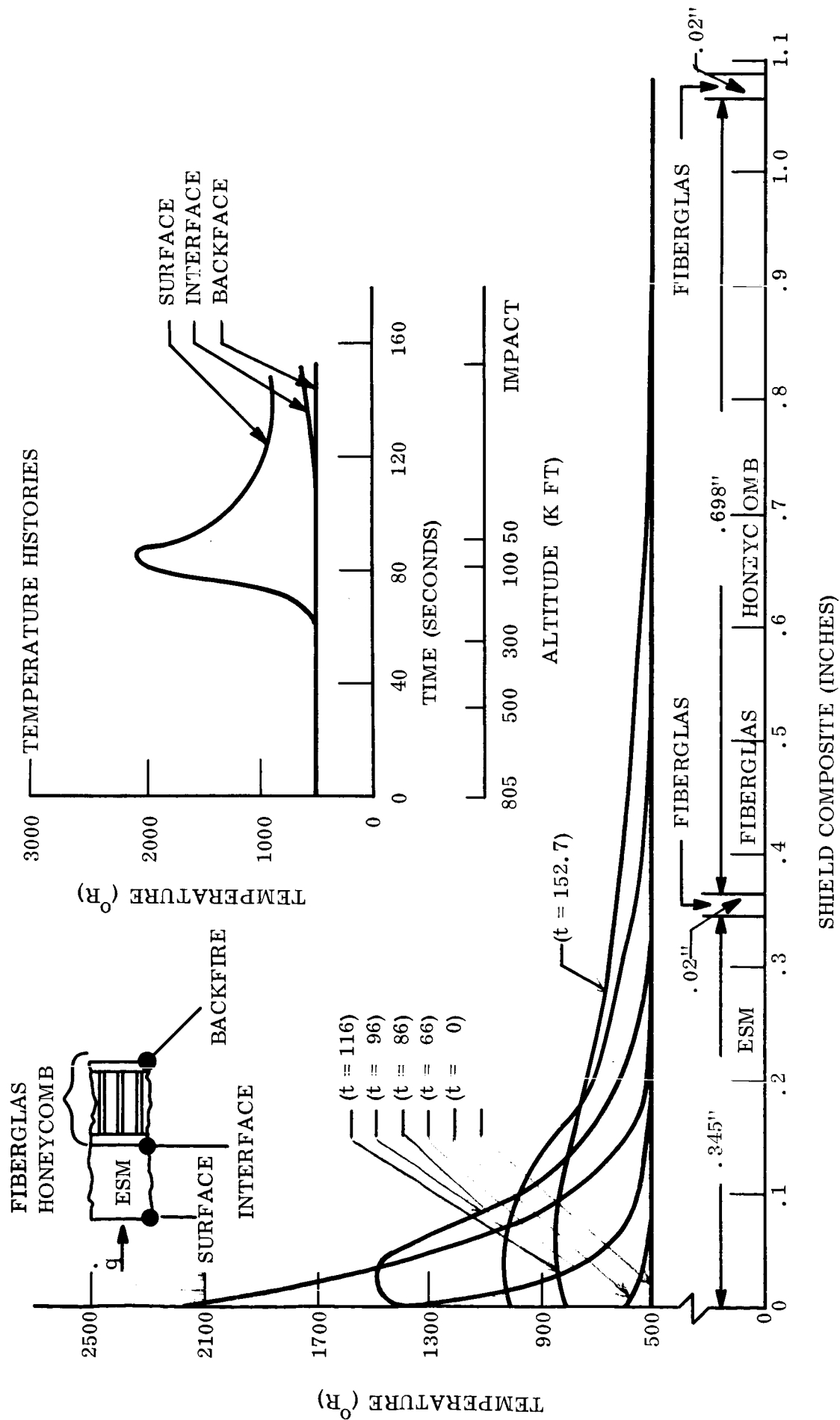
Figure 67. Voyager Temperature Profiles & Histories 60° Sphere Cone R_n = 1.85' End of Skirt

161
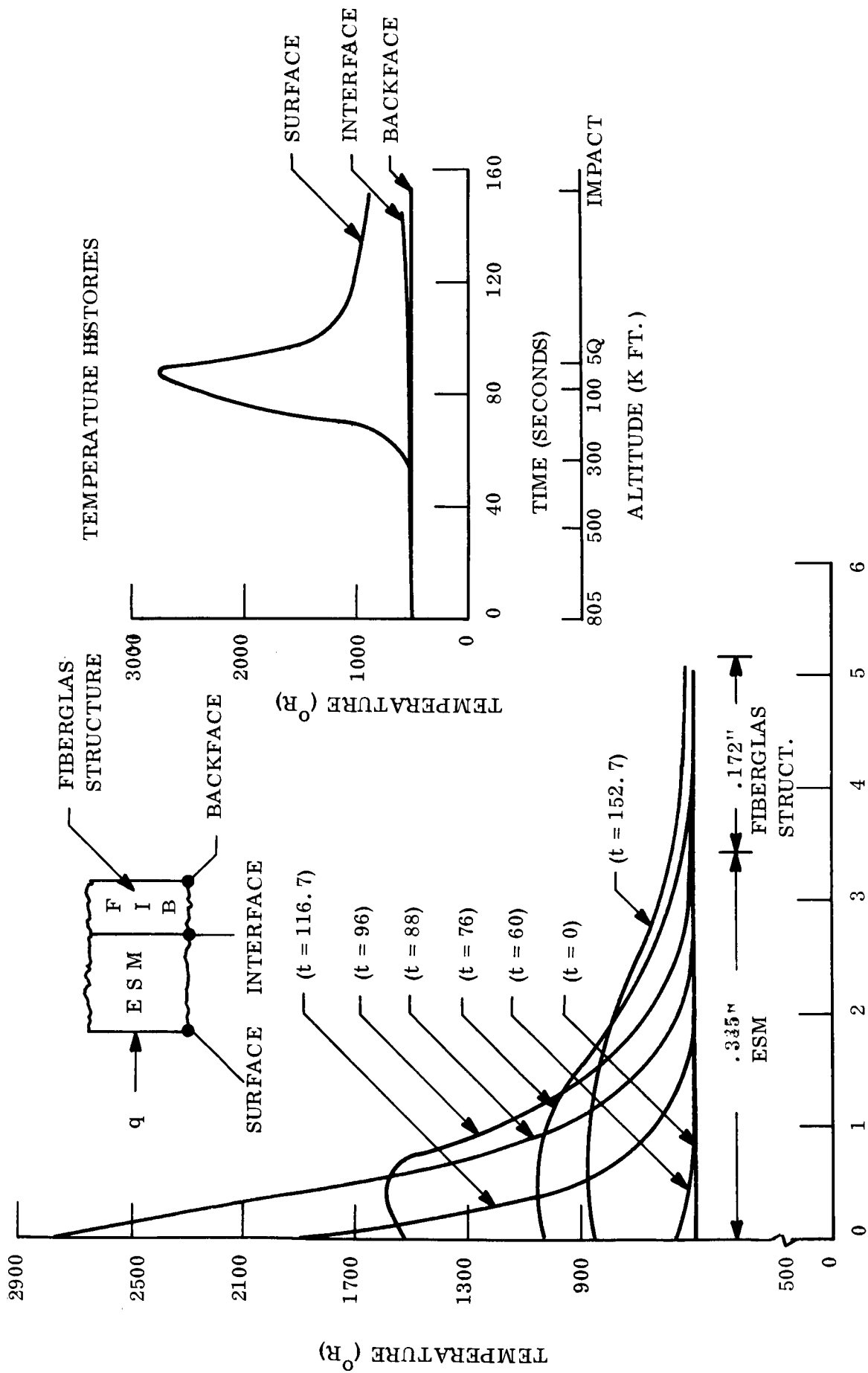
Figure 68. Voyager Temperature Profiles & Histories 60° Sphere Cone R_n = 1.85' Tangency Pt.
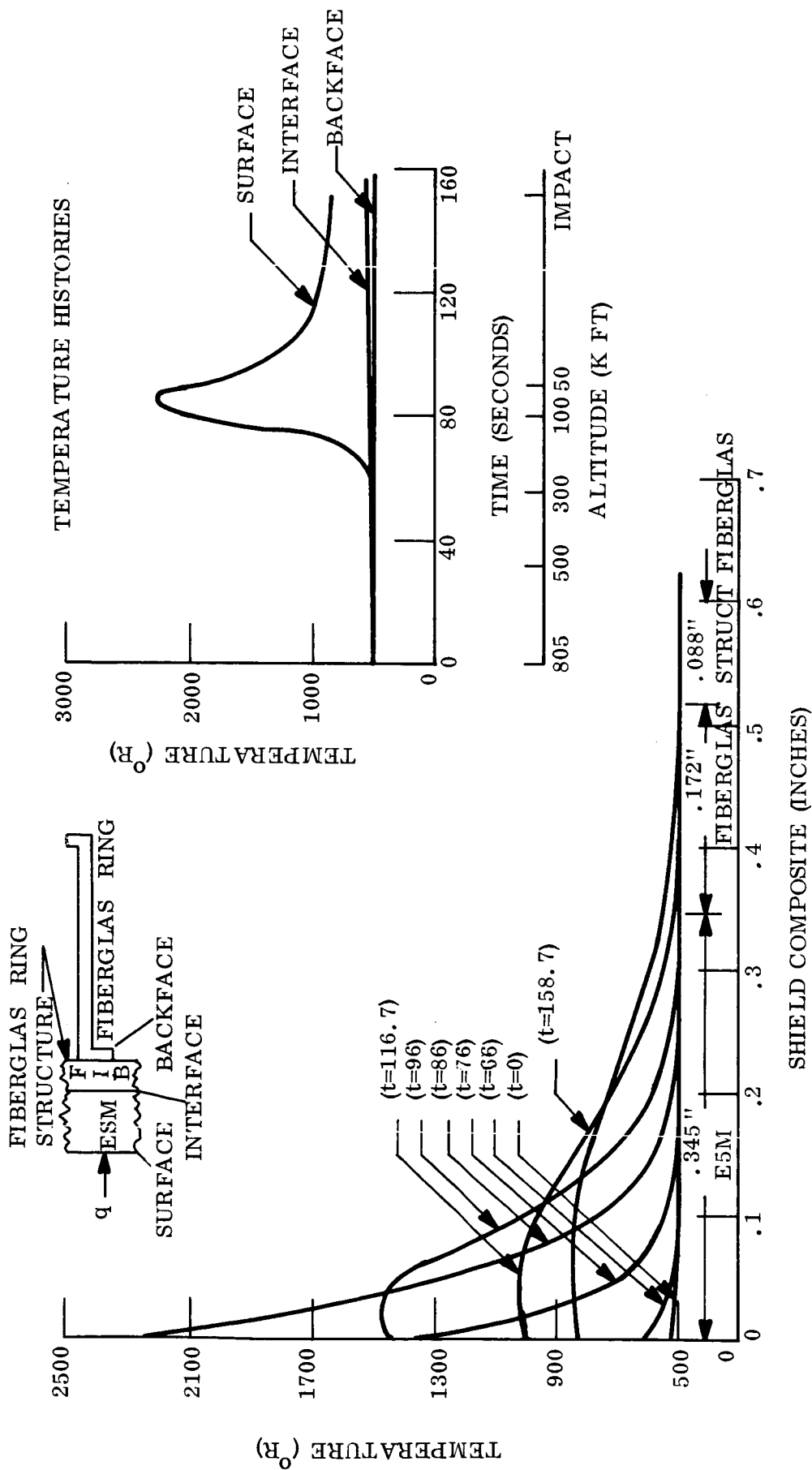
Figure 69. Voyager Temperature Profiles & Histories 60° Sphere Cone R_n = 1.85' End of Skirt
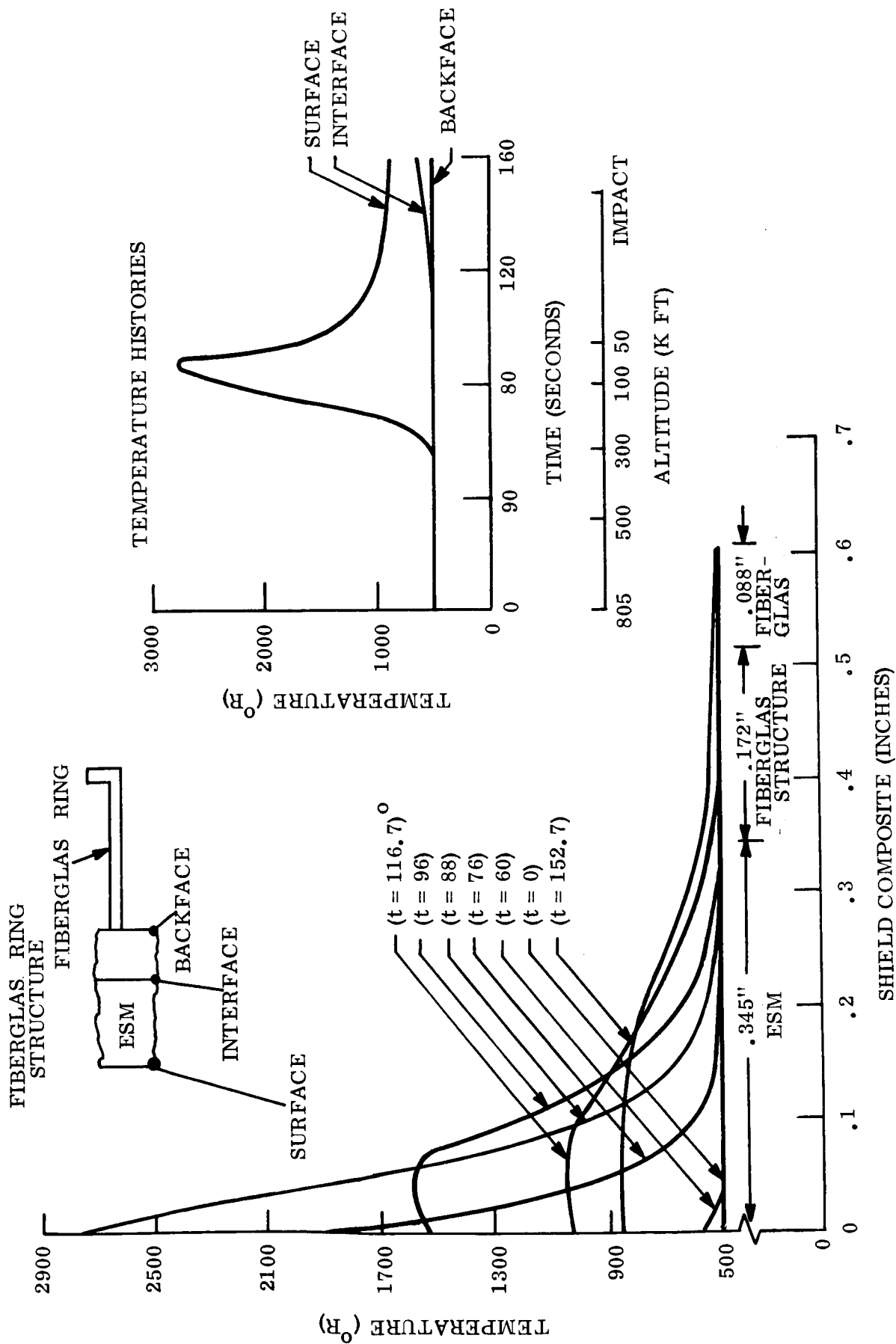
Figure 70. Voyager Temperature Profiles & Histories 60° Sphere Cone $R_n = 1.85'$ Tangency Pt.
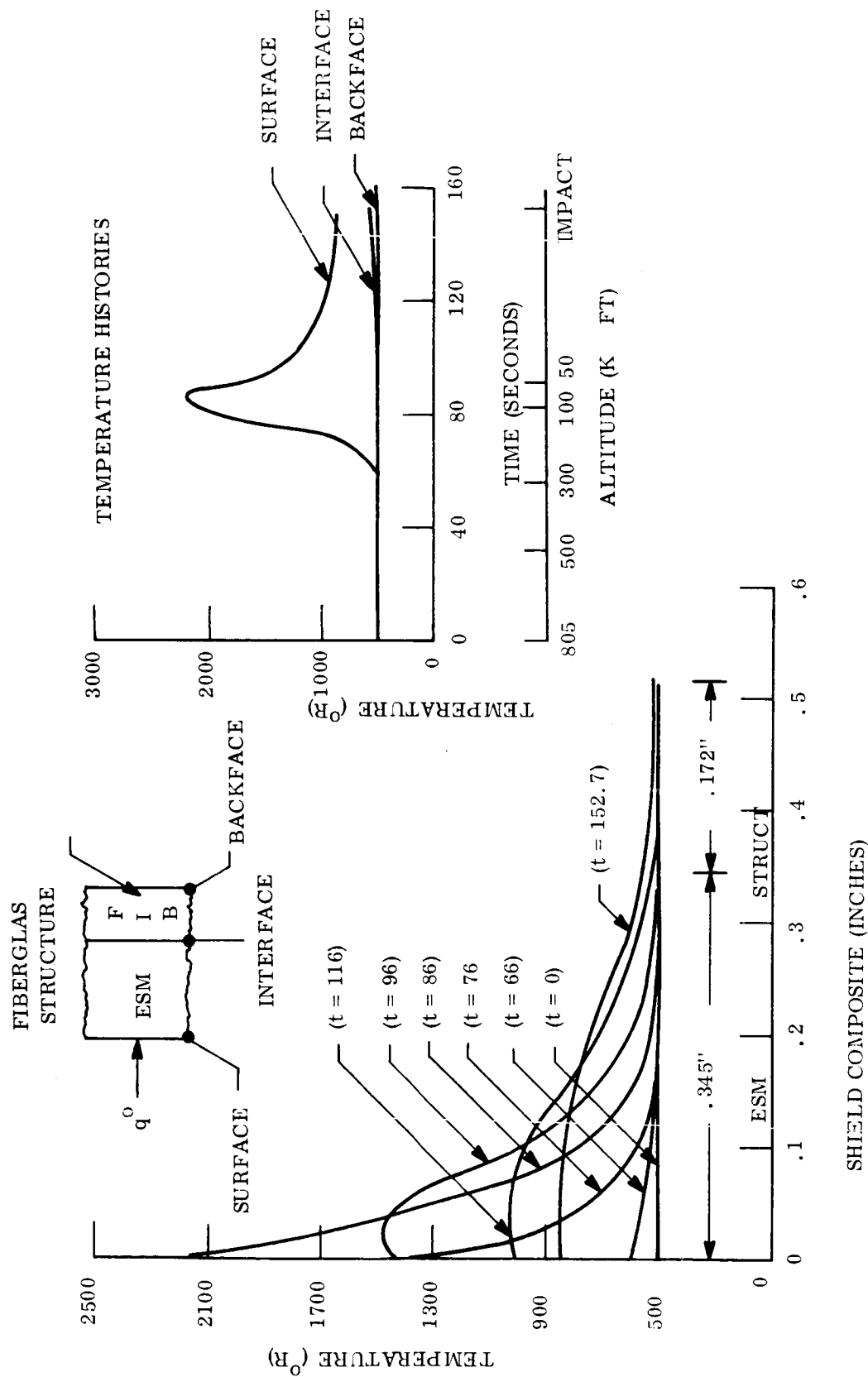
Figure 71. Voyager Temperature Profiles & Histories 60° Sphere Cone R_n = 1.85' End of Skirt

165
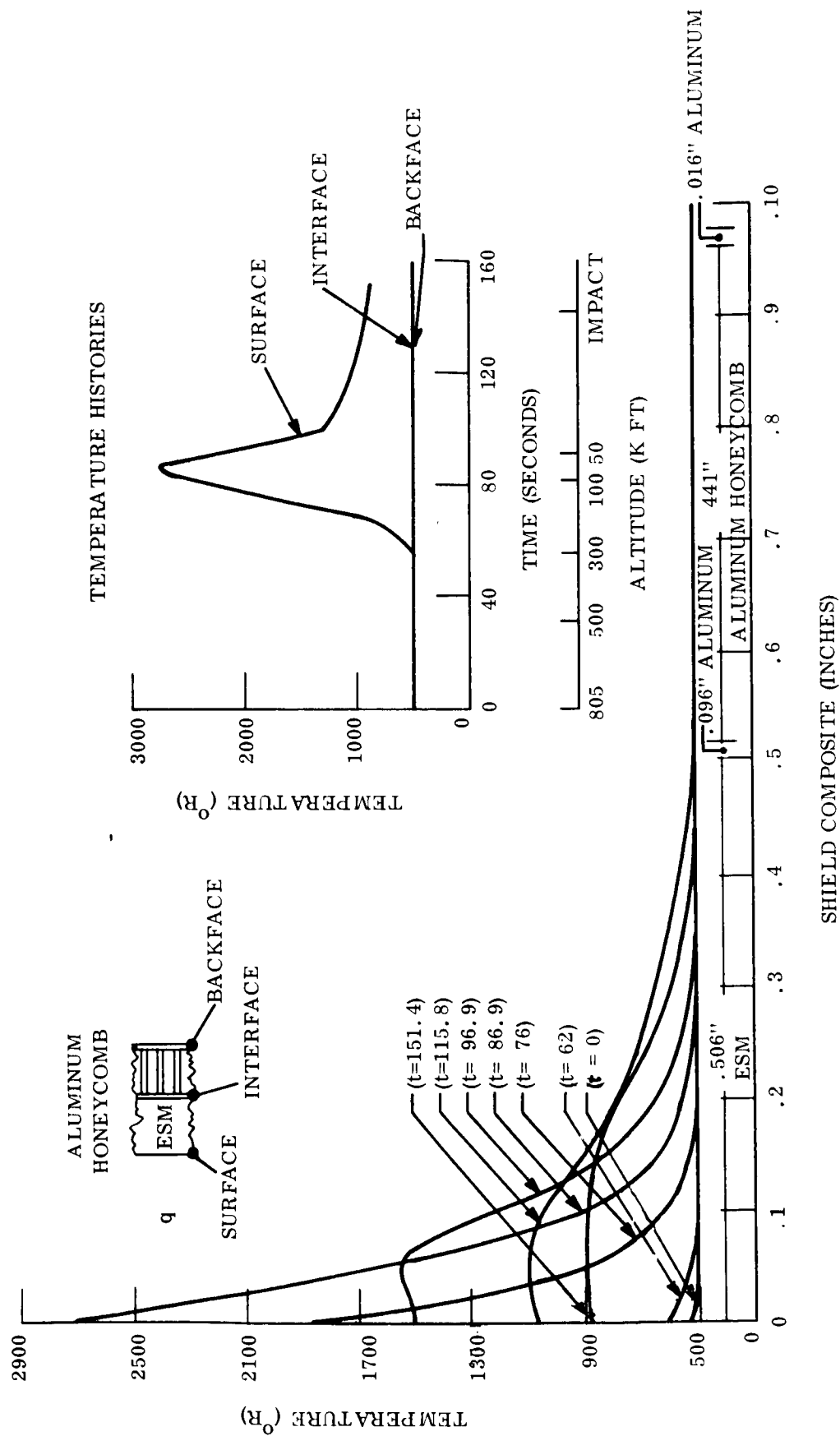
Figure 72. Voyager Temperature Profiles & Histories 60° Sphere Cone R_n = 1.85' Tangency Pt.

Figure 73. Voyager Temperature Profiles & Histories 60° Sphere Cone R_n = 1.85' End of Skirt

167
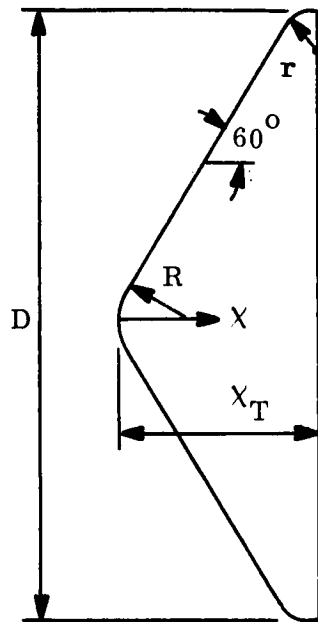
	D = 18.5 FT	D = 12 FT
χ_0	2.974 IN.	1.929 IN.
χ_1	57.447 IN.	37.263 IN.
χ_T	67.06 IN.	43.50 IN.

UP TO THE POINT OF TANGENCY WITH THE CONE

$$\chi = .1D\ (1-\cos \varphi) \qquad\qquad 0 \le \varphi \le 30^{\circ} \qquad\qquad \sin S = \cos \varphi$$

AT THE POINT OF TANGENCY

$$\chi_0 = .1D\ (1-\cos \varphi) \qquad\qquad \varphi_0 = 30^{\circ}$$

AT THE POINT OF TANGENCY WITH r

$$\chi_1 = \chi_0 + D\ \ .5 - .05\ (1-\sin \varphi_0) -.1 \sin \varphi_0 \ \ ctn\ S_0 \qquad\qquad S_0 = 60^{\circ}$$

FOR $\chi \ge \chi_1$

$$\chi = \chi_1 + .05D\ (\cos \varphi_0 - \cos \varphi) \qquad\qquad 30^{\circ} \le \varphi \le 90^{\circ}$$

Figure 74. Sphere-Cone Geometry

y/R_B	x/R_B
0	0
.025	.0032
.050	.0134
.075	.0338
.0885	.0534 ◄──── R tangent to basic shape
.10	.075
.15	.1723
.20	.265
.25	.357
.30	.444
.35	.479
.40	.6125
.45	.6875
.50	.7585
.55	.826
.60	.888
.65	.942
.70	.99
.75	1.034
.80	1.071
.85	1.101
.90	1.125
.95	1.144
.955	1.145 ◄──── r tangent to basic shape
1.000	1.205

$$0 \leq y \leq .0885 \, R_B$$

$$\chi = .1 R_B (1 - \cos \varphi)$$

$$0 \leq \varphi \leq 62^\circ \, 14.5'$$

$$R_B = \frac{D}{2}$$

$$\frac{R}{R_B} = .10$$

$$.955 \, R_B \leq y \leq R_B \qquad \varphi_0 = 16^\circ \, 16'$$

$$\chi = .0625 \, R_B \cdot (\cos \varphi_0 - \cos \varphi) + 1.145 \, R_B$$

$$y = .0625 \, R_B (\sin \varphi - \sin \varphi_0) + .955 \, R_B$$

$$16^\circ \, 16' \leq \varphi \leq 90^\circ$$
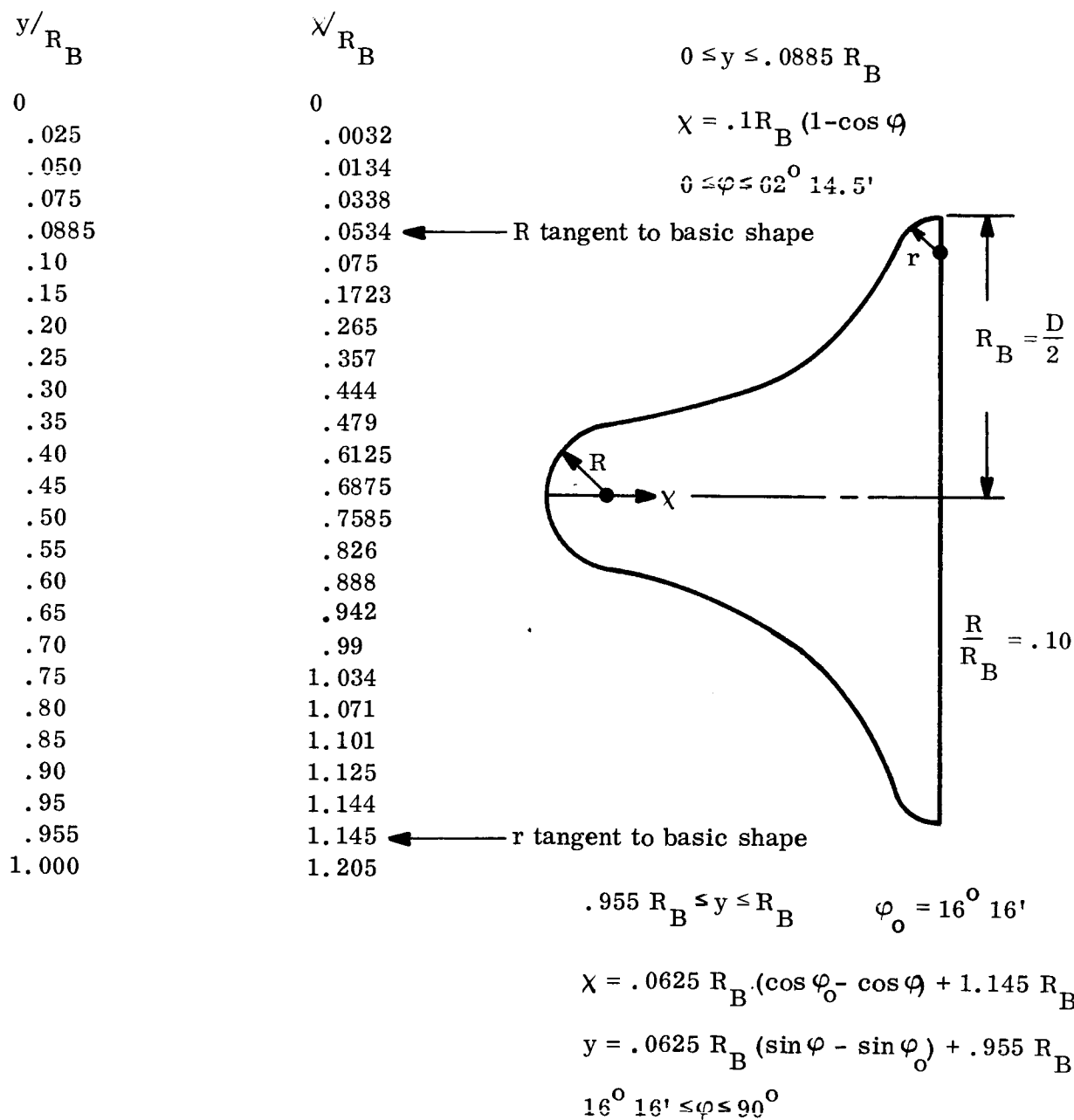
Figure 75. Smooth-Flare Configuration

D = 12 FT

13.775 IN.

20.40 IN.

UP TO THE POINT OF TANGENCY WITH r

$$\chi = 1.2D\,(1-\cos\varphi) \qquad 0 \le \varphi \le 23^{\circ}.02'$$

AT THE POINT OF TANGENCY

$$\chi = \chi_0 = 1.2D\,(1-\cos\varphi) \qquad \varphi_0 = 23^{\circ}\,02'$$

FOR $\chi > \chi_0$

$$\chi = \chi_o + .05D\,(\cos\varphi - \cos\varphi) \qquad 23^{\circ}\,02' \le \varphi \le 90^{\circ}$$

Figure 76. Sphere-Cap Geometry
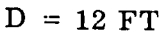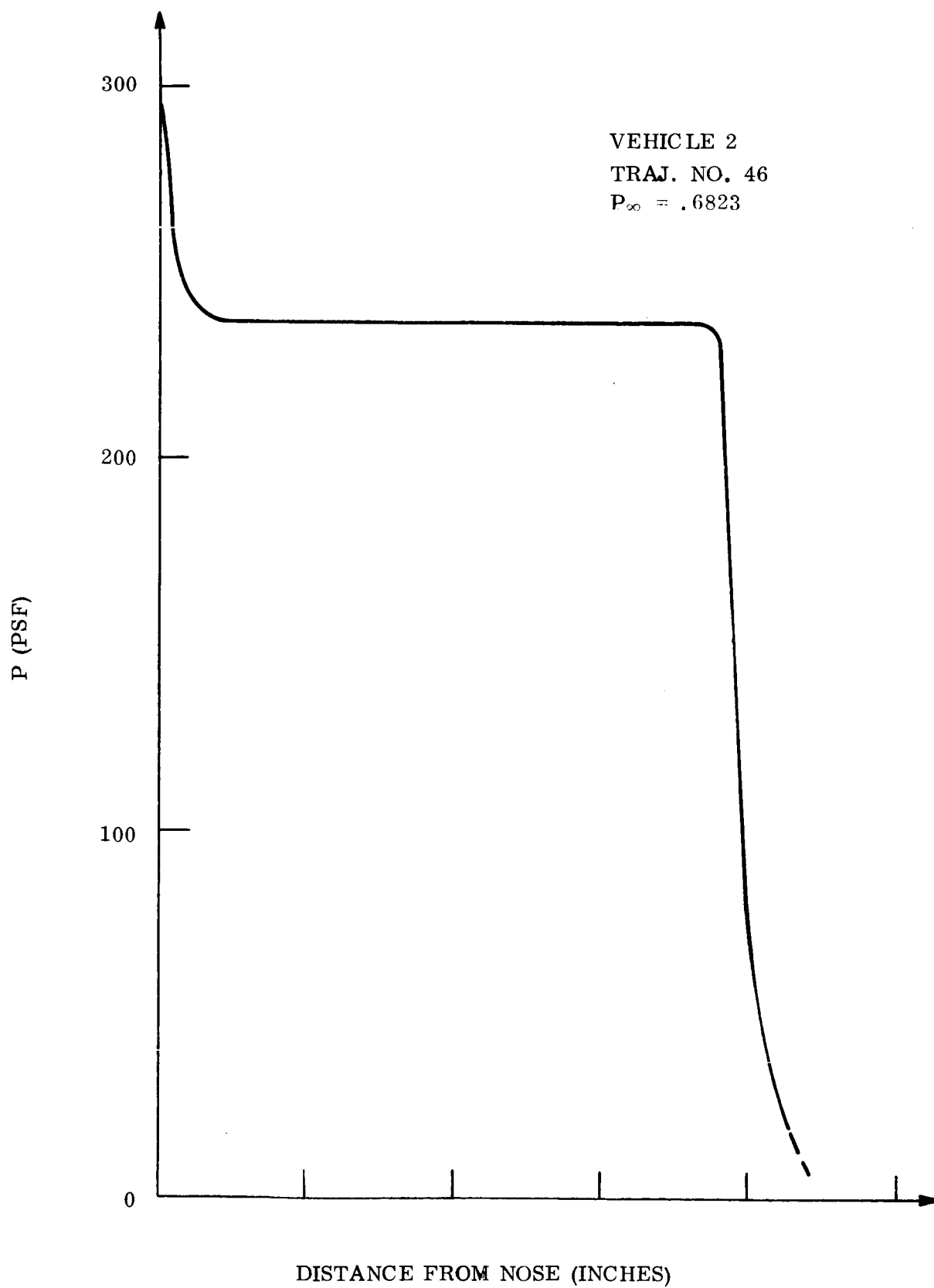
Figure 77. Local Flow, Pressure vs Distance Vehicle 2 Traj. 46

VEHICLE 2
TRAJ. NO. 46
$q_\infty = 154.6$ PSF
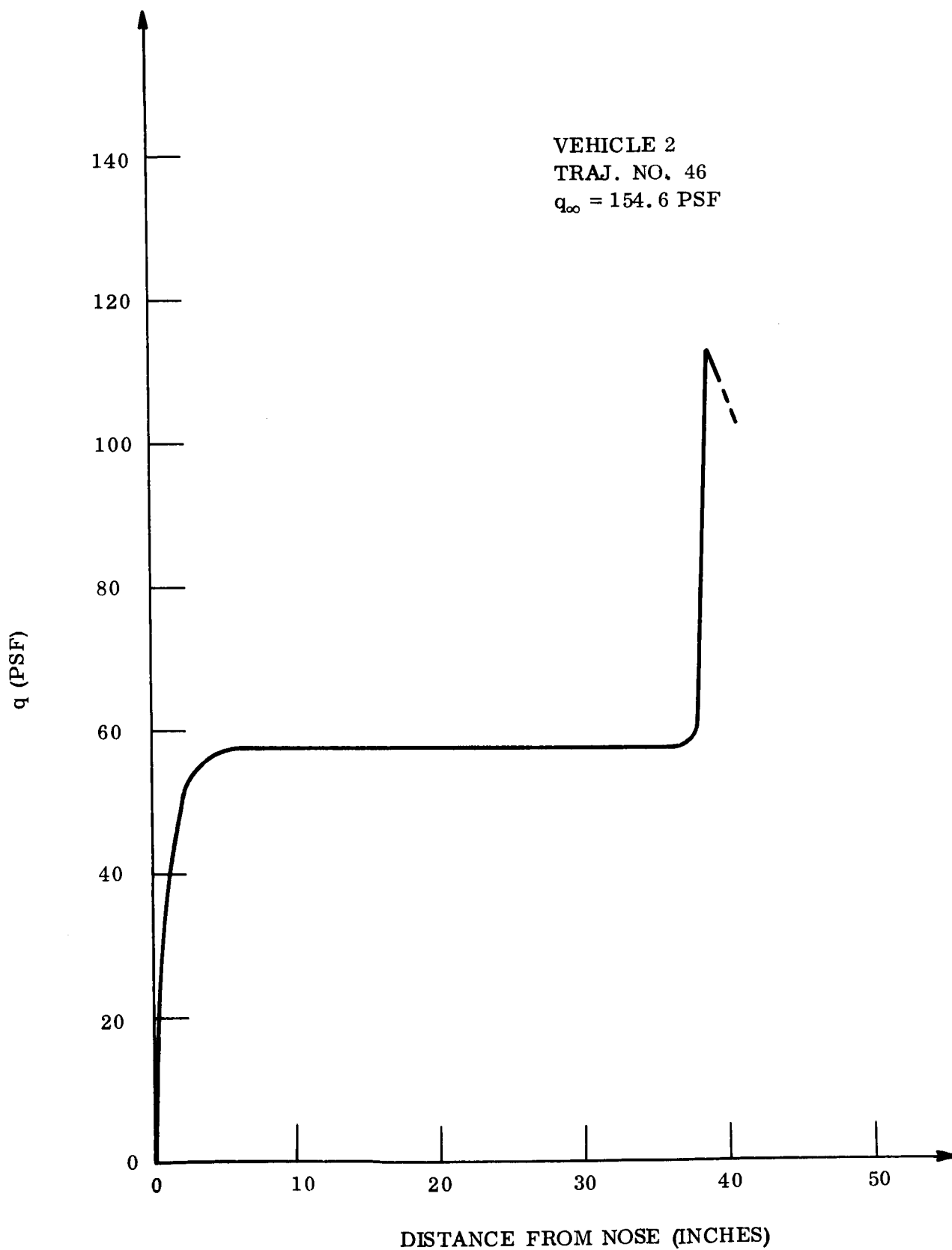
Figure 78.   Local Flow, Dynamic Pressure vs Distance Vehicle 2 Traj. 46

VEHICLE 2
TRAJ. No. 46
$\rho_\infty = .3865 \times 10^{-5}$
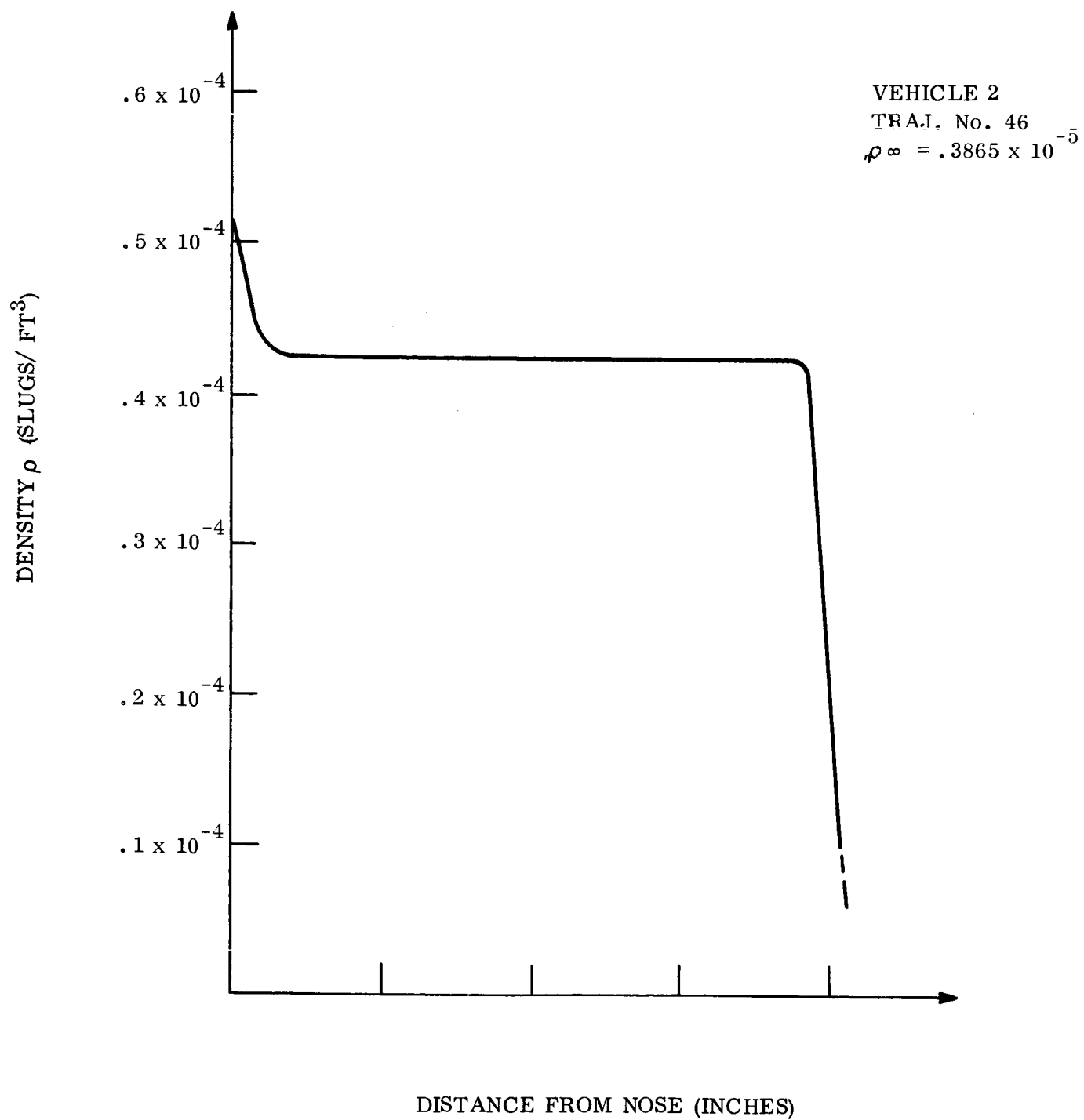
Figure 79. Local Flow, Density vs Distance Vehicle 2 Traj. 46

Y-axis: DENSITY ρ (SLUGS/ FT^3)
$.6 \times 10^{-4}$
$.5 \times 10^{-4}$
$.4 \times 10^{-4}$
$.3 \times 10^{-4}$
$.2 \times 10^{-4}$
$.1 \times 10^{-4}$

X-axis: DISTANCE FROM NOSE (INCHES)
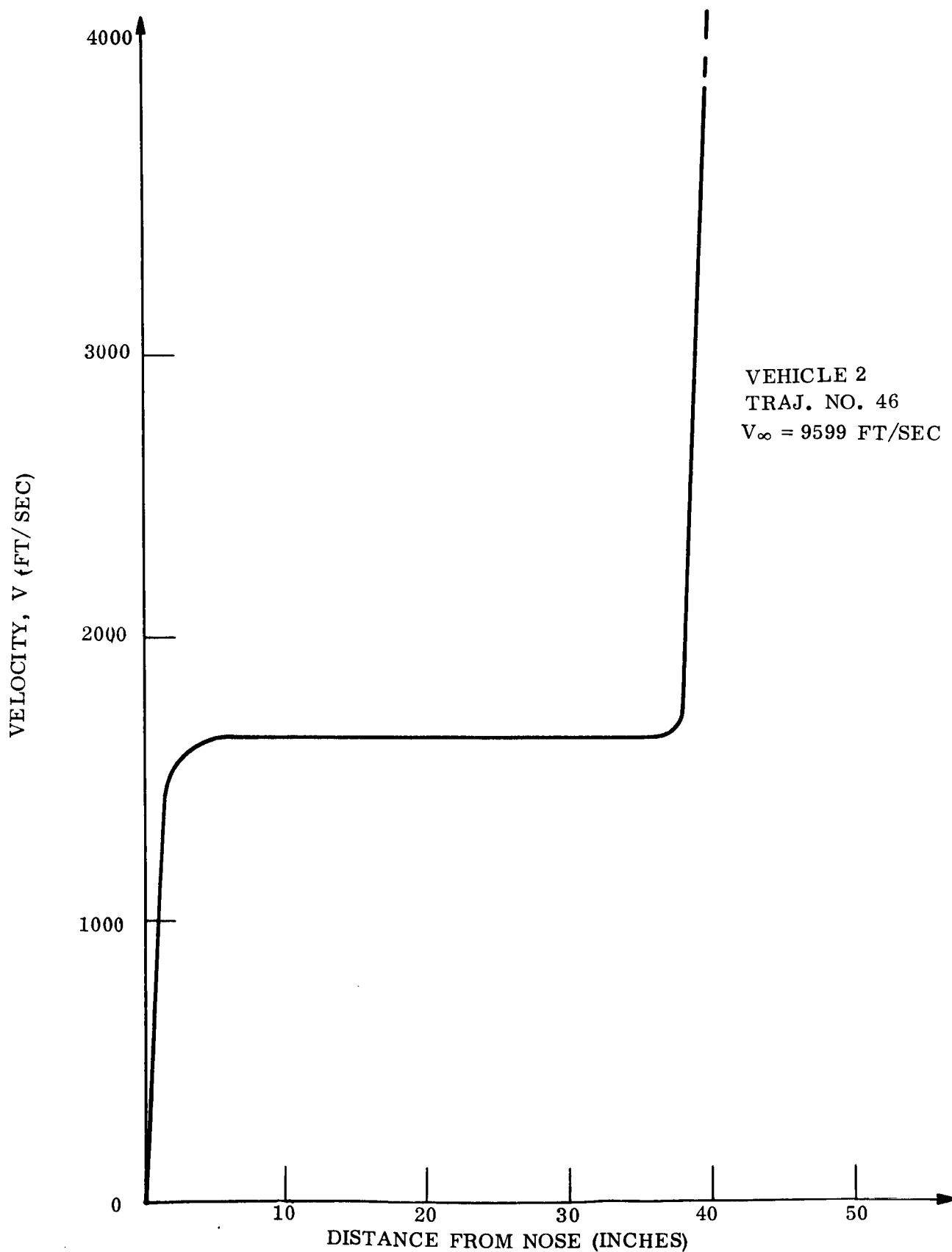
Figure 80. Local Flow, Velocity vs Distance Vehicle 2 Traj. 46
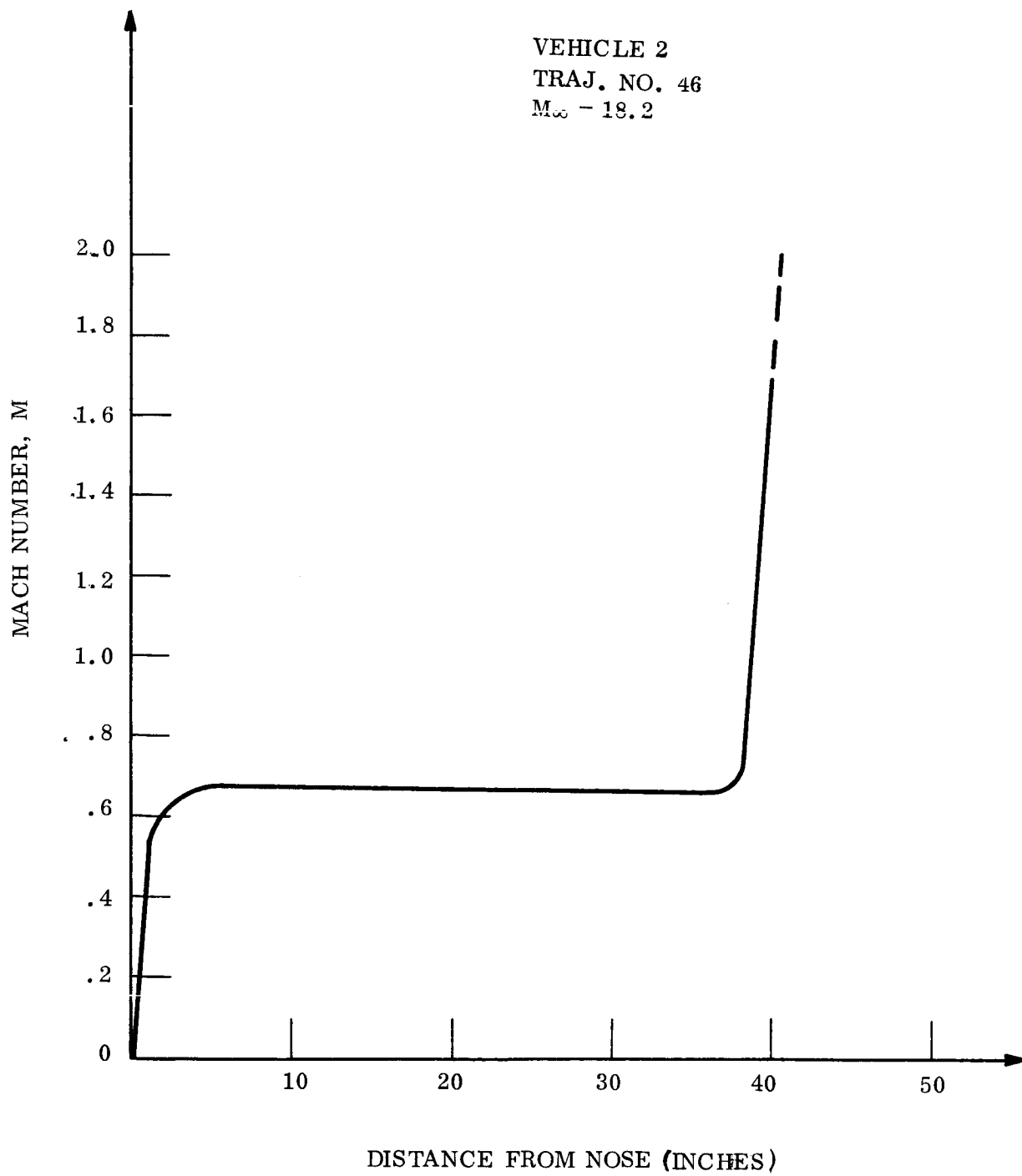
Figure 81. Local Flow, Mach. No. vs Distance Vehicle 2 Traj. 46
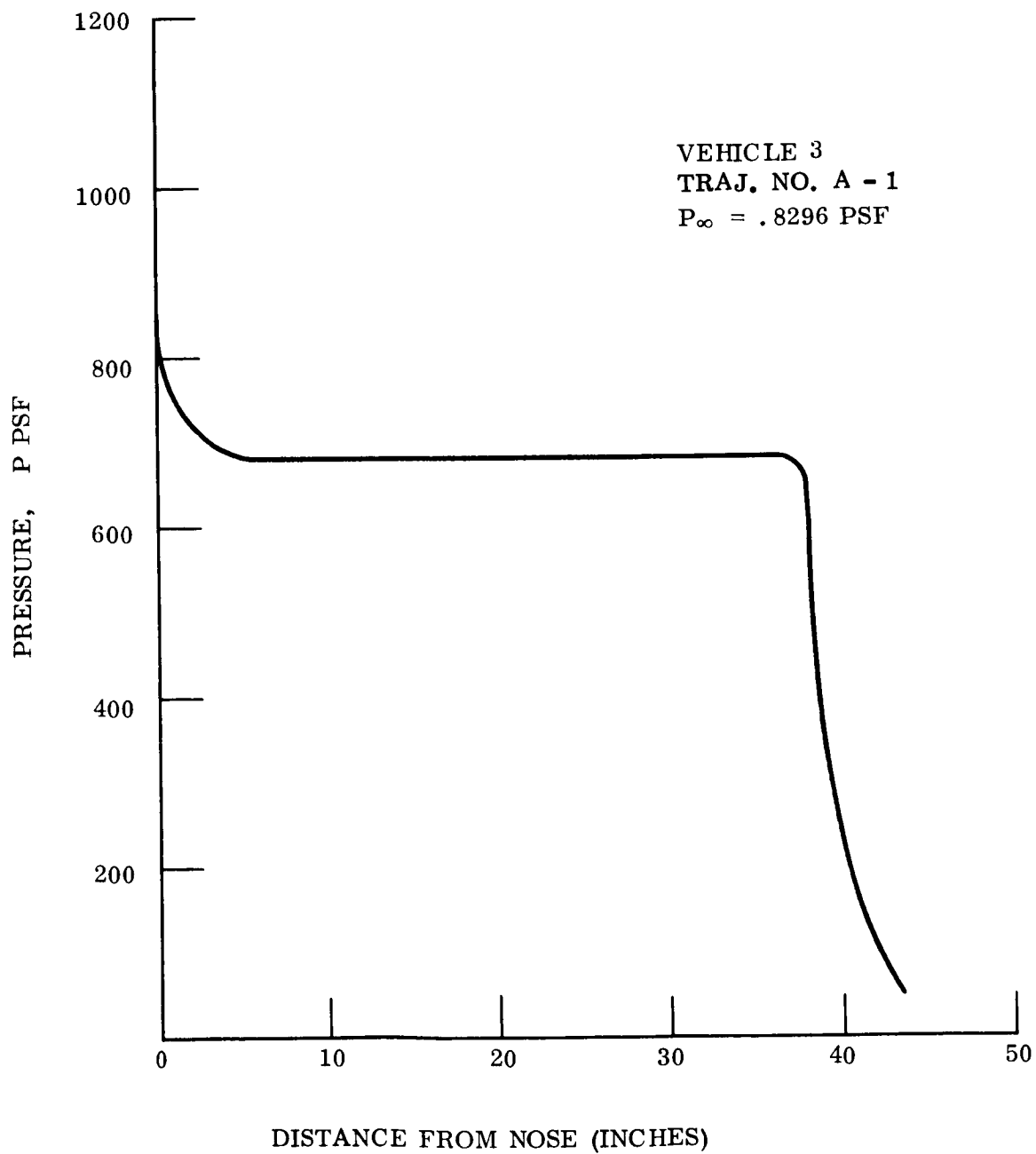
Figure 82. Local Flow, Pressure vs Distance Vehicle 3 Traj. A-1

VEHICLE 3
TRAJ. NO. A-1
$q_\infty = 446.9$ PSF
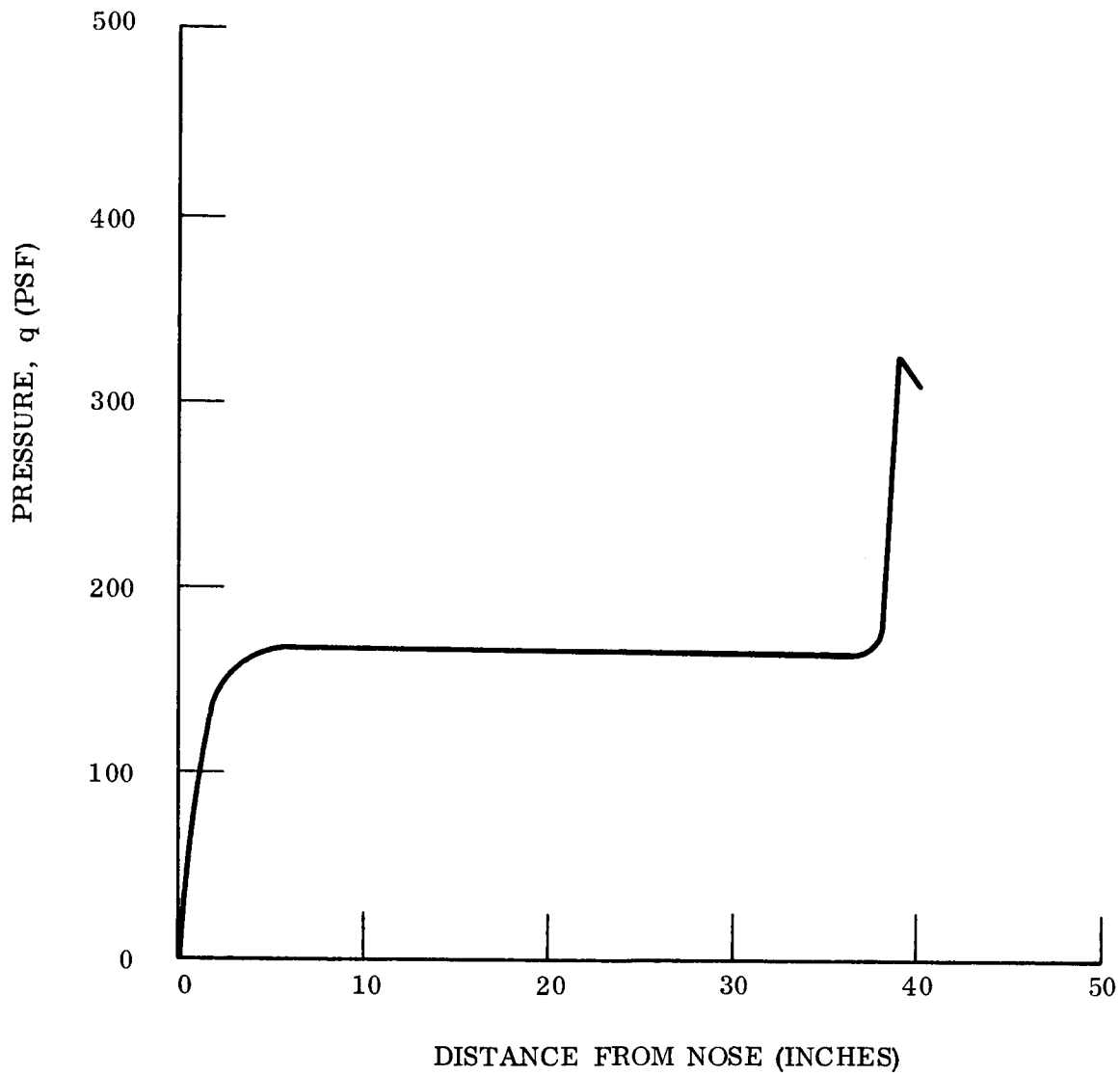
Figure 83. Local Flow, Dynamic Pressure vs Distance Vehicle 3 Traj. A-1

VEHICLE 3
TRAJ. NO. A 1
$\rho = x = 10^4 = 4,0794$ SLUGS/FT^3
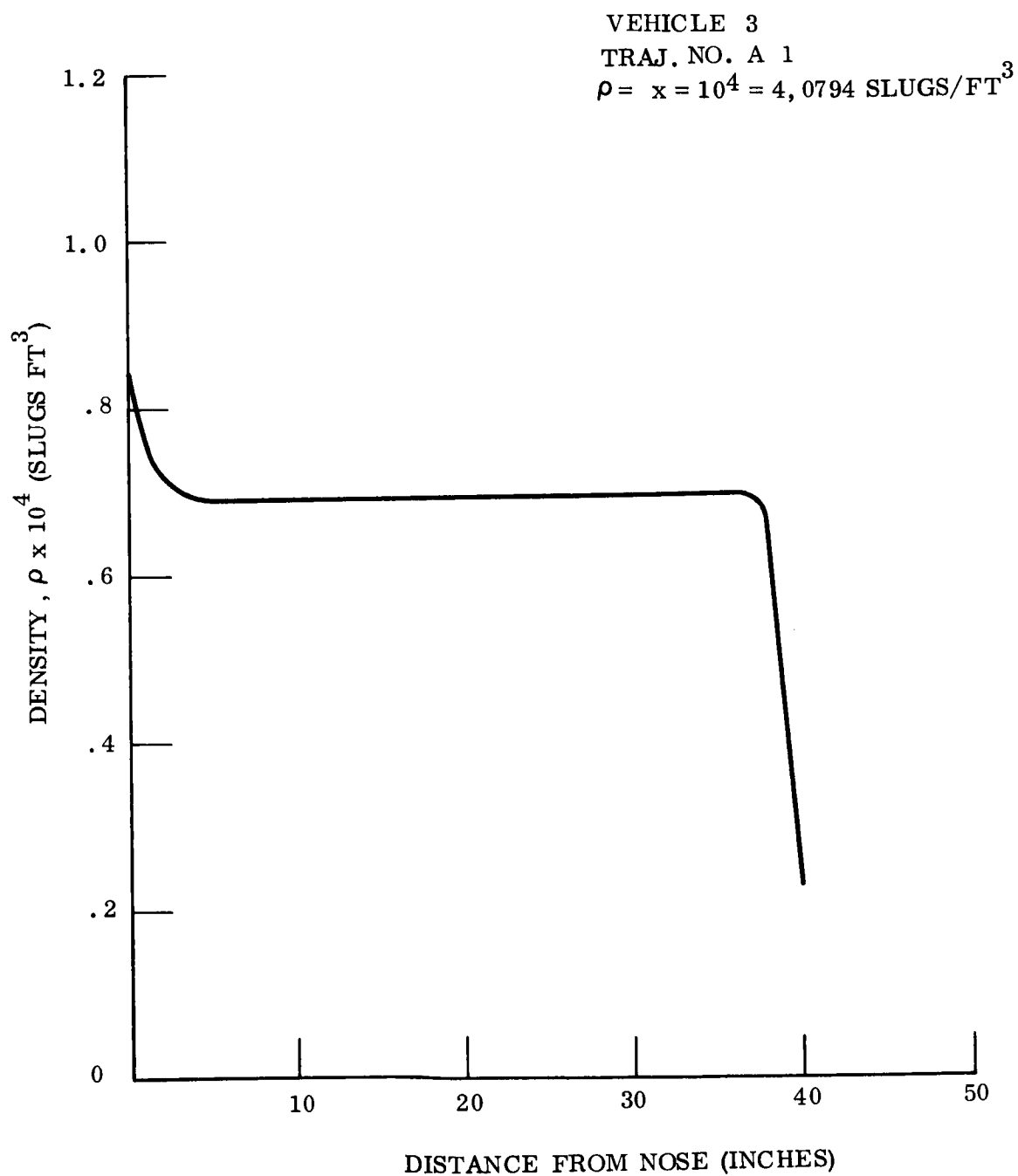
Figure 84.   Local Flow, Density Pressure vs Distance Vehicle 3 Traj. A-1
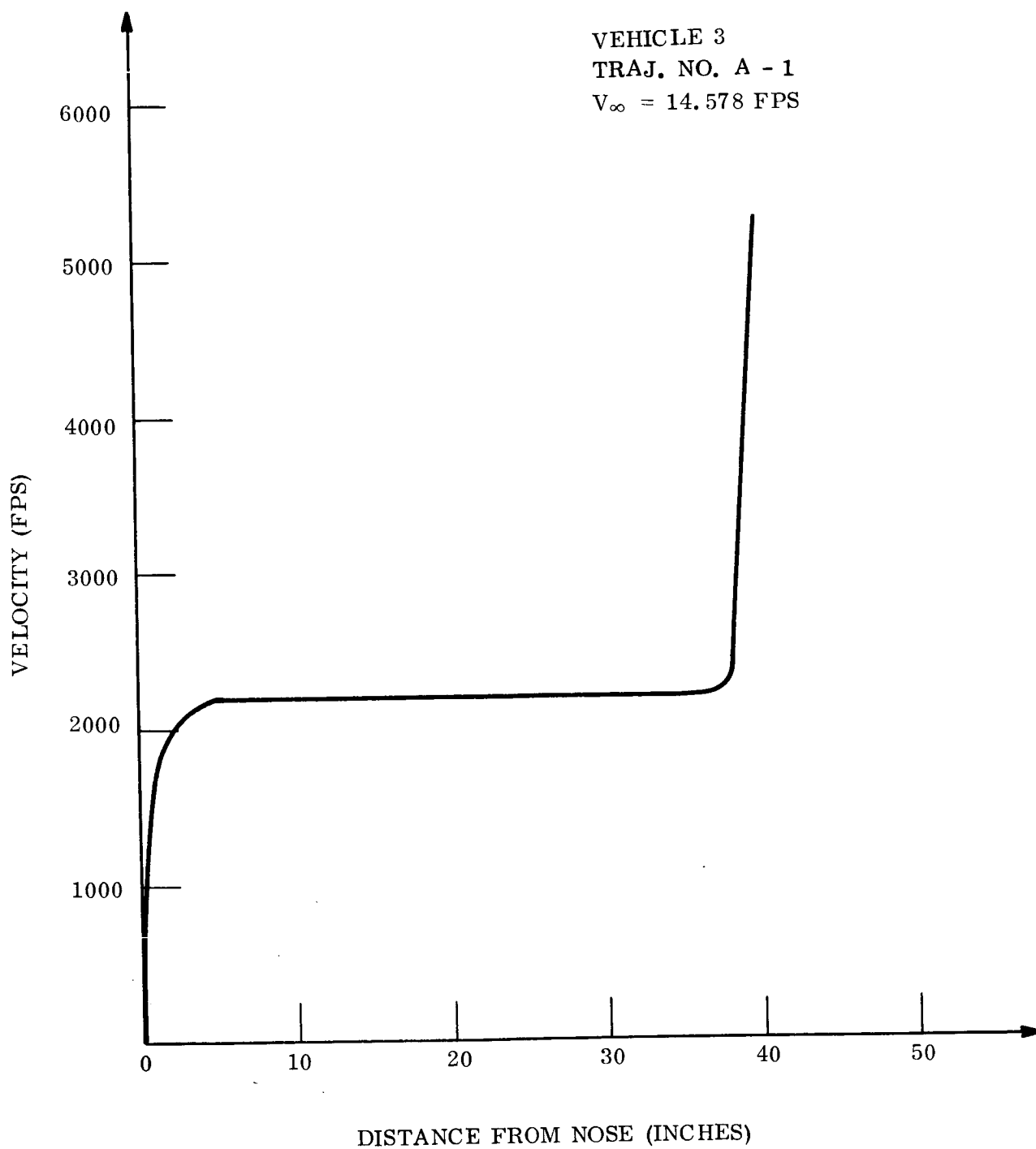
Figure 85. Local Flow, Velocity Pressure vs Distance Vehicle 3 Traj. A-1
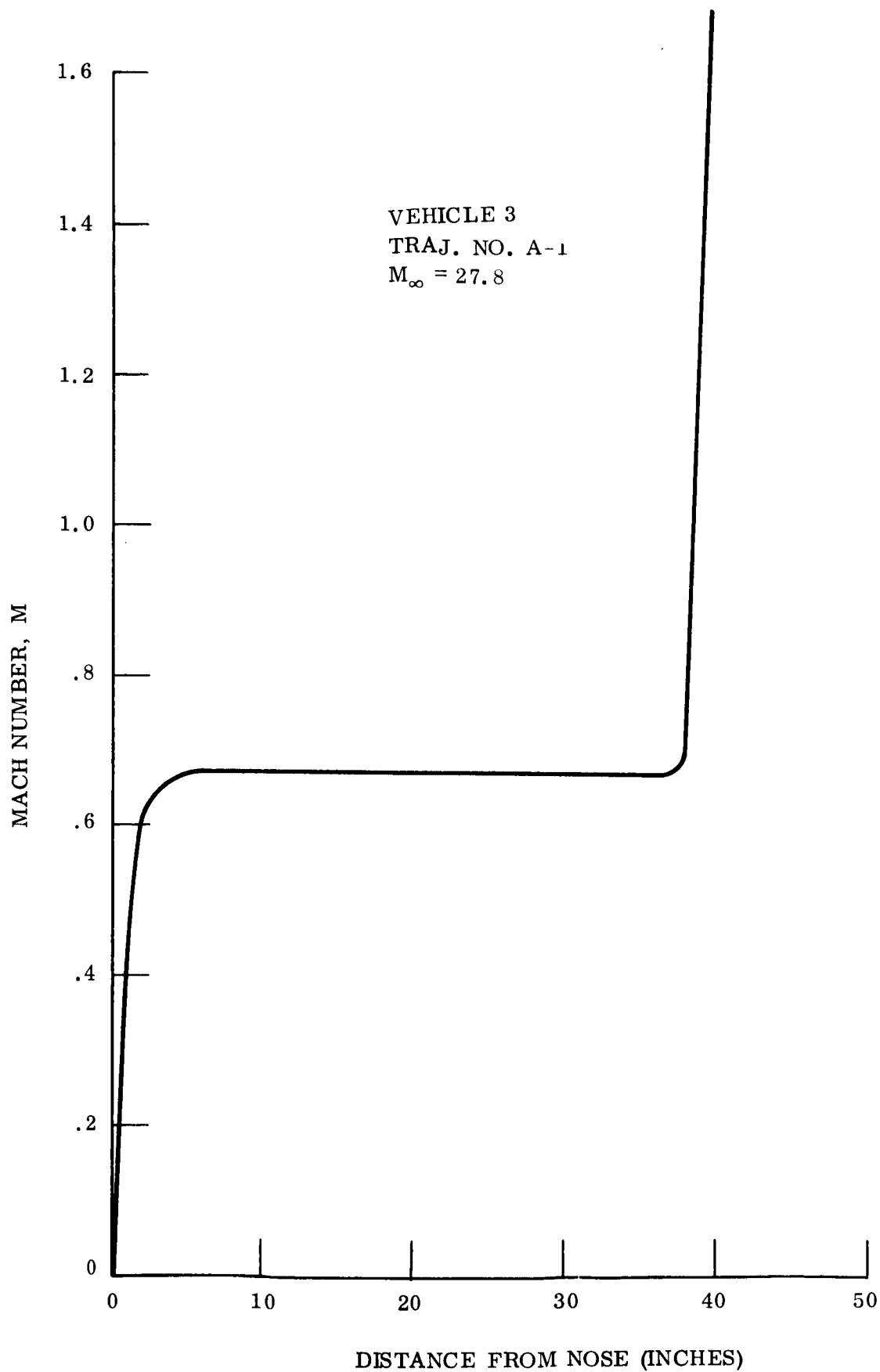
Figure 86.   Local Flow, Mach No. Pressure vs Distance Vehicle 3 Traj. A-1

VEHICLE 6
TRAJ. NO. 46
$P_\infty = .6823$ PSF
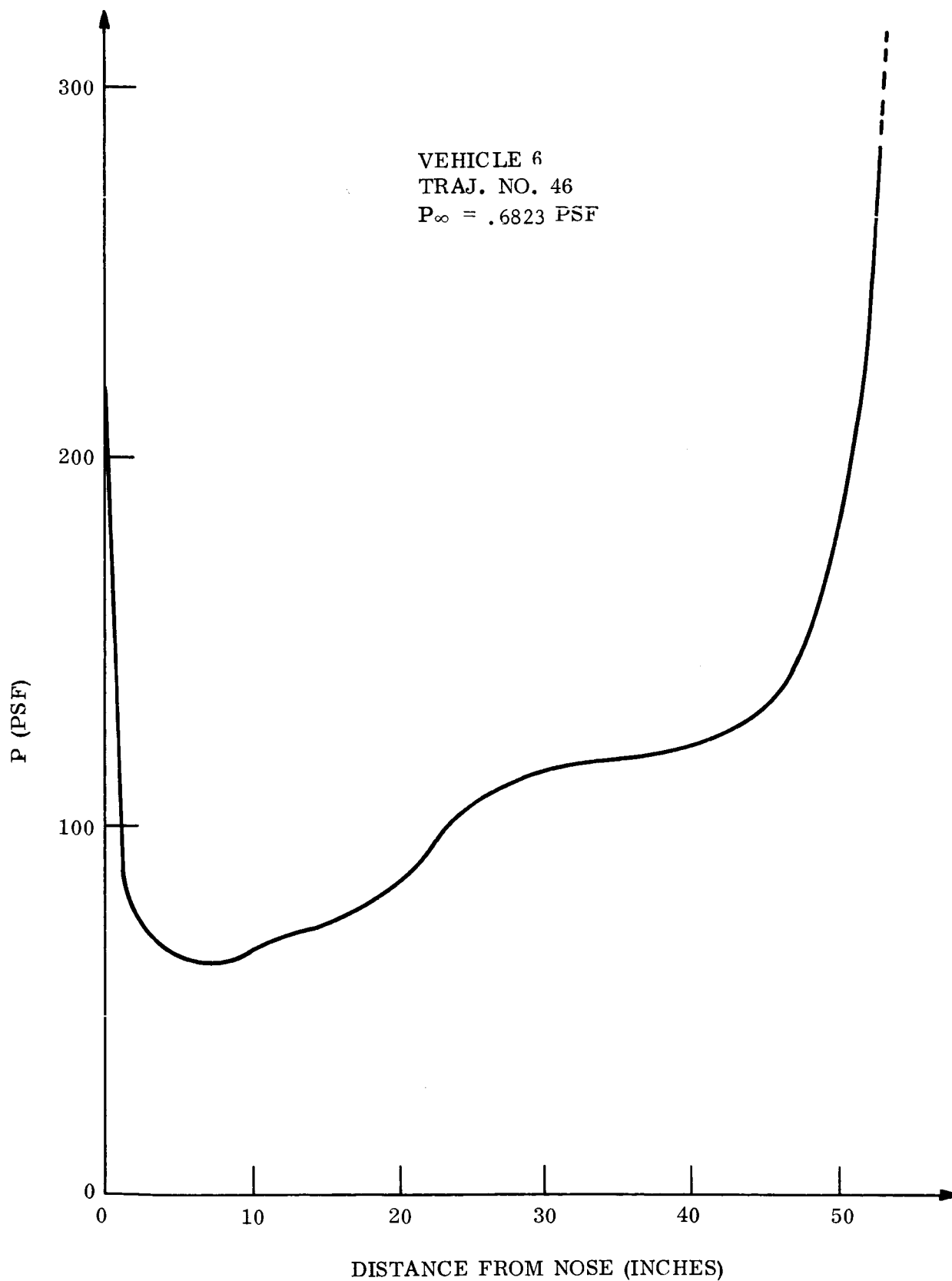
Figure 87. Local Flow, Pressure Pressure vs Distance Vehicle 6 Traj. 46

VEHICLE 6
TRAJ. NO. 46
$q_\infty = 154.6$ PSF
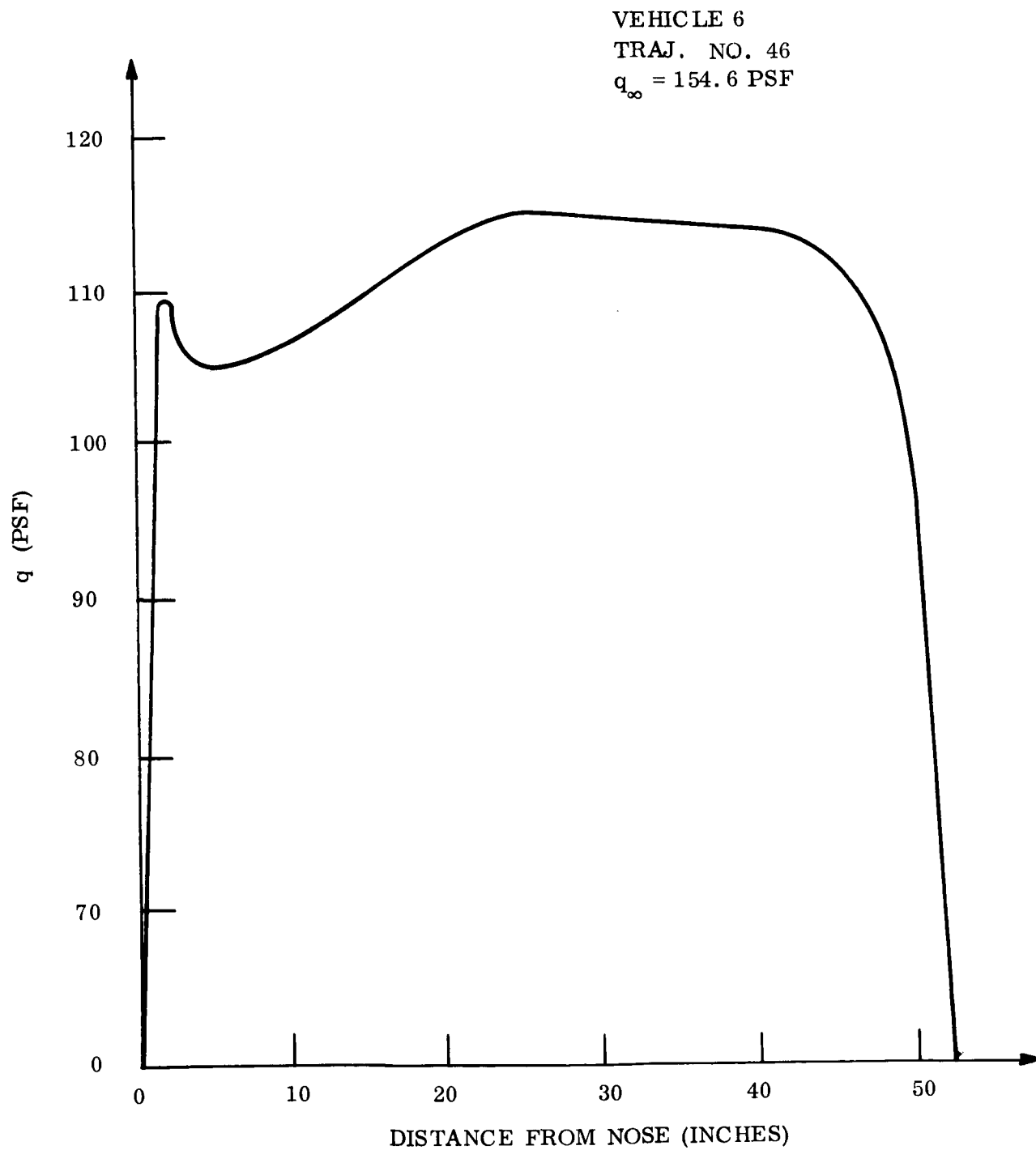
Figure 88.   Local Flow, Dynamic Pressure vs Distance Vehicle 6 Traj. 46
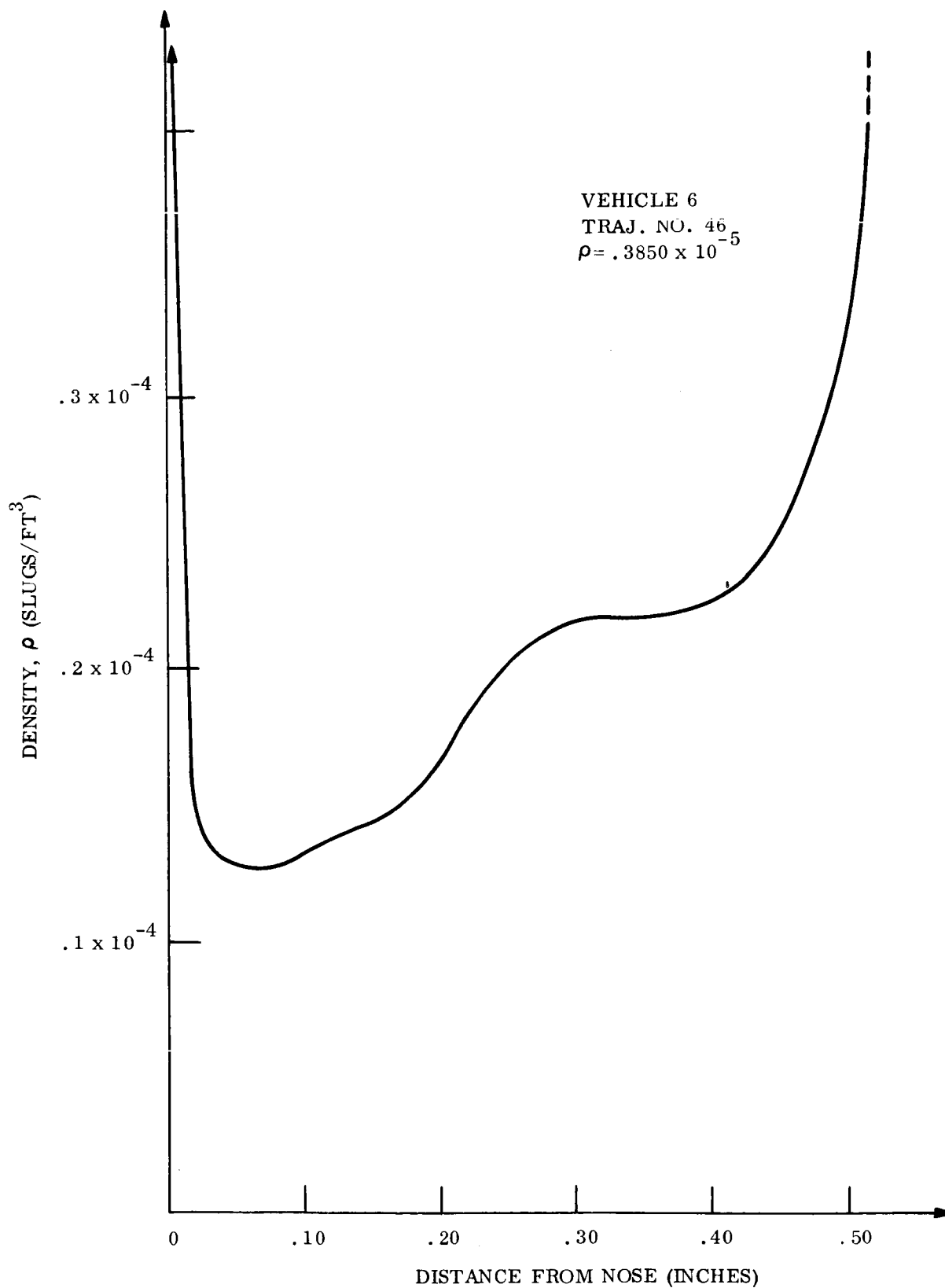
Figure 89. Local Flow, Dynamic Pressure vs Distance Vehicle 6 Traj. 46

VEHICLE 6
TRAJ. NO. 46
$V_e = 9599$ FT/SEC
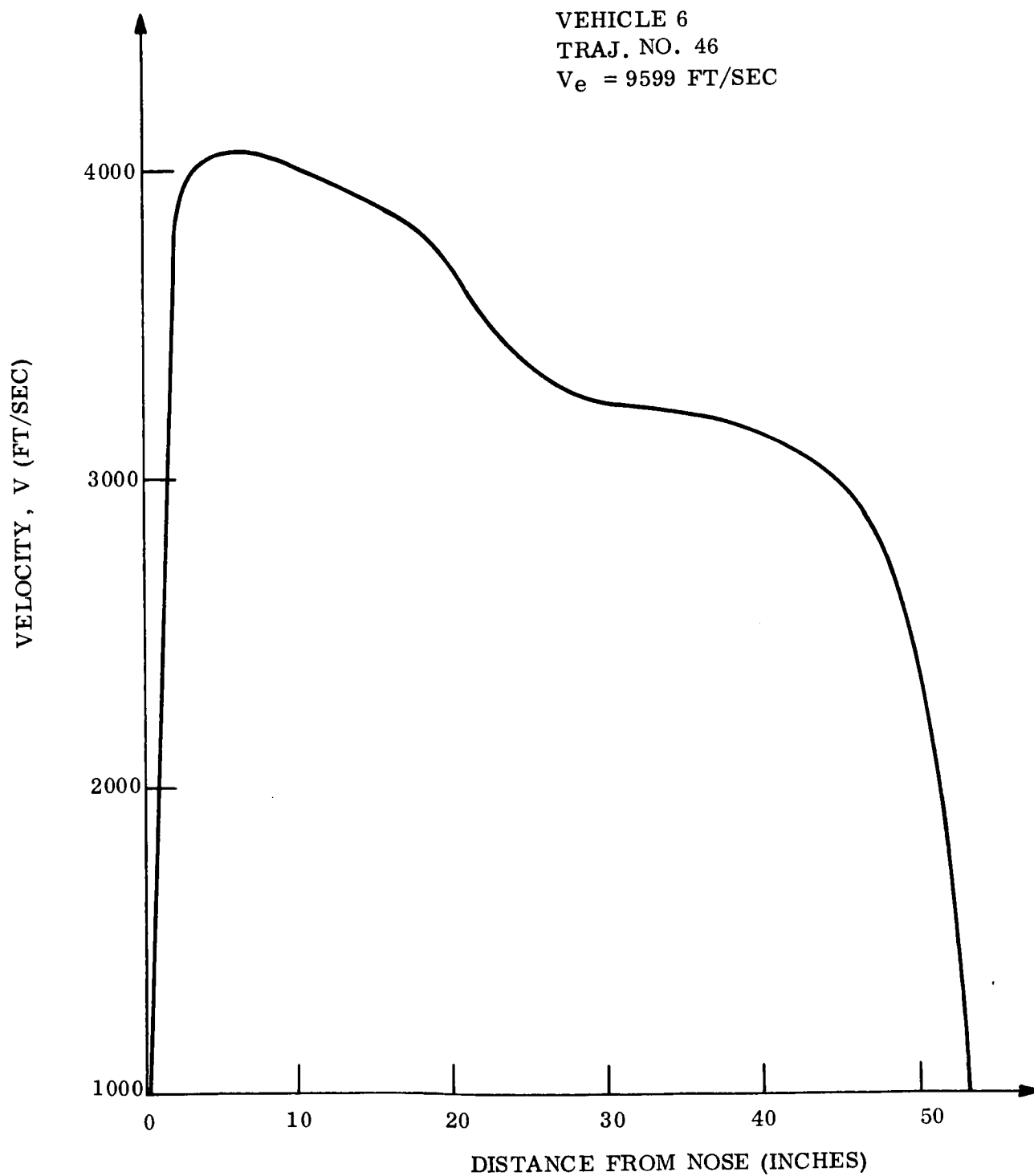
Figure 90. Local Flow, Velocity Pressure vs Distance Vehicle 6 Traj. 46

184

VEHICLE 6
TRAJ. NO. 46

$M_\infty = 18.2$

M = 0
@ X = 0

MACH NUMBER - M

DISTANCE FROM NOSE - INCHES
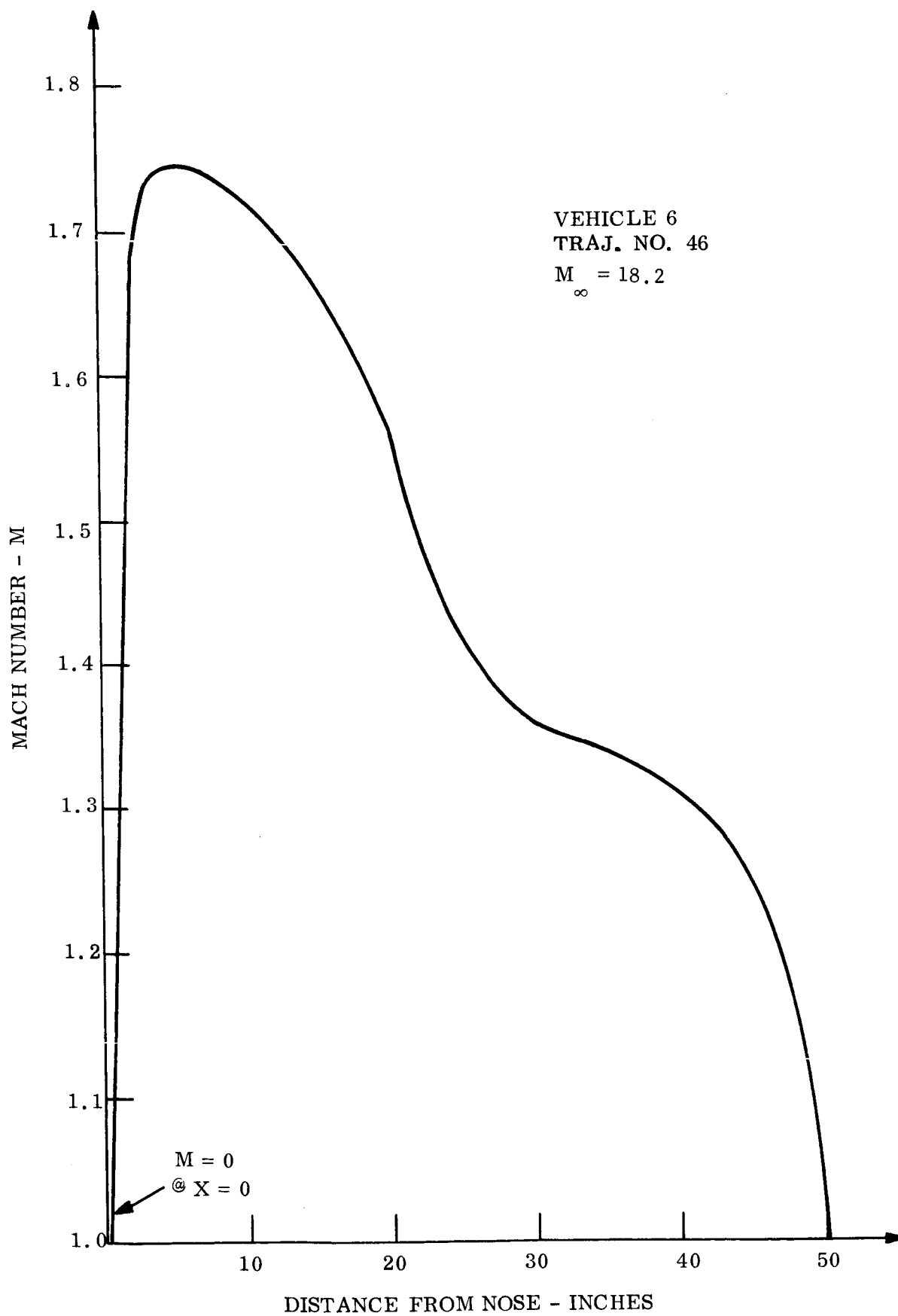
Figure 91. Local Flow, Mach No. Pressure vs Distance Vehicle 6 Traj. 46

R (INCHES)

ZEROTH HARMONIC
(ACCORDIAN)
FREQUENCY = 57.9 CPS

Z (INCHES)
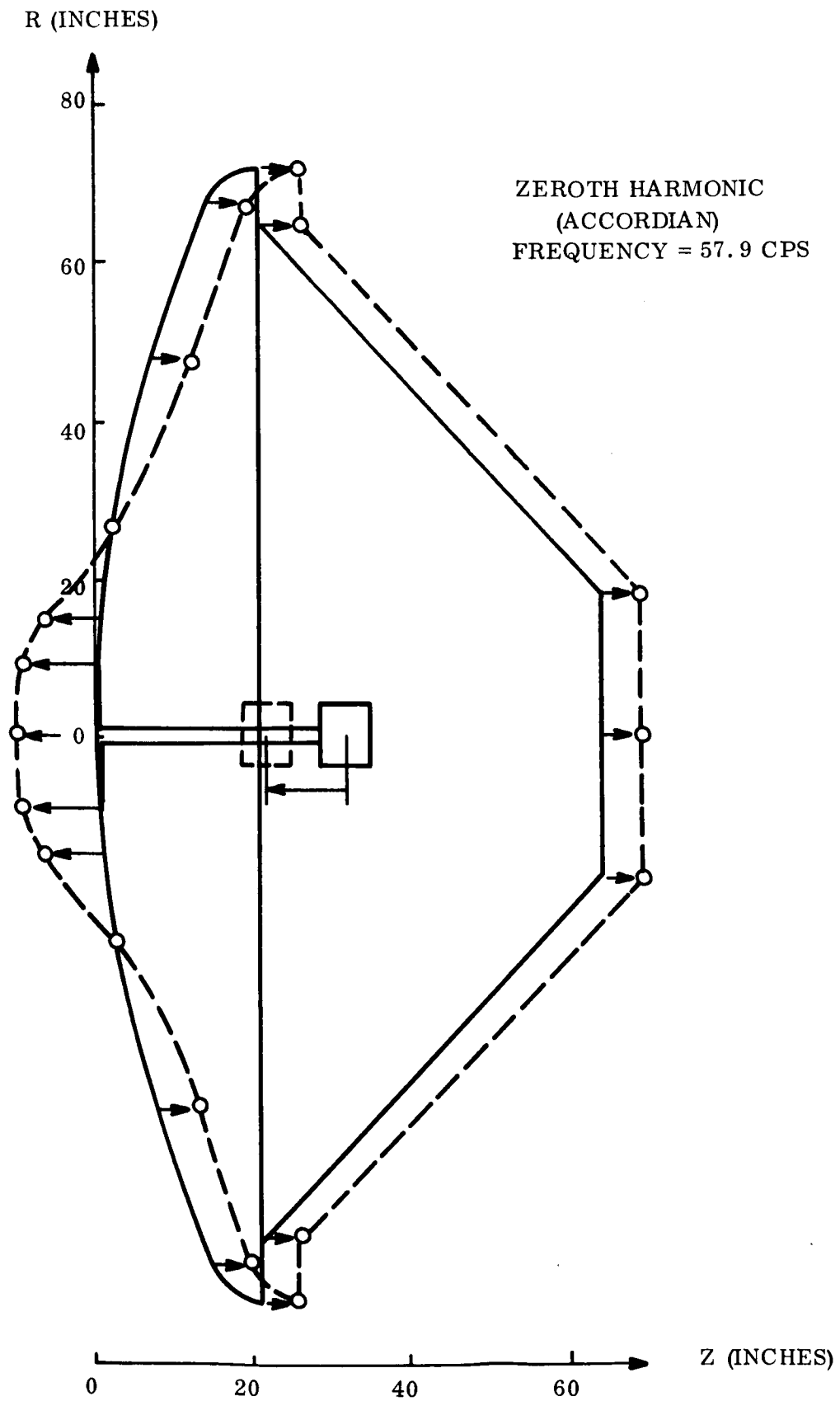
Figure 92. Mode Shape, Sphere Cap – Cone Frustrum Afterbody, Aluminum Monocoque at 100°F

186
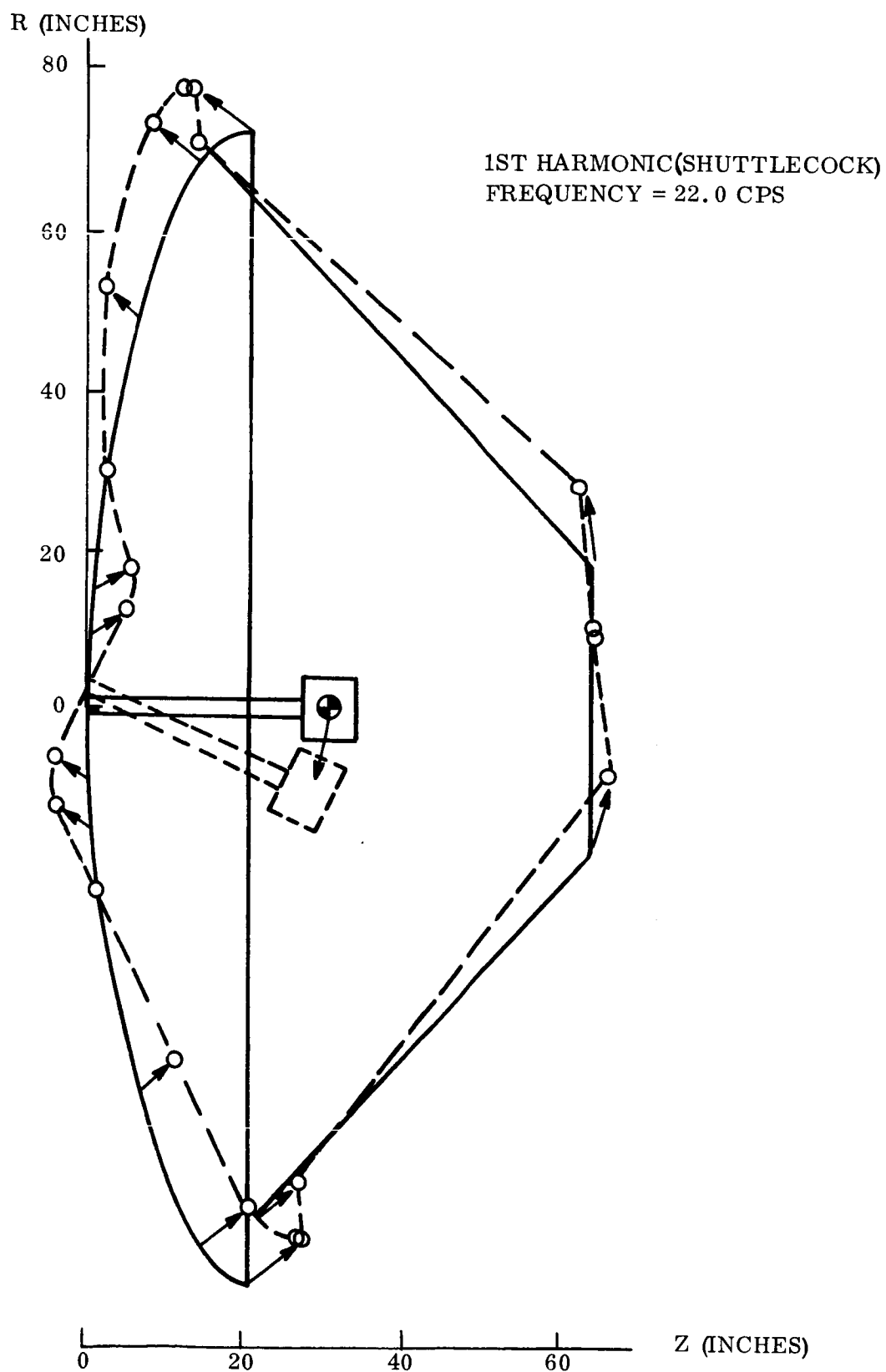
Figure 93. Mode Shape, Sphere Cap – Cone Frustrum Afterbody, Aluminum Monocoque at 100°F

ZEROTH HARMONIC
(ACCORDIAN)
FREQUENCY = 74.9 CPS

Figure 94. Mode Shape, 60° Sphere Cone, 12' Diameter, Aluminum Honeycomb at 100^oF, $M/C_D A$ = .20, No Spin

1ST HARMONIC
(SHUTTLECOCK)
FREQUENCY = 39.7 CPS
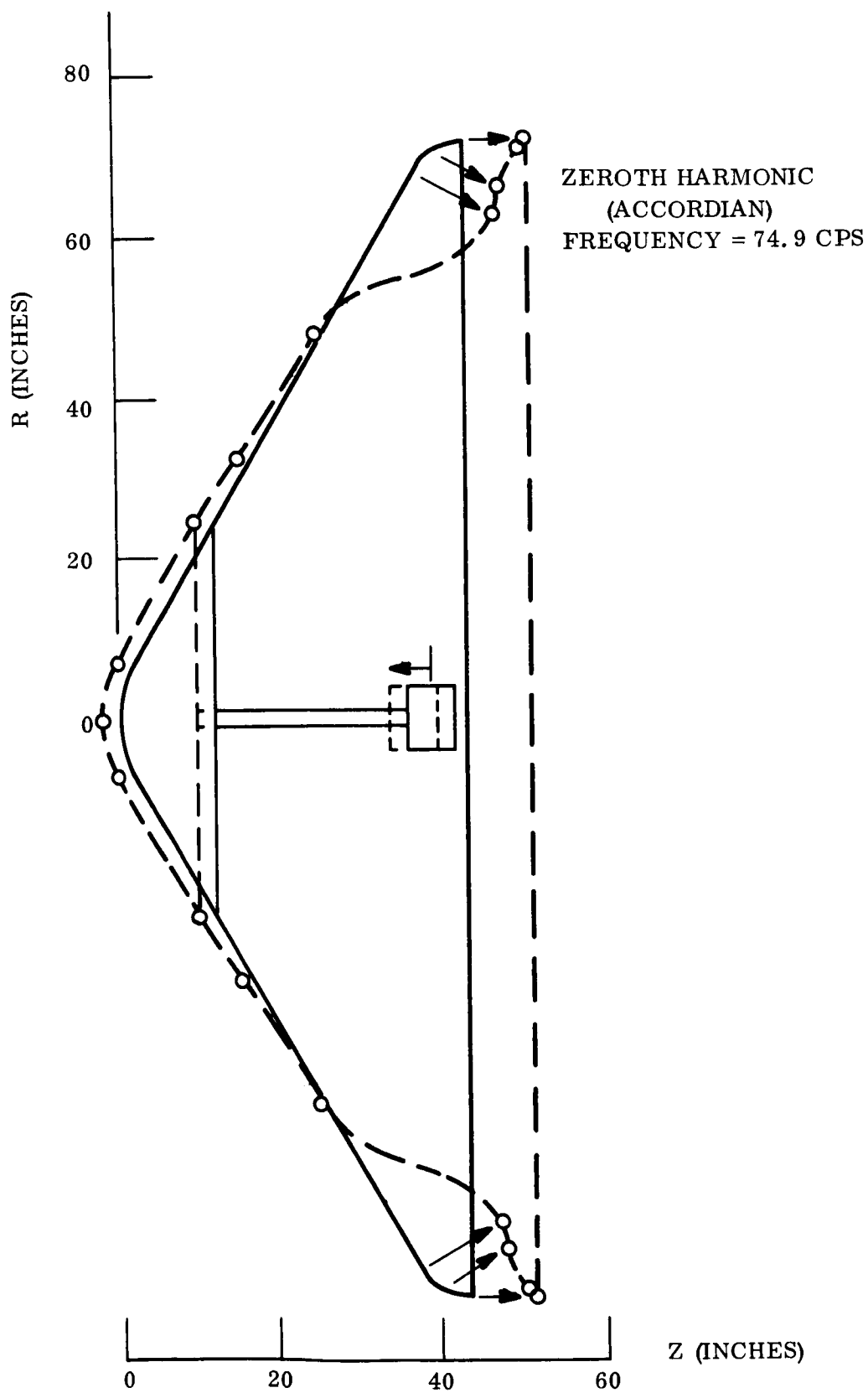
Figure 95.   Mode Shape, 60° Sphere Cone, 12' Diameter, Aluminum Honeycomb at 100°F, M/C_DA = .20, No Spin

1ST HARMONIC (SHUTTLECOCK)
FREQUENCY = 39.8 CPS
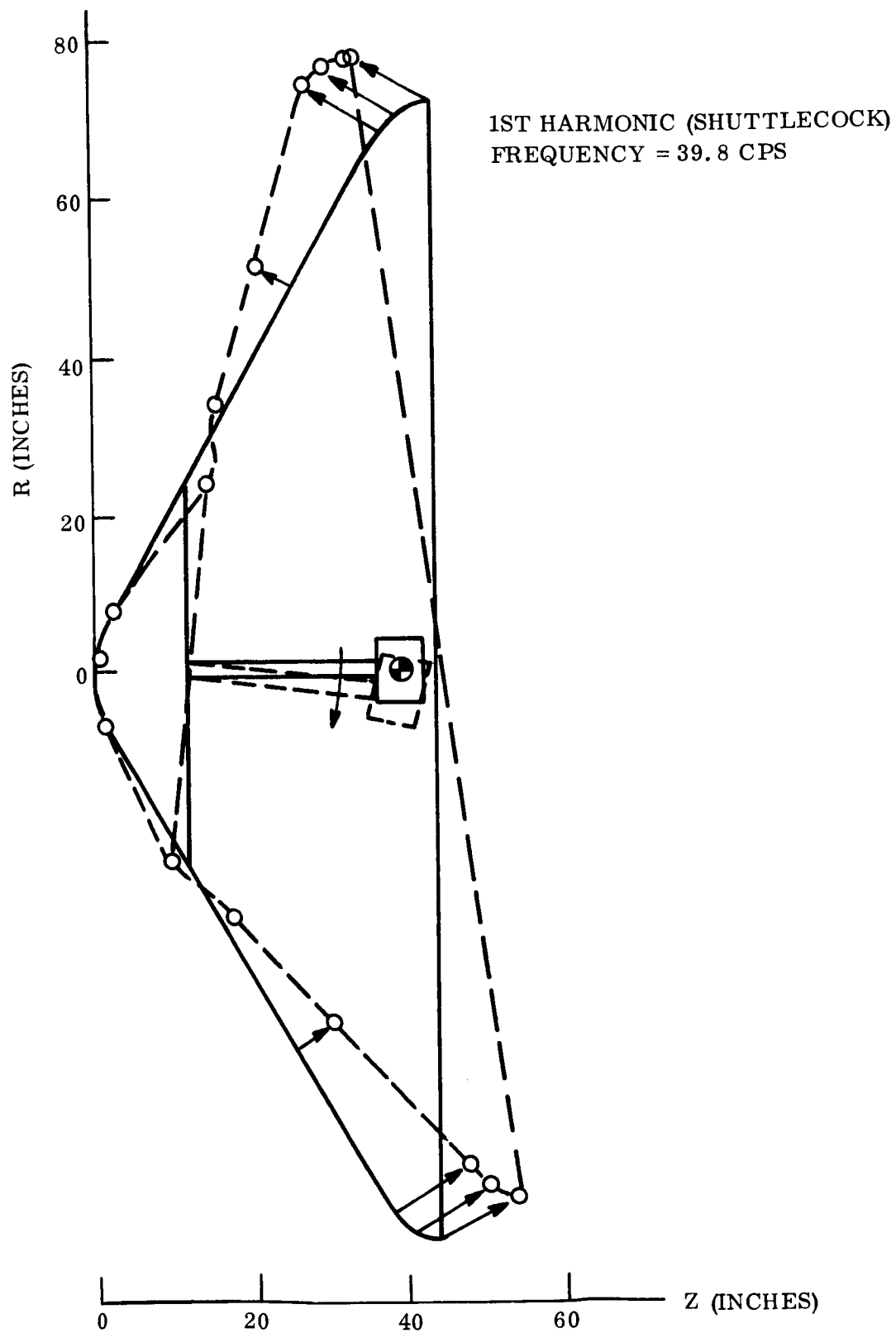
Figure 96. Mode Shape, 60° Sphere Cone, 12' Diameter, Aluminum Honeycomb at 100°F, $M/C_D A$ = .20, Spin Case
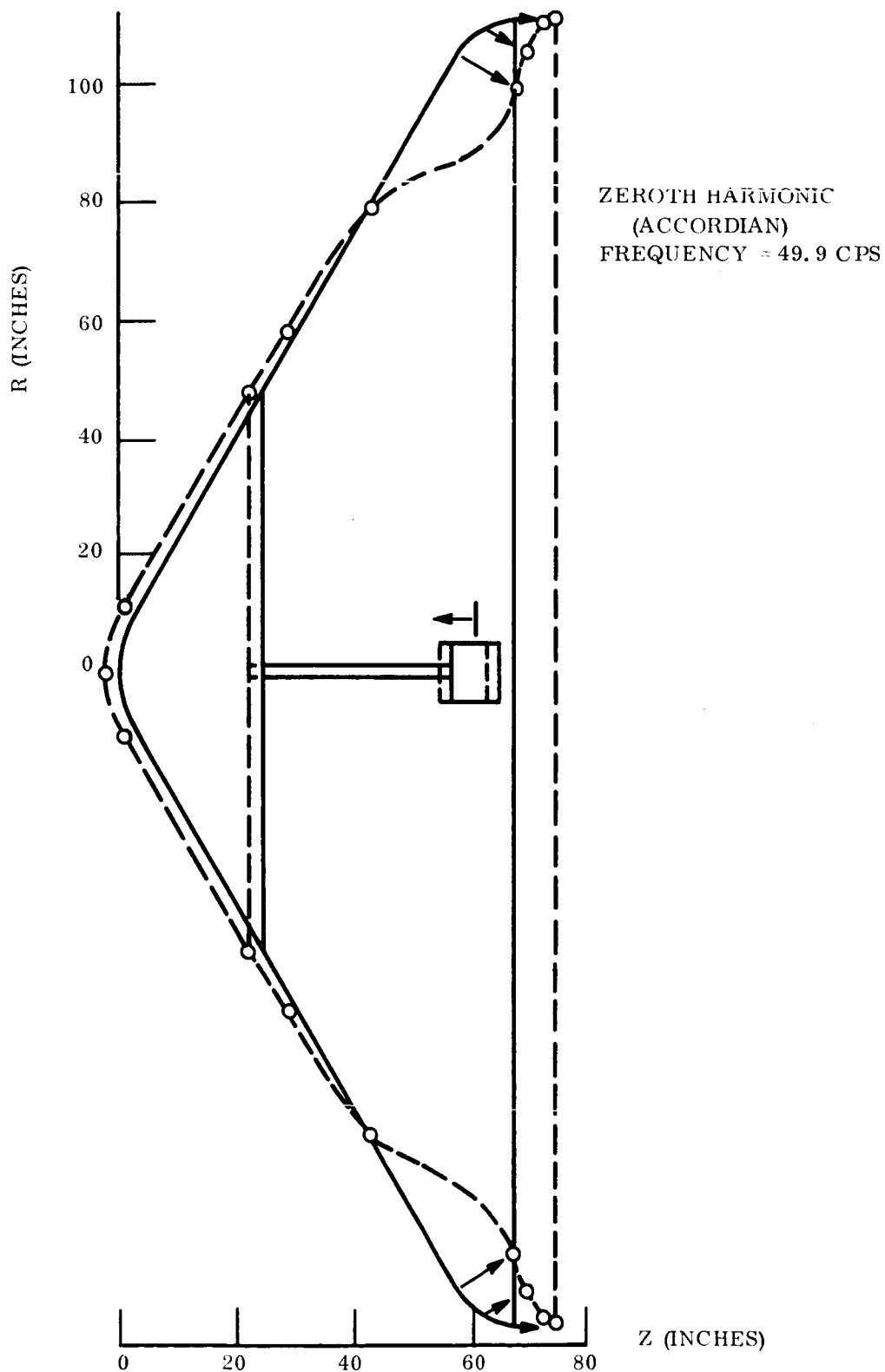
Figure 97. Mode Shape, 60° Sphere Cone, 18.5' Diameter, Aluminum Honeycomb at 100°F, $M/C_DA = .25$

1ST HARMONIC (SHUTTLECOCK)
FREQUENCY = 31.8 CPS
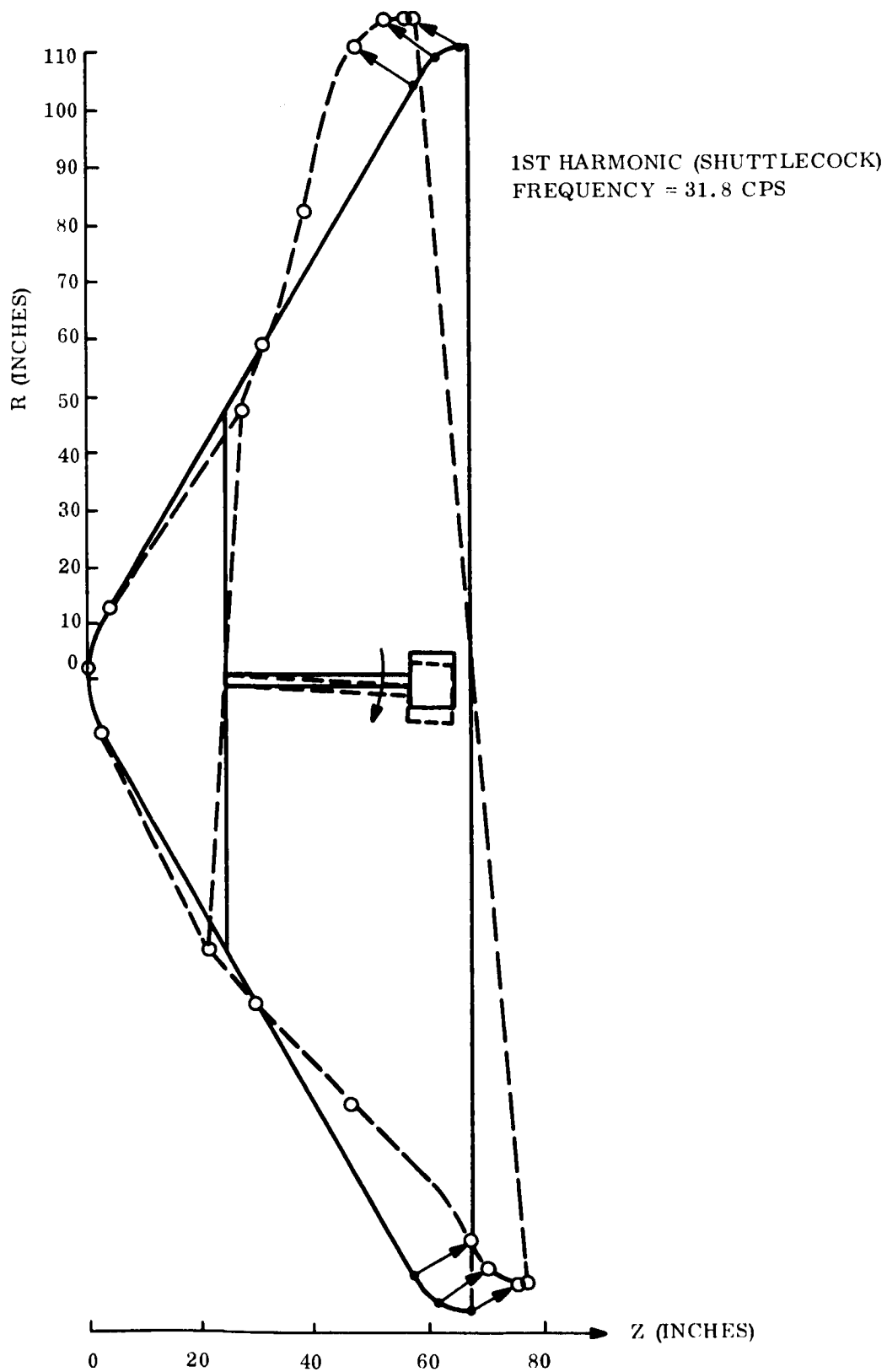
Figure 98. Mode Shape, 60° Sphere Cone, 18.5' Diameter, Aluminum Honeycomb at 100°F, $M/C_DA = .25$

ZEROTH HARMONIC
(ACCORDIAN)
FREQUENCY = 73.5 CPS

R (INCHES)

Z (INCHES)
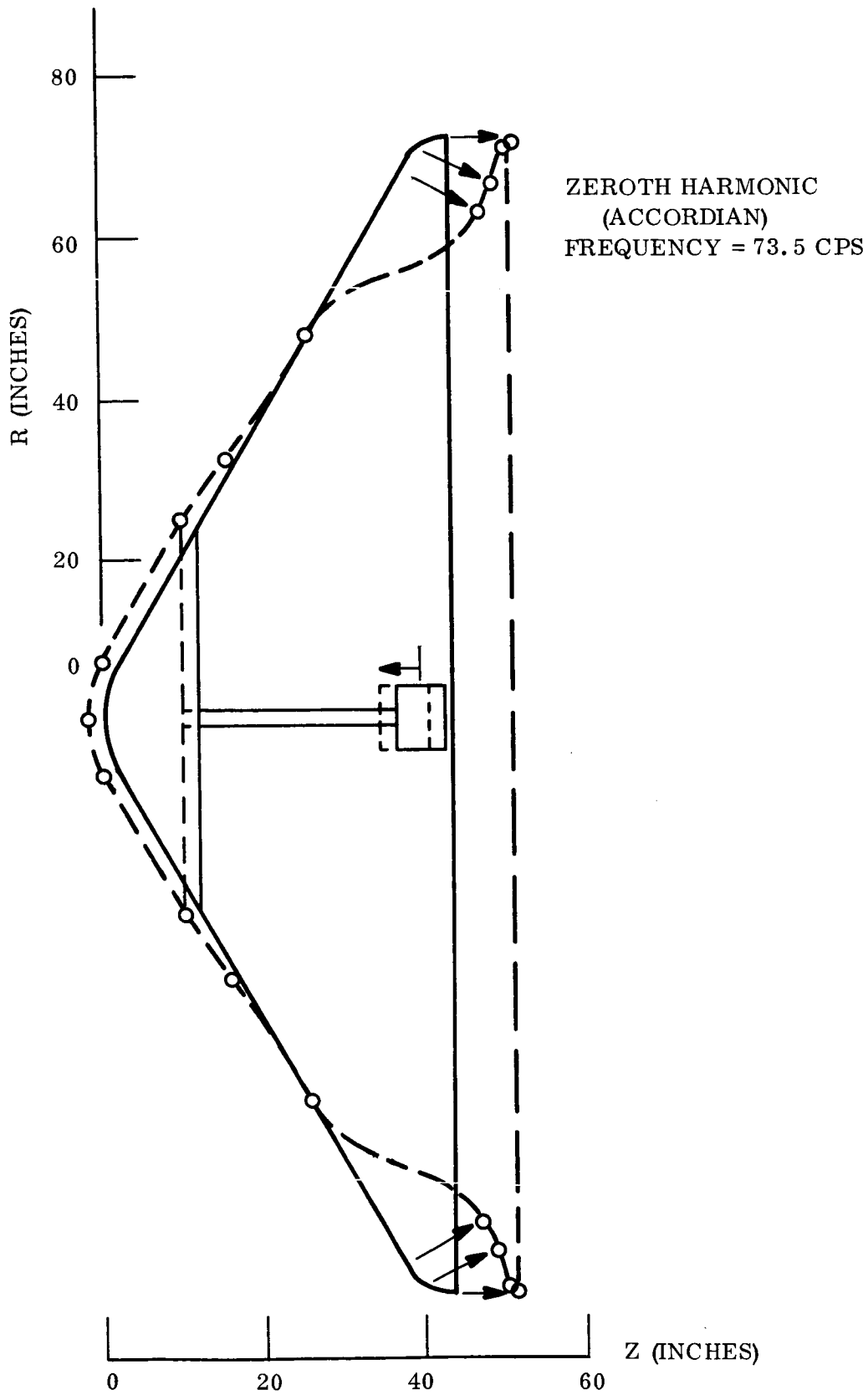
Figure 99. Mode Shape, 60° Sphere Cone, 12' Diameter, Aluminum Honeycomb
at 100°F, $M/C_A = .30$

1ST HARMONIC
(SHUTTLECOCK)
FREQUENCY = 37.7 CPS
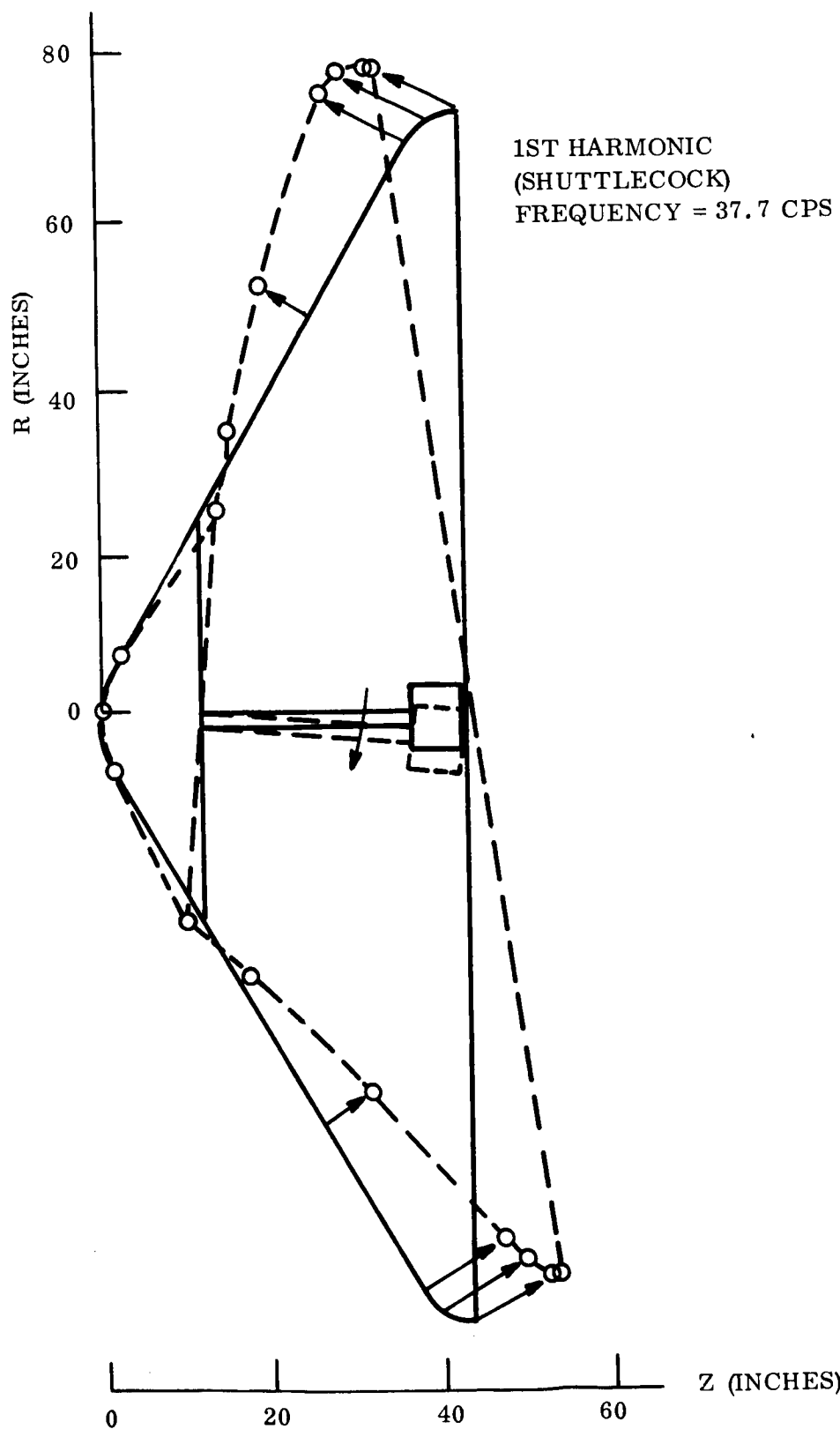
Figure 100. Mode Shape, 60° Sphere Cone, 12' Diameter, Aluminum Honeycomb at 100°F, $M/C_A = 30$

ZERO HARMONIC
(ACCORDIAN)
FREQUENCY = 60.8 CPS
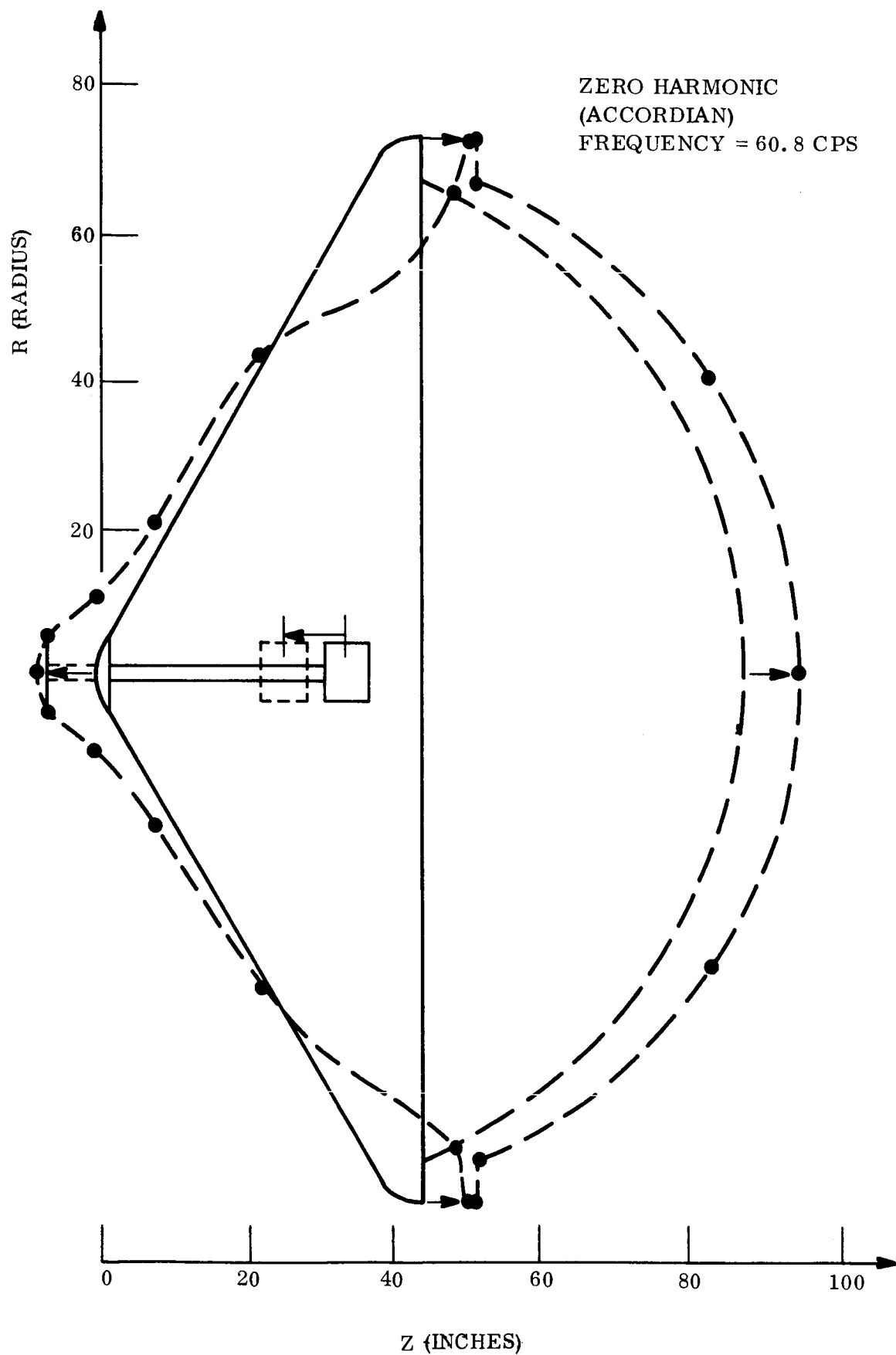
Figure 101. Mode Shape, 60° Sphere Cone - Sphere Cap Afterbody, Aluminum Honeycomb at 100°F, $M/C_D A$ = .20

195
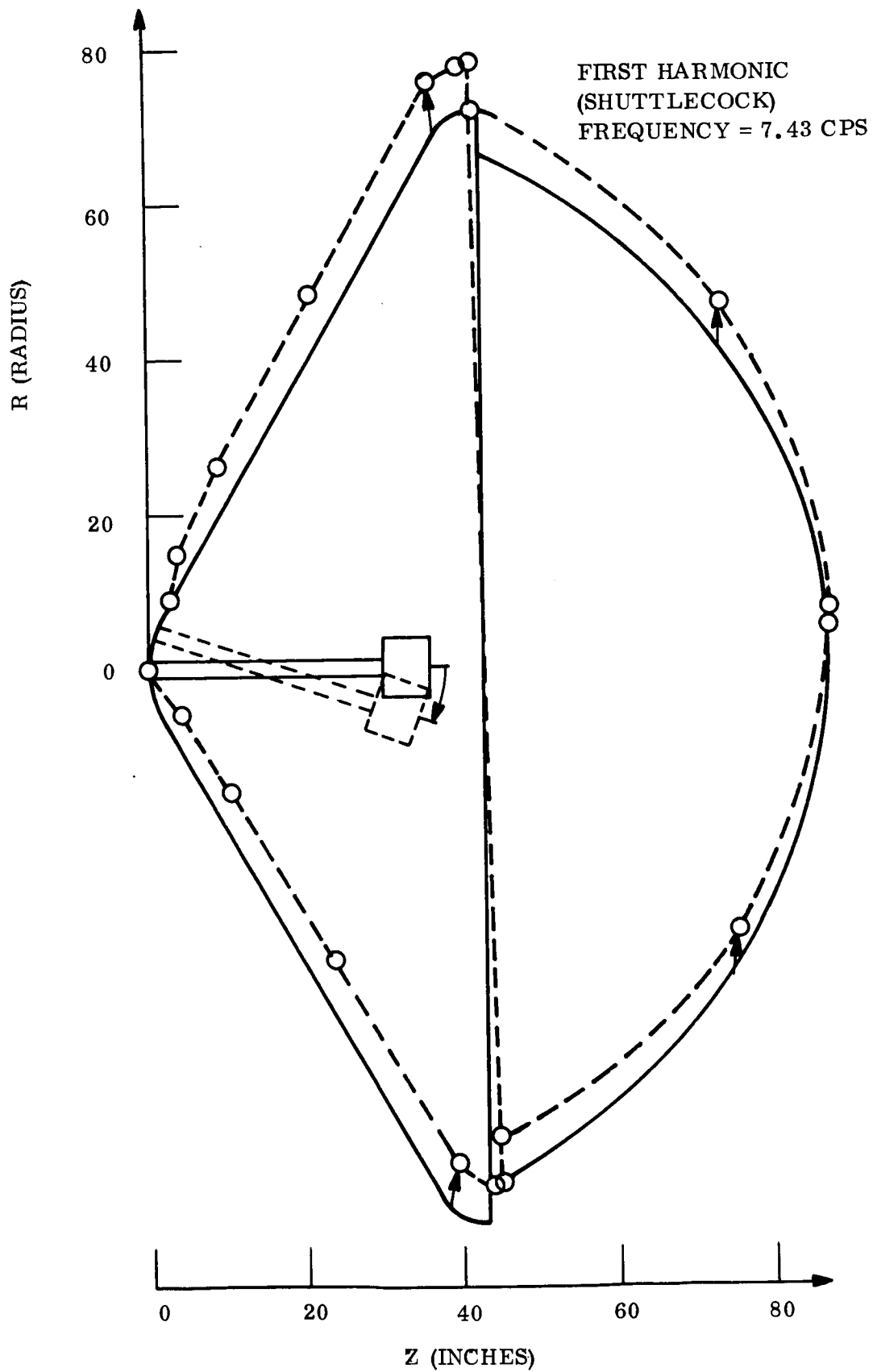
Figure 102. Mode Shape, 60° Sphere Cone – Sphere Cap Afterbody, Aluminum Honeycomb at 100°F, $M/C_D A = .20$
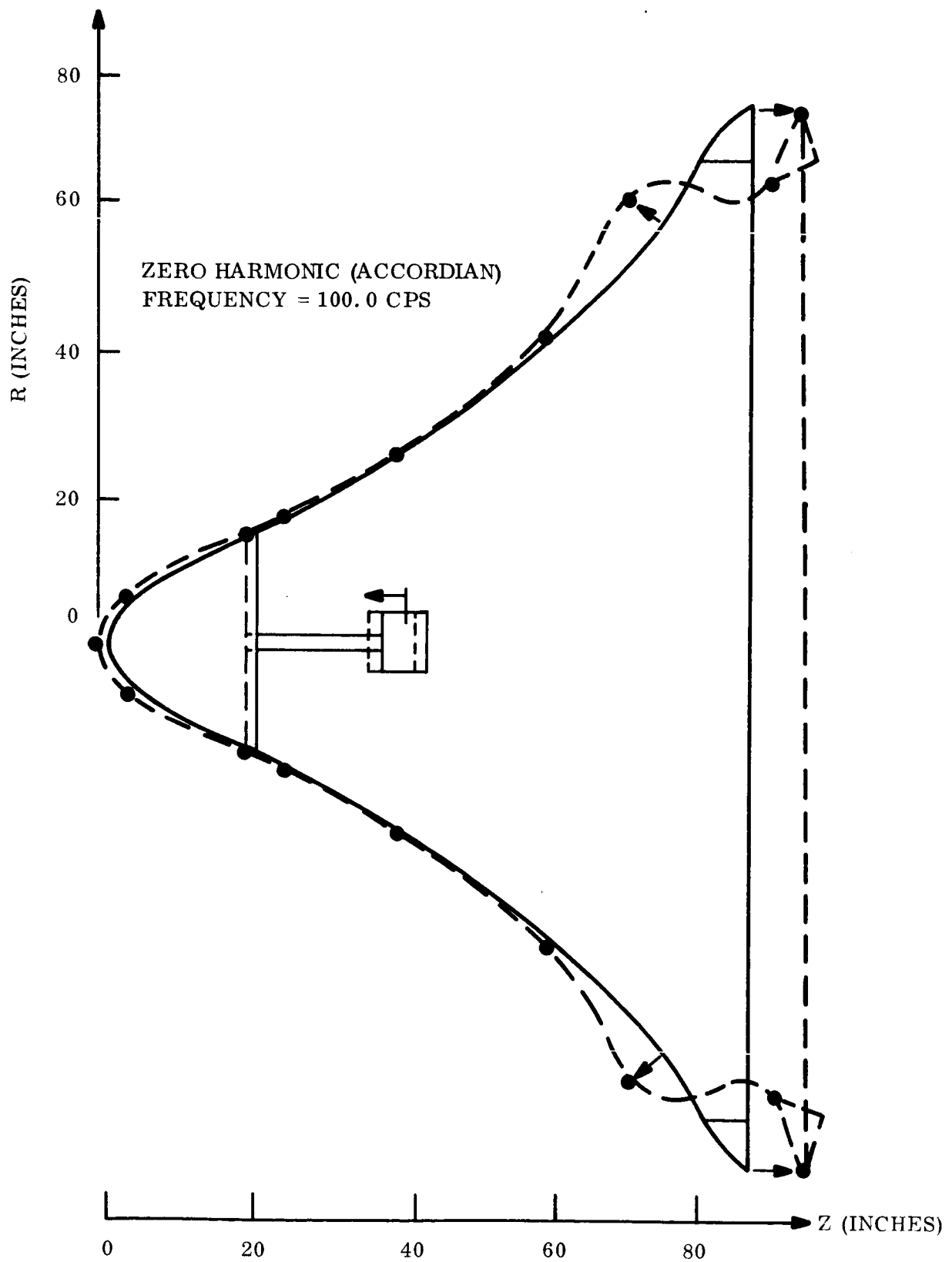
Figure 103. Mode Shape, Tension Shell, Aluminum Monocoque at 100°F
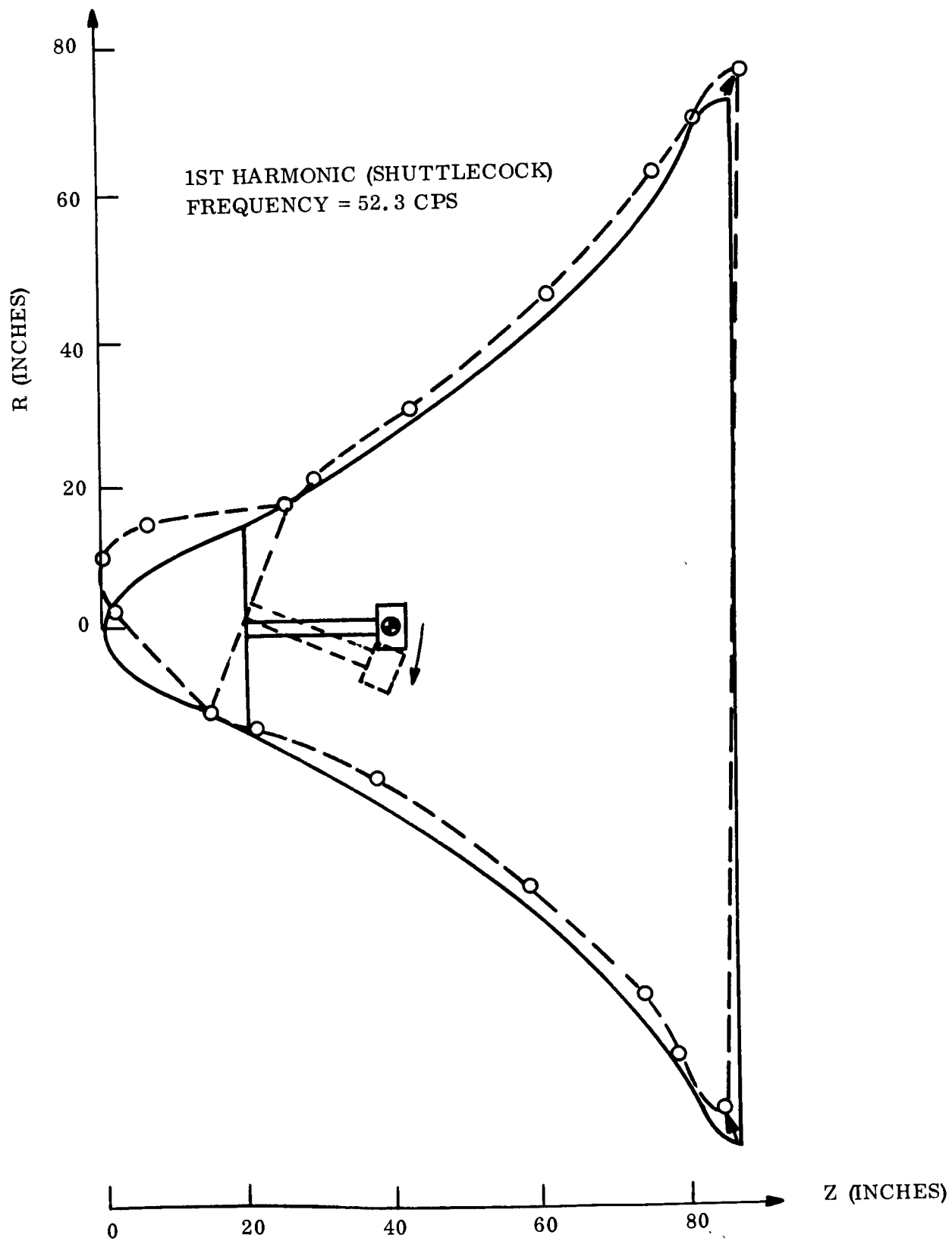
Figure 104. Mode Shape, Tension Shell, Aluminum Monocoque at 100°F

1ST MODE   2ND MODE   3RD MODE

RADIUS (INCHES)
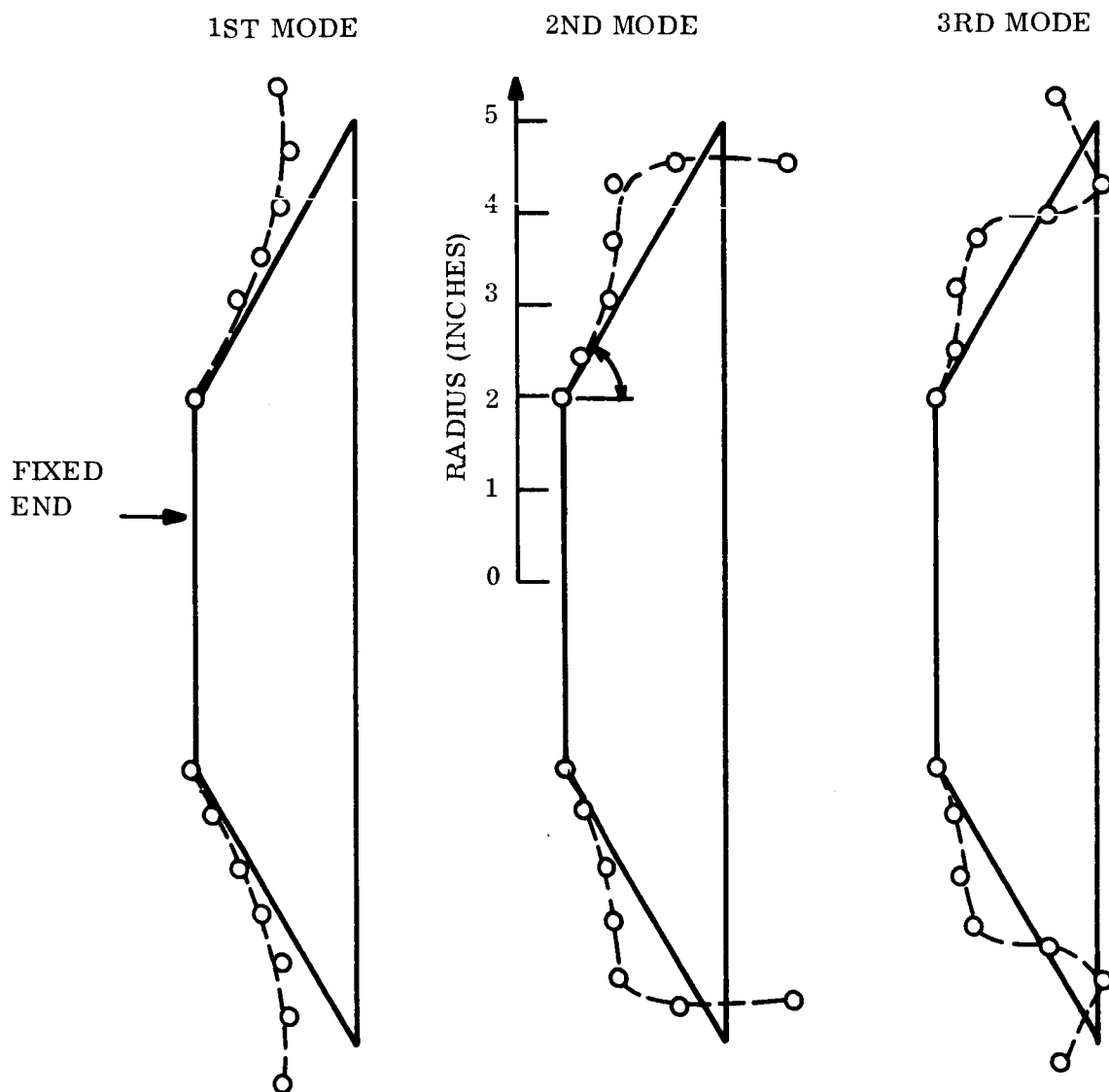
FIXED END →

FREQ.	f_1 (CPS)	f_2 (CPS)	f_3 (CPS)
SABOR O	1062	1332	1645
REF. — — —	1072	1315	1661

$t = .025$ IN , $E = .15 \times 10^6$ PSI

$\nu = .025$, $\rho = 30 \times 10^6$ LB SEC^2/IN^4

Figure 105.   Frequencies & Mode Shapes of a 60° Conical Frustrum (Fixed End); SABOR Results Compared with Theory for the Zeroth Harmonic
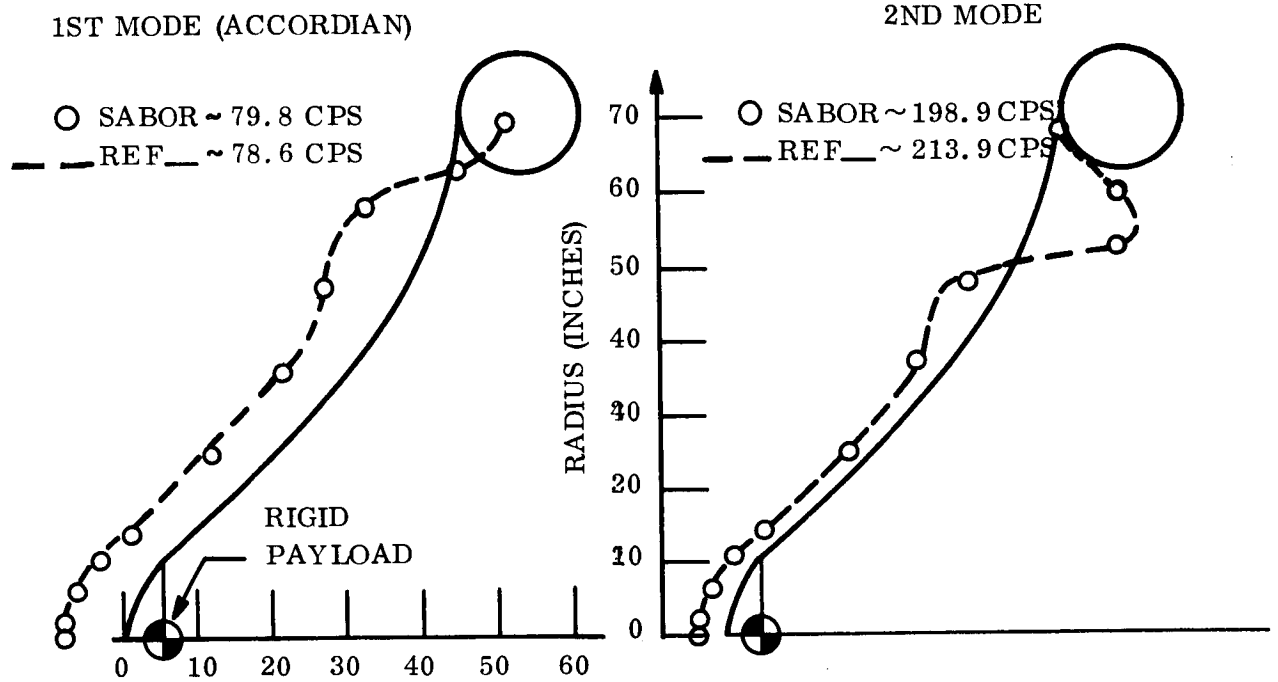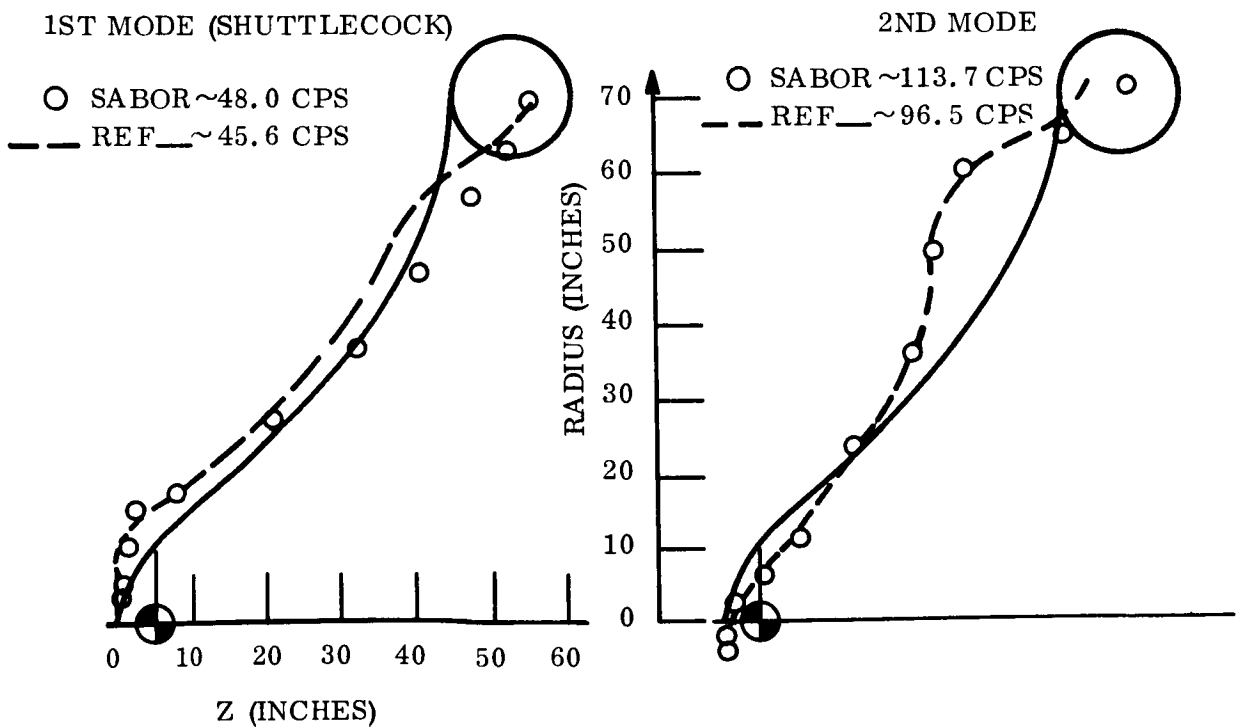
Figure 106. Frequencies & Modes Shapes of a Tension Shell Entry Vehicle (FREE-FREE)

CONICAL
ELEMENT

W

$\beta = \dfrac{\partial W}{\partial Z}$

θ

R

V

u

Z

(B) MOTION FOR ACCORDIAN MODE   NODAL CIRCLE

Y

$\dot{W} = \dot{q}_3^o = 0$ (RESTRAINT)

$\dot{\beta} = \dot{q}_4^o$

$\dot{u} = \dot{q}_1^o$

X

θ

R

$\dot{V} = \dot{q}_2^o$

$V_y = -X_i \left(\dfrac{\dot{q}_2^o}{R}\right)$

$V_x = Y_i \left(\dfrac{\dot{q}_2^o}{R}\right)$

dm_i

V_y

r_i

Y_i

X_i

$V_z = \dot{q}_1^o$

Z_i

Z
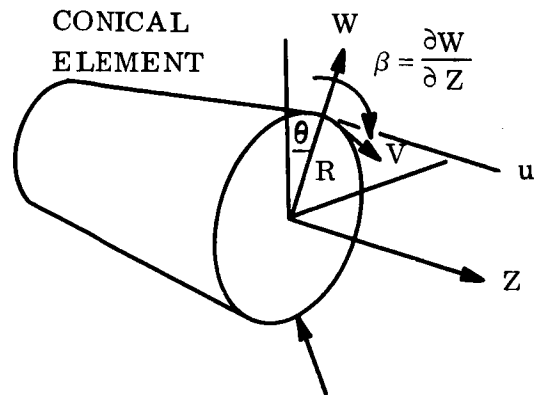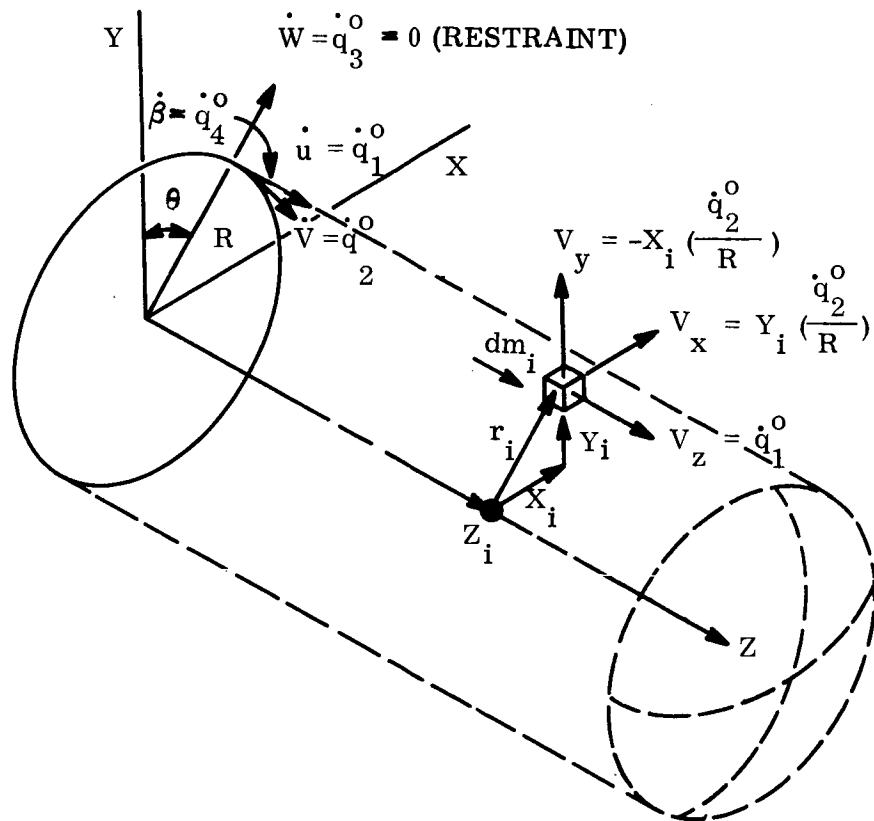
Figure 107. Shell Dynamic Model
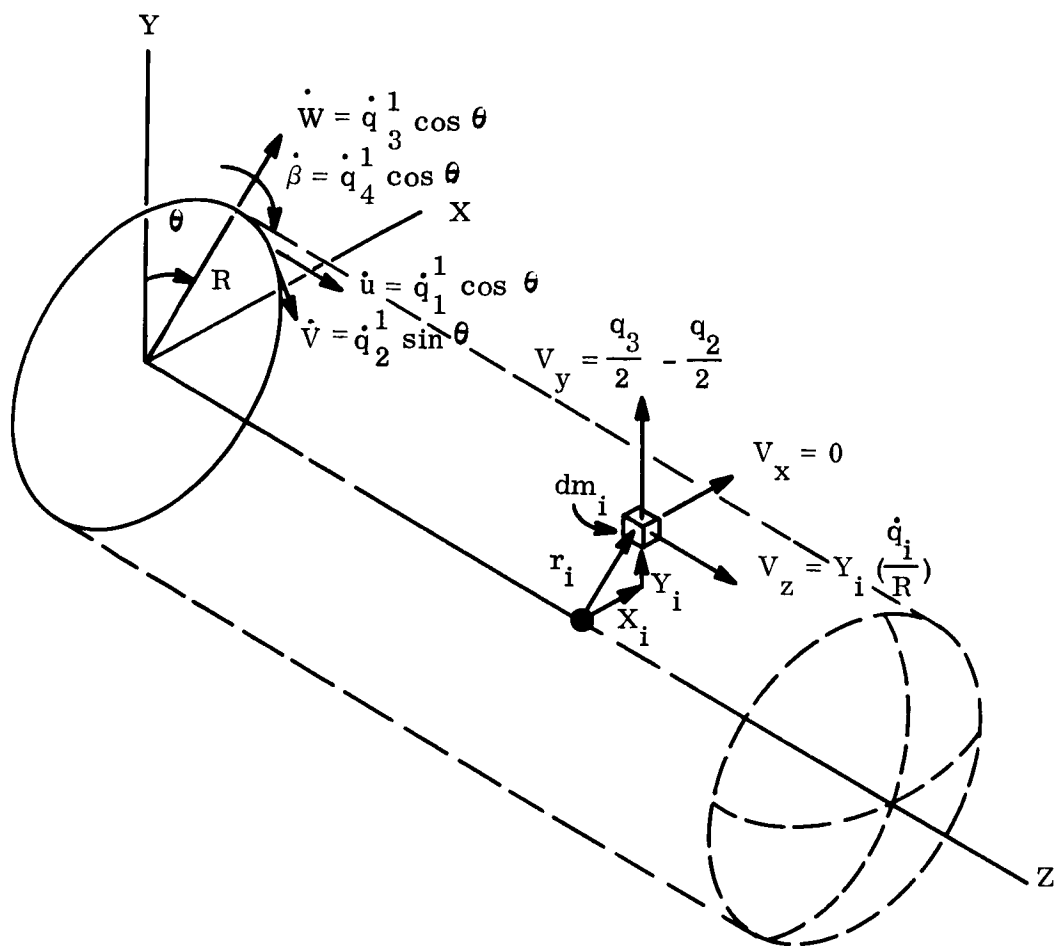
Figure 108. Motion for a Shuttlecock Mode
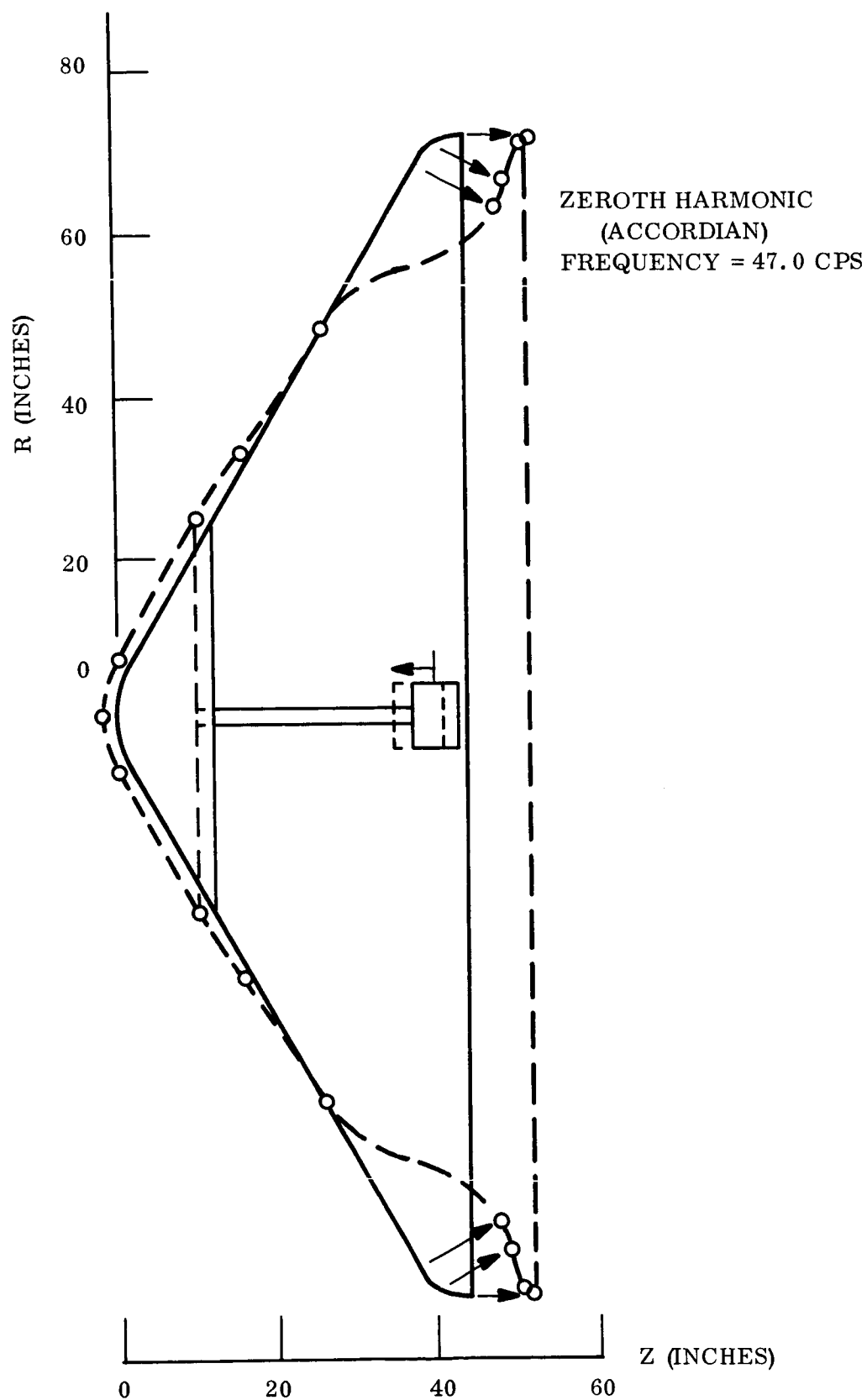
Figure 109. Mode Shape, 60° Sphere Cone, 12' Diameter, Fiberglass Honeycomb at 100°F, $M/C_D A = .30$
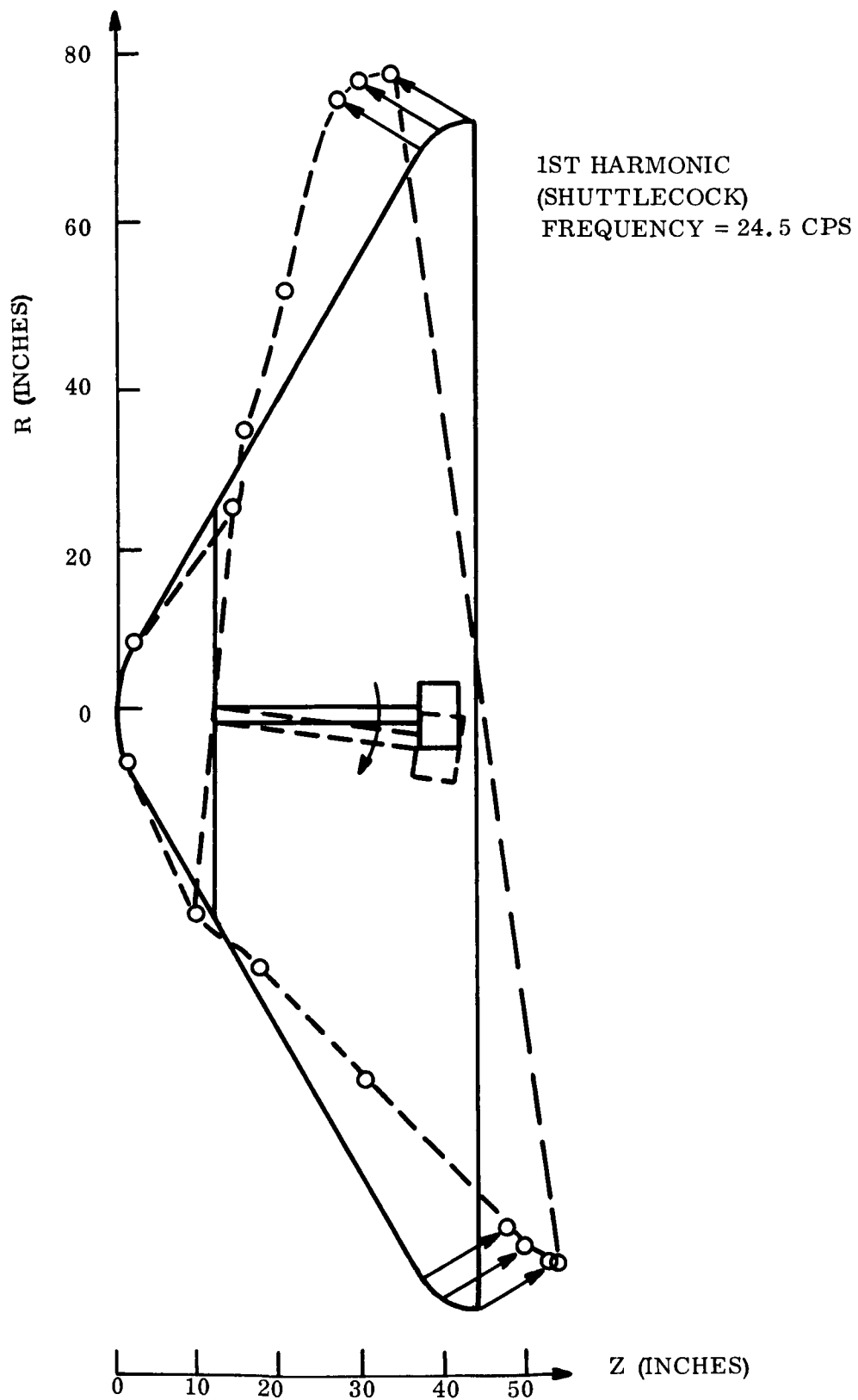
Figure 110. Mode Shape, 60° Sphere Cone, 12' Diameter, Fiberglass Honeycomb
at 100°F, M/C$_D$A = .30
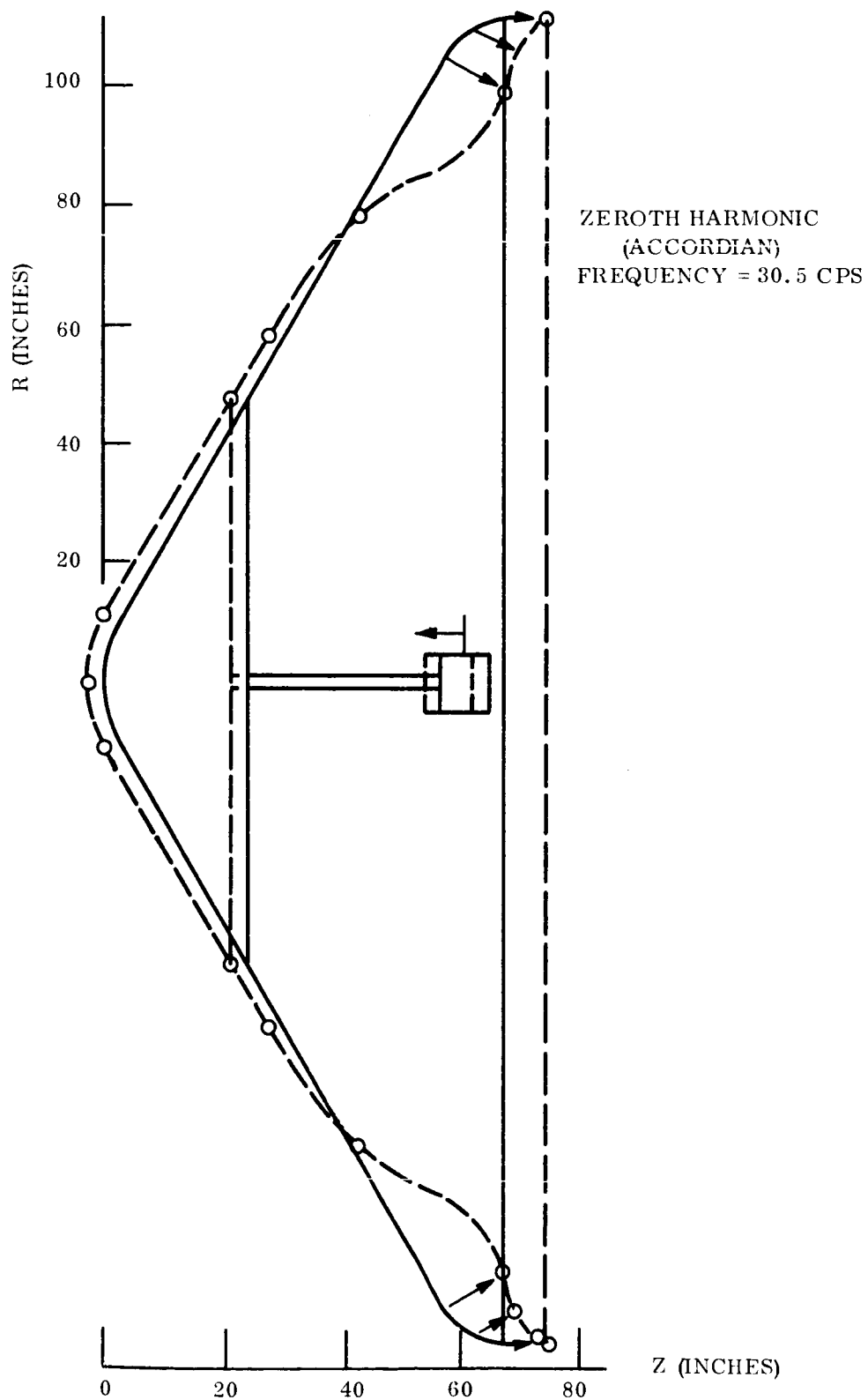
Figure 111. Mode Shape, 60° Sphere Cone, 18.5' Diameter, Fiberglass Honeycomb at 100°F, $M/C_D A = .25$

1ST HARMONIC (SHUTTLECOCK)
FREQUENCY = 20.1 CPS
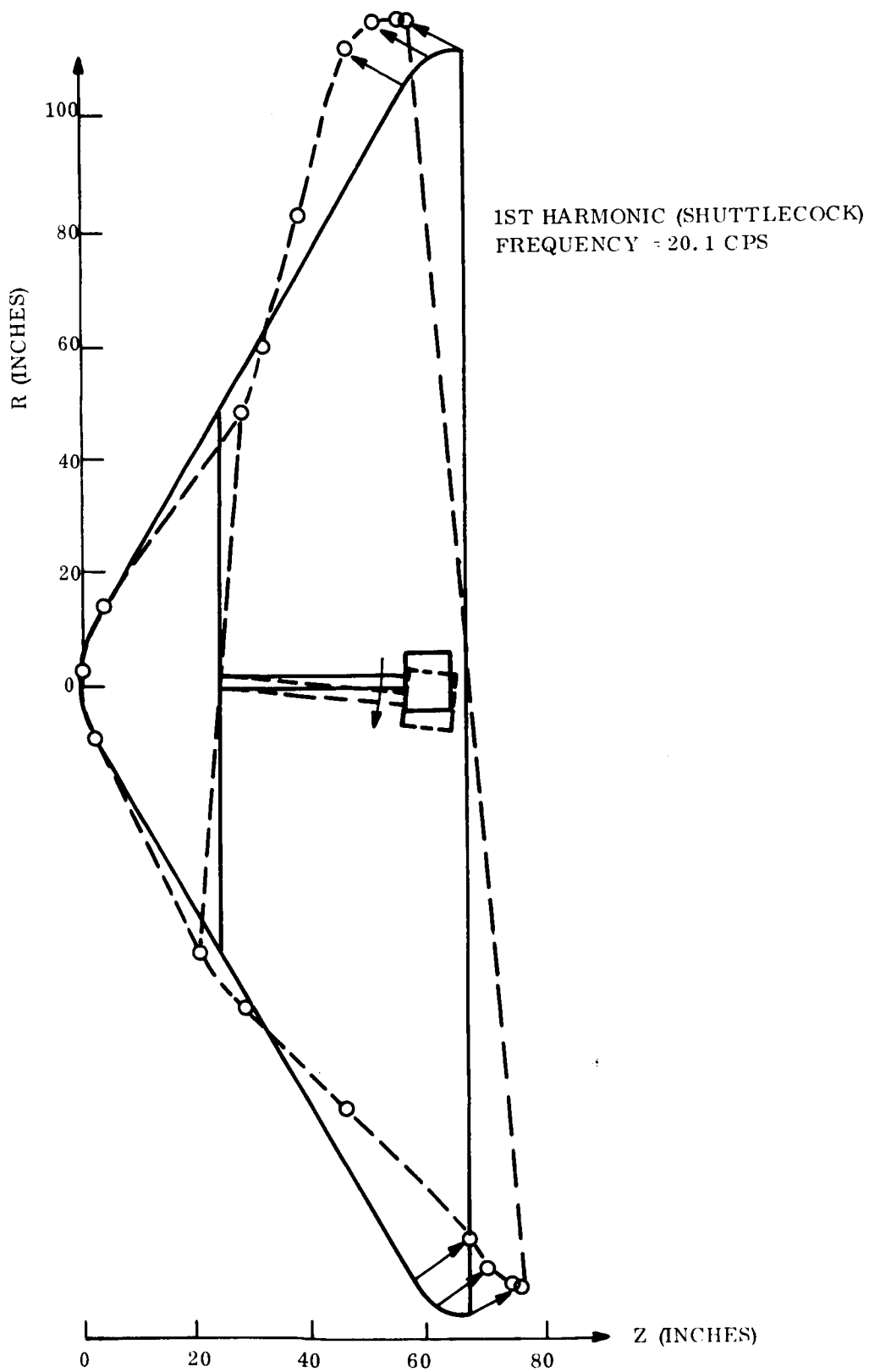
Figure 112. Mode Shape, 60° Sphere Cone, 18.5' Diameter, Fiberglass Honeycomb at 100°F, $M/C_D A = .25$
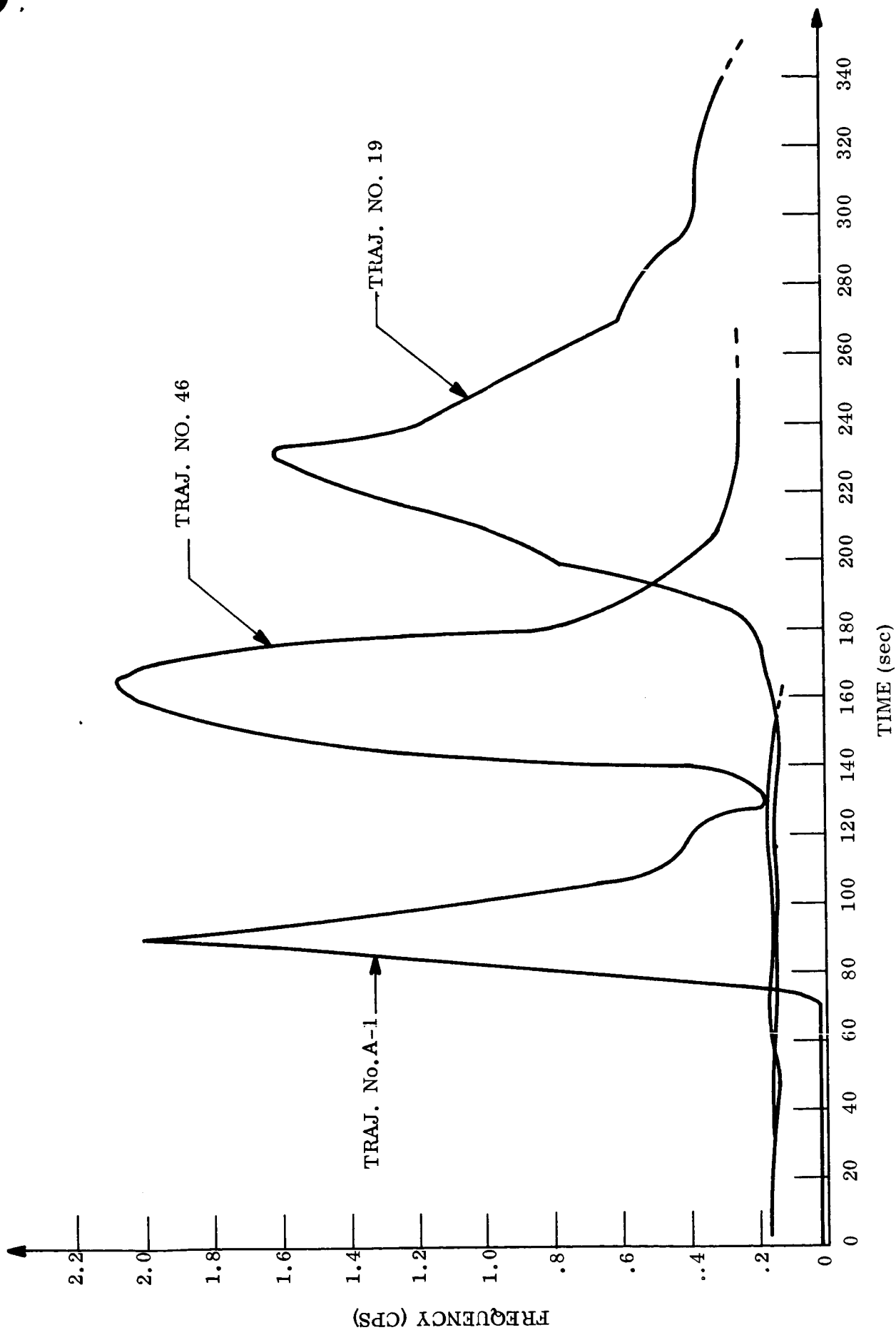
Figure 113. Short Period Oscillation; Frequency vs Time
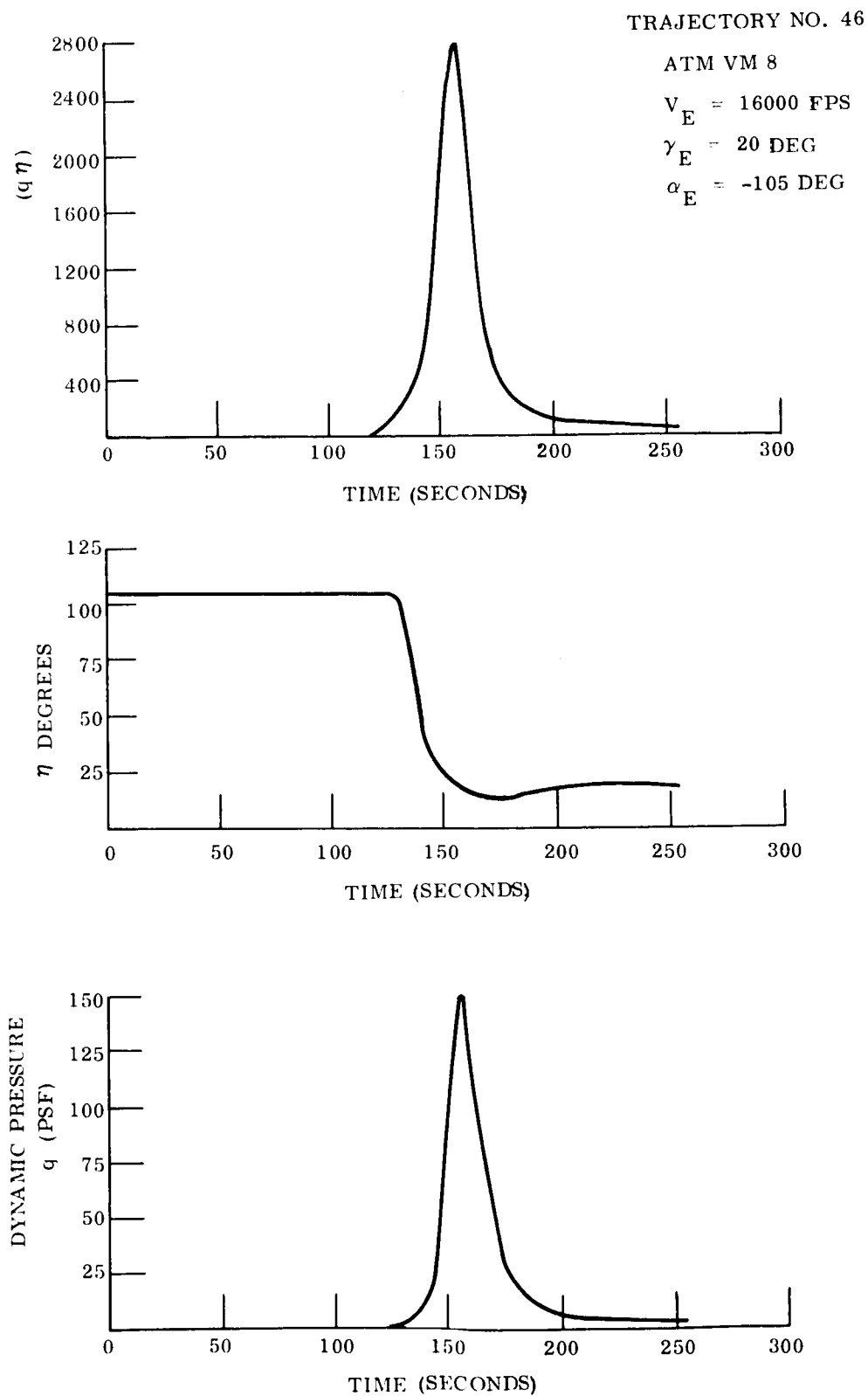
Figure 114.   Trajectory No. 46, VM-8 Atmosphere

GX = 28.7 G'S
GN = 3.75 G'S
GNP = .076 G'S/IN

TENSION SHELL
LOAD DISTRIBUTION

$\alpha = 12^{\circ}$
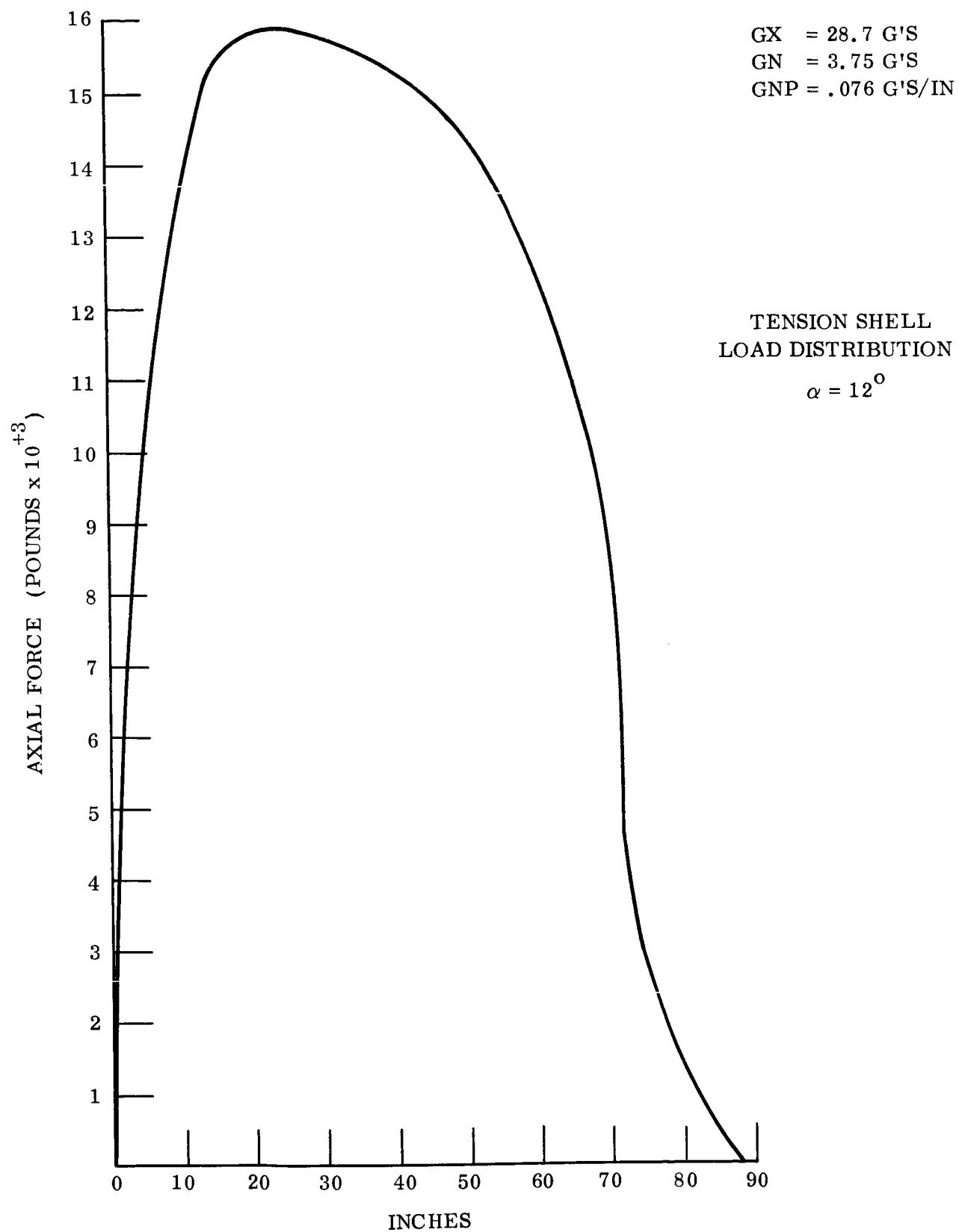
Figure 115. Axial Force vs Axial Station
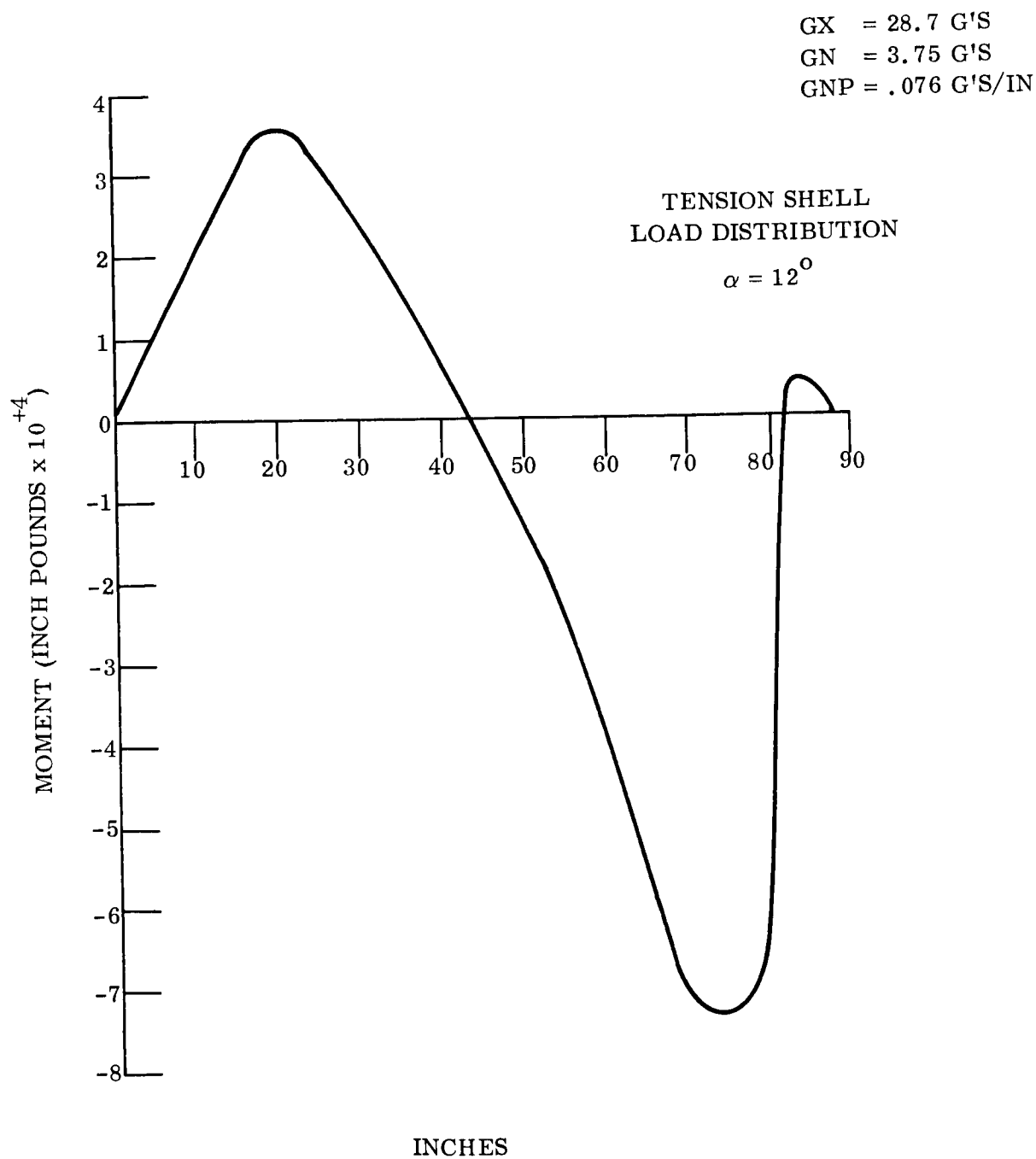
Figure 116.   Moment vs Axial Station

TOTAL MERIDIONAL STRESSES
FOR TENSION SHELL

$\alpha = 12^{\circ}$

$$N_X^{TOTAL} = \frac{P}{2\pi R} - \frac{M}{TR^2}$$
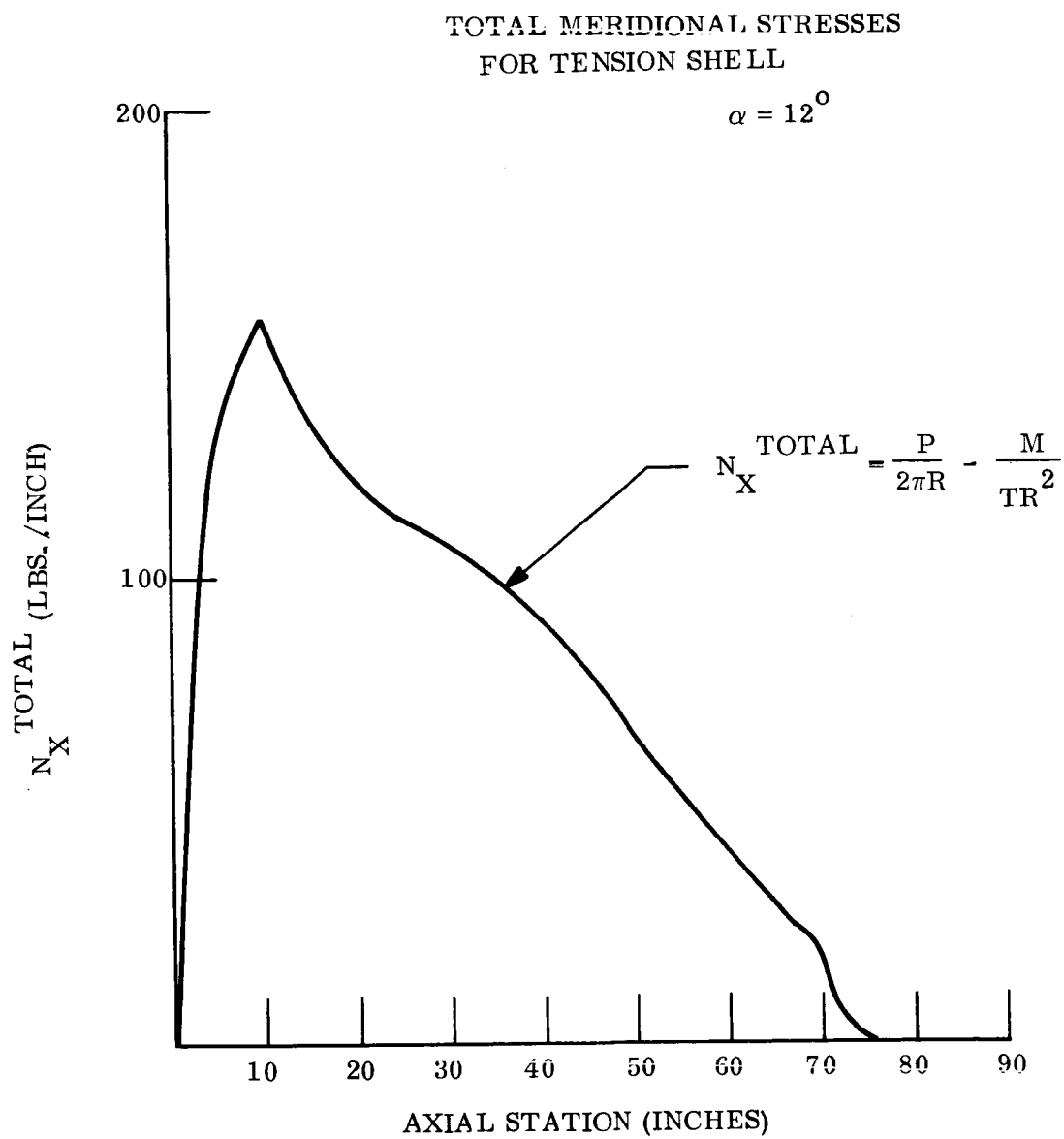
Figure 117. Total Meridional Stresses for Tension Shell
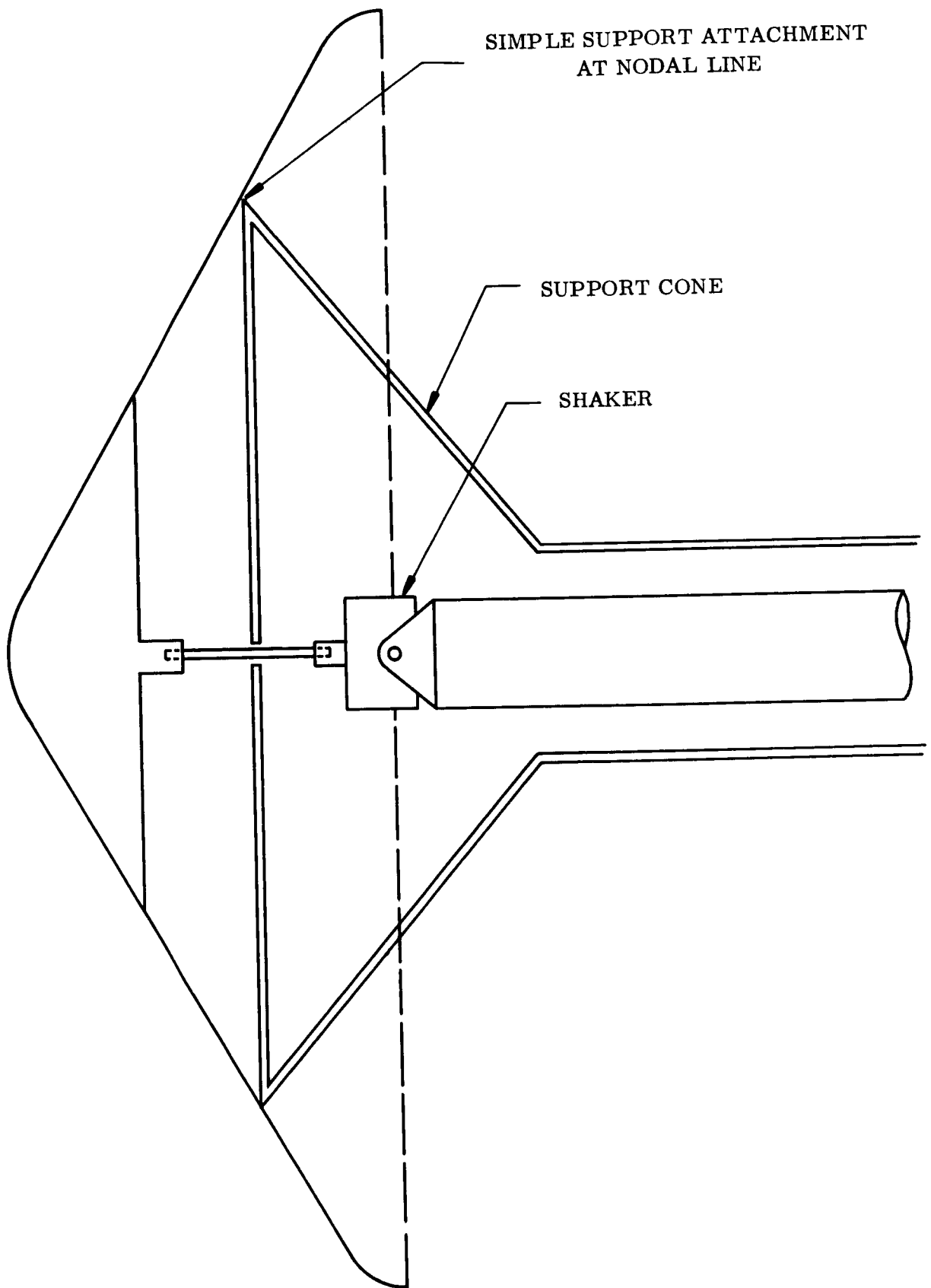
Figure 118. Tunnel Model for Sphere Cone Accordian Mode Dynamic

SIMPLE SUPPORT
ATTACHMENT AT NODAL LINE

SUPPORT CONE

SHAKER
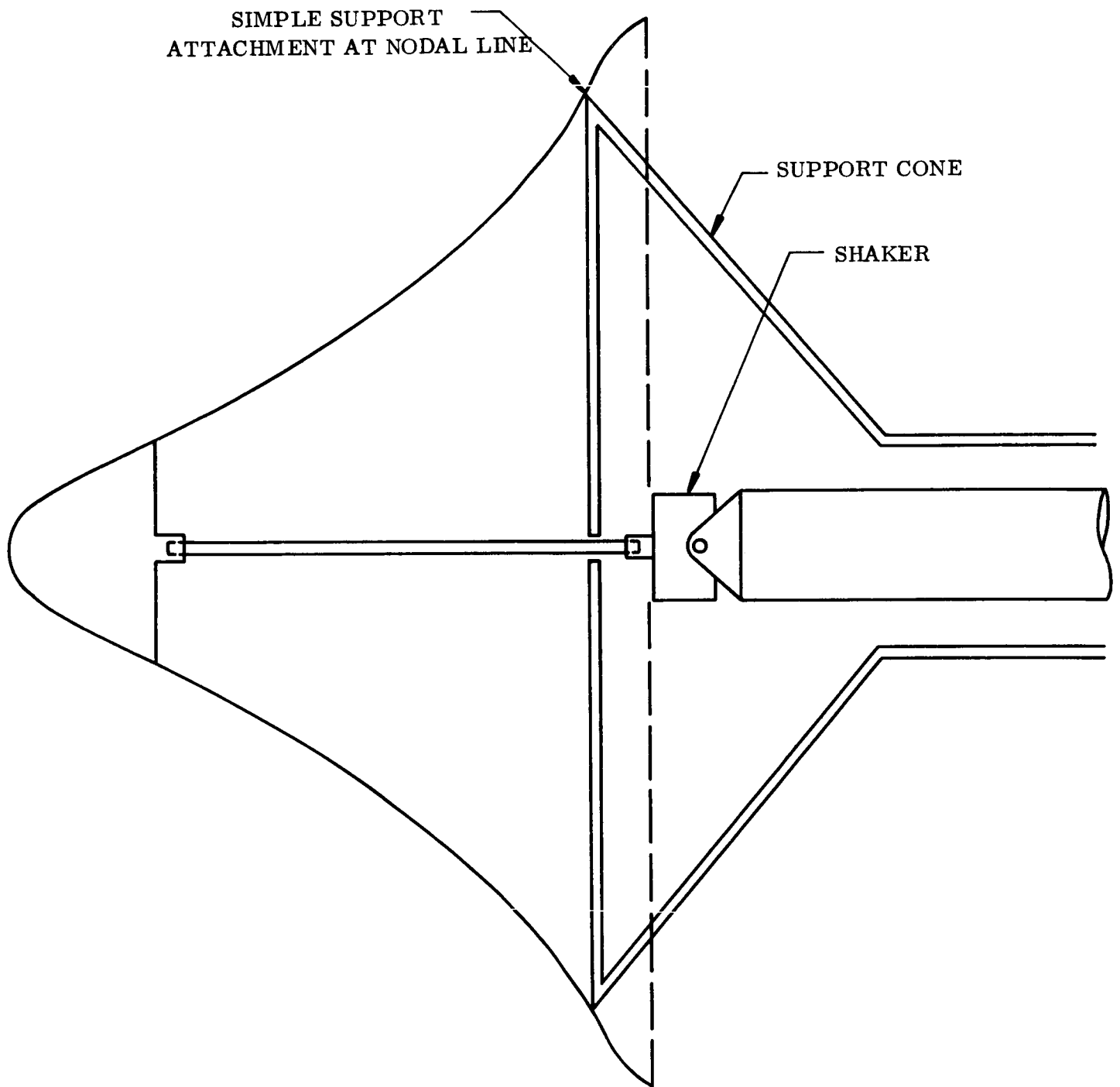
Figure 119. Tunnel Model for Smooth Flare Accordian Mode Dynamic

SHAKER TO EXCITE LATERAL MOTION

SHAKER SUPPORT STING

MODEL SUPPORT STING

PIVOT AT NODAL POINT OF
SHUTTLECOCK MODE
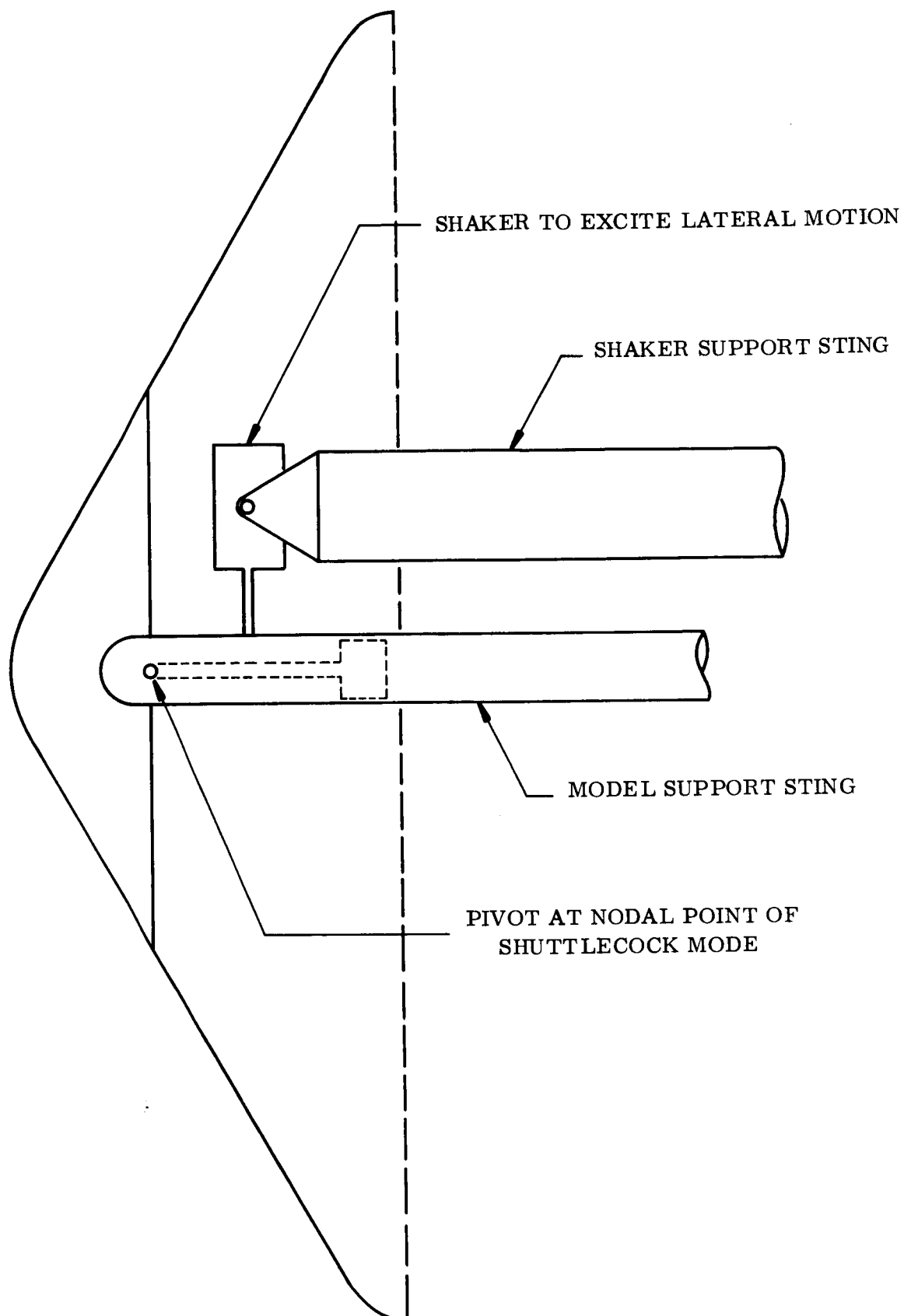
Figure 120. Tunnel Model for Sphere Cone Shuttlecock Mode Dynamics

SHAKER TO EXCITE
LATERAL MOTION

SHAKER SUPPORT
STING

PIVOT AT NODAL
POINT OF SHUTTLECOCK
MODE

MODEL SUPPORT
STING
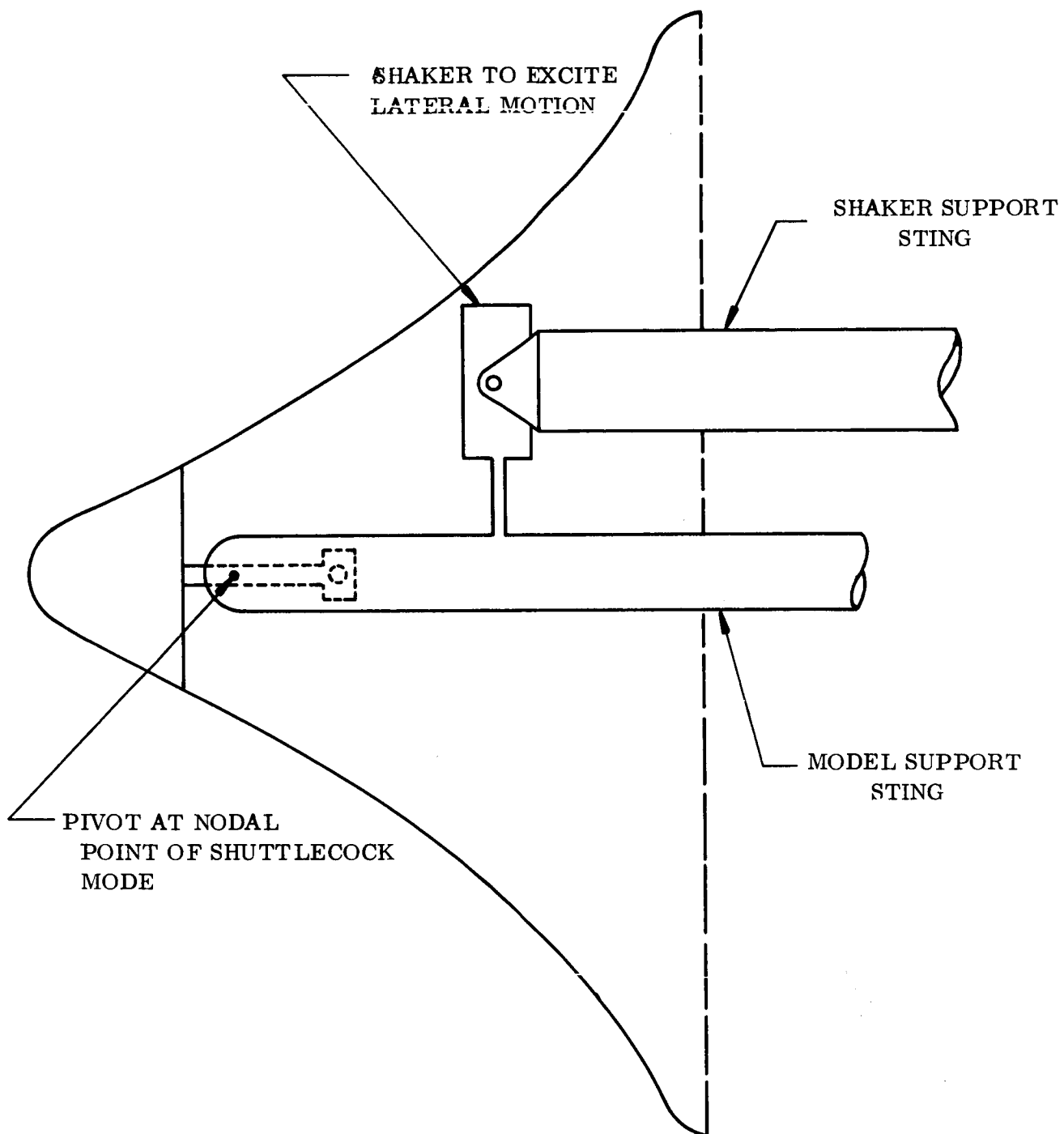
Figure 121. Tunnel Model for Smooth Flare.
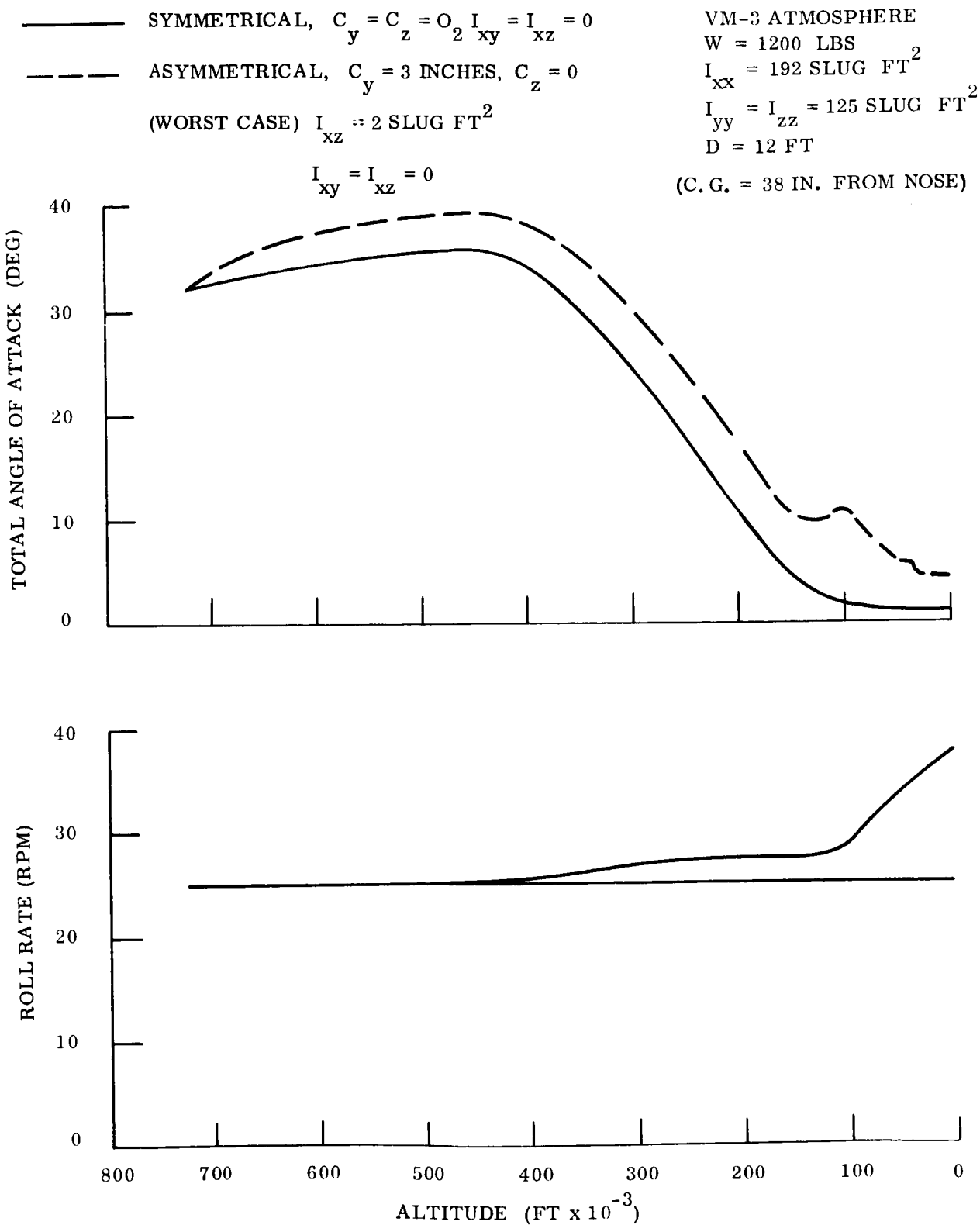
Figure 122. Angle of Attack and Roll Rate History
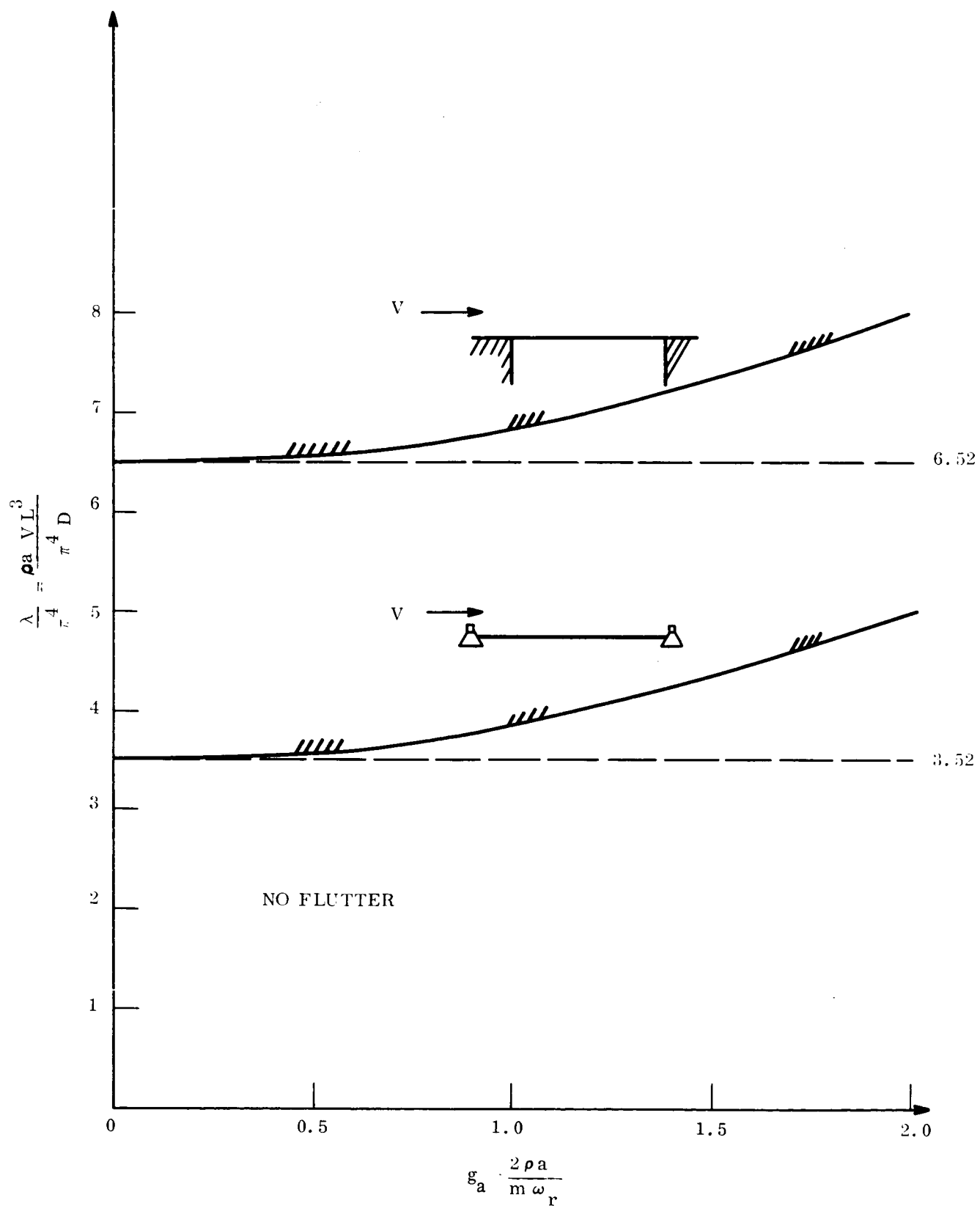
Figure 123.   Flutter Boundaries for Flat Panel
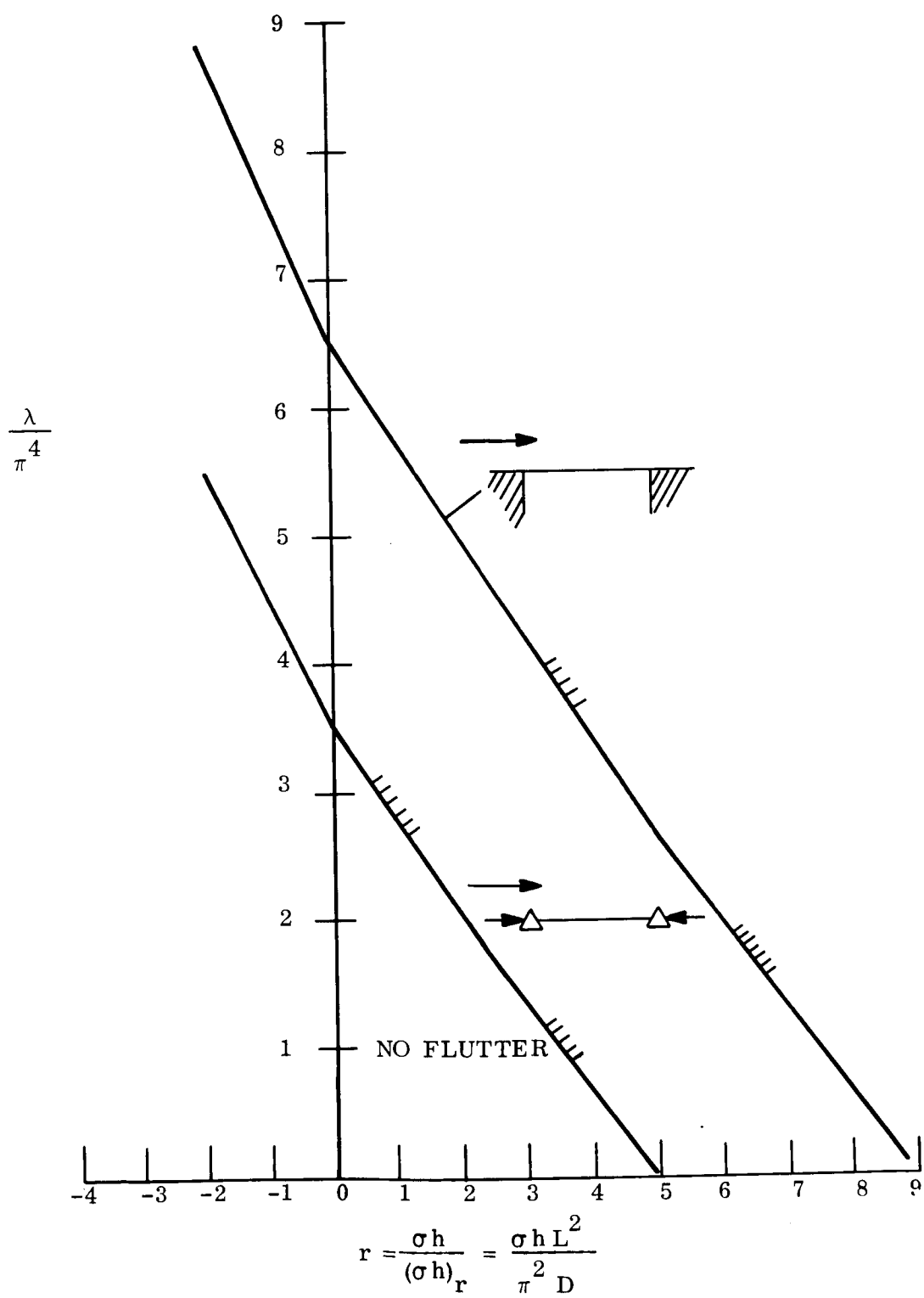
Figure 124.   Flutter Boundaries for Flat Panels with Axial Local

$$r = \frac{\sigma h}{(\sigma h)_r} = \frac{\sigma h L^2}{\pi^2 D}$$

FLUTTER PARAMETER (λ/π^4)

FLUTTER

NO FLUTTER

WAVE LENGTH, L (INCHES)
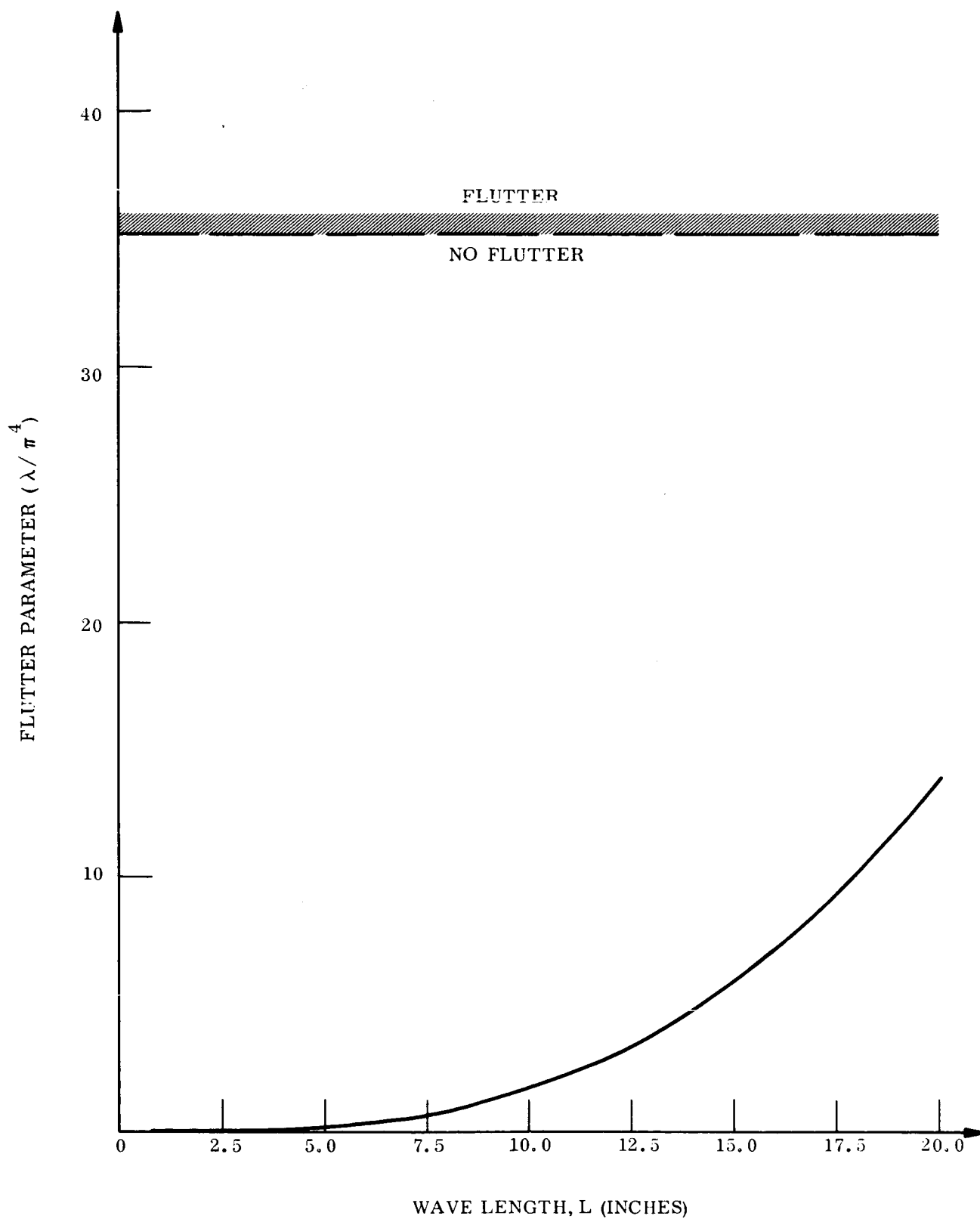
Figure 125. Flutter Parameter (λ) vs Wave Length
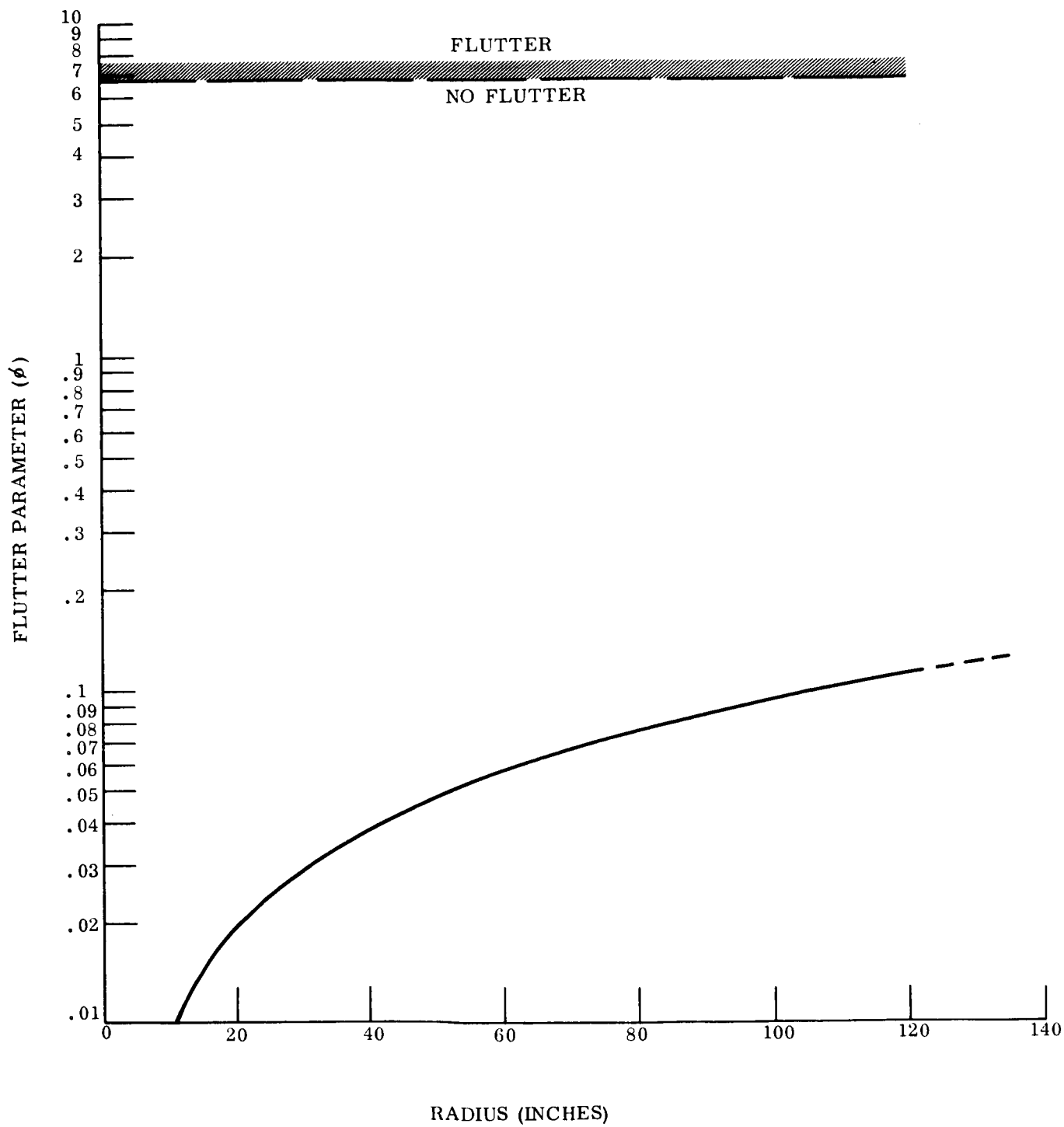
Figure 126.   Flutter Parameter (ϕ) vs Radius

1.68

.68
.67

.67

.67

.67

.67

.67

.67

.67

.62
.56
.42

ORIGINAL
SHAPE

DEFORMED
SHAPE

VEHICLE NO. 3
TRAJ. NO. A-1
MACH. NO. AT MAXIMUM g
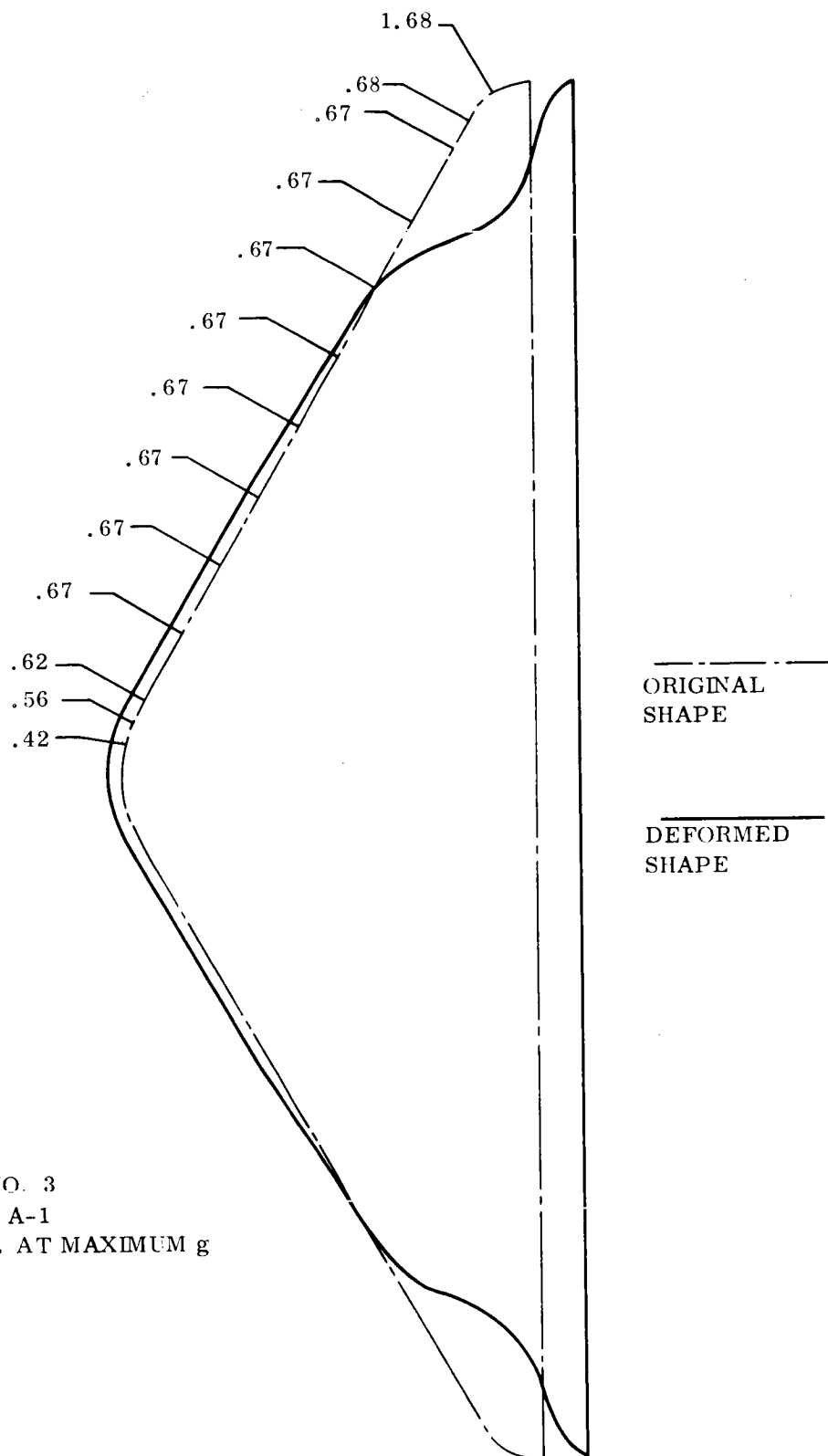
Figure 127. Distribution of Local Mach No. & Structural Deformation for Accordian Mode

221

ORIGINAL
SHAPE

DEFORMED
SHAPE

1.0

1.28

1.34

1.42

1.64

1.74

1.74

1.67

1.25

VEHICLE NO. 6
TRAJ. NO. 46
MACH. NO. AT MAXIMUM g
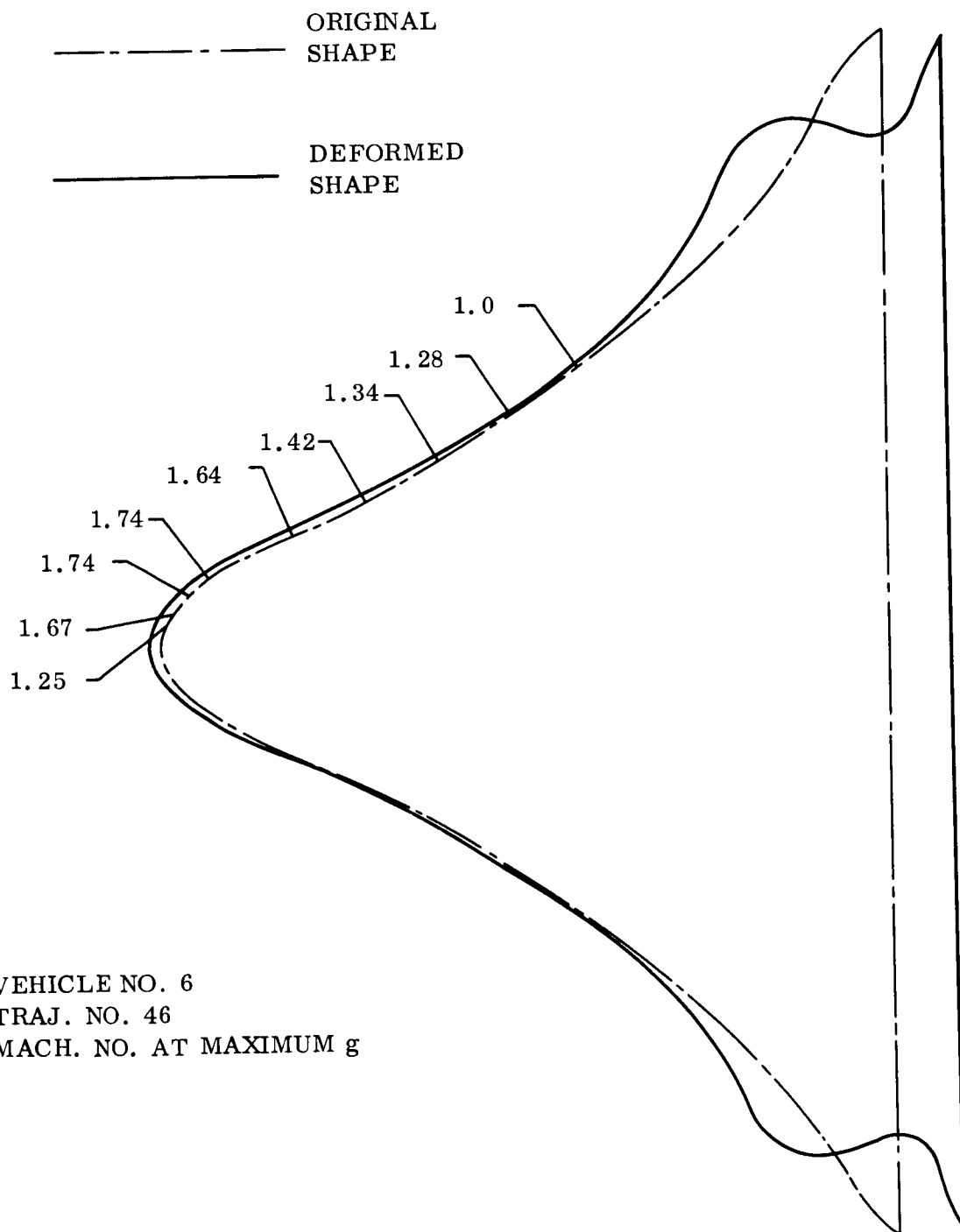
Figure 128. Distribution of Local Mach No. & Structural Deformation for Accordian Mode

ORIGINAL
SHAPE

DEFORMED
SHAPE

VEHICLE NO. 3
TRAJ. NO. A-1
MACH. NO. AT MAXIMUM g
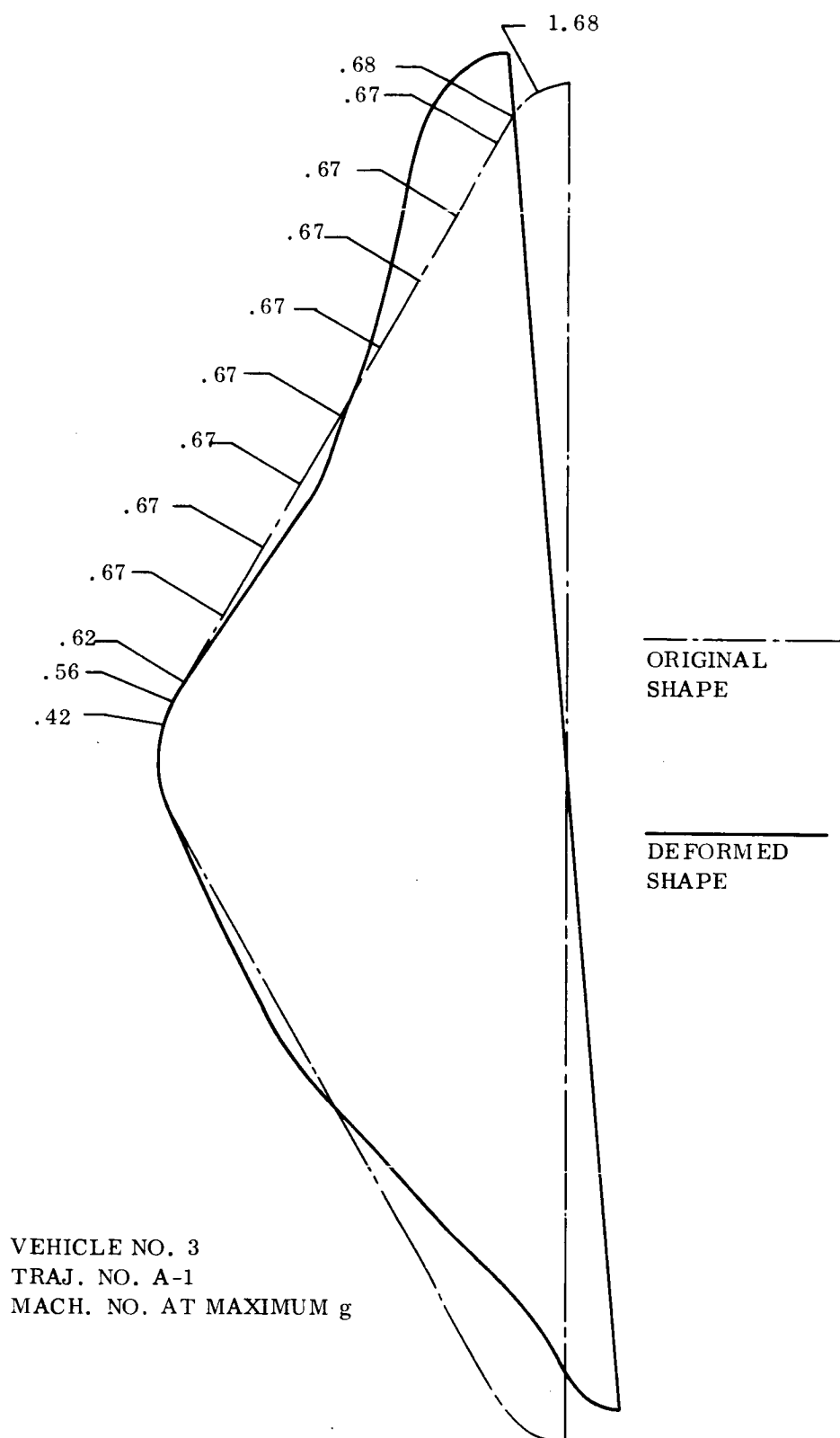
Figure 129. Distribution of Local Mach. No. & Structural Deformation for Shuttlecock Mode

ORIGINAL SHAPE

DEFORMED SHAPE

1. 0

1. 28

1. 34

1. 42

1. 64

1. 74

1. 74

1. 67

1. 25

VEHICLE NO. 6
TRAJ. NO. 46
MACH NO. AT MAXIMUM g
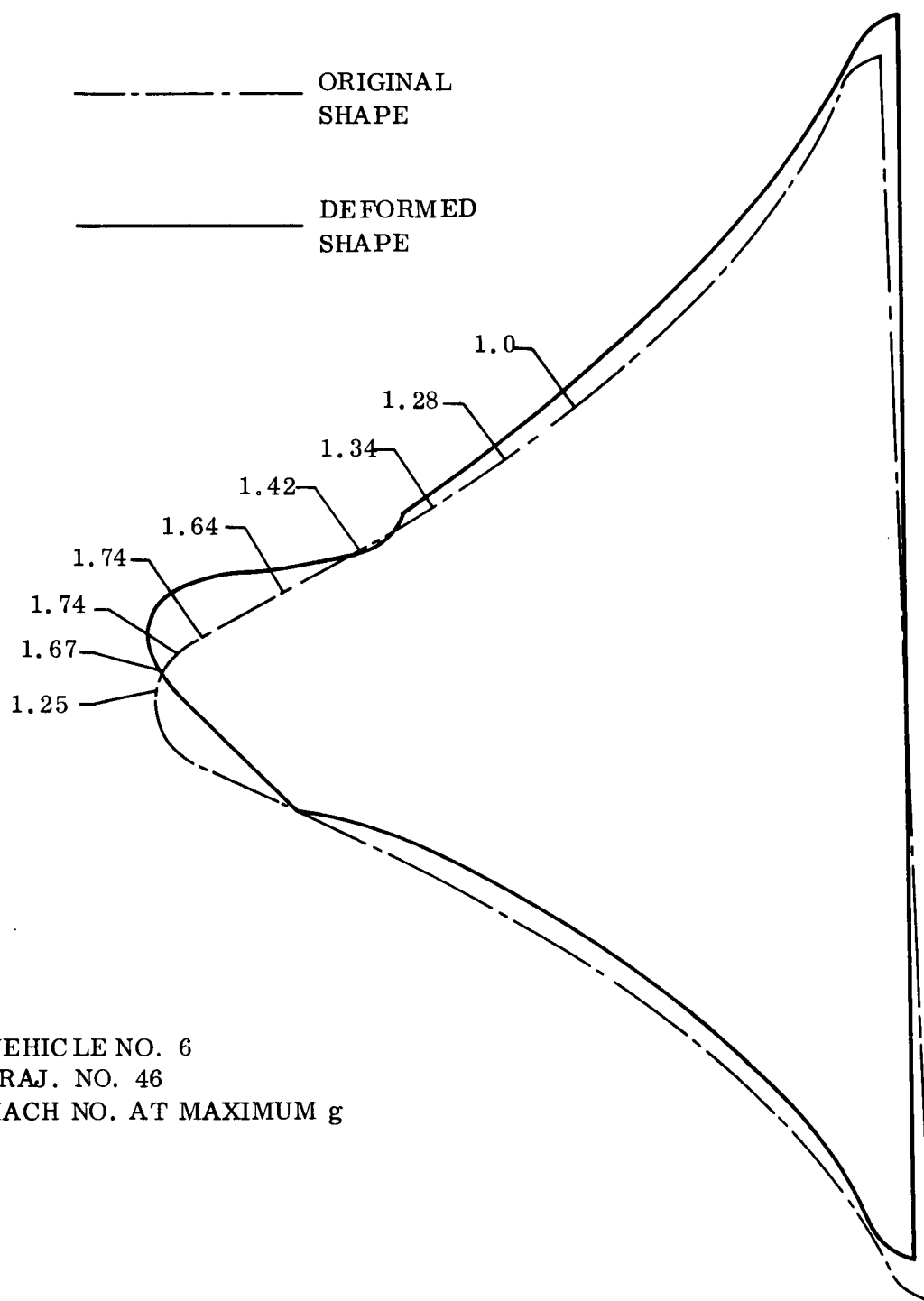
Figure 130. Distribution of Local Mach. No. & Structural Deformation for Shuttlecock Mode
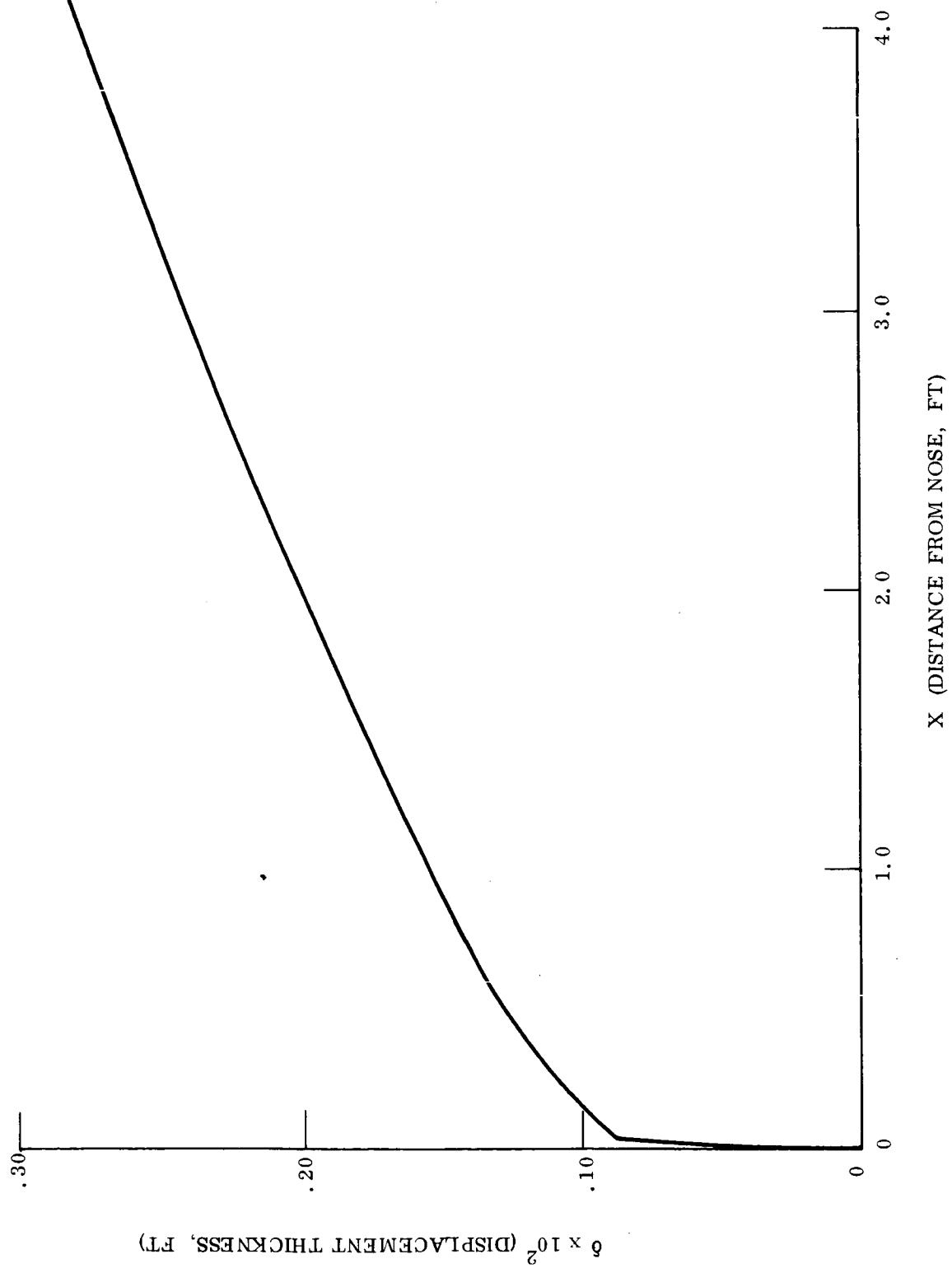
Figure 131. 60° Sphere Cone Laminar Boundary Layer Displacement Thickness
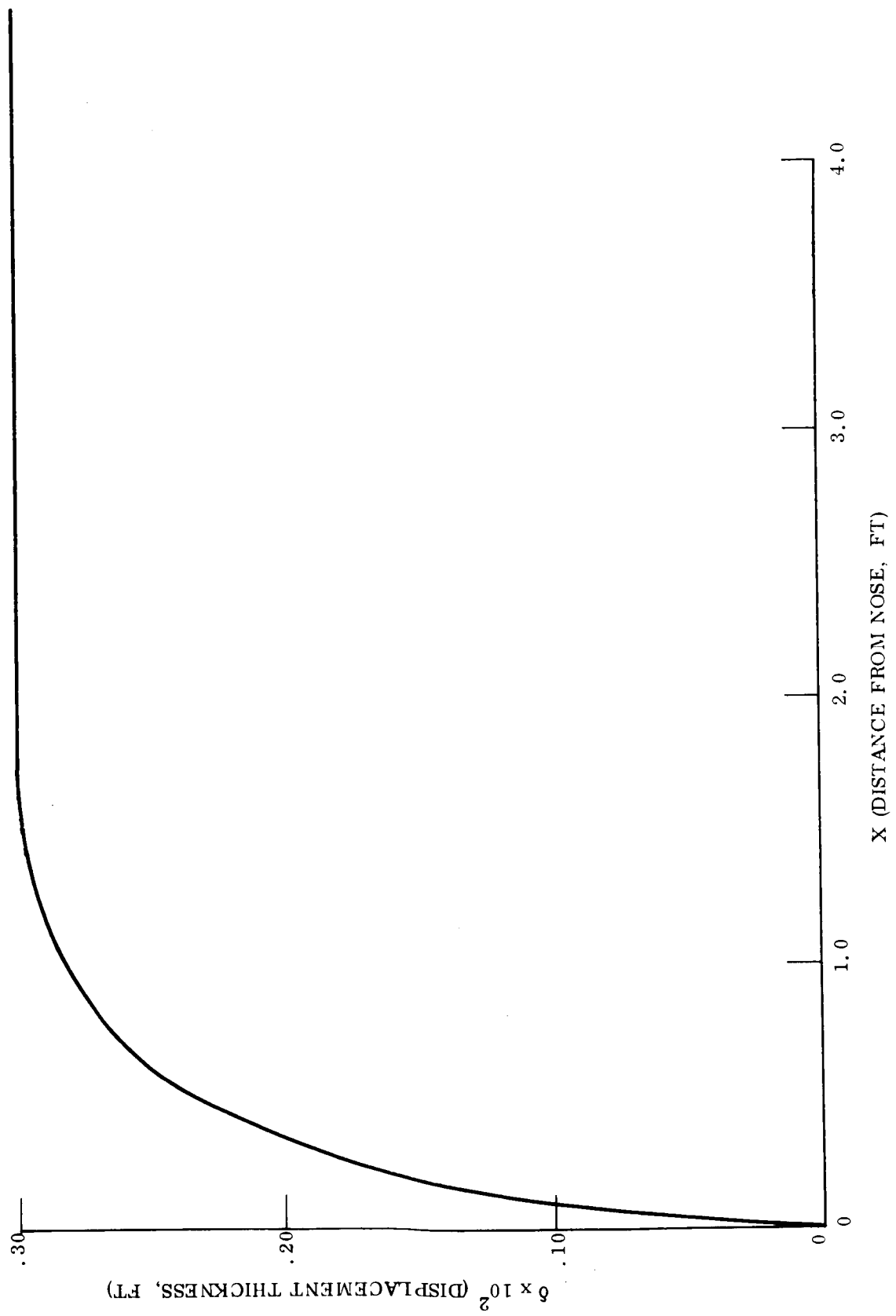
Figure 132. Smooth Flare Laminar Boundary Layer Displacement Thickness
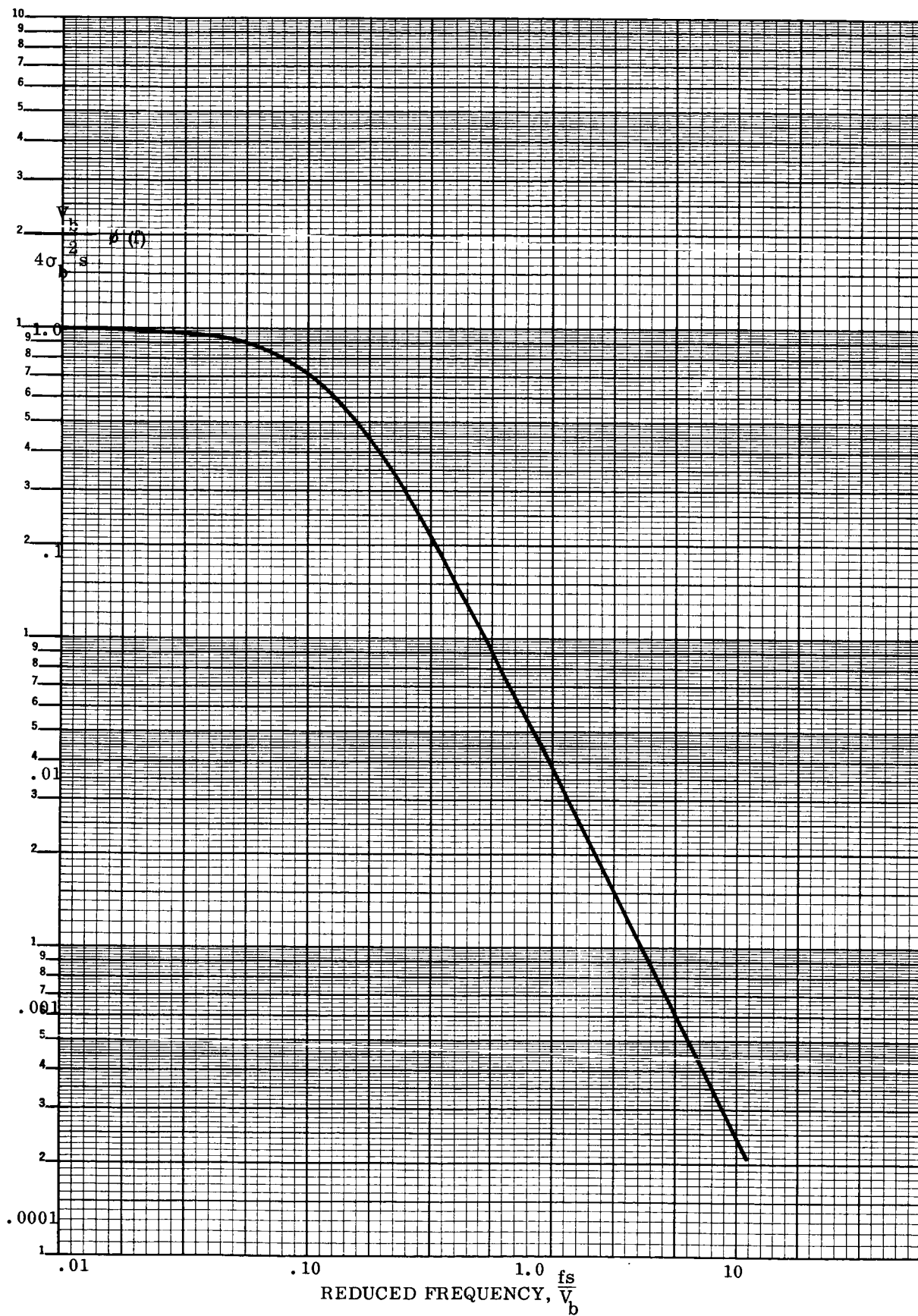
Figure 133. Frequency Spectrum of Wake Acoustic Pressure
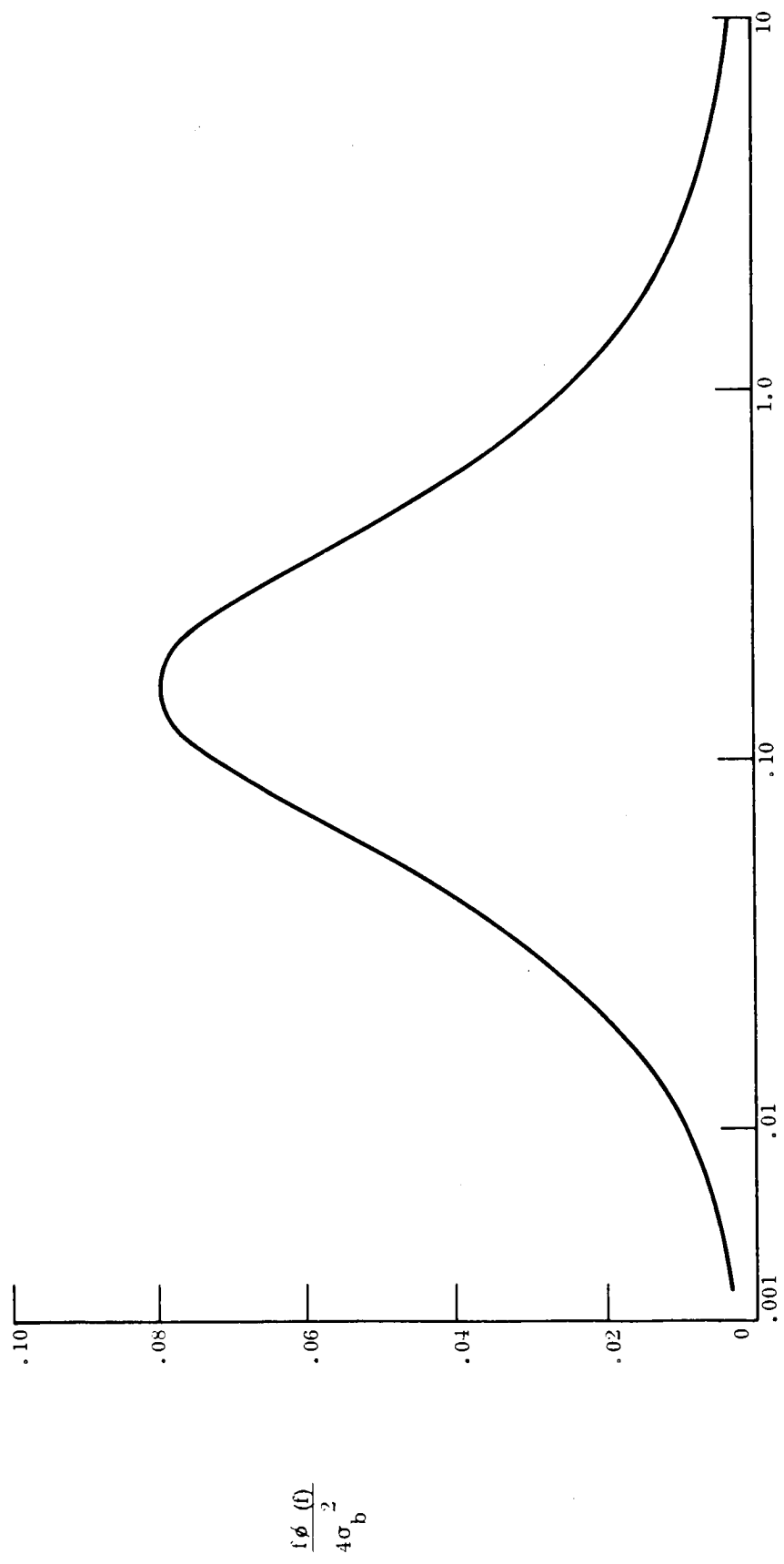
Figure 134. Variation of Wake Acoustic Pressure

$$\frac{f\phi(f)}{4\sigma_b^2}$$

REDUCED FREQUENCY, $\frac{fs}{V_b}$

228

Table 1 Trajectory Conditions

Run No.	ATM Model VM-	V_E K ft/sec	$-\alpha_E$* (800 K ft) deg.	Angle of Attack α_E deg.	Spin Rate, Rad/Sec	Dia. ft.	$\dfrac{M}{1.4A}$ SI/ft²	$W_E = 32.2$ m	$\dfrac{c.g.}{D}$ from nose	I pitch slug-ft²	I roll slug-ft²	I yaw slug-ft²	Dynamic Pressure q_∞ PSF	Comment/Objective
A-1	8	23	25	105	1	18.5	.25	3030	.25	2455	2400	2455	449	
A-2	8	23	25	5	1	18.5	.25	3030	.25	2455	2400	2455	429	with A-1, effect of entry angle of attack
A-3	7	23	25	5	1	18.5	.25	3030	.25	2415	2340	2415	161	with A-1 & A-2, effect of atmosphere
A-4	7	23	25	105	1	18.5	.25	3030	.25	2415	2340	2415	166	
20	8	16	16	- 50	1	12	.20	1020	.25	270	300	270	78.6	
9	8	16	16	5	1	12	.20	1020	.25	270	300	270	73.5	with 20, effect of entry angle of attack
**41	8	16	16	- 50	0	12	.20	1020	.25	270	300	270	74.2	with 20, effect of spin
**46	8	16	20	-105	1	12	.20	1020	.25	270	300	270	155	
47	8	16	20	5	1	12	.20	1020	.25	270	300	270	136	with 46, effect of entry angle of attack
21	7	16	16	- 50	1	12	.20	1020	.25	270	300	270	36.7	with 8, effect of atmosphere
13	8	12.5	12	5	1	12	.20	1020	.25	270	300	270	50.1	
16	8	12.5	12	- 50	1	12	.20	1020	.25	270	300	270	54.9	with 13, effect of entry angle of attack
**19	8	16	16	- 50	1	12	.30	1530	.25	243	407	243	116	with 20, effect of $\dfrac{M}{1.4A}$
15	8	12.5	12	- 50	1	12	.30	1530	.25	243	407	243	81.7	with 16, effect of $\dfrac{M}{1.4A}$

*Entry altitude = 800 Kft

**Trajectories investigated for structural design

229

Table 2 Acceleration Levels

Run No	Time	A_x ft/sec²	A_y ft/sec²	A_z ft/sec²	α_x rad/sec²	α_y rad/sec²	α_z rad/sec²
A-1	88.63	-1856	+ 5.77	+17.07	0	5.39	- 2.30
VM #8	88.51	-1779	+133.5	-15.2	0	- 4.70	+41.7
18.5ϕ	87.49	-1667	- 92.9	+23.5	0	- 7.36	+29.3
A-2	88.6224	-1792	- .149	0	0	0	+ .04
VM #8	88.7439	-1781	+ 2.28	+ 2.30	0	+ .72	- .72
18.5' ϕ	88.7439	-1781	+ 2.28	- 2.30	0	+ .72	- .72
A-3	82.918	- 672	- .134	0	0	0	.04
VM #7	84.300	- 664	- .741	- 1.21	0	- .384	+ .235
18.5' ϕ	82.7204	- 671	- .731	- 1.27	0	- .404	+ .23
A-4	83.2333	- 694	+ 1.35	0	0	- 0.09	- .384
VM #7	81.0964	- 660.9	- 17.9	-34.7	0	-11.0	+ 5.68
18.5'ϕ	81.0876	- 661	- 17.85	-34.8	0	-11.1	+ 5.67
20	225.2089	- 395.3	- 22.3	8.38	0	5.24	13.6
VM #8	221.7101	- 377.3	- 24.7	0	0	0	15.1
12' ϕ	221.8842	- 379.0	- .23	+24.7	0	15.1	.04
9	225.1308	- 383.0	.701	0	0	0	- .43
VM #8	223.3489	- 379	- .709	0	0	0	.434
12' ϕ	223.1849	- 378	- .09	- .70	0	- .429	.06
41	225.2014	- 386.7	0	0	0	- .04	0
VM #8			0				
12' ϕ	222.3875	- 372.5	0	- 8.417	0	- 5.2	0
46	157.5908	- 764	+ 45.7	36.0	0	+21.7	-28.4
VM #8	153.8696	- 633	- 74.5	0	0	.36	+45.9
12' ϕ	157.0173	- 749	- 16.4	+68.96	0	42.4	+ 9.78
47	157.2887	- 707.46	.04	- 6.48	0	- 4.	.02
VM #8	155.5572	- 684	+ 6.64	0	0	- .04	- 4.08
12' ϕ	155.6910	- 687	.06	- 6.64	0	- 4.08	0
21	193.2866	- 175.68	- 12.8	0	0	.04	7.85
VM #7	186.3181	- 170	+ 13.3	0	0	- .035	- 8.1
12' ϕ	186.5682	- 170.7	- .04	+13.3	0	8.1	- .01
13	330.8466	- 260	+ 2.71	0	0	- .013	- 1.66
VM #8	328.7144	- 257	+ 2.757	0	0	.012	+ 1.68
12' ϕ	335.2890	- 250	.99	- 2.28	0	- 1.4	- .59
16	331.1381	- 271	- 20.36	0	0	.101	12.46
VM #8	327.8855	- 264	- 21.1	- .84	0	- .42	+12.9
12' ϕ	327.2756	- 260.9	- .17	+21.1	0	+12.9	.014
19	228.2716	- 392.5	.174	-19.8	0	-19.3	.018
VM #8	222.1552	- 341.4	- 22.33	0	0	.163	21.7
12' ϕ	222.3019	- 343.6	- .149	+22.37	0	21.8	- .015
15	334.8656	- 273.92	+ 16.44	0	0	- .17	-15.8
VM #8	327.5070	- 238	+ 19.14	0	0	- .143	-15.4
12' ϕ	327.3327	- 236	- .076	+19.17	0	18.4	- .073

Note: Underlined accelerations denote the maximum

Table 3a Structure/ Material Study Matrix

		Forebody		Afterbody	
Forebody	Afterbody	Structural Configuration	Structural Material	Structural Configuration	Structural Material
Sphere–Cap	Cone–Frustum	Honeycomb Monocoque	Aluminum Titanium Beryllium Fiberglass	Honeycomb Monocoque	Aluminum Fiberglass
Sphere–Cone	Open	Honeycomb Ring Stiffend	Aluminum Magnesium Beryllium Fiberglass	✕	✕
Sphere–Cone	Sphere–Cap	Honeycomb Ring Stiffened	Aluminum Magnesium Beryllium Fiberglass	Honeycomb Monocoque	Aluminum Fiberglass
Smooth–Flare	Open	Monocoque Honeycomb	Titanium Aluminum Fiberglass Beryllium	✕	✕

231

Table 3b   Minimum Structural Gages

Structural Material	Minimum Gages	
	Monocoque & Ring Stiffened	Honeycomb Face Sheets
Aluminum 7075-T6	.020	.012
Titanium 6AL-4V	.016	.005
Beryllium Y5804 QMV-5	.020	.012
Magnesium HK31A-H24	.032	.016
Fiberglass Phenolic	.030*	.030*

Note: Minimum core thickness for honeycomb = .125 inches

* .020 considered in some cases

Table 4   Sphere Cap Forebody - Cone Frustrum Afterbody Run 46
Structural Configuration - Monocoque

Temperature °F	Structural Material	Sphere Cap Forebody
		T_s
	Aluminum 7075-7b	
100		.30
300		.36
500		.73
650		1.15
	Magnesium	
100		.51
300		.51
500		.65
600		1.22
	Beryllium	
100		.30
400		.385
700		.41
1000		.485
1300		.80
	Fiberglas	
100		.375
300		.40
500		.50
700		.70
900		1.40

T_s - Skin Thickness, In.

Table 5   Sphere Cap Forebody - Cone Frustrum Afterbody Run 46
Structural Configuration - Honeycomb

Temperature °F	Structural Material	Sphere Cap Forebody	
		T_f	T_c
	Aluminum 7075-7b		
100		.12	1.0
300		.135	1.0
500		.27	1.0
	Magnesium		
100		.19	1.0
300		.19	1.0
500		.24	1.0
	Beryllium		
100		.13	1.0
400		.14	1.0
700		.155	1.0
1000		.185	1.0
1300		.30	1.0
	Fiberglas		
100		.15	1.0
300		.155	1.0
500		.20	1.0

T_f - Face thickness, in.
T_c - Core thickness, in.

Table 6 Sphere Cap Forebody-Cone Frustrum Afterbody, Run 46

Structural Configuration - Monocoque

Face Material	Cone Frustrum Afterbody
	T_s
Aluminum	.020"
Magnesium	.032"
Beryllium	.020"
Fiberglas	.030"

Structural Configuration - Honeycomb

Face Material	Cone Frustrum Afterbody			
	Core Density	Wgt	T_f	T_c
Aluminum	1.74 lbs/ft^3	.0181	.012	.125
Magnesium	1.74	.0181	.016	.125
Berylluim	1.74	.0181	.012	.125
Fiberglas	1.74	.0181	.030	.125

Wgt - Weight, PSF of Core thickness

T_f - Face thickness, In.

T_c - Core thickness, In.

Table 7   Sphere Cap Forebody - Cone Frustrum Afterbody

Heat Shield

Backface Temperature	ESM (1004) Shield Thickness Inches	
	Sphere Cap Forebody	Cone Frustrum Afterbody
100	.715	.445
200	.602	.315
300	.495	.220
400	.413	.160
500	.347	.122
600	.285	.095
700	.240	.075
800	.200	.060
900	.170	.045
1000	.140	.035
1100	.120	.030
1200	.100	.025

Table 8 60° Sphere Cone 12' Dia Run 46

Structural Configuration - Honeycomb

Temperature $^{\circ}F$	Structural Material	Section 1			Section 2		
		Wgt	T_f	T_c	Wgt	T_f	T_c
100	Aluminum 7075	.776	.012	.125	.809	.012	.159
300		.776	.012	.125	.815	.012	.166
100	Magnesium	.569	.016	.125	.569	.016	.177
300		.569	.016	.125	.569	.016	.185
100	Beryllium	.481	.012	.125	.481	.012	.125
100	Fiberglas	1.377	.030	.125	1.506	.030	.183
500		1.377	.030	.125	1.580	.030	.217

Wgt   -   Weight, PSF

T_f -   Face thickness, in.

T_c -   Core thickness, in.

Table 9   60° Sphere Cone 12'D Run 46

Structural Configuration - Ring Stiffened

Temperature °F	Structural Material	Section 1				Section 2			
		Wgt	L	T_s	H	Wgt	L	T_s	H
100	Aluminum 7075	.544	3.51	.03	.5	.856	2.74	.04	.830
300		.563	3.51	.031	.566	.900	2.74	.04	.935
500		.654	3.51	.032	.977	1.374	2.74	.045	1.581
100	Magnesium	.441	3.51	.036	.731	.761	2.74	.048	1.196
300		.451	3.51	.037	.736	.764	2.74	.048	1.203
500		.514	3.51	.041	.888	.952	2.74	.056	1.442
100	Beryllium	.254	3.51	.02	.561	.427	2.74	.025	.927
500		.257	3.51	.02	.600	.446	2.74	.025	.988
900		.264	3.51	.02	.670	.541	2.74	.030	1.100
1200		.313	3.51	.022	.904	.691	2.74	.030	1.466
100	Fiberglas	.587	3.51	.049	.595	.814	2.74	.057	.981
500		.651	3.51	.053	.732	1.011	2.74	.068	1.197
900		1.333	3.51	.098	1.662	2.195	2.74	.094	2.624

Wgt - Weight, PSF
L   - Ring Spacing, In.
T_s - Skin Thickness, In.
H   - Ring Height, In.

Table 10   60° Sphere Cone 12' D. Run 46

Heat Shield

Temperature	ESM (1004) Shield Thickness-Incnes
100	.74
200	.611
300	.500
400	.416
500	.348
600	.290
700	.240
800	.200
900	.165
1000	.135
1100	.110
1200	.090

Table 11 60° Sphere Cone 12'D Run 19

Structural Configuration - Ring Stiffened

Temperature (°F)	Structural Material	Section 1				Section 2			
		Wgt	L	T_s	H	Wgt	L	T_s	H
100	Aluminum	.494	3.51	.027	.500	.692	2.74	.035	.603
300		.505	3.51	.028	.500	.716	2.74	.035	.681
500		.565	3.51	.029	.783	1.017	2.74	.040	1.168
100	Magnesium	.389	3.51	.033	.579	.569	2.74	.040	.877
300		.398	3.51	.033	.582	.570	2.74	.040	.882
500		.450	3.51	.037	.709	.715	2.74	.048	1.063
100	Beryllium	.249	3.51	.020	.500	.362	2.74	.025	.676
500		.249	3.51	.020	.500	.373	2.74	.025	.721
900		.251	3.51	.020	.529	.393	2.74	.025	.805
1200		.269	3.51	.020	.721	.535	2.74	.030	1.082
100	Fiberglas	.526	3.51	.044	.500	.664	2.74	.054	.715
500		.580	3.51	.048	.579	.818	2.74	.060	.878
900		1.030	3.51	.078	1.360	1.526	2.74	.078	1.972

Wgt - Weight, PSF

L - Ring spacing, In.

T_s - Skin thickness, In.

H - Ring height, In.

Table 12   60° Sphere Cone 12'D Run 19

Structural Configuration-Honeycomb

Temperature ^{o}F	Structural Material	Section 1			Section 2		
		WGT	T_f	T_c	WGT	T_f	T_c
100	Aluminum 7075	.776	.012	.125	.776	.012	.125
300		.776	.012	.125	.777	.012	.125
100	Magnesium	.569	.016	.125	.569	.016	.133
300		.569	.016	.125	.569	.016	.139
100	Beryllium	.481	.012	.125	.481	.012	.125
100	Fiberglas	1.377	.030	.125	1.400	.030	.135
500		1.377	.030	.125	1.458	.030	.162
WGT — Weight, PSF T_f — Face Thickness, In. T_c — Core Thickness, In.							

Table 13
60° Sphere Cone 12' D Run 19
Heat Shield

Temperature	ESM (1004) Shield Thickness – Inches
100	.745
200	.610
300	.508
400	.420
500	.353
600	.300
700	.260
800	.225
900	.195
1000	.165
1100	.140
1200	.120

Table 14   60° Sphere Cone 18.5'D Run A-1

Structural Configuration - Honeycomb

Temperature (°F)	Structural Material	Section 1			Section 2		
		Wgt	T_f	T_c	Wgt	T_f	T_c
100	Aluminum	.860	.012	.212	1.141	.012	.506
300		.868	.012	.220	1.286	.016	.441
100	Magnesium	.602	.017	.226	.774	.022	.463
300		.781	.021	.195	1.371	.039	.319
100	Beryllium	.481	.012	.125	.510	.012	.213
100	Fiberglas	1.647	.030	.247	2.444	.030	.607
500		1.737	.030	.288	2.646	.030	.698

Wgt - Weight, PSF

T_f - Face thickness, In.

T_c - Core thickness, In.

243

Table 15   60° Sphere Cone 18.5'D Run A-1

Structural Configuration - Ring Stiffened

Temperature °F	Structural Material	Section 1				Section 2			
		Wgt	L	T_s	H	Wgt	L	T_s	H
100	Aluminum 7075	1.733	7.080	.096	1.139	2.095	6.942	.112	1.414
300		1.795	7.080	.098	1.331	2.193	6.942	.114	1.647
500		2.137	7.080	.103	2.618	2.885	6.942	.119	3.209
100	Magnesium	1.409	7.080	.115	1.830	1.751	6.942	.132	2.254
300		1.441	7.080	.118	1.845	1.787	6.942	.135	2.271
500		1.652	7.080	.131	2.329	2.094	6.942	.148	2.859
100	Beryllium	.723	7.080	.057	1.316	.934	6.942	.068	1.629
500		.740	7.080	.058	1.429	.966	6.942	.069	1.767
900		.795	7.080	.060	1.643	1.055	6.942	.072	2.026
1200		1.019	7.080	.072	2.379	1.429	6.942	.084	2.919
100	Fiberglas	1.855	7.080	.154	1.416	2.162	6.942	.172	1.750
500		2.062	7.080	.168	1.833	2.431	6.942	.186	2.257
900		3.936	7.080	.265	4.944	5.838	6.942	.335	6.028

Wgt - Weight, PSF

L   - Ring Spacing, In.

T_s - Skin Thickness, In.

H   - Ring Height, In.

Table 16

60° Sphere Cone 18.5' D Run A-1
Heat Shield

Temperature	ESM (1004) Shield Thickness – Inches
100	.678
200	.595
300	.506
400	.418
500	.345
600	.290
700	.240
800	.205
900	.175
1000	.145
1100	.125
1200	.103

Table 17 60° Sphere Cone 12' D Run 41

Structural Configuration - Honeycomb

Temperature $^\circ$F	Structural Material	Section 1			Section 2		
		Wgt	T_f	T_c	Wgt	T_f	T_c
100	Aluminum 7075	.776	.012	.125	.776	.012	.125
300		.776	.012	.125	.776	.012	.125
200	Magnesium	.569	.016	.125	.569	.016	.125
300		.569	.016	.125	.569	.016	.125
100	Beryllium	.481	.012	.125	.481	.012	.125
100	Fiberglas	1.377	.030	.125	1.377	.030	.125
500		1.377	.030	.125	1.377	.030	.125

Wgt   - Weight, PSF

T_f - Face thickness, in.

T_c - Core thickness, in.

Table 18   60° Sphere Cone 12' D   Run 41

Structural Configuration – Ring Stiffened

Temperature (°F)	Structural Material	Section 1				Section 2			
		Wgt	L	T_s	H	Wgt	L	T_s	H
100	Aluminum	.419	3.51	.023	.500	.608	2.74	.030	.613
300		.428	3.51	.023	.500	.632	2.74	.030	.690
500		.478	3.51	.024	.737	.922	2.74	.035	1.152
100	Magnesium	.381	3.51	.032	.555	.569	2.74	.040	.877
300		.381	3.51	.032	.559	.570	2.74	.040	.883
500		.391	3.51	.032	.672	.622	2.74	.040	1.054
100	Beryllium	.249	3.51	.020	.500	.306	2.74	.020	.684
500		.249	3.51	.020	.500	.316	2.74	.020	.728
900		.250	3.51	.020	.510	.336	2.74	.020	.809
1200		.265	3.51	.020	.683	.473	2.74	.025	1.071
100	Fiberglas	.446	3.51	.037	.500	.605	2.74	.045	.722
500		.490	3.51	.040	.556	.731	2.74	.053	.878
900		.868	3.51	.066	1.235	1.375	2.75	.070	1.884

Wgt - Weight, PSF

L - Ring Spacing, In.

T_s - Skin thickness, In.

H - Ring height, In.

Table 19   60° Sphere Cone 12'D Run 41

Heat Shield

Temperature	ESM (1004) Shield Thickness (Inches)
100	.74
200	.611
300	.500
400	.416
500	.348
600	.290
700	.240
800	.200
900	.165
1000	.135
1100	.110
1200	.090

Table 20   60° Sphere Cone Forebody - Sphere Cap Afterbody

Structural Configuration - Honeycomb

Temperature °F	Structural Material	Sphere Cone Forebody		
		Wgt	T_f	T_c
100	Aluminum 7075	1.2	.02	.125
300		2.23	.039	.125
100	Magnesium	1.9	.054	.125
300		3.341	.094	.125
100	Beryllium	1.027	.027	.125
100	Fiberglas	1.61	.031	.211
300		2.578	.063	.125

Face Material	Sphere Cap Afterbody			
	Core Density	Wgt	T_f	T_c
Aluminum	1.74 lb/ft^3	.0181	.012	.125
Magnesium	1.74 lb/ft^3	.0181	.016	.125
Beryllium	1.74 lb/ft^3	.0181	.012	.125
Fiberglas	1.74 lb/ft^3	.0181	.030	.125
Wgt - Weight, PSF T_f - Face thickness, in. T_c - Core thickness, in.				

249

Table 21   60° Sphere Cone Forebody – Sphere Cap Afterbody

Structural Configuration – Ring Stiffened

Temperature °F	Structural Material	Sphere Cone Forebody			
		Wgt	L	T_s	H
100	Aluminum 7075	.901	3.065	.043	.879
300		1.16	3.065	.055	.990
500		4.489	3.065	.225	1.676
100	Magnesium	1.428	3.065	.107	1.268
300		1.451	3.065	.109	1.276
500		2.31	3.065	.177	1.529
100	Beryllium	.761	3.065	.054	.982
500		.897	3.065	.064	1.047
900		1.186	3.065	.086	1.166
1200		2.485	3.065	.185	1.555
100	Fiberglas	.904	3.065	.065	1.039
500		1.476	3.065	.108	1.269

Wgt   –   Weight, PSF

L   –   Ring Spacing, in.

T_s –   Skin thickness, in.

H   –   Ring height, in.

Table 22   60° Sphere Cone Forebody-Sphere Cap Afterbody

Structural Configuration-Monocoque

Face Material	Sphere Cap Afterbody
	T_s
Aluminum	.020
Magnesium	.032
Beryllium	.020
Fiberglas	.030

Table 23   60° Sphere Cone Forebody–Sphere Cap Afterbody

HEAT SHIELD

Backface Temperature	ESM (1004) Shield Thickness (Inches)
100	.780
200	.610
300	.505
400	.415
500	.340
600	.285
700	.230
800	.190
900	.155
1000	.130
1100	.100
1200	.085

Table 24 Tension Shell

Nose and Tension Shell
Monocoque Shell Thicknesses

Temperature Range - °F	Material	Thickness - Inches
100 ⟶ 400	Aluminum	.02
100 ⟶ 700	Fiberglas	.032
100 ⟶ 1200	Beryllium	.02
100 ⟶ 1000	Titanium	.016

Honeycomb Shell Thicknesses

Temperature Range - °F	Material	Thickness - Inches	
		Face	Core
100 ⟶ 400	Aluminum	.012	.125
100 ⟶ 700	Fiberglas	.03	.125
100 ⟶ 1200	Beryllium	.012	.125
100 ⟶ 1000	Titanium	.005	.125

Table 25
Tension Shell
Aft Ring Requirements
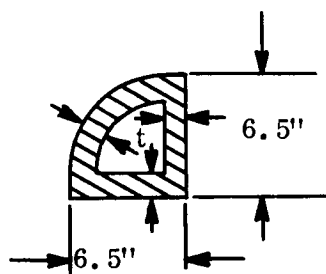
$$I_x = I_y = 137.5\,t$$

$$A = 23.2\,t$$

Material	Temperature - °F	Thickness, t - Inches
Aluminum 7075-T6	100	.045
	200	.045
	400	.046
Beryllium	100	.028
	400	.028
	700	.028
	1000	.030
	1200	.034
Fiberglas	100	.068
	300	.069
	500	.074
	700	.082
Titanium	100	.039
	200	.039
	400	.041
	600	.042
	800	.043
	1000	.044

254

Table 26   Tension Shell

Heat Shield

Backface Temperature	ESM (1004) Shield Thickenss - Inches
100	.805
200	.695
300	.585
400	.500
500	.425
600	.365
700	.310
800	.260
900	.225
1000	.186
1100	.145
1200	.115

Table 27   Aft Ring for Sphere Cap
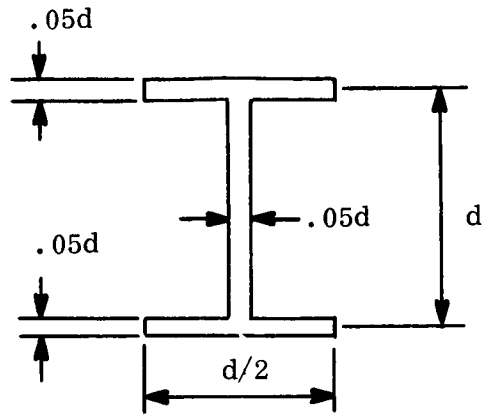
Diameter	Vehicle Weight	Material	d, inches
12'	1030^{lbs}	7075-T6 Alum.	1.75"
12'	1030^{lbs}	HK31A Mag.	2.5"
12'	1030^{lbs}	Y5804 QMV5 Bery.	2.0"
12'	1030^{lbs}	Fiberglas	2"

Table 28 Aft Ring for 60° Sphere Cone
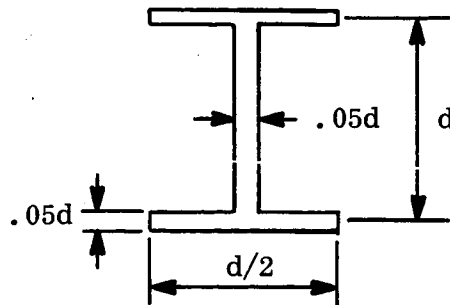
Diameter	Vehicle Weight	Material	Depth, d inches
* 18.5'	3030^{lbs}	7075-T6 Aluminum	3.5"
* 18.5'	3030^{lbs}	HK31A Magnesium	4.5"
18.5'	3030^{lbs}	Y5804 QMV5 Beryllium	3."
* 18.5'	3030^{lbs}	Fiberglas	5.0"
12.0'	1020^{lbs}	7075-T6 Aluminum	1.75"
12.0'	1020^{lbs}	HK31A Magnesium	2.75"
12.0'	1020^{lbs}	Y5804 QMV5 Beryllium	1.75"
* 12.0	1020^{lbs}	Fiberglas	2.25"
12.0	1530^{lbs}	7075-T6 Aluminum	2.0"
12.0	1530^{lbs}	HK31A Magnesium	2.75"
12.0	1530^{lbs}	Y5804 QMV5 Beryllium	2.0"
12.0	1530^{lbs}	Fiberglas	2.25"

*Buckling governed cases

Table 29 Minimum Weight Designs

Vehicle No.	Forebody Type	$M/C_D A$	Material/Construction Type

1	Sphere Cap	.20	Honeycomb
			  Beryllium
			  Fiberglas
			Monocoque
			  Beryllium
			  Fiberglas

2	Sphere Cone
	(Includes zero
	spin case also)
		.20	Honeycomb
			  Magnesium
			  Fiberglas
			Ring Stiffened
			  Beryllium
			  Fiberglas

3	Sphere Cone	.25	Honeycomb
			  Beryllium
			  Fiberglas
			Ring Stiffened
			  Beryllium
			  Magnesium

4	Sphere Cone	.30	Honeycomb
			  Magnesium
			  Fiberglas
			Ring Stiffened
			  Beryllium
			  Magnesium

5	Sphere Cone	.20	Honeycomb
			  Beryllium
			  Aluminum
			Ring Stiffened
			  Beryllium
			  Fiberglas

6	Smooth – Flare	.20	Honeycomb
			  Beryllium
			  Titanium
			Monocoque
			  Beryllium
			  Fiberglas

Table 30   Flight Environment At Maximum g Level

RUN No.	ATM MODEL VM-	ALT. FT.	M_∞	V_∞ FT/SEC.	ρ_∞ PSF	$\rho_\infty \times 10^{-5}$ SLUGS/FT³	q_∞ PSF	α' DEG	α DEG	β DEG	$C_{P_{MAX}}$
A-1	8	60,300	27.8	14,758	.8296	.40794	446.9	- 1.88	-1.78	- .60	1.951
A-2	8	60,819	27.7	14,626	.8161	.40132	429.0	- 0.016	—	.016	1.951
A-3	7	119,668	15.4	13,690	.9855	.17179	160.9	0.039	—	.039	1.915
A-4	7	117,306	15.2	13,570	1.0361	.18060	166.0	- 0.38	—	- .38	1.925
20	8	75,489	18.4	9,702	.3396	.16702	78.6	-11.1	-3.97	10.4	1.936
9	8	76,158	18.1	9,574	.3263	.16047	73.5	0.356	—	- .356	1.935
41	8	75,993	18.1	9,572	.3295	.16205	74.2	—	—	—	1.935
46	8	63,853	18.2	9,599	.6823	.33550	154.6	-13.5	-8.48	-10.6	1.934
47	8	65,740	18.1	9,542	.6093	.29950	136.4	1.78	1.78	—	1.934
21	7	157,718	10.8	9,597	.4414	.07695	35.4	13.1	—	13.1	1.905
13	8	73,913	14.0	7,395	.3733	.18356	50.2	- 2.02	—	-2.02	1.917
16	8	72,810	14.2	7,480	.3988	.19609	54.9	13.4	—	13.4	1.917
19	8	69,139	18.5	9,744	.4969	.24435	116.0	9.55	9.55	- .01	1.936
15	8	66,049	14.1	7,453	.5981	.29409	81.7	11.1	—	-11.1	1.916

NOTE:

VM - 8 ~ 100% CO_2

VM - 7 ~ 20% CO_2, 80% N_2 by Volume

Table 31 Stagnation Environment at Maximum g Level

Run No.	$\dfrac{P_t}{PSF}$	$\dfrac{\rho_t \times 10^4}{Slug/ft.^3}$
A-1	867.8016	.86225
A-2	838.5302	.84799
A-3	308.8786	.21321
A-4	318.9547	.22250
20	152.4847	.26658
9	142.6074	.25302
41	143.9552	.25539
46	299.666	.52680
47	264.3893	.46807
21	67.7687	.08154
13	96.5756	.22886
16	105.5748	.24625
19	225.0199	.39041
15	157.1421	.36614

Table 32   Body Surface Flow Properties

$\dfrac{C_p}{C_{p_{MAX}}}$	M	$\dfrac{\rho}{\rho_t}$	$\dfrac{q}{p_t}$
.70	.814	.7232	.2535
.69	.830	.7138	.2601
.68	.847	.7044	.2665
.67	.863	.6949	.2728
.66	.879	.6854	.2791
.65	.896	.6760	.2851
.64	.912	.6665	.2910
.63	.928	.6570	.2968
.62	.945	.6474	.3024
.61	.961	.6380	.3078
.60	.977	.6284	.3131
.59	.993	.6188	.3182
.58	1.010	.6092	.3232
.57	1.026	.5996	.3280
.56	1.042	.5900	.3327
.55	1.059	.5804	.3372
.54	1.075	.5708	.3414
.53	1.092	.5611	.3456
.52	1.109	.5514	.3495
.51	1.126	.5418	.3533
.50	1.142	.5321	.3568
.48	1.177	.5124	.3633
.46	1.211	.4930	.3690
.44	1.247	.4734	.3739
.42	1.283	.4537	.3779
.40	1.320	.4339	.3810
.38	1.358	.4141	.3830
.36	1.397	.3942	.3841
.34	1.437	.3742	.3840
.32	1.478	.3541	.3828
.30	1.522	.3338	.3803
.28	1.567	.3135	.3764
.26	1.615	.2930	.3712
.22	1.718	.2517	.3557
.20	1.775	.2307	.3453

Table 33   60° Sphere Cone Skirt Pressure, $Cp/C_{p_{max}}$

α \ α	0°	5°	10°	15°
0°	.785	.840	.900	.940
90°	.785	.775	.750	.720
180°	.785	.715	.620	.533

Table 34. Body Surface Flow Properties

$\dfrac{C_p}{C_{p_{max}}}$	M	$\dfrac{\rho}{\rho_t}$	$\dfrac{q}{p_t}$
1.0	.0	1.0	0
.98	.195	.9818	.0203
.96	.245	.9635	.0397
.94	.338	.9452	.0587
.92	.392	.9268	.0773
.90	.441	.9084	.0955
.88	.485	.8900	.1133
.86	.527	.8716	.1307
.84	.567	.8531	.1477
.82	.605	.8345	.1642
.80	.642	.8160	.1803
.78	.678	.7973	.1959
.76	.713	.7787	.2110
.74	.747	.7600	.2257
.72	.780	.7412	.2398
.70	.814	.7232	.2535

Table 35   Voyager/Mars Engineering Model Atmosphere

Property	Symbol	Dimension	VM3	VM8
Surface Pressure	Po	lbs/ft^2	20.9 (10 mb)	10.4 (5 mb)
Surface Density	ρo	$slugs/ft^3 \times 10^5$	2.65	2.56
Surface Temperature	To	^{o}R	495	366
Stratospheric Temp.	Ts	^{o}R	360	180
Accel. of Gravity at Surface	G	fps	12.3	12.3
Composition Carbon Dioxide (By Mass) Carbon Dioxide (By Volume) Nitrogen (By Mass) Nitrogen (By Volume)			28.2 20 71.8 80	100 100 0.0 0.0
Argon (By Mass) Argon (By Volume)			0.0 0.0	0.0 0.0
Molecular Weight	M		31.2	44
Specific Heat of Mixture	Cp		.23	.166
Specific Heat Ration	γ		1.38	1.37

Table 36   ESM Rekap Input Parameters and Properties

Quantity	Symbol	Units	Temp. ($^\circ$R)	ESM
Virgin Thermal Conductivity	K	Btu/ft-sec$^\circ$R	460 860 1335 2075 3460	.000025 .000022 .000021 .000027 .000042
Char Thermal Conductivity	K	Btu/ft-sec$^\circ$R	460 860 1335 2075 3460	.000093 .000081 .000078 .0001 .000155
Char Specific Heat	Cp	Btu/lb$^\circ$R	Same as Virgin Specific Heat	
Virgin Density	ρ	lb/ft^3		36
Char Density	ρ_c	lb/ft^3		14.4
Pre-Exponential Factor (1) (2) (3)	A_1 A_2 A_3			30000 --
Activation Energy (1) (2) (3)	E_1 E_2 E_3			47500 --
Order of Reaction	n			2
Virgin Specific Heat	C_p	Btu/lb$^\circ$R	460 860 1335 2075 3460	.305 .429 .44 .44 .87

Table 37 Thermal Properties of Structural Materials

Property / Material	Temperature °R	Thermal Conductivity Btu/ft. Sec °R	Specific Heat Btu/ Lb - °R	Density Lbs/ft³
Aluminum	500	.0344	.22	170
	2000	.0344	.22	170
Fiberglas	500	.000065	.247	119
	2000	.000065	.247	119
Aluminum Honeycomb — Aluminum Facing	500	.0344	.22	170
	2000	.0344	.22	170
Aluminum Honeycomb Core	500	.0003	.25	1.74
	2000	.0003		1.74
Aluminum Facing	500	.0344	.22	170
	2000	.0344	.22	170
Fiberglas Honeycomb — Fiberglas Facing	500	.000065	.247	119
	2000	.000065	.247	119
Fiberglas Honeycomb Core	500	.00000134	.281	1.74
	2000	.00000134	.281	1.74
Fiberglas Facing	500	.000065	.247	119
	200	.000065	.247	119

Table 38 Vehicle Frequencies for Various Materials with Effects of Temperature
(Heat Shield Mass & Stiffness Included)

Vehicle #1, Sphere Cap with Cone Afterbody, Honeycomb

Material	Temp. (°F)	Frequency (CPS) (Accordian Mode)	Frequency (CPS) (Shuttlecock Mode)
Aluminum	100	57.8	22.0
Aluminum	500	73.4	28.8
Magnesium	100	56.9	21.6
Magnesium	500	55.0	20.9
Beryllium	100	125.9	47.0
Beryllium	1300	117.3	45.0
Fiberglas	100	34.3	13.0
Fiberglas	500	36.4	13.8

Vehicle #1, Sphere Cap with Cone Afterbody, Monocoque

Material	Temp. (°F)	Frequency (CPS) (Accordian Mode)	Frequency (CPS) (Shuttlecock Mode)
Aluminum	100	69.1	25.7
Aluminum	500	98.2	38.9
Magnesium	100	69.5	26.0
Magnesium	500	70.2	27.2
Beryllium	100	145.8	53.3
Beryllium	1300	147.1	55.3
Fiberglas	100	41.8	15.4
Fiberglas	500	57.0	19.4

Vehicle No. 2, 12' Dia. Sphere Cone, M/ $C_D A$ = .2 (Spin Case); Honeycomb

Material	Temp. (°F)	Frequency (CPS) (Accordian Mode)	Frequency (CPS) (Shuttlecock Mode)
Aluminum	100	74.6	39.5
Aluminum	300	76.1	42.0
Magnesium	100	69.5	36.8
Magnesium	300	75.1	39.7
Beryllium	100	154.6	81.6
Fiberglas	100	47.3	25.2
Fiberglas	500	47.3	25.1

Table 39   Vehicle Frequencies for Various Materials, with Effects of Temperature (Cont'd)
(Heat Shield Mass & Stiffness Included)

Vehicle #2, 12' Dia. Sphere Cone, $M/C_D A = .2$ (No Spin), Honeycomb

Material	Temp. ($^\circ$F)	Frequency (CPS) (Accordian Mode)	Frequency (CPS) (Shuttlecock Mode)
Aluminum	100	74.9	39.7
Aluminum	300	79.8	42.2
Magnesium	100	69.5	36.8
Magnesium	300	75.1	39.7
Beryllium	100	154.6	81.9
Fiberglas	100	47.9	25.4
Fiberglas	500	48.8	25.8

Vehicle #3, 18.5' Dia. Sphere Cone, $M/C_D A = .25$, Honeycomb

Material	Temp. ($^\circ$F)	Frequency (CPS) (Accordian Mode)	Frequency (CPS) (Shuttlecock Mode)
Aluminum	100	49.9	31.8
Aluminum	300	58.3	37.0
Magnesium	100	61.1	35.2
Magnesium	300	70.4	44.9
Beryllium	100	107.9	68.4
Fiberglas	100	30.2	19.5
Fiberglas	500	28.5	18.3

Vehicle #4, 12' Dia. Sphere Cone, $M/C_D A = .3$, Honeycomb

Material	Temp. ($^\circ$F)	Frequency (CPS) (Accordian Mode)	Frequency (CPS) (Shuttlecock Mode)
Aluminum	100	73.3	37.7
Aluminum	300	84.4	40.3
Magnesium	100	68.0	35.0
Magnesium	300	74.2	38.0
Beryllium	100	151.7	78.0
Fiberglas	100	46.4	24.0
Fiberglas	500	47.3	24.3

Table 40   Vehicle Frequencies for Various Materials, with Effects of Temperature (Cont'd)
(Heat Shield Mass & Stiffness Included)

Vehicle #5, Sphere Cone with Sphere Cap Afterbody, Honeycomb

Material	Temp. ($^\circ$F)	Frequency (CPS) (Accordian Mode)	Frequency (CPS) (Shuttlecock Mode)
Aluminum	100	60.8	7.43
Aluminum	300	81.4	10.0
Magnesium	100	76.5	9.5
Magnesium	300	92.0	12.0
Beryllium	100	142.8	17.5
Fiberglas	100	38.7	4.7
Fiberglas	300	55.1	6.1

Vehicle #6, Tension Shell, Monocoque

Material	Temp. ($^\circ$F)	Frequency (CPS) (Accordian Mode)	Frequency (CPS) (Shuttlecock Mode)
Aluminum	100	100.0	52.0
Aluminum	400	105.6	52.2
Fiberglas	100	53.1	27.6
Fiberglas	700	49.6	23.5
Beryllium	100	205.7	108.3
Beryllium	1200	248.2	111.7
Titanium	100	106.8	55.5
Titanium	100	114.5	52.9

Vehicle #6, Tension Shell, Honeycomb

Material	Temp. ($^\circ$F)	Frequency (CPS) (Accordian Mode)	Frequency (CPS) (Shuttlecock Mode)
Aluminum	100	105.4	55.8
Aluminum	400	108.6	55.4
Fiberglas	100	71.4	37.8
Fiberglas	700	63.1	31.2
Beryllium	100	218.9	115.6
Beryllium	1200	239.8	112.6
Titanium	100	81.7	43.8
Titanium	1000	89.2	50.2

Table 41 Aft Ring Dynamic Stability

FREQUENCY RATIO

EXCITATION PARAMETER
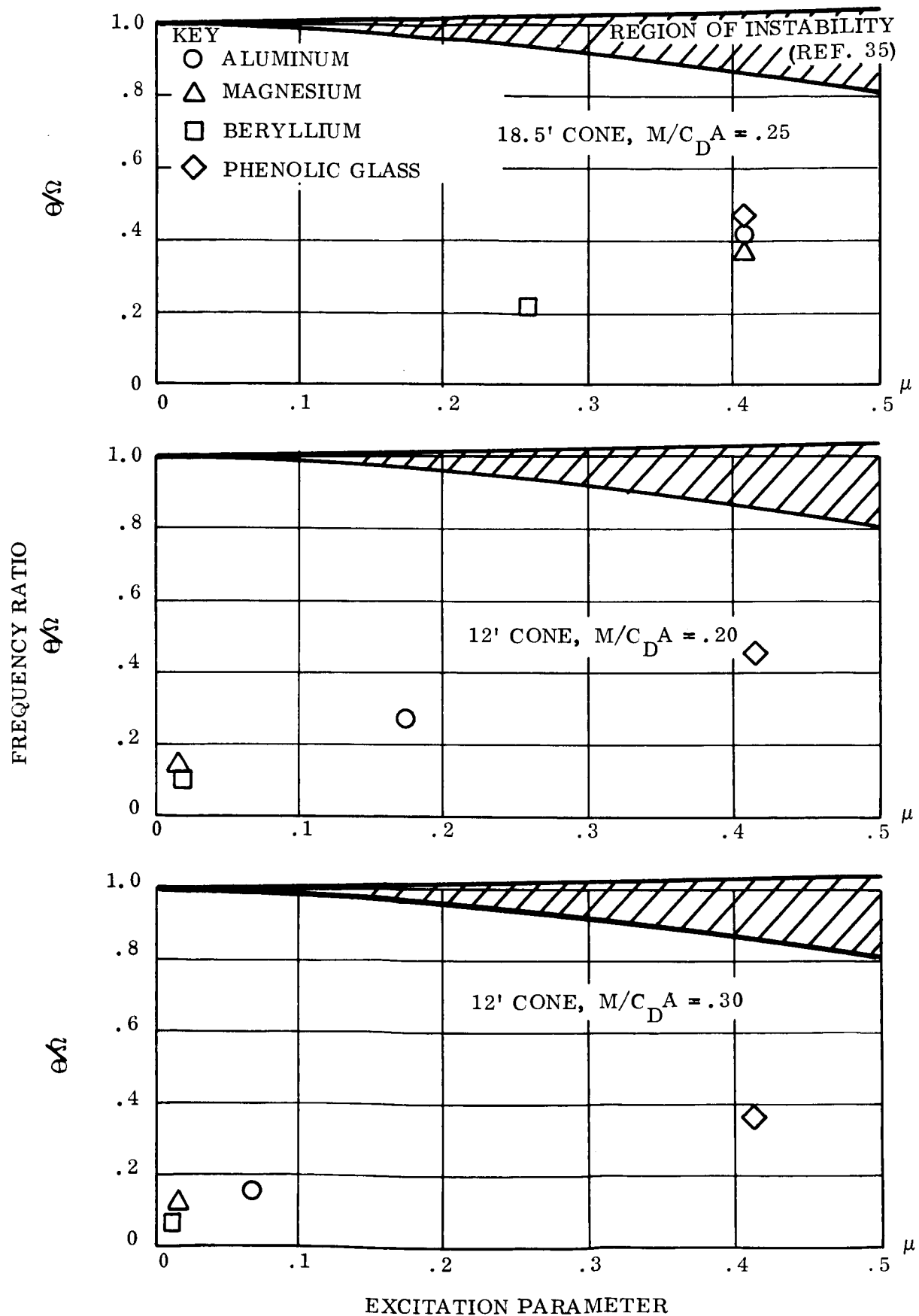
Table 42   Angle of Attack at Peak Dynamic Pressure

TRAJECTORY OR RUN NUMBER	ζ (DEGREES)	q (PSF)	TIME (SEC)
A-1 VM # 8 18.5' dia	13.5	446.99	88.63
46 VM # 8 12' dia	16.5	154.57	157.5908
19 VM # 8 12' dia	9.55	115.99	228.2716

Table 43

Roll Resonance Analysis

p= roll rate = 1 rad/sec						
time (t) (sec)	Mach No.	Total Angle of Attack (σ) (deg)	dynamic pressure (q) (lbs/ ft^2)	Altitude (h) (ft)	ω_o (cyc/ sec)	$\Delta\omega$ (cyc/ sec)
125	29.5	105	$\approx$ 0	190000	.089	.070
140	29	48	9	125000	.43	
157	18	18	155	70000	2.0	↓
170	6	15	50	50000	1.06	
225	1.0	17	3	20000	.2	

p = 10 rads/sec						
125	29.5	105	$\approx$ 0	190000	.89	.7
140	29	48	9	125000	.98	
157	18	18	155	70000	2.19	↓
170	6	15	50	50000	1.36	
225	1.0	17	3	20000	.91	

Table 44

Panel Flutter Parameters

Station	Mat./Temp	Traj No. A-1		Traj No. 46	
		$\phi \times 10^4$	$\dfrac{\lambda}{\pi^4}$	$\phi \times 10^4$	$\dfrac{\lambda}{\pi^4}$
5	Alum/100	39.44	54.22	28.00	18.81
	Alum/400	51.78	123.52	37.07	42.85
	FG/100	43.22	69.44	30.30	24.09
	FG/700	88.37	598.42	62.10	207.60
	Bery/100	32.17	28.60	22.54	9.92
	Bery/1200	45.69	82.10	32.07	28.48
	Titan/100	40.86	58.67	28.66	20.35
	Titan/1000	71.39	312.70	50.04	108.48
25	Alum/100	105.32	72.47	74.19	25.21
	Alum/400	139.30	165.10	97.49	57.44
	FG/100	114.79	92.83	80.60	32.30
	FG/700	235.28	799.86	164.75	278.29
	Bery/100	85.16	38.24	59.87	13.30
	Bery/1200	121.36	109.736	85.07	38.18
	Titan/100	108.44	78.416	76.09	27.28
	Titan/1000	189.61	417.97	133.07	145.42
45	Alum/100	212.17	80.17	149.54	27.44
	Alum/400	280.84	182.62	196.62	62.50
	FG/100	201.27	102.67	162.34	35.14
	FG/700	395.5	884.78	331.71	302.81
	Bery/100	171.55	42.29	120.64	14.47
	Bery/1200	243.69	121.38	171.83	41.54
	Titan/100	219.25	86.74	153.40	29.69
	Titan/1000	381.16	462.33	268.10	158.23

Table 45. Sphere-Cone Inviscid Wake Characteristics

M_∞	$\dfrac{Pb}{P_\infty}$	Mb	$\dfrac{\rho b}{\rho t}$	$\dfrac{qb}{Pt}$	θb (deg)
14.2	2.02	3.44	.0145	.0522	37.1
18.2	2.20	3.64	.0100	.0384	43.8
27.8	2.30	4.04	.00485	.0205	53.3

$$\frac{r}{D} = 0.05 \qquad \frac{R}{D} = 0.1$$
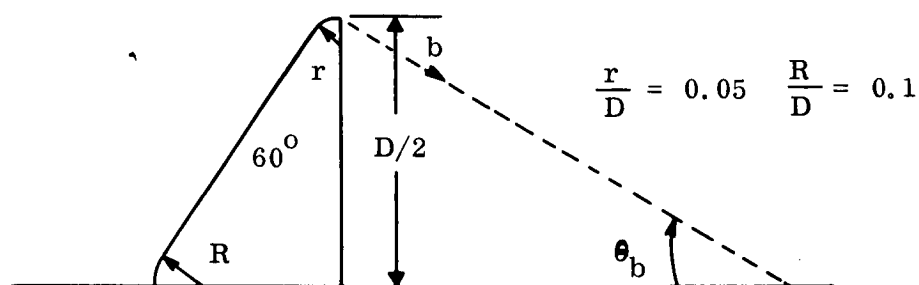
ρt Stagnation Density given in Table II

Pt Stagnation Pressure given in Table II

274

Table 46 Boundary Layer and Wave Acoustics Vehicle No. 2 - 12 ft Dia.,
Sphere Cone, $M/C_D A = .2$ Trajectory No. 46

	Free Stream	Boundary Layer	Wake
Velocity, fps (V)	9594	1650	6594
Mach No. (M)	18.2	.67	3.64
Dynamic Pressure, psf (g)	154.6	57.5	-
Pressure, psf (p)	.6823	235	1.501
Density, lb $\sec^2/\text{ft}^4$ (ρ)	$.3355 \times 10^{-5}$	$.4225 \times 10^{-4}$	-
Acoustic Pressure, psf (σ)	-	.402	.059
Acoustic Pressure, db (σ)	-	120	103
Frequency Max Acoustic Power cps (f)	-	246000	131
Shell Vibration, g^2/cps	-	$.63 \times 10^{-6}$	$.17 \times 10^{-9}$
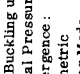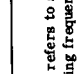
Table 47 Boundary Layer and Wake Acoustics Vehicle No. 3
18.5 ft Dia. Sphere Cone, $M/C_D A = .25$

	Free Stream	Boundary Layer	Wake
Velocity, fps (V)	14578	2200	9219
Mach No. (M)	27.8	.67	4.04
Dynamic Pressure, psf (g)	446.9	165	-
Pressure, psf (p)	.8296	680	1.908
Density, lb sec^2/ft^4 (ρ)	4.079×10^{-4}	$.69 \times 10^{-4}$	-
Acoustic Pressure, psf (σ)	-	1.15	.0587
Acoustic Pressure, Db (σ)	-	129	103
Frequency, Max Acoustic Power cps	-	82,000	126
Shell Vibration, g^2/cps	-	$.38 \times 10^{-5}$	$.18 \times 10^{-9}$

Table 48   Boundary Layer and Wake Acoustics

Vehicle No. 6 12 ft dia. Flare Cone	Free Stream	Boundary Layer	Wake
Trajectory No. 46			
Velocity, fps (V)	9599	3150	6594
Mach No. (M)	18.2	1.33	3.64
Dynamic Press., psf (q)	154.6	114	-
Pressure, psf (p)	.6823	120	2.10
Density, lb $\sec^2/\text{ft}^4$ (ρ)	$.335 \times 10^{-5}$	$.217 \times 10^{-4}$	-
Acoustic Pressure, psf (σ)	-	.798	.082
Acoustic Pressure, Db (σ)	-	125	106
Frequency of Max Acoustic Power, cps	-	104,000	131
Shell Vibration, g^2/cps	-	$.44 \times 10^{-5}$	$.31 \times 10^{-9}$

Table 49 Summary of Results

AEROELASTIC MECHANISM	DEFORMATION MODES INVOLVED	VEHICLE FAMILY	SECTIONS OF REPORT	CHARACTERISTIC FREQUENCY (CPS)	RESULTS	MAJOR REASON FOR RESULTS	NEED FOR FUTURE EFFORT
STATIC DIVERGENCE: TENSION SHELL NOSE DIVERGENCE / UMBRELLA COLLAPSE	Umbrella Collapse: Static Buckling under External Pressure / Nose Divergence: Asymmetric Buckling Mode	Sphere Cone / Smooth Flare	2.0 3.3.3.1 3.3.5	0 * 0	• Designed Against Static Collapse • No Nose Divergence	• Basic Design Condition • Tension Field Not Destroyed by Angle of Attack	
AFT RING PARAMETRIC RESONANCE	Coupling of Short Period and Ring Bending Mode	Sphere Cone / Smooth Flare	3.3.3.3 3.3.5	0-2 *	• No Parametric Resonance Found	• Frequencies Well Separated	
ACCORDIAN MODE INSTABILITY:	Primary Vehicle Longitudinal Mode	Sphere Cone / Smooth Flare	2.0 3.3.3.2 3.3.5	28-155 * 50-248	• Nodal Location Near Aft End • Instability Not Envisioned	Complete Stability Analysis Not Possible Because Analytical Tools Do Not Exist at the Moment	Tunnel Test Recommended to Explore Existence of Instability Mechanism
SHUTTLECOCK INSTABILITY:	Primary Vehicle Lateral Mode	Sphere Cone / Smooth Flare	2.0 3.3.3.3	18-82 24-116	• Nodal Location Just Aft of Nose Instability Not Envisioned, But More Possible Than Previous Case	Same as Above	Same as Above
SPIN-SHORT PERIOD RESONANCE:	Rigid Body Rotation Modes	Sphere Cap / Sphere Cone / Smooth Flare	2.0 3.3.3.4 3.3.5	0-2 * 0-2 0-2	• No Coning Difficulties Found	• Moment of Inertia (Roll/Pitch) Preclude Resonance	
PANEL FLUTTER:	Local Skin Panel Modes	Sphere Cone / Smooth Flare	2.0 3.3.3.5 3.3.5	Above 200	• No Flutter Found	• Dynamic Pressure Too Low	
ACOUSTIC NOISE EXCITATION:	Local Skin Panel Modes	Sphere Cap / Sphere Cone / Smooth Flare	2.0 3.3.4.1 3.3.5	Above 200	• No Excitation Difficulties	• Boundary Layers are Laminar, No Difficulties Even if the B.L. is Taken to be Turbulent (Low DB, Energies Distributed, and Small Correlation Effects)	
SHOCK INSTABILITY:	Local Skin Panel Modes (Possibly Vehicle Lateral Mode)	Sphere Cap / Sphere Cone / Smooth Flare	2.0 3.3.4.2 3.3.5	Above 200	• Excitation Not Likely	• Shock Pressure Variation Probably Small (Associated With Low q)	• Tunnel Test Considered Worthwhile
BUFFETING & WAKE NOISE	Local Skin Panel Modes	Sphere Cap / Sphere Cone / Smooth Flare	2.0 3.3.4.3 3.3.5	Above 200	• No Excitation Difficulties	• Very Low DB (or RMS) Excitation Levels	

* The 0-2 cps frequency range refers to static conditions (0 cps) and the short period rigid body frequencies with on upper limit of 2 cps; remaining frequencies refer to structural frequencies.

Jet Propulsion Laboratory
Pasadena, California

ERRATA AND CHANGES* TO FINAL REPORT

JPL Contract 951312 "Aerothermoelastic Effects
on Unmanned Entry Vehicles for Mars"

by

General Electric
Re-Entry Systems Department
25 October 1966

Page

i   add "(Minor changes by JPL, 25 Nov. 1966)*" below date

ii   6th line, 1st paragraph, "Institude" should be "Institute"
7th line, 1st paragraph, "Spiegal" should be "Spiegel"

iii/iv 3.2.2 should be "Heat Shield Requirements and Aerodynamic Heating"
3.2.3 should be "Aeroshell Thermal Response" (Remove "Aerodynamic Heating")

1   4th line from bottom "...on the order of 300,000 PSF." should be
"...on the order of up to 300,000 PSF.*"
add footnote "*ballistic entry"

11   "ANALYSIS AND DISCUSSION" should be "ANALYSIS AND RESULTS"

12   2nd line from bottom, "assummed" should be "assumed"
place * after "...follows:", add footnote, "*All heat shield tabulations
are from section 3.2.2"

17,18 "tan ϕ" should be "tan θ"

20   2nd equation, delete $(1-\mu/2)$ and change Sin ϕ to Cos ϕ
3rd equation, delete subscript 3 on R^3 and change t_{eff} to t_{eff}^3

21   replace paragraph at bottom of p. 21 with attached overlay

22   replace entire page with attached overlay

31   middle of page "$(10)^{13}$" should be "10^{-3}"

33   2nd line from bottom, "stesses" should be "stresses"

35   add to title of 3.2.2 "...AND AERODYNAMIC HEATING"

37   in title of 3.2.3, remove "AERODYNAMIC HEATING" and replace with
"AEROSHELL THERMAL RESPONSE"

*in consultation with contractor

39	top of page, replace the first sentence by the attached overlay. middle of page, replace sentence starting with "Temperature histories..." by attached overlay
43	top of page below right hand side of equation "φ = circumferential angle from windward meridian"
44	10th line from bottom, "frequenceis" should be "frequencies"
60	1st sentence, 2nd paragraph, change "investiagte" to "investigate"
61	4th line, 2nd paragraph, change "mught" to "might"
69	2nd paragraph, add "(ref. 1):" after "relationship"
74	2nd paragraph, 5th line, change "accommodating" to "precluding"
78	11th line from bottom, change "or to" to "order to" 10th line from bottom, add comma after "solution" 9th line from bottom, add comma after "analytically"
81/82	1st line, "Table 48" should be "Table 49"
83/84	item (4), remove last sentence, add a comma after "testing" in first sentence and add "... such as entry vehicle dynamic stability."
86	top line change "(or mass)" to "(or entry vehicle mass)"
87/88	12th line down, add "α' " after "α " and "total angle of attack" after "angle of attack"
96	Figure 2 geometry of vehicle numbers 2 and 4 should be changed to that vehicle no. 3 (sphere-cone)
103	change γ_2 to r_2
155	in caption "θ = 60 Ft" should be "θ = 60°"
173	add number to abscissa same as Figure 78
262	Table 33, lower "α " should be "φ "

To calculate an equivalent monocoque shell of the same stiffness, the following equations are used:

$$t_{eff} = \sqrt{3} \ (t_c + t_f)$$

$$E_{eff} = \frac{2 \ E_f \ t_f}{t_{eff}}$$

Having determined the load Q from the previous equations, it now remains to investigate the ring for buckling due to a radial loading. The critical load Q_{cr} is given as follows:

$$Q_{cr} = \frac{3 \ E_R \ I_R}{R^3}$$

Where E_R = modulus of elasticity of the ring material

I_R = moment of inertia of the ring

In checking the ring for buckling, any inertia relief of the shell has been neglected. The only loading that is considered is the aerodynamic pressure acting on the shell. Results for the aft ring designs for the sphere cap and 60° sphere cone are listed in Tables 27 and 28. Rings that are designed based on buckling due to external pressure have been so designated. All other rings are based on boost loading conditions.

<u>Selection of Optimum Structural Materials for Forebody Configurations</u>

In order to reduce the number of materials to be investigated from four to two, the materials that result in the minimum weight design will be retained for further study. Figures 11 thru 24 depict the weights of the forebody and heat shield* for each of the vehicles under study. The materials listed for Vehicle No. 2 include both the spin and no-spin cases.

It must be noted that for Vehicles No. 2, 3, 4, and 5 the beryllium honeycomb has been designed for only one outer face (bondline) temperature (as shown in Figures

*All heat shield weights are from section 3.2.2

11 to 24). These designs, for the all honeycomb materials, were generated thru the use of the SILC-SILO computer program which assumes that the inner face of the honeycomb is at a constant 100°F while the outer face attains the heat shield back face temperature. This induces severe thermal stresses for the beryllium honeycomb designs (due to the high modulus of elasticity), and consequently the outer face is not allowed to operate at more than 100°F for the computer generated designs. The other materials are also affected by thermal stresses, but the effect is not as great as for beryllium (due to the relatively high modulus to yield strength ratio for beryllium). It can be concluded that the beryllium honeycomb designs are usually among the two lightest weight designs, independent of the 100°F limitation.

Some of the fiberglass honeycomb shells, and one monocoque, are based on 0.03 inch minimum gauge which results in a heavier structure. However it has been ascertained that 0.02 inch is feasible, thus resulting in lighter structures. The designs that are affected are indicated on the figures. In determining the two minimum weights, the 0.02 inch fiberglass was considered instead of the 0.03 inch. Even though fiberglass is not always among the two lightest weight designs, it will still be considered for all designs because of its desirable transparent radio frequency properties.

Figures 25 thru 26 depict the unit weights for the nominal vehicle No. 2. Since the sections of the vehicle forward and aft of the payload attachment consists of different design parameters (skin thickness, ring spacing, etc) the unit weights are divided into two sections. For definition of sections 1 and 2, see Figures 5 and 7.

Shell Bending Effects for the 60-Degree Sphere Cone Voyager Aeroshell

The design practice of selecting structural gages for the Voyager aeroshell is based on shell membrane theory. That is, the effect of shell bending is neglected in the first approximation for sizing the main structural loadcarrying member, the 60-degree conical frustum.

22

The ESM shield thicknesses chosen for this study were determined from section 3.2.2 (Table 16, T = 300, 500°F). These shield design curves (sect. 3.2.2) are conservative as they are based on a single layer of ESM with an adiabatic backface (bondline).

The development of a REKAP model for ESM was reported in Reference 26. Table 36 presents the input parameters required for the current ESM REKAP Model. Table 37 lists thermal property data for all the structures considered.

ESM shield material over the following Fiberglass structures were evaluated:

    a.   Fiberglass Honeycomb

    b.   Fiberglass thin skin

    c.   Fiberglass thin skin plus structural rings

Temperature histories and profiles for the above composites are presented in Figures 66 through 71 for both the tangency point and the end of skirt. These temperature profile curves show lower interface temperatures than the shield design curves of section 3.2.2 due to heat sink effect of the structure.

ESM shield material over the following aluminum structures were evaluated.

    a.   Aluminum Honeycomb

    b.   Aluminum thin skin

    c.   Aluminum thin skin plus structural rings.

Temperature histories and profiles are reported in Figures 72 and 73 (tangency point and end of skirt respectively) for only the ESM/Aluminum honeycomb shield structure composite since a negligible temperature rise is experienced at the ESM backface.

Description of Charring Ablator Mathematical Model

To describe the thermal behavior of a material in a re-entry environment, Reference 25, it is necessary to solve the transient heat conduction equation for each element of material through the char (if a char exists), the reaction zone, and the virgin material continuously